D 2025

U.PORTO
FEUP FACULDADE DE ENGENHARIA
UNIVERSIDADE DO PORTO

ADVANCED NUMERICAL MODELLING OF COMPLEX SINGLE AND TWO-PHASE EJECTOR FLOWS

KARLA GONÇALVES JACINTO
PhD THESIS SUBMITTED
TO FACULDADE DE ENGENHARIA DA UNIVERSIDADE DO PORTO IN
MECHANICAL ENGINEERING

ADVANCED NUMERICAL MODELLING OF COMPLEX SINGLE AND TWO-PHASE EJECTOR FLOWS

U.PORTO
FEUP FACULDADE DE ENGENHARIA
UNIVERSIDADE DO PORTO

KARLA ISABEL FREITAS GONÇALVES JACINTO

PRODEM – Doctoral Program in Mechanical Engineering

Department of Mechanical Engineering

This dissertation is submitted for the degree of Doctor in Mechanical Engineering

By the

Universidade do Porto

January 2025

Para mi papá...

Abstract

Cooling and air-conditioning (AC) systems account for 20% of global energy consumption in buildings, with mechanical compressors being the primary contributors to energy use and maintenance costs. Reducing compressor work offers a direct pathway to improving energy efficiency in AC and heat pump systems. Ejectors provide a promising solution, either by assisting the mechanical compressor in transcritical systems or by replacing it in an ejector cooling cycle. However, the design of high-performance and cost-effective ejector systems remains a significant challenge, particularly due to the complex flow dynamics involved. Existing ejector flow models lack the capacity to predict local flow variables with high accuracy. The primary objective of this thesis is to make a step-forward in ejector research by developing new approaches that result in an improved description of the flow physics in ejectors with reasonable computational effort. Both single-phase and two-phase flow ejectors were considered.

The analysis was performed using Computational Fluid Dynamics (CFD) modelling in ANSYS Fluent. For single-phase flow, a hybrid Embedded Large Eddy Simulation (ELES) model was adopted and applied to an ejector using R1234ze(E) as the working fluid. LES was employed in critical regions such as the mixing chamber and constant-area section to better resolve turbulence and shock dynamics. The results were compared to experimental data for model validation. The LES framework provided deeper insights into the flow physics within the ejector, particularly in the mixing process, including shock structure decay and turbulent mixing. A key step of the ELES approach was the use of real fluid properties and its ability to characterise turbulent mixing layers and shock structures in the mixing chamber, offering a more comprehensive understanding of ejector flow dynamics.

For two-phase flow, a novel Homogeneous Equilibrium Model (HEM-e) was developed based on the internal energy equation to improve the prediction of flow dynamics in two-phase ejectors. This model explicitly accounted for pressure work and dilatation effects. Transport source terms, as well as fluid properties, were implemented in ANSYS Fluent using User-Defined Functions (UDFs). The HEM-e model was compared against a conventional enthalpy-based approach (HEM-h) and experimental data. Results showed that the HEM-e model offered enhanced numerical stability and achieved approximately six times faster convergence compared to the HEM-h approach. It also predicted a longer shock train at the constant-area section inlet. Validation against experimental data demonstrated that both models accurately predicted motive mass flow rates, with deviations below 2%. However, both models exhibited poor performance in predicting the secondary flow rate under off-design operating conditions, highlighting the need for improved and more comprehensive experimental datasets—including both local and global flow variables—to support model development and validation.

Based on the results, it was concluded that ELES was highly effective in providing a deeper understanding of ejector mixing processes, as it significantly outperformed RANS in predicting ejector dynamics, offering detailed insights into turbulent mixing, shock structures, and supersonic-to-subsonic transitions. The newly developed HEM-e model demonstrated superior numerical stability and faster convergence compared to the conventional HEM-h model. Additionally, vapour quality was found to be highly sensitive to compressibility effects accounted for by pressure work and dilatation.

Keywords: Embedded Large Eddy Simulation, two-phase flow, ejector, Homogeneous Equilibrium Model, Computational Fluid Dynamics

Resumo

Os ar-condicionado (AC) representam 20% do consumo global de energia em edifícios, sendo os compressores mecânicos os principais responsáveis pelo consumo energético e pelos custos de manutenção. Reduzir o trabalho dos compressores é uma forma direta de melhorar a eficiência energética de sistemas de AC e de bombas de calor. Os ejetores apresentam-se como uma solução promissora, seja por auxiliar o compressor mecânico em sistemas transcríticos ou substituindo-o completamente num ciclo de refrigeração por ejetor. Contudo, o design de sistemas de ejetores de elevado desempenho continua a ser um desafio significativo, devido às dinâmicas de escoamento complexas envolvidas. Os modelos atuais de escoamento em ejetores muitas vezes não conseguem prever com precisão as variáveis locais do escoamento. O principal objetivo desta tese é contribuir para o avanço da investigação em ejetores, desenvolvendo novas abordagens que permitam uma melhor descrição da dinâmica do escoamento nos ejetores, com um esforço computacional razoável. Foram analisados ejetores com escoamento monofásico e bifásico.

A análise foi realizada através de modelação da Dinâmica de Fluidos Computacional (CFD) no ANSYS Fluent, abrangendo escoamentos monofásicos e bifásicos. Para o escoamento monofásico, foi aplicado um modelo híbrido Embedded Large Eddy Simulation (ELES) aplicado a um ejetor que utilizou R1234ze(E) como fluido de trabalho. O método LES foi utilizado em regiões críticas, como a câmara de mistura e a secção de área constante, para resolver de forma mais precisa a turbulência e a dinâmica dos choques. Os resultados foram validados com dados experimentais, demonstrando que a abordagem ELES forneceu maior precisão para os parâmetros globais do escoamento. Esta metodologia ofereceu uma compreensão mais aprofundada da física do escoamento dentro do ejetor, particularmente no processo de mistura, capturando fenómenos como o decaimento de estruturas de choque e a mistura turbulenta. Uma inovação chave da abordagem ELES foi o uso de propriedades reais do fluido e a sua capacidade de caracterizar camadas de mistura turbulenta e estruturas de choque na câmara de mistura, proporcionando uma compreensão mais abrangente da dinâmica de escoamento em ejetores.

Para o escoamento bifásico, foi desenvolvido um novo modelo de equilíbrio homogéneo (HEM-e) baseado na equação de energia interna, com o objetivo de melhorar a previsão das dinâmicas do escoamento em ejetores bifásicos. Este modelo considerou explicitamente os efeitos do trabalho de pressão e da dilatação. Os termos-fonte de transporte e as propriedades dos fluidos foram implementados no ANSYS Fluent através de User-Defined Functions (UDFs). O modelo HEM-e foi comparado com uma abordagem convencional baseada na entalpia (HEM-h) e com dados experimentais. Os resultados mostraram que o modelo HEM-e proporcionou maior estabilidade numérica e alcançou uma convergência cerca de seis vezes mais rápida do que a abordagem HEM-h. O HEM-e também previu uma cadeia de choques mais longa na entrada da secção de área constante. A validação com dados experimentais demonstrou que ambos os modelos previram com precisão os caudais mássicos do escoamento primário, com desvios inferiores a 2%. No entanto, ambos os modelos apresentaram fraco desempenho na previsão do caudal secundário em condições de operação fora do ponto de projeto, sublinhando a necessidade de conjuntos de dados experimentais mais completos e abrangentes—incluindo variáveis locais e globais—para suportar o desenvolvimento e validação de modelos.

Com base nos resultados, concluiu-se que o ELES foi altamente eficaz em fornecer uma compreensão mais aprofundada dos processos de mistura no ejetor, superando significativamente o RANS na previsão da dinâmica do escoamento no ejetor, oferecendo detalhes importantes sobre a mistura no escoamento turbulento, as estruturas de choque e as transições de escoamento supersónico para subsónico. O modelo HEM-e desenvolvido

nesta tese demonstrou maior estabilidade numérica e convergência mais rápida em comparação com o modelo convencional HEM-h. Além disso, verificou-se que o título do vapor-húmido é altamente sensível aos efeitos de compressibilidade contabilizados pelo trabalho de pressão (pressure work) e pela pressão de dilatação.

Palavras-chave: Embedded Large Eddy Simulation, escoamento bifásico, ejetor, Homogeneous Equilibrium Model, Dinâmica de Fluidos Computacional

Acknowledgments

I would like to begin by extending my heartfelt gratitude to my supervisor, Doctor Szabolcs Varga, whose remarkable expertise, steadfast guidance, and continuous support have been invaluable throughout this doctoral journey. His ability to provide clarity during challenging moments, coupled with his encouragement and genuine dedication to my success, has been a source of inspiration. I am deeply appreciative of his patience, availability, and unwavering commitment to fostering both my academic and personal growth, for which I will always be profoundly thankful.

I would like to acknowledge the financial support provided by the Fundação para a Ciência e a Tecnologia (FCT) through the doctoral grant under reference number UI/BD/150846/2021, as well as the grant 2022.28078.CPCA (https://doi.org/10.54499/2022.28078.CPCA.A0) for providing the computational resources that enabled the initiation of this research. My sincere appreciation also extends to the Institute of Science and Technology for Advanced Energy (INEGI) and the Laboratory for Energy and Transport Applications (LAETA) for their invaluable institutional support during my studies at the Faculty of Engineering, University of Porto (FEUP).

I would also like to extend my heartfelt gratitude to the Department of Thermal Engineering at the Faculty of Mechanical Engineering, Białystok University of Technology, particularly to Doctor Dariusz Butrymowicz, Doctor Kamil Śmierciew, and Doctor Wojciech Angielczyk. Their generosity in introducing me to their experimental facilities, allowing me to observe various ejector designs and industrial systems, was instrumental for my research. I am especially grateful to Doctor Dariusz Butrymowicz for providing the experimental data essential for this work.

To the professors of the Mechanical Engineering Department at FEUP, I extend my sincere thanks for their guidance, support, and invaluable advice throughout this journey. I am equally grateful to my colleagues, whose friendship and assistance made this experience both enriching and enjoyable. I would like to particularly thank Behzad Shahzamanian for his friendship and guidance during the early stages of my work, and Kashif Mushtaq, whose support and practical help in the field of investigation were immensely valuable. My special thanks go to Rui Silva, whose contributions were instrumental to this thesis. By using my code in different simulations, he provided valuable insights that greatly enhanced its functionality. His assistance in developing EES procedures, along with his support in many other aspects, was truly invaluable.

I owe my deepest gratitude to my family—my father, mother, brother, and sister—for their unwavering support and unconditional love. Since childhood, they have always made me feel capable of achieving anything, and their belief in me has been a constant source of strength. To my beloved children, Gabriel and Isabel, I am forever thankful for their understanding and sacrifices. They gave up precious time with me and yet always respected and supported my efforts. I am so proud of the incredible individuals they are. Finally, to my husband, José, I extend my heartfelt appreciation. His constant belief in me, his encouragement during the most difficult times, and his unwavering support were the foundation that allowed me to begin and successfully complete this journey.

Table of contents

1. Introduction 1
   1.1 Motivation 1
   1.2 Principal objectives of the thesis 3
   1.3 Structure of the thesis 4
2. Literature review 6
   2.1 A short introduction to ejectors and an insight into their operation principle 6
      2.1.1 Classification of ejectors 9
      2.1.2 The integration of ejectors into cooling cycles 12
      2.1.3 Definition of the ejector performance metrics and their dependence on the operating conditions 16
      2.1.4 Classification of ejector flow models 19
   2.2 Turbulence Modelling Approaches 21
      2.2.1 Reynolds Averaged Navier-Stokes (RANS) for Ejector Flow Simulations 22
         2.2.1.1 Literature Review of RANS Models Applied to Ejector Flow Dynamics 23
      2.2.2 Large Eddy Simulation (LES) in Ejector Turbulence Modelling 27
         2.2.2.1 Subgrid Scale models 28
         2.2.2.2 Subgrid Length Scale 29
         2.2.2.3 Case Studies and Applications in Ejector Flow Simulations 30
      2.2.3 Embedded LES (ELES) Modelling for Complex Ejector Flows 32
      2.2.4 Near-Wall Treatments for turbulent flows 34
   2.3 Multi-fluid dynamics 36
      2.3.1 Two-phase flow modelling in ejector 36
      2.3.2 LES two-phase flow modelling 38
3. Mathematical model development 39
   3.1 Thermodynamic property considerations 39
   3.2 The Governing equations of fluid flow 39
      3.2.1 Single-phase flow 42
      3.2.2 Two-phase flow 43
   3.3 Favre Averaging description of the governing equations of turbulence 46
      3.3.1 Favre averaged continuity equation 47
      3.3.2 Favre averaged momentum equation 47
      3.3.3 Favre averaged energy equation 48
      3.3.4 Closure equations for the governing equations 52
      3.3.5 Turbulence scales for RANS 54

3.3.6 RANS Near-Wall Treatment 55
3.4 Formulation of the large eddy simulation model 56
3.4.1 Filtering Processes for LES 57
3.4.2 Subgrid Length Scale 61
3.4.3 Turbulence scales for LES 62
3.4.4 LES Near-Wall Treatment 62
3.4.5 Interface between RANS and LES zones 63
4. Model implementation and numerical considerations 66
4.1 Computational domains for the numerical simulations 66
4.1.1 Computational domain and boundary conditions for the RANS simulation of the R1234ze(E) ejector 66
4.1.2 Computational domain and boundary conditions for ELES 69
4.1.3 Computational domain and boundary conditions for the RANS simulation of the CO_2 ejector 69
4.2 Meshing Strategy for Ejector Flow Simulations 72
4.2.1 3D Mesh Generation and Optimization for R1234ze(E) ejector flow RANS simulation 72
4.2.1.1 Surface Meshing and Refinement 73
4.2.1.2 Boundary Layer Resolution 73
4.2.1.3 Mesh Quality base line 74
4.2.2 3D Hybrid Mesh Generation for ELES 74
4.2.2.1 LES mesh preliminary assessment 74
4.2.2.2 Surface Meshing and Refinement 75
4.2.2.3 Boundary Layer Resolution 76
4.2.3 2D Mesh Generation and Optimization for CO_2 two-phase ejector flow RANS simulation 77
4.2.4 3D Mesh Generation and Optimization for CO_2 two-phase ejector flow RANS simulation 78
4.3 Development and Application of User-Defined Functions (UDFs) for Ejector Simulation 78
4.3.1 Header Configuration and Memory Allocation for UDFs in FLUENT 79
4.3.2 Implementation of a Real Gas Model Using UDRGM 80
4.3.3 Integration of the Homogeneous Equilibrium Model (HEM) with UDFs 82
4.4 Numerical considerations during the RANS ejector flow simulation 85
4.4.1 Flow Solver Algorithm for FLUENT energy equation 85
4.4.2 Flow Solver Algorithm for internal energy equation 87
4.4.3 Numerical Methods and Spatial Discretization 87
4.4.4 Convergence Time and Criteria 88

4.4.5 Mesh Independence Study 89
4.4.5.1 3D R1234ze(E) Mesh Independence Study 89
4.4.5.2 2D CO_2 Mesh Independence Study 91
4.4.5.3 3D CO_2 Mesh Independence Study 93
4.5 Numerical considerations during the ELES ejector flow simulation 96
4.5.1 Numerical Methods and Time and Space Discretization for ELES 96
4.5.2 ELES Mesh Assessment 97
5. R1234ze(E) ejector simulation results and discussion 99
5.1 Experimental Validation of the RANS CFD Model 99
5.2 Results of the 3D Embedded LES 107
5.2.1 LES Mesh Validation: TKE Resolution 108
5.2.2 Discussion of the instantaneous flow field results 111
5.2.3 Discussion of the mean flow results 118
5.2.4 Mixing layer evolution during the mixing process 124
5.3 Comparison of the ELES results with experimental data 128
5.4 Comparison of the ELES and RANS model flow field results 131
6. CO_2 ejector simulation results and discussion 135
6.1 Experimental results and definition of the boundary conditions for the CO_2 models 135
6.2 Experimental validation of the 2D axisymmetric benchmark ejector model. 137
6.3 Discussion of the 2D axisymmetric and 3D CFD model results for the HEM-h formulation 139
6.4 Comparison of 3D Symmetric Results for the HEM-h and HEM-e Models 145
6.5 Discussion of the HEM-e model results with and without considering the turbulent kinetic energy source terms 151
7. Conclusions and recommendations for future research 154
7.1 Embedded large eddy simulation model for single-phase R1234ze(E) ejector 154
7.2 Two-phase CO_2 ejector simulation 155
7.3 Suggestions for future work 156
References 159
A. Mathematical convection 175
A.1 Vectors and notation 175
A.2 Planes and Summation Notation 175
A.3 Matrices and Tensors 175
A.4 Summative Derivative 176
A.5 Gradient and Divergence Operators 177

A.6 Tensor Operations 177
A.7 Expansion of the Viscous Stress Tensor 178
B. Favre averaging rules 179
B.1 Foundational Principles of Reynolds and Favre Averaging 179
B.1.1 Scalar Decomposition and Reynolds Averaging 179
B.1.2 Favre Averaging Definitions 179
B.1.3 Pressure and Density Averaging 180
B.1.4 Key Relations in Favre Averaging 180
B.2 Application of Favre Averaging to Governing Equations 181
B.2.1 Favre Averaging the Continuity Equation 181
B.2.2 Favre averaging the momentum equation 181
B.2.3 Favre averaging the single-phase energy equation 182
B.2.4 Favre averaging the two-phase energy equation 184
B.2.5 Favre averaging the kinetic energy equation 185
C. Major differences between the HEM-e and HEM-h models 188
C.1 Integration of the Homogeneous Equilibrium Model enthalpy-based (HEM-h) with UDFs 189
D. Experimental setup details 191
D.1 R1234ze-E - Experimental setup and instrumentation details 191
D.1.1 Experimental Setup 192
D.1.2 Measurement Points and Parameters 192
D.1.3 Measurement Instruments 192
D.2 CO_2 - Experimental setup and instrumentation details 193
D.2.1 Experimental Setup 193
D.2.2 Measurement Points and Parameters 194
D.2.3 Measurement Instruments 194
E. Turbulence Modelling Parameters and Terms in FLUENT 195
E.1 Turbulent viscosity 195
E.2 Turbulent Prandtl number for k and ω 196
E.3 Turbulent kinetic energy dissipation 196
E.4 Specific dissipation rate production 196
E.5 Specific dissipation rate dissipation 197
E.6 Cross-diffusion 197
F. Properties interpolation algorithm 198
G. Sound speed models assessment – the impact on the numerical simulations 200

List of Tables

Table 2.1 – Summary of NXP designs for ejectors: main advantages, disadvantages and recommended literature with detailed information. 9

Table 2.2 – Different flow phases in the ejector (Besagni et al., 2016)..... 11

Table 2.3 – Summary of RANS Model Performance in Ejector Simulations. 26

Table 2.4 – Overview of filtering strategies in LES: advantages, disadvantages, and best applications..... 27

Table 4.1 – List of UDS defined. 80

Table 4.2 – List of macros included in the UDRGM. 80

Table 4.3 – External files with the thermodynamic table..... 81

Table 4.4 – Discretization schemes used in the CFD models..... 88

Table 4.5 – Mass flow rate convergence criteria for 3D HEM-h and 3D HEM-e models. 89

Table 4.6 – Characteristics of the meshes tested for the 3D RANS R1234ze(E) simulation. 90

Table 4.7 – Characteristics of the meshes tested for the 3D RANS CO_2 simulation. 94

Table 4.8 – Discretization schemes used in the ELES. 97

Table 5.1 – Boundary conditions for the different RANS simulations. 100

Table 5.2 – Motive and entrained mass flow rate in g/s – experimental data vs CFD results. 100

Table 5.3 – Motive mass flow rate in g/s – experimental data vs simulation results for Run1..... 130

Table 5.4 – Entrained mass flow rate in g/s – experimental data vs simulation results for Run1..... 131

Table 6.1 – Results obtained during the experimental. 136

Table 6.2 – Boundary conditions for the different RANS simulations, includes enthalpy (h) and internal energy (e) values computed using EES with Span and Wagner (1996) EoS. 137

Table 6.3 – Motive Mass Flow Rate Comparison (Experimental vs CFD Results)..... 137

Table 6.4 – Entrained Mass Flow Rate Comparison (Experimental vs CFD Results). 138

Table 6.5 – Mass flow rate results for the operating curve prediction for the 2D HEM-h. 145

Table 6.6 – Predicted mass flow rates and corresponding mass imbalance..... 145

Table 6.7 – Predicted mass flow rates and corresponding mass imbalance..... 146

Table 6.8 – Predicted mass flow rates and corresponding mass imbalance..... 151

List of Figures

Figure 1.1 – Global primary energy consumption by source. Note: In the absence of more recent data, traditional biomass consumption was assumed constant since 2015. Chart generated by Our World in Data (2024). 1

Figure 1.2 – Global air conditioner stock: recorded data from 1990 and predictions up to 2050 (International Energy Agency, 2018). 2

Figure 1.3 – Schematic representation of the thesis structure. 4

Figure 2.1 – Schematics of the Henri Giffard injector (Giffard, 1860). 6

Figure 2.2 – Ejector cross-section view and idealised pressure and velocity variation inside the ejector for refrigeration applications. 7

Figure 2.3 – An instantaneous schlieren images of the flow through a supersonic ejector (from Rao and Jagadeesh (2014)) 8

Figure 2.4 – NXP for a) constant mixing area ejector and a b) constant pressure mixing ejector. 10

Figure 2.5 – General aspect of the mixing and diffuser section for a CRMC or CRKEC ejector. 10

Figure 2.6 – a) convergent-primary nozzle and b) convergent-divergent primary nozzle. 12

Figure 2.7 –p-h diagram and component layout of a vapour-compression cooling cycle. 12

Figure 2.8 –p-h diagram and component layout of an ejector cooling cycle. 13

Figure 2.9 –p-h diagram and component layout of a cooling cycle with an ejector as an expansion device. 14

Figure 2.10 –p-h chart and component layout of a cooling cycle with a transcritical ejector. 15

Figure 2.11 – Ejector operation regimes. 17

Figure 2.12 – Motive flow expansion after the nozzle and impact in the secondary flow. 18

Figure 2.13 – Idealized isotropic turbulent kinetic energy spectrum as a function of wavenumber k. I: Largest turbulent eddies; II: Inertial subrange; III: Dissipative range, representing the smallest eddies. 21

Figure 2.14 – Different approaches to resolving eddies in turbulent flows (*adapted from* Fröhlich and Terzi (2008)). 33

Figure 2.15 – Schematic representation of interface between LES and RANS regions in ELES. 33

Figure 2.16 – Schematization of the wall regions in terms of y^+ (adapted from Pope (2000)). 35

Figure 3.1 – CO_2 typical values for vapour index (gg) and liquid index (gl) as a function of pressure (Brennen, 2005). 45

Figure 3.2 – Schematic of different eddy sizes and mesh resolution. Δcell is the characteristic cell dimension size. A, B and C represent eddies larger than the mesh size, and D is an eddy smaller than the mesh size. 57

Figure 3.3 – Schematic representation of a grid cell, where xi is the cell centre, xi' is one of the integrations points and the coloured area is the integration region. 58

Figure 3.4 – Schematic of a grid mesh with the identification of the shortest distance of the cell centre to the wall (dw), the maximum cell edge length ($hmax$) and the wall-normal grid distance (hwn) 61

Figure 3.5 – Schematic representation of the ejector simulated in this work, identifying the LES and RANS zones in the ELES, and the not-simulated zones. The inflow interface is depicted by a dashed red and grey line, while the outflow interface is indicated by a yellow double dashed line. 63

Figure 4.1 – Details of the R1234ze(E) ejector geometry in millimetres for the 3D simulation, indicating the positions of pressure transducers (P) and temperature sensors (T). 67

Figure 4.2 – R1234ze(E) ejector geometry: each colour corresponds to an ejector section. (a) Cut view of the domain (scale factor: 1:5.5). (b) 3D isometric view of the complete ejector. 67

Figure 4.3 – R1234ze(E) ejector RANS simulation flow domain, each colour corresponds to different boundary type 68

Figure 4.4 – R1234ze(E) ejector simulation flow domain, each colour corresponds to a different boundary type. 69

Figure 4.5 – (a) CO_2 ejector geometry (dimensions in mm) for the 3D simulation, indicating the positions of pressure and temperature sensors. (b) Ejector body showing sensor slots. 70

Figure 4.6 – CO_2 ejector geometry (dimensions in mm) for the 2D simulation. 70

Figure 4.7 – CO_2 ejector geometry. Each colour corresponds to a specific ejector section: (a) Cross-sectional view of the domain (scale 1:1). (b) 3D isometric view of the complete ejector. 71

Figure 4.8 – 2D axisymmetric flow domain, and corresponding boundary conditions for the CO_2 ejector RANS simulation. 71

Figure 4.9 – 3D symmetrical flow domain, and corresponding boundary conditions for the CO_2 ejector RANS simulation 72

Figure 4.10 – R1234ze(E) ejector 3D RANS mesh with identification of boundaries. 73

Figure 4.11 – Boundary layer in the ejector constant-area section interface with the diffuser: a) symmetry plan and b) xz-plan cut. 74

Figure 4.12 – Visualisation of the $\boldsymbol{f}$ –value in the LES region of a RANS R1234ze(E) simulation. 75

Figure 4.13 – Example of local refinement using the body of influence (BOI) tool. 75

Figure 4.14 – Schematic representation of a cell adjacent to the wall, with dimensions A and B identified. 76

Figure 4.15 – Schematization of a cell adjacent to the wall. 77

Figure 4.16 – Axisymmetric 2D mesh for the CO_2 ejector, with identification of blocks and boundaries. 77

Figure 4.17 – CO2 ejector 3D RANS mesh with identification of boundaries. 78

Figure 4.18 – Example of local refinement using the body of influence (BOI) tool for the CO_2 3D mesh. 78

Figure 4.19 – Header of the UDRGM with property table details for CO_2. 81

Figure 4.20 –Transport equation of the UDS internal energy, and identification of the model specific macros to compute the diffusivity term and sources 82

Figure 4.21 – Sources for the internal energy transport equation, with general-purpose macros and auxiliary UDSs: a) heat diffusion; b) work due to normal stresses; c) work due to viscous stresses and TKE dissipation. 83

Figure 4.22 – Sources for TKE transport equation, with general-purpose macros and auxiliary UDSs: a) pressure dilatation; b) pressure work. 83

Figure 4.23 – Sources for the internal energy transport equation in LES, with general-purpose macros and auxiliary UDSs: a) heat diffusion; b) work due to normal stresses; c) work due to viscous stresses and TKE dissipation. 84

Figure 4.24 – Solution procedure for the density-based solver in FLUENT. 85

Figure 4.25 – Solution procedure for the segregated and coupled pressure-based solver in FLUENT. 86

Figure 4.26 – Solution procedure for the coupled pressure-based solver in FLUENT using the internal energy-based energy equation and UDRGM. 87

Figure 4.27 – Impact of the mesh size on the ejector inlet mass flow rates. 90

Figure 4.28 – Predicted static wall pressure using meshes a) A to C, and b) D to F vs experimental results for run 1 91

Figure 4.29 – Impact of mesh size on the ejector motive mass flow rate with varying axial divisions 92

Figure 4.30 – Impact of mesh size on the ejector entrained mass flow rate with varying axial divisions. 93

Figure 4.31 – Impact of the mesh size on the ejector inlet mass flow rates. 94

Figure 4.32 – Impact of the boundary layer resolution and mesh cell count on the ejector inlet mass flow rates. 95

Figure 4.33 – Predicted static axial pressure profiles for a) meshes A, B, C, and F, and b) meshes D, E, G, H, and I 96

Figure 4.34 – Maximum characteristic cell size for LES mesh according to equation (4.1). 98

Figure 4.35 – Computed f-value distribution for the selected LES region of the ELES mesh. 98

Figure 5.1 – Simplified diagram (left) and photo of the experimental rig (right) (Kracik et al., 2018). 99

Figure 5.2 – The ejector entrainment ratio (λ) vs. outlet pressure for experimental data and CFD results (note: boundary conditions vary across runs) 101

Figure 5.3 – Experimental wall pressure profile and CFD RANS results for Run 1 102

Figure 5.4 – Experimental wall pressure profile and CFD RANS results for Run 2 102

Figure 5.5 – Experimental wall pressure profile and CFD RANS results for Run 3 102

Figure 5.6 – Experimental wall pressure profile and CFD RANS results for Run 4 103

Figure 5.7 – Experimental wall pressure profile and CFD RANS results for Run 5.....103
Figure 5.8 – Experimental wall pressure profile and CFD RANS results for Run 6.....103
Figure 5.9 – Experimental wall pressure profile and CFD RANS results for Run 7.....103
Figure 5.10 – Comparison of experimental and CFD temperature data obtained for Run 1.....104
Figure 5.11 – Comparison of experimental and CFD temperature data obtained for Run 2.....105
Figure 5.12 – Comparison of experimental and CFD temperature data obtained for Run 3.....105
Figure 5.13 – Comparison of experimental and CFD temperature data obtained for Run 4.....105
Figure 5.14 – Comparison of experimental and CFD temperature data obtained for Run 5.....105
Figure 5.15 – Comparison of experimental and CFD temperature data obtained for Run 6.....106
Figure 5.16 – Comparison of experimental and CFD temperature data obtained for Run 7.....106
Figure 5.17 – Cross section view of the LES region in the 3D simulation domain with identification of the different sections for local result analysis.....107
Figure 5.18 – Evolution of predicted mass flow rate over simulation time.....108
Figure 5.19 – Energy spectra of axial velocity fluctuations in the ejector axis for different x/L.....109
Figure 5.20 – Cell percentage vs resolved TKE for different axial locations in the ELES computational domain.....110
Figure 5.21 – Percentage of resolved turbulent kinetic energy in the LES section.....111
Figure 5.22 – Instantaneous static pressure field over two axial direction cross-section planes.....111
Figure 5.23 – Instantaneous static pressure field over two transversal planes within the constant-area section.....112
Figure 5.24 – Static pressure range at various sections represented in Figure 5.17.....112
Figure 5.25 – Instantaneous static temperature field over two streamwise midspan plane.....113
Figure 5.26 – Static temperature range at various sections represented in Figure 5.17.....113
Figure 5.27 – Numerical pseudo-Schlieren images showing flow structure and shock identification in the flow domain.....114
Figure 5.28 – Numerical pseudo-Schlieren images showing flow structure details at the primary nozzle exit, the arrow indicates the vortex structure present in the shear layer.....114
Figure 5.29 – Numerical pseudo-Schlieren images showing the flow structure after reaching subsonic conditions.....115

Figure 5.30 – Q-criterion contours showing vortex structures over two streamwise midspan planes, overlaid on numerical pseudo-Schlieren images. 115

Figure 5.31 – Pseudo-Schlieren images overlaid with Q-criterion contours, showing vortex rotational direction near the domain entrance. 116

Figure 5.32 – Instantaneous axial velocity field over two streamwise midspan planes. 116

Figure 5.33 – Instantaneous Mach number field over two streamwise midspan planes, with the sonic line in blue. Vertical lines indicate the compound flow regime: red for compound supersonic flow and yellow for compound subsonic flow. 117

Figure 5.34 – Mean streamwise velocity profile normalised by the centreline velocity plotted against the normalised radius at different streamwise positions in the mixing section. 119

Figure 5.35 – Mean streamwise velocity profile normalised by the centreline velocity plotted against the normalised radius at different streamwise positions for the constant area section inlet until x/L=0.181. 119

Figure 5.36 – Overlay of the normalised mean streamwise velocity profile and the instantaneous pseudo-Schlieren image for the ejector cross-section at x/L=0. 120

Figure 5.37 – Mean streamwise velocity profile normalised by the centreline velocity plotted against the normalised radius at different streamwise positions for the constant area section: a) for $0.181 \leq x/L \leq 0.50$; b) for $0.661 \leq x/L \leq 0.911$ and c) corresponding pseudo-Schlieren image. 121

Figure 5.38 – Mean streamwise velocity profile normalised by the centreline velocity plotted against the normalised radius at different streamwise positions for $x/L \geq 0.92$. 122

Figure 5.39 – Static pressure profile distribution along the mixing and constant area section; the dashed line represents the centreline pressure, and the solid line represents the wall pressure, both normalized with the corresponding x/L=0 pressure value. 122

Figure 5.40 – Wall shear stress profile distribution along the mixing and constant area sections, normalized with the x/L=0 value. 123

Figure 5.41 – Relative to the maximum radius displacement (dashed line) and momentum thickness (solid line). 123

Figure 5.42 – Shape factor ($\delta * / \gamma$) distribution. 124

Figure 5.43 – Contours of instantaneous radial velocity fluctuations in a streamwise midplane: a) covering the mixing chamber and constant-area section; b) a zoomed-in view of the mixing chamber and constant-area entrance, identifying the wall shear stress, oblique shocks and mixing layer positions. 125

Figure 5.44 – Profiles of the normalised radial RMS velocity fluctuation at different locations in the mixing section: a) for the mixing section entrance and $x/L \leq -0.037$; b) for $-0.024 \leq x/L \leq 0$ 125

Figure 5.45 – Profiles of the normalised radial RMS velocity fluctuation at different locations in the mixing section: a) for $0 \leq x/L \leq 0.073$; b) for $0.109 \leq x/L \leq 0.181$. 126

Figure 5.46 – Profiles of the normalised radial RMS velocity fluctuation at different locations in the mixing section: a) for $0.181 \leq x/L \leq 0.5$; b) for $0.661 \leq x/L \leq 0.911$. 127

Figure 5.47 – Profiles of the normalised radial RMS velocity fluctuation at different locations in the mixing section for $0.920 \leq x/L \leq 0.978$. 128

Figure 5.48 – Comparison of static wall pressure profiles through the mixing and constant-area sections for RANS, LES, and experimental data. The shaded area represents the range of LES instantaneous results. 129

Figure 5.49 – Comparison of static temperature profiles through the mixing and constant area sections for RANS, ELES, and experimental results. The shaded area represents the variation range of ELES instantaneous results. 130

Figure 5.50 – RANS and LES region instantaneous static pressure field. 131

Figure 5.51 – RANS and LES region instantaneous static temperature field: a) using the same temperature scale for both results; b) without scale. 132

Figure 5.52 – RANS and LES region instantaneous axial velocity field. 133

Figure 5.53 – Instantaneous Mach number field for the RANS and LES region, with the sonic line in blue. Vertical lines indicate the compound flow regime: red for compound-supersonic flow and yellow for compound-subsonic flow. 133

Figure 6.1 – Simplified diagram of the experimental rig. 136

Figure 6.2 – Comparison of experimental wall pressure profile with CFD HEM-h results for Runs 1, 2, and 3 in the constant area section of the ejector. 138

Figure 6.3 – Comparison of experimental and simulated static axial temperature profiles for Runs 1, 2, and 3. 139

Figure 6.4 – Static pressure field on the symmetry plane in the mixing chamber and constant-area section for the 2D and 3D models. 139

Figure 6.5 – Static pressure along the ejector axis in the mixing chamber and constant-area section for the 2D and 3D models. 140

Figure 6.6 – Static pressure at transversal sections:(constant-area section inlet (x=0 mm) and sensor positions 1, 2, and 3, each with a different pressure scale. 140

Figure 6.7 – CFD-predicted static temperature along the ejector axis compared to experimental measurements. 141

Figure 6.8 – CFD-predicted specific enthalpy along the ejector axis for 2D and 3D HEM-h. 142

Figure 6.9 – Density (solid lines) and vapor quality (dashed lines) along the ejector axis for the 3D and 2D models (single point experimental density at the ejector outlet also indicated). 143

Figure 6.10 – Mach number field over the symmetry plane for the motive nozzle for 2D and 3D HEM-h. 143

Figure 6.11 –a) Mach number contours over the symmetry plane for the mixing chamber and constant area section; b) Speed of sound (solid lines) and axial Mach number profiles (dashed lines). 144

Figure 6.12 – a) Static pressure field and b) axial static pressure profile for the mixing chamber and constant area section. 147

Figure 6.13 – CFD-predicted static temperature along the ejector axis compared to experimental measurements. 147

Figure 6.14 – a) Specific internal energy field for the 3D HEM-h model (top) and the 3D HEM-e model (bottom) displayed over a streamwise midspan plane encompassing the mixing chamber and constant-area section; b) CFD-predicted specific internal energy profiles along the ejector axis for HEM-h and HEM-e. 148

Figure 6.15 – Mach number at the ejector axis for the 3D HEM-h and 3D HEM-e B and LF models. 149
Figure 6.16 – Mach number at the motive nozzle in the symmetric plane for HEM-e and HEM-h model. 150
Figure 6.17 – Mach number distribution in the mixture chamber and in constant area section for HEM-e (top half) and HEM-h (bottom half) models. 150
Figure 6.18 – Static pressure along the ejector axis for HEM-e, and HEM-e TKE. 151
Figure 6.19 – Density along the ejector axis, focusing on the shock train. 152
Figure 6.20 – Vapour quality along the ejector axis for HEM-e, and HEM-e TKE. 152
Figure C.1 –Transport equation of the UDS enthalpy, and identification of the model specific macros to compute the diffusivity term and sources. 189
Figure C.2 – Sources for the enthalpy transport equation for a 3D simulation: a) mechanical energy; b) irreversible dissipation of kinetic energy fluctuation; c) dissipation of turbulent kinetic energy. 189
Figure C.3 – Sources for the enthalpy transport equation for a 2D axisymmetric simulation: a) mechanical energy; b) irreversible dissipation of kinetic energy fluctuation; c) dissipation of turbulent kinetic energy. 190
Figure D.1 - Simplified diagram of the ejector test rig (a) and the corresponding theoretical p-h diagram (b). 191
Figure D.2 - Simplified diagram of the ejector test rig (a) and the corresponding theoretical p-h diagram (b). 193
Figure F.1 – Flow chart of the interpolation algorithm. 198
Figure F.2 – Flow chart of the algorithm of the function used to compute iP. 199
Figure G.1 – Predicted pressure profiles along the ejector axis. 200
Figure G.2 – Predicted density profiles along the ejector axis. 200
Figure G.3 – Predicted specific internal energy profiles along the ejector axis. 201
Figure G.4 – Predicted vapour quality profiles along the ejector axis. 201
Figure G.5 – Predicted sound speed along the ejector axis. 202
Figure G.6 – Predicted Mach number profiles along the ejector axis for different sound speed models. 202

Nomenclature

List of Abbreviations

1/2/3D	One/Two/Three-dimensional
AC	Air conditioner
BC	Boundary condition
BOI	Body of Influence
cas	Contant-area section
CBP	Critical back pressure
CFD	Computational fluid dynamics
CMA	Constant mixing area
CO_2	Carbon dioxide
COP	Coefficient of Performance
CPM	Constant pressure mixing
CPU	Central processing unit
CRKEC	Constant rate of kinetic energy change
CRMC	Constant rate of momentum change
DEM	Delayed equilibrium model
DNS	Direct numerical simulation
EES	Engineering Equation Solver
ELES	Embedded large eddy simulation
EoS	Equation of State
GWP	Global warming potential
HC	Hydrocarbon
HCFC	Hydrochlorofluorocarbons
HEM	Homogeneous equilibrium model
HEM-e	HEM internal energy equation based
HEM-h	HEM enthalpy energy equation based
HFC	Hydrofluorocarbons
HFO	Hydrofluoroolefin
HPC	High performance computing
HRM	Homogeneous relaxation model
LDKM	Lagrangian dynamic kinetic model
LES	Large eddy simulation
MILES	Monotonically integrated large-eddy simulation
NH_3	Ammonia
NIST	National Institute of Standards and Technology
NXP	Nozzle exit position
ODP	Ozone depletion potential
PIV	Particle image velocimetry
PLIF	Planar laser-induced fluorescence
PP	Pressure profile
PR	Pressure recovery
RANS	Reynolds-averaged Navier–Stokes
RMS	Root-mean-square
RNG	Renormalization Group
RSM	Reynolds stress model

SGS	Subgrid scale
SMFR	Secondary mass flow rate prediction
SST	Shear stress transport
SWP	Shock wave position
TFM	Two-fluid model
TKE	Turbulent kinetic energy
T-SST	Transition shear stress transport
UDF	User defined function
UDM	User defined memory
UDRGM	User defined real gas model
UDS	User defined scalar
VGE	Variable geometry ejector
WALE	Wall-adapting local eddy viscosity
WMLES	Wall-modelled large eddy simulation
WTP	Wall temperature profile

Latin Symbols

A	Area	m^2
AR	Aspect ratio	-
B	Empirical constant.	-
b_{ij}	Normalized anisotropy tensor	-
c	Speed of sound	m/s
c_p	Specific heat capacity	J/(kg K)
C_ε	Constant for the turbulent kinetic energy dissipation in the subgrid scale	
d	Number of molecular degrees of freedom	-
d_w	Wall distance	m
e	Specific internal energy	J/kg
E	Total specific energy	J/kg
ER	Entrainment ratio	-
f	Function of the thermodynamic property for the two phases	-
$\boldsymbol{f}$	Indicator variable for LES mesh assessment	-
g	Function of the thermodynamic property of the fluid	-
G	Gibbs free energy	J
G_i	Filters function	-
h	Specific enthalpy	J/kg
$\mathcal{H}$	Heat transfer relaxation	-
H	Source term for the heat transfer between phases	W/m^3
h_{max}	Maximum cell edge length	m
h_{wn}	Wall-normal grid distance	m
I	Source term for the volume transfer between phases	1/s
iP, iU	Pressure and internal energy index	-
K	Source term for the mass transfer between phases	$Pa.s/m^2$
k	Turbulent kinetic energy	m^2/s^2
$\mathscr{k}$	Angular waver number	rad/m
$\boldsymbol{\kappa}$	Thermal conductivity	W/(m.K)
$\mathcal{K}$	Mass transfer relaxation	-
l	Length scale	m
ℓ_{eddy}	Eddy size	m

L_Δ	Eddy length scale	m
M	Source term for the momentum transfer between phases	Pa/m
$\mathcal{M}$	Momentum transfer relaxation	-
$\dot{m}$	Mass flow rate	kg/s
Ma	Mach number	-
Ma_{T0}	Threshold turbulent Mach number	-
N	Number of moles	-
n	Number of cells faces in the injection plane	-
$\boldsymbol{N}$	Number of vortices	-
$N_\mathrm{x}, N_\mathrm{y}, N_\mathrm{z}$	Number of cells in the x, y and z directions	-
$\wp$	Volume transfer relaxation	-
$\mathcal{P}$	Turbulent kinetic energy production	kg/(m.s^3)
p	Static pressure	Pa
p_crt	Critical pressure	Pa
p_m	Mechanical pressure	Pa
q	Heat flux	W/m^2
R	Total radius of the section	m
r	Radial coordinate	m
r_A	Area ratio	-
s	Specific entropy	J/(kg K)
$\mathcal{S}$	Inlet cross-sectional area	m2
S	Strain rate	1/s
$\dot{S}$	Source term in a transport equation	W/m^3
t	Time	s
T	Temperature	K or °C
t	Time length scale	s
t	Relaxation time	s
t_c	Characteristic flow-through time	s
$\mathrm{TKE}_\mathrm{res}$	Percentage of resolved TKE in LES	%
u	Velocity length scale	m/s
U, V, W	Mean velocity	m/s
u, v, w	Velocity vector components in Cartesian coordinates	m/s
u_τ	Shear or friction velocity	m/s
V	Volume	m^3
$\boldsymbol{x}$	Vapour quality	-
x, y, z	Cartesian coordinates	m
Δy	Distance from the wall	m

Greek Symbols

α	Void fraction	-
$\alpha_2, \alpha_3, \alpha_4$	Constant values for pressure dilatation correlation	-
β	Compound choke indicator	-
β^*	Coefficient considering compressibility effects	-
β_i^*, ξ^*	Constants for compressibility corrections	-
Γ	Diffusion coefficient	m^2/s
$\mathit{\Gamma}$	Blending function	-
Γ_j	Vortex circulation	m^2/s
γ	Momentum thickness	m^2

Δ	Cell length	m
Δ_i	Cut-off box size in the i^{th} direction	m
δ	Relative error	%
δ_{ij}	Kronecker delta ($\delta_{ij} = 1$ if $i = j$ and $\delta_{ij} = 0$ if $i \neq j$)	-
δ^*	Displacement thickness	m^2
ϵ	Fraction of vapour or liquid that exchange heat with each other	-
ε	Turbulent kinetic energy dissipation rate	m^2/s^3
η	Efficiency	-
$\eta_j(\vec{x})$	Vortex spatial distribution	-
θ	Angular coordinate	rad
κ	Von Kármán constant	-
λ	Entrainment ratio	-
μ	Dynamic viscosity	kg/(m.s)
μ^*	Chemical potential	J/kmol
ξ	Vortex size	M
Π	Compression ratio	-
ρ	Density	kg/m^3
ς	Longitudinal viscosity (second viscosity)	kg/(m.s)
σ_{ii}	Normal stress	Pa
σ_T	Turbulent Prandtl number	-
σ_{SGS}	Subgrid Prandtl number	-
τ	Shear stress	Pa
φ,$\emptyset$	Scalar	--
ψ	Bulk viscosity	kg/(m.s)
Ψ	Relaxation scale for $\overline{u''}$	S
Ω	Vorticity magnitude	1/s
ω	Specific turbulence dissipation rate	s^{-1}
$\omega(\vec{x}, t)$	Vorticity field	m^2/s

Subscripts

0	Reference position (constant-section inlet)
ASH	ASHRAE
aux	Auxiliary variable
c	centreline
cas	Constant-area section
comp	compressor
d	dilatation
eff	Effective (considers turbulent and laminar properties)
EH	Elbel and Hrnjak
EVP	Ejector vapour compression
evap	evaporator
exp	Experimental value
g	Vapour phase
i, j, k	indices in the Einstein summation notation
int	interface
l	Liquid phase

log	Logarithm region
out	Ejector outflow
$\mathrm{p, m}$	Defines the phase
pr	Primary ejector inlet - motive inlet flow
RANS	RANS result
s	solenoidal
sec	Secondary ejector inlet - entrained flow
SGS	Subgrid scale
T	turbulent
tan	all-adjacent cell centroid
th	Nozzle throat
visc	Viscous sublayer
w	wall
η	Kolmogorov scales
∞	Free stream

Superscript

$+$	Non-dimensional / characteristic value near-wall
$*$	dimensionless velocity (or alternative velocity scale)
$\overline{\varphi}$	averaged component of the scalar φ
$\tilde{\varphi}$	density-weighted average
φ'	fluctuation around the mean
φ''	Favre fluctuation
SGS	subgrid sacale
R	residual

Chapter 1

So why go to all this trouble?
The answer is,
we have only just begun.

David Wilcox (2006)

Introduction

1.1 Motivation

The exponential growth in global energy consumption since the industrial revolution has been supported primarily by the use of fossil fuels such as coal, oil, and gas (Figure 1.1). This reliance on non-renewable resources has led to unsustainable carbon dioxide emissions and an accelerated climate change that may threaten the ecosystem as we know. Therefore, a global shift towards the exploitation of renewable energy sources, energy-efficient technologies, and environmentally friendly materials is required to combat greenhouse gas emissions and climate change.

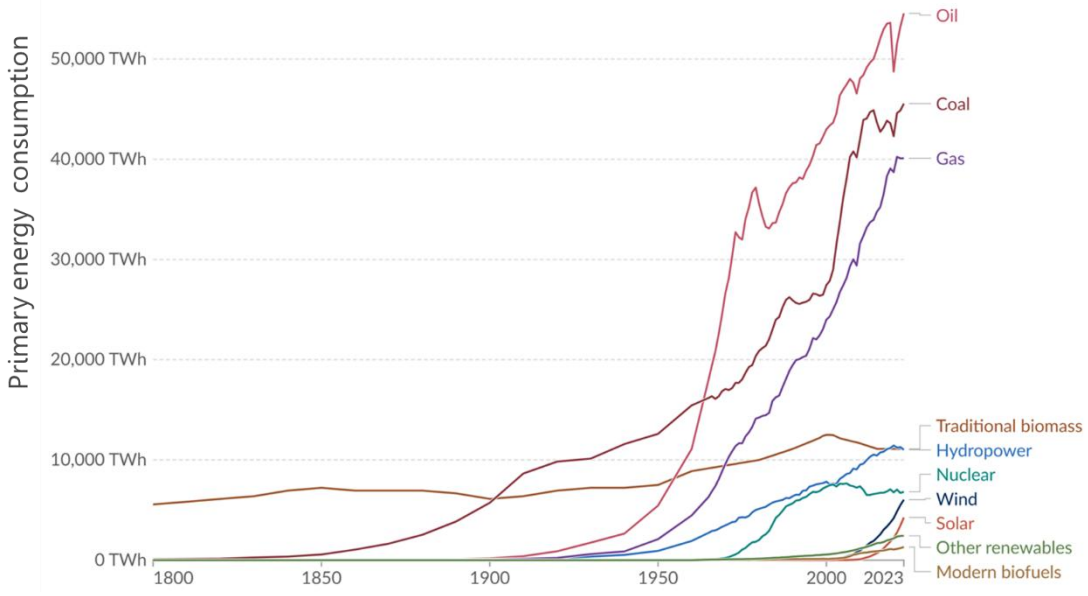


Figure 1.1 – Global primary energy consumption by source. Note: In the absence of more recent data, traditional biomass consumption was assumed constant since 2015. Chart generated by Our World in Data (2024).

Among the sectors with the highest energy demands, cooling and air conditioning systems stand out as major contributors. Air conditioners alone account for approximately 20% of final energy use in buildings (International Energy Agency, 2018), with demand expected to grow substantially in the coming decades, as shown in Figure 1.2.

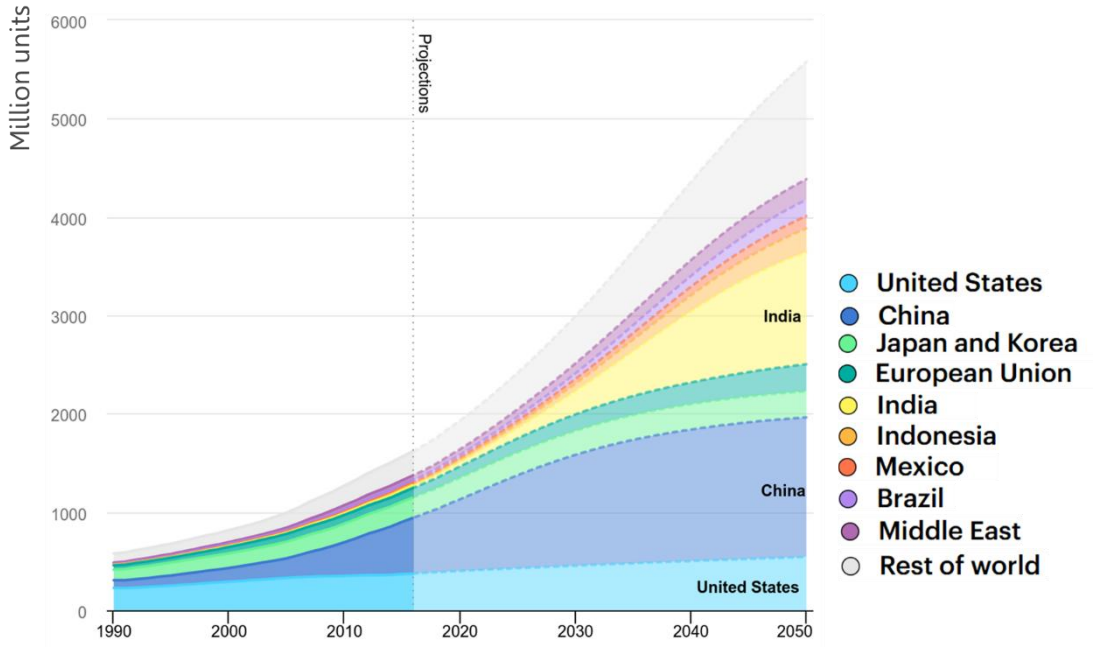


Figure 1.2 – Global air conditioner stock: recorded data from 1990 and predictions up to 2050 (International Energy Agency, 2018).

Given that the primary energy consumer in air conditioning systems is the mechanical compressor, it becomes imperative to find innovative solutions for reducing their electricity consumption. Ejectors emerge as promising technological options by offering means to assist or replace mechanical compressors in refrigeration systems (Sarkar, J., 2012). Their lack of moving parts, relatively low capital and operating costs, and energy efficiency improvement potential make them attractive for sustainable cooling technologies. Several studies indicate that the integration of ejector technology for example into transcritical cooling cycles can improve system efficiency by 10–30% (Nakagawa et al., 2011; Elbel and Lawrence, 2016).

While the advantages of ejectors integration into refrigeration and air conditioning cycles are evident, the choice of working fluid also plays a critical role in determining overall system performance and environmental impact. Historically, refrigerants such as hydrofluorocarbons (HFCs) and hydrochlorofluorocarbons (HCFCs) were widely used. However, their high Global Warming Potential (GWP) and Ozone Depletion Potential (ODP) have motivated policymakers and manufacturers to shift towards low-GWP alternatives hydrofluoroolefins (HFO) (e.g. R1234ze(E)), inorganic (e.g. CO_2 and NH_3) and hydrocarbon (HC) (e.g. R290 and R600a). These refrigerants offer significant advantages, including low environmental impact, excellent thermodynamic properties, and compatibility with modern cooling technologies (Bai et al., 2019; Ringstad et al., 2020).

Carbon dioxide stands out for its low GWP and favourable characteristics such as non-flammability, non-toxicity, low cost and favourable thermodynamics properties (Ringstad et al., 2020). However, its low critical temperature (30.98°C) leads to some technological challenges, especially for applications in relatively warm climates, such as Portugal. When the heat rejection temperature is higher than the critical temperature, the cooling cycle using CO_2 as a working fluid must operate in a transcritical mode. In a transcritical CO_2 cooling system, the high compressor exit pressures demand significant compression work and a robust construction. To reduce mechanical compression work and to recover a part of the expansion losses, ejectors can be integrated into the refrigeration system.

Innovative CO_2 flashing ejector cycles have been extensively studied (Palacz et al., 2015) to improve performance and operation stability of high-pressure transcritical systems. Studies have demonstrated that CO_2 ejector refrigeration can achieve up to 25% energy savings compared to HFC-based systems (Gullo et al., 2019).

Despite their potential, the full understanding of ejector flow, which is characterised by supersonic velocities and unique turbulence, often accompanied by phase change, remains to be achieved. Without thorough understanding, it is difficult to design optimal systems that operate with maximum performance under different conditions. The development of mathematical models will play an important role in this. Accurate modelling of the ejector flow field is rather challenging due to the inherent interactions between shockwaves, turbulence, and phase change. While computational models have progressed significantly from relatively simple empirical approaches and zero-dimensional models to sophisticated three-dimensional simulations, many challenges still remain. Reynolds-Averaged Navier-Stokes (RANS) models, though computationally efficient, are limited in realistically capturing local flow details such as shock structures and turbulence (Varga, Soares, et al., 2017). Advanced techniques such as Large Eddy Simulation (LES) could provide improved accuracy but they require significant computational resources and cause additional complexity (Jiang, X. et al., 2010). Direct Numerical Simulation (DNS) could be an option with no compromise to simulate ejector flows, however, today this type of model is still impractical due to prohibitive computational demands (Jiang, X. et al., 2010).

These challenges show the need for advanced numerical modelling approaches that balance accuracy and efficiency. This research aimed to address the limitations of commonly used numerical models for simulating ejector flows by providing a step forward in understanding the local physics of ejector operation, thereby contributing to the design of more sustainable cooling systems. This study advances ejector research by applying innovative turbulence modelling techniques to the analysis of ejectors operating with environmentally sustainable refrigerants, thereby addressing global energy challenges and promoting environmental sustainability.

1.2 Principal objectives of the thesis

The primary goal of this research was to achieve advancement in ejector flow modelling concerning both single-phase and two-phase applications. Existing models are known to have their limitations in capturing the complex dynamics of ejector flow fields, particularly the local physics of mixing. This study seeks to make a step-forward in ejector research by developing new approaches that result in an improved description of the flow physics in ejectors with reasonable computational effort.

To achieve the main goals, the research was structured around two specific objectives. The first objective was to develop advanced numerical models for two-phase ejectors by extending the capabilities of the Homogeneous Equilibrium Model (HEM). This extension involved incorporating pressure work and dilatation effects into the internal energy-based formulation, enabling a more accurate representation of key flow phenomena, such as compressibility, shockwave dynamics, and turbulence in high-speed ejector flows. The second objective focused on investigating turbulence modelling strategies and assessing the performance of RANS methods and hybrid approaches such as Embedded LES (ELES). Particular effort was made to describe turbulence, mixing layers, and shockwave dynamics in ejector flows in detail. Validation of the developed models

with experimental data was another objective of the thesis. Comparison to experimental results, permitted the assessment of how close the numerical results were to observations and point out the urgent need for high-quality data for ejector research.

By achieving these defined objectives, the advancement in numerical modelling methodologies creates a robust framework for the analysis and optimisation of ejector performance. The findings are expected to contribute to the development of next-generation ejector designs, enabling their improved efficiency and integration into practical applications such as refrigeration systems.

1.3 Structure of the thesis

This thesis is organised into seven chapters in agreement with the work performed, and additionally a reference list and appendixes. The structure of the main body of the document is schematized in Figure 1.3, identifying the interconnection between chapters and the information flow between topics addressed.

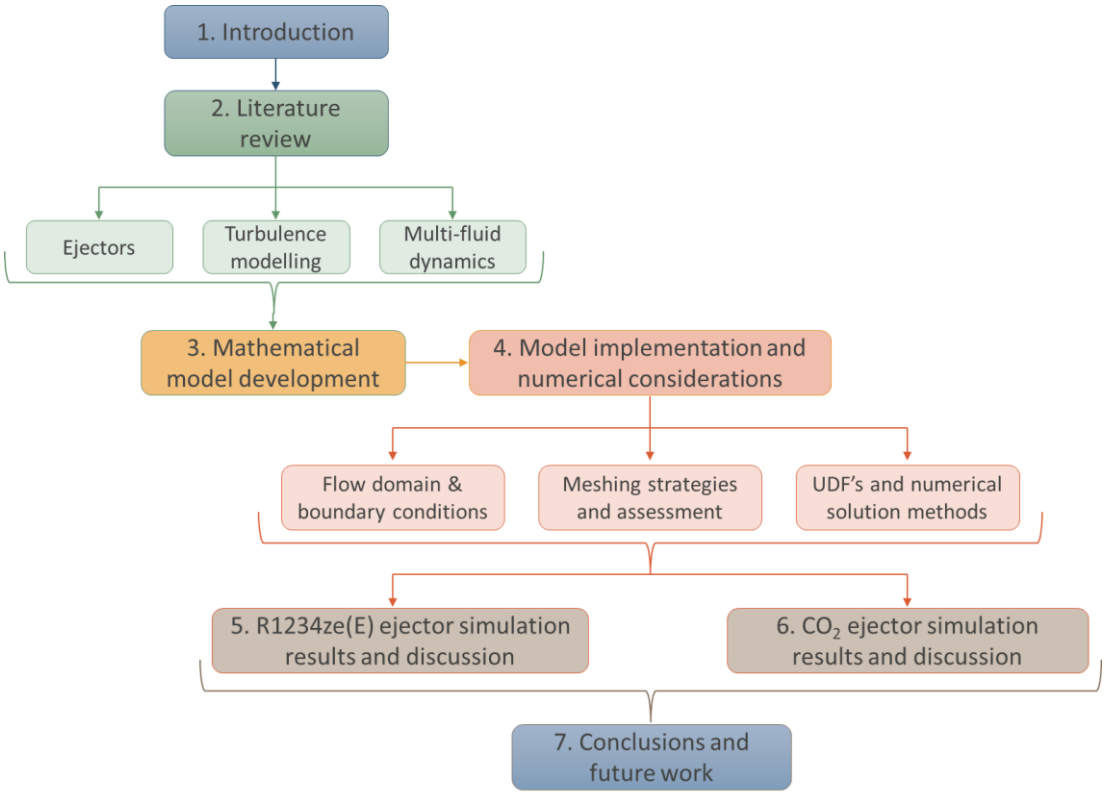


Figure 1.3 – Schematic representation of the thesis structure.

The first introductory chapter establishes the context for the research motivations and presents the main objectives of the work performed.

A comprehensive literature review is provided in the second chapter, covering three critical areas: ejectors, turbulence modelling, and multi-fluid dynamics. Ejectors are introduced by discussing their operating principles, classifications, integration into cooling systems, performance metrics, and dependencies on operating conditions. This is followed by an overview of modelling techniques, starting with the discussion of simplified one-dimensional approaches to more advanced two- and three-dimensional computational fluid dynamic (CFD) simulations. The second section focuses on turbulence modelling, specifically RANS and LES methods, including relevant strategies

such as ELES to reduce computational costs. The third section examines multi-fluid dynamics, particularly its application to two-phase flow in ejectors, reinforcing the relevance of these methods for accurately modelling compressible flows.

Chapter 3 provides details of the mathematical models developed in this study. It starts with the thermodynamic property definitions and presents the governing equations for single- and two-phase turbulent flows. The process of Favre averaging, along with the turbulence models developed for RANS and LES simulations, is discussed in depth. Specific source terms required to address the challenges of ejector flow modelling are also introduced.

Chapter 4 focuses on the implementation of these models and the numerical methods employed into the FLUENT software. Key considerations include the definition of computational domains, meshing strategies, and boundary conditions for both RANS and LES simulations. The chapter also discusses the experimental data used for model validation. The development of User-Defined Functions (UDFs) in FLUENT, and the numerical solution methods, including discretisation schemes and mesh assessments are also presented.

The fifth chapter discusses the results of the R1234ze(E) ejector simulations. It starts with the validation of RANS results against experimental data, establishing a benchmark for subsequent LES simulations. The analysis of mesh quality, instantaneous flow fields, mean flow features, and the mixing layer evolution are addressed. Finally, the ELES results are compared with experimental observations and the results from RANS simulations.

Chapter 6 focuses on the results obtained for simulating a two-phase CO_2 ejector using low motive pressure conditions. First, the validation of a benchmark model is performed with experimental data. A comparison between 2D axisymmetric and 3D simulations are presented, followed by a detailed analysis of the developed two-phase flow model results.

The main conclusion of the work performed are summarised in Chapter 7 highlighting the thesis's contributions to ejector flow modelling and research. Based on the finding of the thesis, recommendations for future research are proposed.

Chapter 2

the whole phenomenon of turbulence
[was] probably invented by the Devil
on the seventh day of Creation
(when the Good Lord wasn't looking)
Peter Bradshaw (1993)

Literature review

2.1 A short introduction to ejectors and an insight into their operation principle

The first reference to an ejector was found in the patent "Feed Water Apparatus for Steam Boilers" filed by Henri Giffard in 1860 (Giffard, 1860) to supply water to steam boilers. The motive fluid was steam from the boiler, and the secondary fluid was liquid water. The so-called injector device disclaimed in the patent is depicted in Figure 4.1.

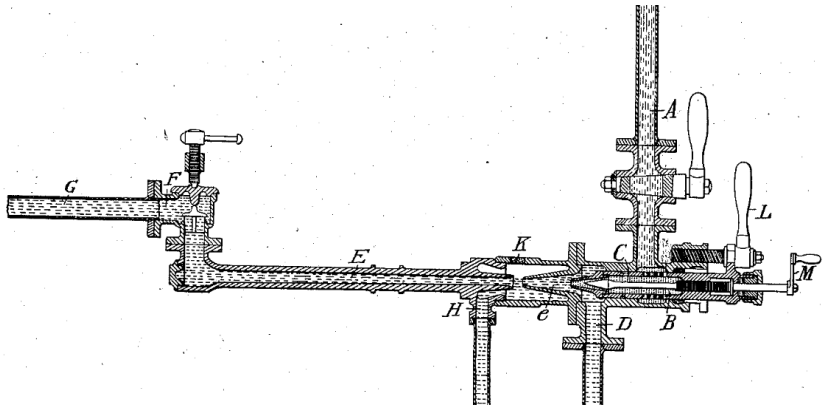


Figure 2.1 – Schematics of the Henri Giffard injector (Giffard, 1860).

Later in the 20th century, Gay (1931) proposed the first refrigeration cycle using a two-phase ejector, marking significant progress in ejector technology. Since then, several scientific publications have been available, including experimental works on the different applications of ejectors (Rankine, 1869; Langmuir, 1916; Ashley, 1934; Work and Miller, 1940; Fondrk, 1952).

Despite early developments, a comprehensive understanding of ejector operation has not been achieved until the past few decades. Kornhauser (1990) made significant contributions by developing mathematical models for two-phase ejectors. However, ejector performance remained difficult to predict accurately due to the complexity of fluid interactions. Over the past two decades, interest in ejector technology has grown exponentially, as evidenced by the increasing number of scientific publications on the topic (Sarkar, J. 2012; Hafner et al., 2014; Elbel and Lawrence, 2016; Aidoun et al., 2019; Besagni, 2019). Ejectors are now used not only in refrigeration cycles but also in other important fields of applications (Besagni et al., 2016; Shahzamanian et al., 2021).

Generally speaking, an ejector is a device that increases the pressure of a low-pressure fluid (secondary flow) to a higher-level using heat, without the need of a rotating shaft or other moving parts. It utilizes the energy from a high-pressure fluid, known as the primary flow, to boost the pressure of the secondary flow. Figure 2.2 shows the

schematics of a conventional supersonic ejector with the idealised pressure and velocity profiles along its length, particularly for refrigeration applications. Its key components: are the motive nozzle, suction chamber, mixing chamber, constant-area section, and diffuser.

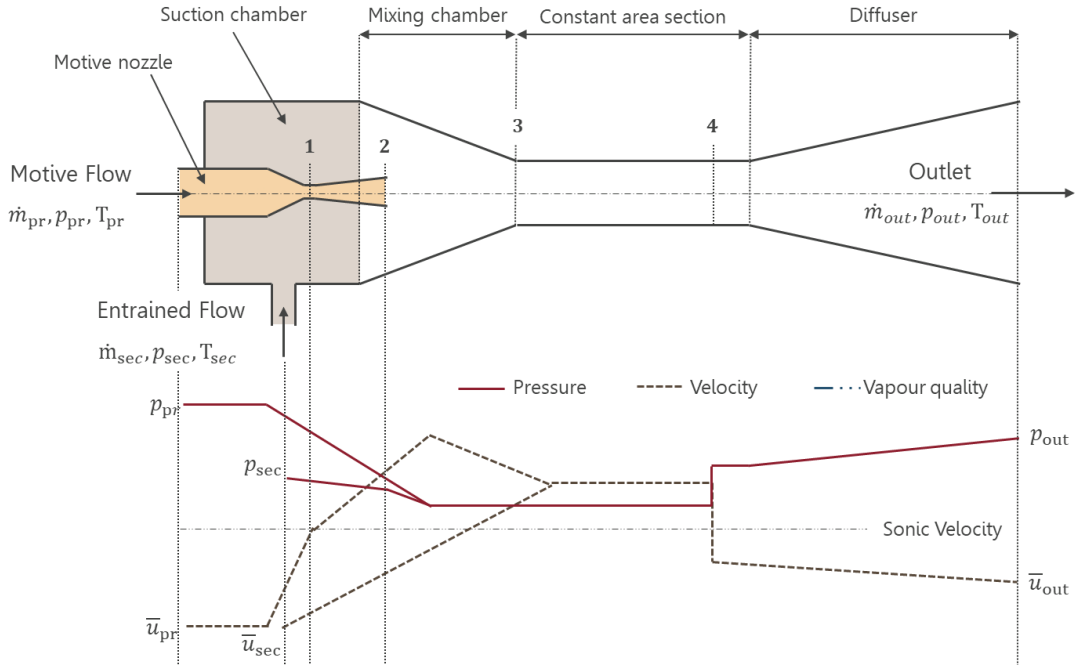


Figure 2.2 – Ejector cross-section view and idealised pressure and velocity variation inside the ejector for refrigeration applications.

In the case of an idealised ejector operation, the primary flow, commonly referred to as the motive flow, enters the device through the motive nozzle. As the flow passes through the nozzle throat (position 1), its static pressure decreases while its velocity increases. Ideally, at the nozzle throat, the primary flow reaches sonic velocity. Downstream of the throat, the diverging cross-section of the nozzle causes an expansion of the stream to high kinetic energy supersonic flow and low static pressure. In fact, a low-pressure zone is created at the nozzle outlet (2), which draws the secondary flow through the secondary inlet into the suction chamber. The secondary flow is entrained by the primary flow due to this pressure differential. The secondary flow then accelerates first to sonic (choking) and then to supersonic velocities in the constant-area section (between positions 3 and 4). After choking the secondary and primary flow mixes. At the end of the mixing process, a normal shock wave occurs, resulting in a sharp increase in pressure and a corresponding decrease in velocity, transitioning the flow from supersonic to subsonic conditions. In the diffuser, the subsonic mixed flow is decelerated and pressurised due to the increasing ejector cross-section area. The working fluid then leaves the ejector at an intermediate pressure (p_{out}) that is lower than the primary (p_{pr}) and higher than the secondary (p_{sec}) pressures. This idealised ejector operation theory forms the basis for simplified mathematical models used to predict ejector performance (Samaké et al., 2016).

Although the idealised operation provides a useful theoretical background, the real behaviour of ejector flow is considerably more complex. In practical applications, phenomena such as under expanded jets may occur. For instance, when the pressure at the primary nozzle outlet is higher than the secondary inlet pressure (p_{sec}), shear forces between the high-speed primary jet and the slower secondary flow drive the entrainment

(Samaké et al., 2016). Additionally, turbulence, shock waves, and non-uniform mixing lead to significant deviations from the ideal case (Mazzelli et al., 2015). Consider these complexities is particularly important when analysing ejector efficiency, since experimentally tested real ejectors rarely achieve the predicted performance by simplified models (Little and Garimella, 2016).

In the real case, the mixing process between the primary and secondary flows is often non-uniform. Variations in velocity and temperature between the two streams result in the formation of a boundary layer with significant shear forces (Samaké et al., 2016), causing irreversible oblique shocks and energy losses (Little and Garimella, 2016). Figure 2.3 shows the experimental flow schlieren visualisation results by Rao and Jagadeesh (2014), where a set of oblique waves are clearly visible. This set phenomena are often referred to as the shock-expansion train.

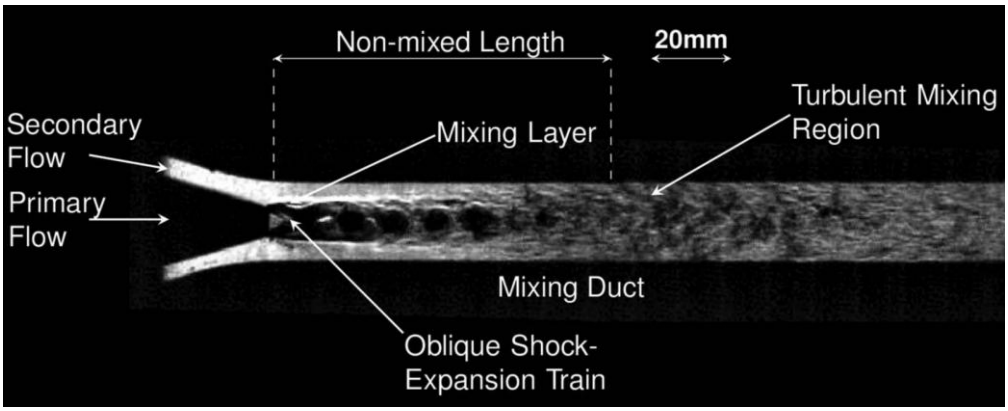


Figure 2.3 – An instantaneous schlieren images of the flow through a supersonic ejector (from Rao and Jagadeesh (2014)).

Boundary layer interaction between the jets creates zones of turbulence and flow separation that are not accounted for in the idealised ejector flow models. Consequently, the entrainment ratio and overall efficiency can be significantly lower than anticipated (Banasiak and Hafner, 2011; Rao and Jagadeesh, 2014). In many cases, experimental and computational fluid dynamics (CFD) studies reveal substantial deviations from the idealised flow. The flow structure complexity escalates when the working fluid inside the ejector is in two-phase or it undergoes a phase change process (Little and Garimella, 2016). In such cases, the presence of both liquid and vapour phases significantly alters the fluid dynamics. For example, the speed of sound in two-phase mixtures is much lower, weakening shock waves and making flow transitions less predictable (Giacomelli, 2019). Evaporation and condensation introduce sudden variations in fluid properties, such as density and temperature, which further complicate flow predictions. Non-equilibrium conditions during phase changes cause localised temperature and pressure gradients, creating additional challenges for both experimental analysis and CFD modelling. By integrating these real-world phenomena into advanced CFD models and leveraging experimental data, researchers have been improving the accuracy of their ejector performance predictions and optimise their ejector designs for the different applications. This is particularly important in sectors such as refrigeration, power generation, and air conditioning, where ejector efficiency is critical.

2.1.1 Classification of ejectors

Ejector can be classified in terms of construction design and working fluid characteristics (Besagni et al., 2016). Table 2.1 presents a brief summary of the various construction designs and ejector configurations, according to the ejector nozzle exit position (NXP), which will be discussed in detail in this section.

Table 2.1 – Summary of NXP designs for ejectors: main advantages, disadvantages and recommended literature with detailed information.

NXP design	Advantages	Disadvantages	Recommended Literature
Constant mixing area - CMA	– Higher entrainment ratio than CPM; – Simple design.	– Limited flexibility for varying outlet pressures; – Inefficient at higher backpressures.	(Pianthong et al., 2007) (Varga et al., 2009b)
Constant pressure mixing - CPM	– Handles wider outlet pressure ranges; – Performs well with higher backpressures; – Simple design.	– Lower pressure lift ratio compared to CRMC; – Performance loss at off-design conditions.	(Eames, 2002) (Pianthong et al., 2007) (Varga et al., 2009b) (Kitrattana et al., 2017)
Constant rate of momentum change – CRMC	– Reduced pressure loss from shock waves; – Higher pressure lift ratio; – Higher entrainment ratio.	– Complex geometry; – High fabrication cost; – Difficult to implement in real problems; – Only suited for on-design operation.	(Eames, 2002) (Kitrattana et al., 2017) (Kumar, A. et al., 2022)
Constant rate of kinetic energy change - CRKEC	– Entrainment ratio similar to CRMC; – Optimised kinetic energy transfer; – Potential gains in performance and efficiency.		(Kumar, V. et al., 2018) (Kumar, A. et al., 2022)

One of the criteria is the location of the primary nozzle exit position which plays a crucial role in determining the performance of the ejector. Ejectors are typically classified into constant pressure mixing (CPM) ejectors and constant mixing area (CMA) ejectors. In CPM ejectors, the NXP is in the converging mixing chamber, as shown in Figure 2.4a). This configuration leads to better performance under a wider range of outlet pressures and higher backpressures, making it the more common choice in industrial applications (Pianthong et al., 2007). In contrast, in CMA ejectors the NXP is place inside the constant-area section (see Figure 2.4b)). This configuration often results in a higher entrainment ratio due to the larger area available for mixing, but it is less effective when handling higher backpressures (Pianthong et al., 2007). However, CMA ejectors can achieve a higher entrainment ratio under optimal conditions. The choice between CMA and CPM depends heavily on the specific application and required operating conditions.

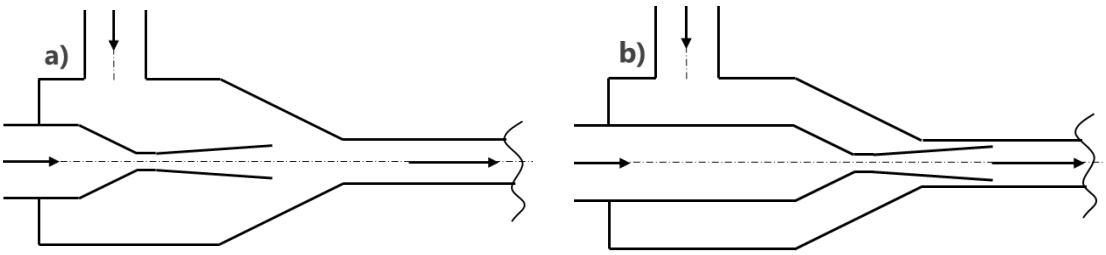


Figure 2.4 – NXP for a) constant mixing area ejector and a b) constant pressure mixing ejector.

Some alternative ejector designs have been proposed to improve performance. Eames (2002) introduced the constant rate of momentum change (CRMC) ejector. In a CRMC ejector, the mixing section is specifically shaped to promote a constant change in flow momentum during mixing and recompression. This leads to a gradual increase in static pressure without the occurrence of shock waves. In a comparative study between CPM and CRMC ejectors, Eames (2002) found that the CRMC design led to a 50% higher pressure lift than the CPM design under identical operating conditions. Similarly, Kitrattana et al. (2017) reported a 40% entrainment ratio increase for the CRMC design, demonstrating its advantage under certain operating conditions. By avoiding the total pressure loss, usually associated with shock phenomena in conventional diffusers, this design significantly improved the pressure lift ratio (p_{out}/p_{sec}). This characteristics makes it a superior choice for applications where high-pressure recovery is critical (Eames, 2002).

Another recent configuration is called the constant rate of kinetic energy change (CRKEC) ejector, developed by Kumar, V. et al. (2018). This configuration promotes a constant change of kinetic energy between motive and entrained streams. Unlike traditional designs, CRKEC ejectors focus on optimizing the transfer of kinetic energy from the primary to secondary streams, potentially offering distinct advantages in performance and efficiency, when compared with CPM and CMA (Kumar, V. et al., 2022). Kumar, V. et al. (2018) conducted computational and experimental studies comparing the performance of CRMC and CRKEC steam ejectors under identical design conditions. Their results showed that both exhibited similar entrainment ratios and efficiencies. All studies were performed under on-design operating conditions. Figure 1.3 presents a schematic design for CRMC and CRKEC ejectors, with the most noticeable visual distinction being the difference in the length and diameter of the ejector throat. Despite their performance potential, both CRMC and CRKEC configurations present challenges due to their very specific ejector tail geometries designed for particular operating conditions, which makes manufacturing costs relatively high for practical application (Pianthong et al., 2007).

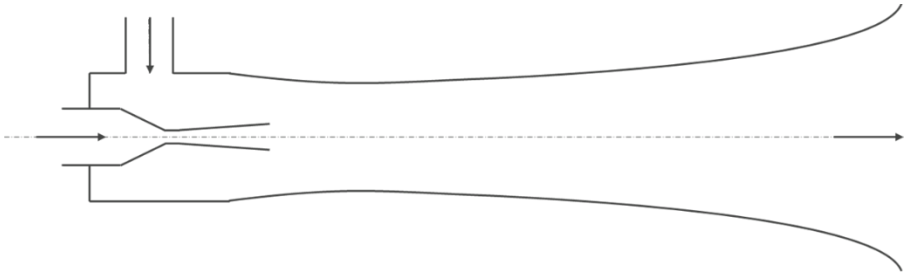


Figure 2.5 – General aspect of the mixing and diffuser section for a CRMC or CRKEC ejector.

Ejectors can also be classified according to the working fluid's thermodynamic state inside during the operation. The most typical ones are summarized in Table 2.2. Single-phase ejectors, both liquid and gas phase, are widely studied in the literature. Vapor jet ejectors have been developed for a range of applications, such as air conditioning (Ashley, 1934; Varga et al., 2009b, 2011; V. Van Nguyen et al., 2020) and desalination (Shahzamanian et al., 2021; Ren, X. et al., 2022) among others. Valuable reviews were published regarding the applications of single-phase ejectors by Power (1994), Bartosiewicz et al. (2005) and Elbel (2011).

Liquid jet ejectors, or jet pumps, are often employed as alternatives to mechanical pumps (Reis and Gioria, 2021). Jet pumps can be found in district heating and cooling systems (Fangzhou Liu et al., 2017; Wang and Wang, 2019) the oil industry (Yan et al., T. 2018), boiling water reactors (Mangialardo et al., 2014), and fish transport (Xu et al., 2017). The fluid flow in jet pumps is relatively simple to analyse by being incompressible, adiabatic and in single-phase free of shock waves (Besagni et al., 2016).

Table 2.2 – Different flow phases in the ejector (Besagni et al., 2016).

Ejector classification		**Primary flow phase**	**Secondary flow phase**	**Exit flow phase**
Single-phase	Vapour jet	Vapour	Vapour	Vapour
	Liquid jet	Liquid	Liquid	Liquid
Two-phase	Condensing	Vapour	Liquid	Liquid
	Flashing	Liquid	Vapour	Two-phase

In two-phase condensing ejectors, the motive fluid is vapour, and the secondary fluid is liquid. Due to the temperature difference between the two streams, the vapour phase, primary stream, condenses as it passes through the ejector, forming a liquid stream. This condensation process can result in a stagnation pressure higher than the secondary flow inlet pressure, increasing the momentum of the liquid phase (Besagni et al., 2016). The rapid condensation can cause the formation of shock waves, leading to liquid state downstream of the shock (Besagni et al., 2016). Consequently, the outlet flow is typically in liquid state. Applications of condensing ejector can be found in various fields, including nuclear engineering, where they are typically part of the emergency core cooling systems (Beithou and Aybar, 2000), in Rankine cycles (Li et al., 2022), in liquid–gas vacuum systems (Ren, J. et al., 2022) and other industrial processes as direct contact condensation equipment (Song, C. H. et al., 2012).

Flashing ejectors operate with the working fluid in both liquid and vapour phases. In this case, the primary flow is liquid, undergoing a rapid expansion and evaporation (flashing) in the mixing chamber. The secondary flow is typically superheated vapour. The formation of shock waves may occur during the mixing of the streams, depending on the operating conditions and flow properties. The ejector flow generates a two-phase mixture at the exit. The expansion of the primary flow in the primary nozzle can induce strong, multidimensional, and multiple shock waves inside the mixing chamber (Banasiak and Hafner, 2011).

Ejectors can also be classified based on the primary nozzle design as shown in Figure 2.6. The nozzle configuration determines whether the primary flow is subsonic, sonic or supersonic at the nozzle exit plane. Subsonic ($Ma<1$) or sonic ($Ma=1$) flow occurs when the primary nozzle has a convergent shape, as depicted in Figure 2.6a). In such design, the motive flow is not significantly compressed, making it suitable, for instance, for exhausting gas in industrial plants or fuel cells recirculation (Besagni et al., 2015).

In contrast, a convergent-divergent nozzle (see Figure 2.6 b)) is designed to accelerate the primary flow to supersonic velocities (Ma>1) downstream the nozzle throat. This design is adequate for the application ejector in systems requiring high-pressure gradients, such as organic Rankine cycles for waste heat recovery or refrigeration systems (Besagni et al., 2016).

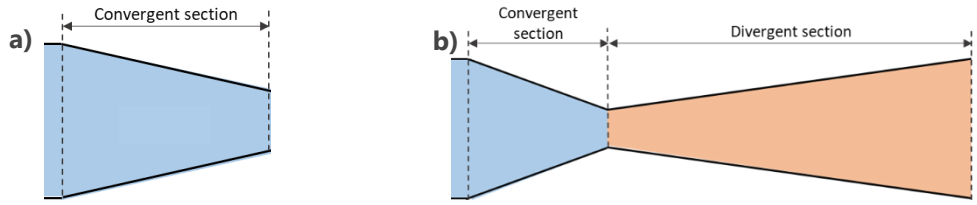


Figure 2.6 – a) convergent-primary nozzle and b) convergent-divergent primary nozzle.

2.1.2 The integration of ejectors into cooling cycles

The schematics of a conventional vapour compression cooling cycle comprising four main components: evaporator, compressor, condenser, and expansion device is shown in Figure 2.7. In this cycle, the refrigerant undergoes a series of thermodynamic processes, also shown in the figure, that are irreversible. One of the main sources of entropy generation is during isenthalpic expansion, leading to an energy loss that increases the load on mechanical compressor, especially under varying operating conditions (Śmierciew et al., 2017). Partial recovery of the expansion losses represent an opportunity for improving system performance (Sawalha, 2008; Varga et al., 2009a).

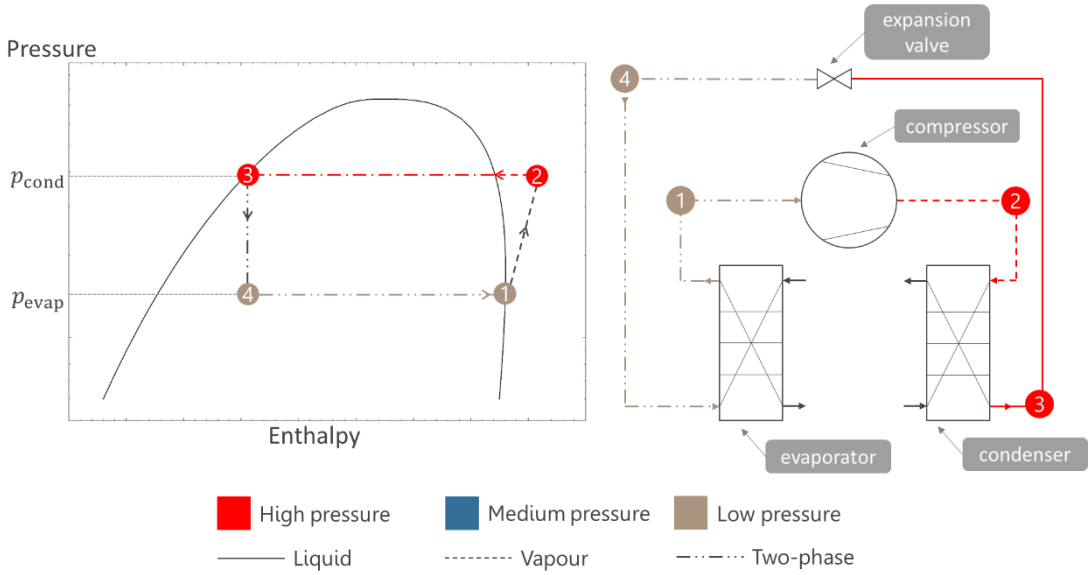


Figure 2.7 –p-h diagram and component layout of a vapour-compression cooling cycle.

The conventional vapour compression cycle starts with the compression of the refrigerant leaving the evaporator (1) in a mechanical compressor. The refrigerant leaves the compressor (2) at a high pressure and at a relatively high temperature. In the condenser (2→3), heat is released to the environment. Depending on the heat release method and the environmental conditions, the working fluid leaves the condenser at a saturated liquid state (3) or even with some degree of subcooling. After condensation, the refrigerant passes through an expansion device, typically a throttling valve. During

this process (3→4) the pressure of the working fluid is reduced to the evaporation pressure. Finally, the refrigerant enters the evaporator, where the cooling effect takes place by absorbing heat from a low temperature heat source. At the outlet of the evaporator, the refrigerant is in saturated (1), or in many cases, somewhat superheated vapour state.

Ejectors can be integrated into cooling systems with two different objectives. One of the options is to use the ejector as a thermal compressor device in a heat driven cooling cycle (Varga et al., 2009a). Another objective of integrating ejectors is for expansion work recovery. Expansion work recovery with ejectors can be performed in both sub-critical (Hassanain et al., 2015) and in transcritical cycles (Fang Liu et al., 2016). These latter applications offer advantages such as reducing electric consumption and thus increasing the system's coefficient of performance (COP).

In heat driven ejector cooling cycles, the ejector works as the primary compression device and the working fluid is in a single vapour phase inside the ejector. The main cycle components are the generator, ejector, condenser, evaporator, pump, and throttling device. The thermodynamic stated at the inlet and outlet of each component are shown in Figure 2.8.

The refrigerant leaving the evaporator (1) is compressed in the ejector to the condenser pressure (2) by mixing with the primary flow as described in Section 2.1 After compression, the refrigerant condenses in the condenser (2→3) at constant pressure. Part of the liquid refrigerant undergoes isenthalpic expansion (3→4) in a throttling device until the desired evaporation pressure. The cooling effect takes place in the evaporator (4→1) as the refrigerant absorbs heat from a low temperature heat source. Another part of the liquid refrigerant leaving the condenser (3) is led through a pump that performs the necessary pressure lift to the generator pressure, where the working fluid is evaporated at a relatively high temperature and pressure, using an external heat source. The high-pressure gas phase refrigerant from the generator (6) enters the ejector as motive flow to compress the secondary fluid from the evaporator (1).

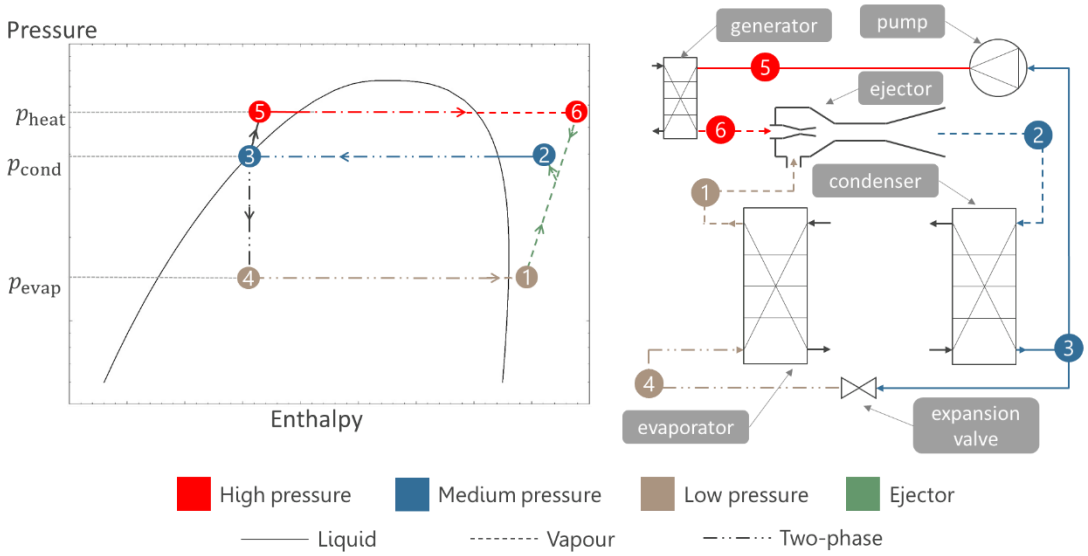


Figure 2.8 –p-h diagram and component layout of an ejector cooling cycle.

In ejector vapour compression systems, the ejector is used for the recovery of the expansion work, which would be otherwise lost using a conventional throttling valve. If the ejector is well designed, its integration can lead to substantial efficiency

improvement (Hassanain et al., 2015). The schematics and the p-h diagram of a sub-critical ejector vapour compression cycle is shown in Figure 2.9. The major components of the cycle are the compressor, ejector, separator, condenser, evaporator, and expansion valve.

One major difference in comparison to the ejector cooling cycle (see Figure 2.8) is the need for a mechanical compressor. Another important characteristic of this type of system is that the flow inside the ejector occur with the fluid in the humid vapour region thus the flow is two-phase type. It can be seen from Figure 2.9 that the working fluid enters the compressor from the separator in a saturated vapour state (1). After compression (2), the refrigeration undergoes a conventional condensation process in the condenser by releasing heat to the environment.

The liquid working fluid at high pressure enters the ejector on the motive fluid side (3). As the motive fluid expands in the ejector to an intermediate pressure (4), it converts part of its enthalpy content to the low-pressure secondary stream coming from the evaporator (7), causing both streams to mix. The mixed fluid leaves the ejector at the intermediate pressure level, thus recovering part of the expansion losses during the expansion process. This pressure recovery reduces the load on the compressor, leading to lower electricity consumption and thus enhanced efficiency.

Expansion work recovery is only possible when the two-phase ejector is properly designed for the specific working fluid and operating conditions. Suitable design however is rather complex, due to the challenges in accurately predicting phase transitions, fluid mixing, and separation of vapour and liquid phases (Ringstad et al., 2020). The working fluid leaves the ejector as wet vapour (4). As the name suggests, the vapour and liquid phases are separated in the separator.

The vapour (1) part is then compressed in the compressor, while the pressure of the liquid phase (5) is reduced in a valve to the evaporator pressure (6). Such as in the case of the conventional cooling cycle, the cooling effect takes place in the evaporator, where heat is supplied to the refrigerant by a low temperature heat source. The ejector's role is to increase the pressure of the fluid leaving the evaporator (7) from p_{evap} to p_{out} without using any mechanical mean, thus reduce the compression work using electricity.

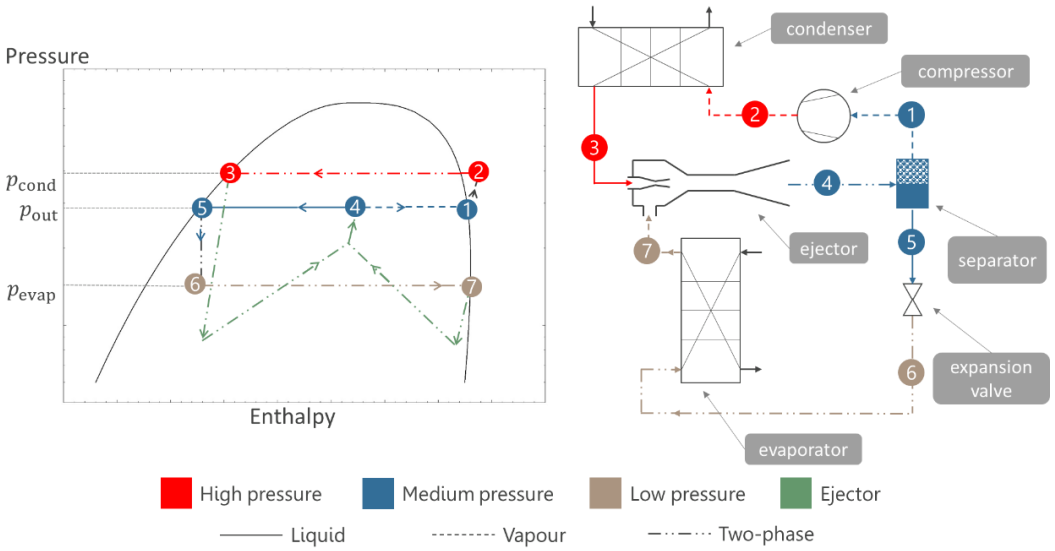


Figure 2.9 –p-h diagram and component layout of a cooling cycle with an ejector as an expansion device.

As it was mentioned before, ejector can be also integrated into transcritical cooling cycles. A transcritical ejector cycles is composed by similar main components as in the case of a subcritical one, with the exception that the condenser is replaced by a gas cooler. The expansion work recovery by integrating an ejector into the cycle leads to an improvement of the system COP. The schematic representation of the ejector cooling cycle with the corresponding p-h diagram is shown Figure 2.10. It can be seen from the figure that working fluid flow inside the ejector, more particularly inside the primary nozzle is very different from the subcritical case. The motive fluid enters the ejector in supercritical state. During the expansion in the primary nozzle, it becomes subcritical, and it starts to condensate in the nozzle throat. The low-pressure secondary fluid is typically in vapour state. Such as in the case of the subcritical ejector compression cycle, here the mixed stream leaves the ejector at an intermediate pressure and as humid vapour, therefore the liquid and vapour phases need to be separated before entering the compressor and expansion valve, respectively.

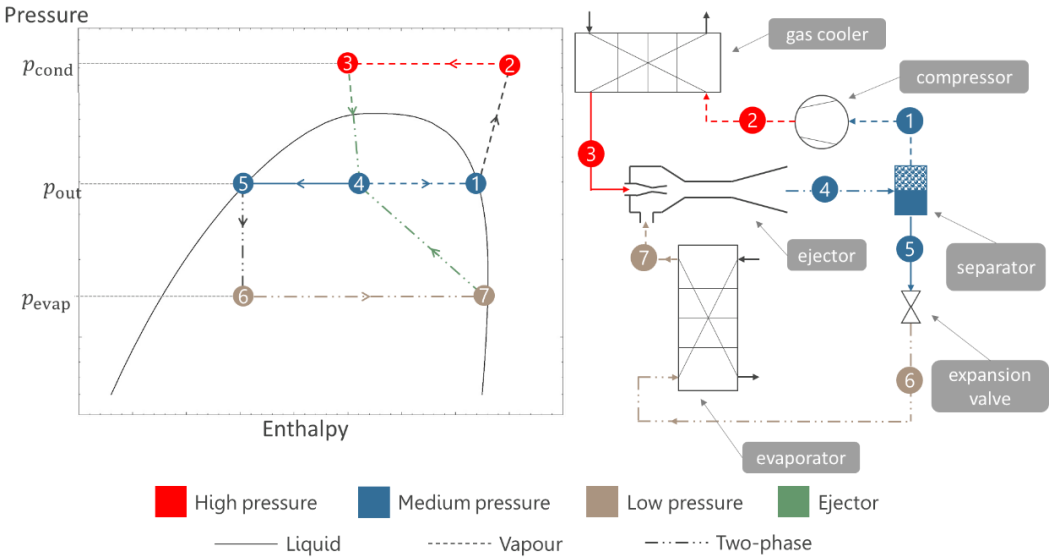


Figure 2.10 –p-h chart and component layout of a cooling cycle with a transcritical ejector.

Each type of these ejector application presents unique benefits and limitations. Single-phase ejectors offer simplicity and directly convert the energy of the primary flow into compression energy for the secondary flow. However, their performance is susceptible to operating conditions, such as inlet pressure and temperature. Expansion work recovery ejectors have the potential to significantly enhance system efficiency by recovering energy otherwise lost during throttling. Nevertheless, managing the two-phase flow introduces added complexity due to challenges such as phase transitions, fluid mixing, and vapour-liquid separation. Transcritical ejectors, particularly those using CO_2, offer significant performance gains, including improved cooling capacity and efficiency. Nevertheless, their operation requires careful design and precise control to handle the demanding pressures and heat transfer characteristics of transcritical cycles (Little and Garimella, 2016).

In summary, the selection of R1234ze(E) for single-phase ejector simulations and CO_2 for expansion work recovery aligns with the dual goals of meeting environmental standards and enhancing system efficiency. The use of a single-phase ejector with R1234ze(E) provides an alternative to traditional mechanical compression, reducing electricity consumption. However, the heat required to drive the ejector must also be considered

when evaluating the overall energy balance, which can be sourced from renewable options such as solar energy. Meanwhile, employing a two-phase ejector with CO_2 leverages its favourable thermodynamic properties and enables efficient energy recovery, making it particularly suitable for transcritical cooling systems. These choices reflect the growing trend toward sustainable and efficient refrigeration technologies, justifying the focus of this thesis on these two refrigerants and their respective ejector applications.

2.1.3 Definition of the ejector performance metrics and their dependence on the operating conditions

The performance of an ejector in cooling cycles is often assessed using three metrics: entrainment ratio (λ), compression ratio (Π), and expansion ratio (ER). The entrainment ratio is defined as:

$$\lambda = \frac{\dot{m}_{sec}}{\dot{m}_{pr}} \tag{2.1}$$

Typically, a higher entrainment ratio indicates better performance (Sun, 1996). For a given cooling load, the secondary flow rate is approximately constant. The higher the entrainment ratio is, the lower the flow rate on the primary nozzle side and consequently the required energy input in the generator (ejector cooling cycle) or for the mechanical compressor (ejector vapour compression cycle). The relationship between the entrainment ratio and the backpressure, known as the ejector operating curve, is shown in Figure 2.11 for a supersonic ejector. Under constant inlet conditions, ejectors can operate in double-choking or single choking regimes, depending on the flow characteristics (Varga et al., 2012). In the double-choking regime, both the primary and secondary flows reach sonic speeds, and the entrainment ratio becomes independent of the backpressure (see Figure 2.2). This is the on-design operating regime for the ejector, as the flow rates of both streams are maximised and no longer influenced by downstream pressure variations. However, when the backpressure is higher than the critical pressure, the ejector transitions operate in single choking regime, where the secondary flow remains subsonic. In single choking, the secondary flow rate and consequently, the entrainment ratio, are determined by the pressure difference between the inlet and outlet. With increasing backpressure, the entrainment ratio decreases (Varga et al., 2012). Beyond a certain value, the flow in the suction chamber is reversed, stopping the ejector from operating. This backflow occurs when the backpressure exceeds the ejector's capacity to entrain secondary fluid.

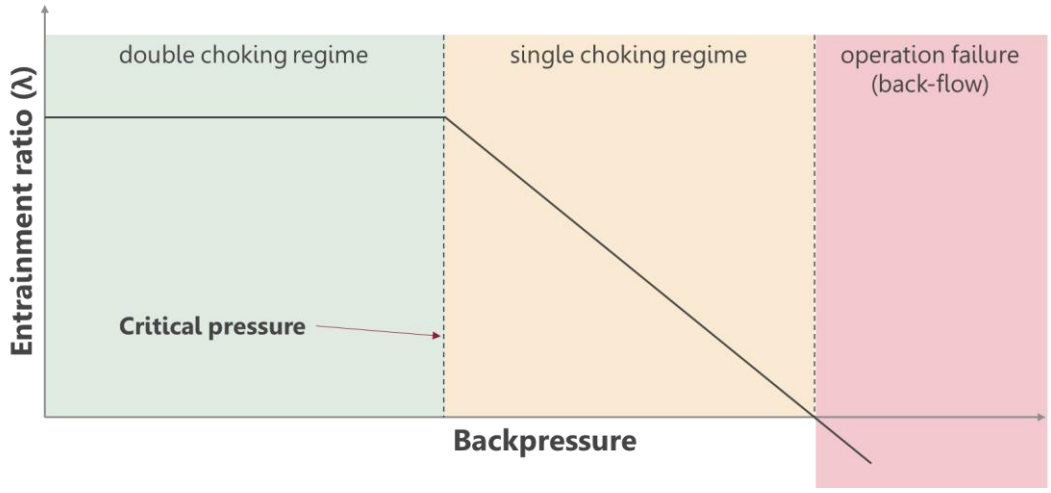


Figure 2.11 – Ejector operation regimes.

In contrast, a sonic ejector operates only in the single choking regime. In this case, the primary fluid reaches sonic velocity at the nozzle throat, but the secondary flow remains subsonic throughout the operation. Unlike supersonic ejectors, which maximise the entrainment ratio under double-choking conditions, sonic ejectors are more sensitive to their operating conditions and the backpressure as the secondary flow remains subsonic. The entrainment ratio is usually lower compared to a double choked supersonic ejector.

The compression ratio (Π) measures the ejector's ability to increase the pressure of the entrained flow. It is defined as the ratio between the outlet and the secondary inlet pressures (Elbel and Lawrence, 2016):

$$\Pi = \frac{p_{out}}{p_{sec}} \tag{2.2}$$

A high value of Π is particularly important pressure recovery applications, such as in ejector vapour compression refrigeration systems. A higher compression ratio is directly associated to improved thermodynamic efficiency within the cycle, as demonstrated by Reddick et al. (2016).

The expansion ratio (ER) calculated by the ratio between the primary and secondary inlet pressures as (Chen, X. et al., 2013):

$$ER = \frac{p_{pr}}{p_{sec}} \tag{2.3}$$

This ratio provides insight into the level of the primary flow expansion before interacting with the secondary flow. A higher ER generally indicates a greater potential for entrainment of the secondary flow and is often associated with improved cooling system efficiency (Sankarlal and Mani, 2007). Besides the operating conditions, the ejector performance is strongly influenced by its geometrical design such as the nozzle exit position (NXP) and the area ratio (r_A). This latter is defined as (Varga et al., 2012):

$$r_A = \frac{A_{\text{cas}}}{A_{\text{th}}} \tag{2.4}$$

In equation (2.4) A_{cas} is the size of the constant-area section and A_{th} is the area of the primary nozzle throat. r_A and NXP has a strong influence on the primary fluid expansion and the momentum exchange between the jets in the mixing section as shown in Figure 2.12. Downstream the primary nozzle exit, the high velocity primary jet core occupies the

central flow area. The outside surface of the jet core creates a separation layer between the primary and secondary flows, reducing the effective flow area available for the secondary stream (Pianthong et al., 2007). This phenomenon influences the entrainment because the effective area for the secondary stream limits the maximum mass flow rate. Optimising the NXP and r_A is essential for the overall ejector performance for a given set of operating conditions.

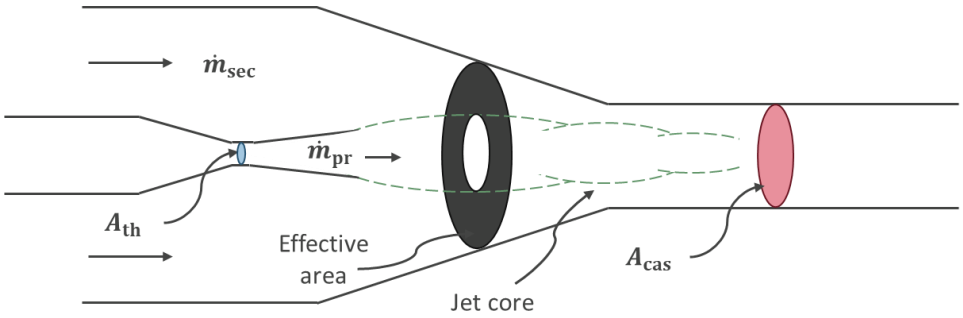


Figure 2.12 – Motive flow expansion after the nozzle and impact in the secondary flow.

To address the sensitivity and performance limitations of traditional ejectors, variable geometry ejectors (VGE) have emerged as a significant advancement. Sun (1996) highlighted exactly that, the ejector geometry plays a crucial role in its performance, presenting the variable-geometry ejectors being key to achieving both efficient system operation and stable cooling capacity across varying conditions. Unlike fixed-geometry ejectors, which struggle to deliver consistent performance across different loads, VGEs are equipped with a nozzle that adapts its area based on the operating conditions, ensuring optimal performance even when loads fluctuate. This adaptability enables the ejector to perform efficiently over a broader range of conditions. Varga et al. (2009b) proposed technical solution for a VGE by controlling r_A using an adjustable spindle in the primary nozzle and by controlling the effective area by a changeable nozzle exit position. This adaptability allows VGEs to optimise the entrainment and compression ratios dynamically, ensuring superior performance. Studies have shown that VGEs can achieve up to 85% higher coefficient of performance (COP) compared to fixed-geometry ejectors (Pereira et al., 2014), particularly in applications where system loads fluctuate (Varga et al., 2009a; Pereira et al., 2014; Nguyen, V. et al., 2020). These findings underscore the potential of VGEs to significantly enhance ejector efficiency and operational flexibility.

Several efficiency definitions have been defined in the literature to evaluate ejector performance under different operating conditions. According to Little and Garimella (2016), ASHRAE proposed a definition for ejector efficiency (η_{ASH}) as the ratio between the actual compression energy recovered, and the theoretical energy available in the motive stream, given by:

$$\eta_{\mathrm{ASH}} = \frac{(h_{out} - h_{sec}) \cdot (\dot{m}_{pr} + \dot{m}_{sec})}{\dot{m}_{pr} \cdot (h_{pr} - h_{sec})} \tag{2.5}$$

This definition of the efficiency quantifies the amount of energy recovered from the motive fluid. Elbel and Hrnjak (2008) proposed an alternative efficiency (η_{EH}) definition as:

$$\eta_{\mathrm{EH}} = \lambda \cdot \frac{h(p_{out}; s_{sec}) - h_{sec}}{h_{pr} - h(p_{out}; s_{pr})} \tag{2.6}$$

In equation (2.6), the numerator represents the ejector work recovery while the denominator expresses the maximum work that the ejector could recover from the motive flow.

A third definition was proposed by Carrillo et al. (2017) as the ratio between the actual pressure rise and the ideal isentropic pressure rise in the ejector:

$$\eta_{\mathrm{C}} = \frac{\Delta p}{\Delta p'} = \frac{p(h_{out}; s_{out}) - p_{sec}}{p(h_{out}; s_{sec}) - p_{sec}} \tag{2.7}$$

The expression in equation (2.7) measures how effectively the ejector converts kinetic energy into pressure recovery.

On the system level, the coefficient of performance (COP) is a key measure of system performance in refrigeration and heat pump cycles. COP is defined as the ratio between the useful heating or cooling effect produced by the system and the energy input required to achieve that effect (Sankarlal and Mani, 2007). For systems employing ejectors, the calculation of the COP can vary depending on the primary form of energy that is used to drive the cycle:

- Ejector vapour compression and transcritical cycles: primary source of energy is the electricity to drive the mechanical compressor, thus:

  $$COP_{\mathrm{EVP}} = \lambda \cdot \frac{\Delta h_{\mathrm{evap}}}{\Delta h_{\mathrm{comp}}} \tag{2.8}$$

  In equation (2.8), Δh_{evap} and Δh_{comp} are the enthalpy variations in the evaporator and in the compressor, respectively (Hassanain et al., 2015).

- Ejector cycle: primary source of energy is heat, thus (Varga, Oliveira, et al., 2017):

  $$COP = \lambda \cdot \frac{\Delta h_{\mathrm{evap}}}{\Delta h_{\mathrm{heat}}} \tag{2.9}$$

  In equation (2.9), Δh_{heat} refers to the heat supplied to unit mass of the working fluid in the vapour generator.

2.1.4 Classification of ejector flow models

The simplest approach to simulate ejector flow is using a 1D model (Song, Y. et al., 2020). These models apply the conservation laws to some predefined sections (real and imaginary) along the ejector flow. The first 1D model for a single-phase ejector was introduced by Keenan and Neumann (1942), while Kornhauser (1990) developed the model for two-phase ejectors. Since then, a number of alternatives have been proposed. Common assumptions for single-phase flow include (He et al., 2009):

- Ideal gas behaviour;
- Constant pressure or constant area mixing;
- Adiabatic and rigid ejector walls;
- Negligible kinetic energy at inlets and outlet;
- Uniform properties across any given cross-section;

- Isentropic flow (Ringstad et al., 2020);
- Isentropic efficiency constants for to consider irreversibility's.

In the case of two-phase flow, the real fluid properties are typically accounted for; however, the flow is commonly assumed to be homogeneous and in thermodynamic quasi-equilibrium within the fluid (Y. Song et al., 2020).

When empirical constants are well chosen, 1D models can predict global ejector performance, including entrainment ratio, critical backpressure and flow rates, with reasonable accuracy. For instance, Huang et al. (1999) reported that 1D models can predict the entrainment ratio within an error range mostly within ±15%, depending on the specific operating conditions. However, they fail to capture fundamental aspects of ejector flow, such as turbulence and shockwave structures. Consequently, their utility lies in their simplicity, which allows for a rapid estimation of ejector dimensions and performance for a given set of operating conditions (Taleghani et al., 2018). While valuable for preliminary ejector design and performance screening, 1D models cannot fully describe the actual physics of ejector flows due to their inherent limitations in resolving complex flow phenomena (Varga, Soares, et al., 2017).

To more accurately capture the local physics of ejector flows, two-dimensional (2D) and three-dimensional (3D) models using CFD methods are required (Y. Song et al., 2020). Many studies assume axisymmetry (Pianthong et al., 2007; Varga et al., 2009c; Smolka et al., 2016; Y. Song et al., 2020), although this assumption reduces computational effort, it can lead to inaccurate results, particularly for predicting the secondary flow behaviour and mixing. For example, Song, Y. et al. (2020) argue that axisymmetry may apply to the primary flow, but not necessarily to the secondary flow, where disturbances in mixing and pressurisation can occur depending on the design of the secondary flow inlet. A study by Smolka et al. (2013) showed that the axisymmetric assumption led to unrealistic results for a two-phase CO_2 ejector with tangential or radial secondary flow entrance. The pressure increases within the mixing section and the entrainment ratio varied significantly based on the inlet design, even though the velocity field appeared nearly symmetrical in the mixing section. Therefore, the authors recommend the use of 3D models for more accurate simulations of ejector flow dynamics.

In two-phase ejectors, the working fluid undergoes phase change, which significantly affects the resulting shockwave structure and the overall flow dynamics (Ishii and Hibiki, 2006). Accurate modelling of these effects requires the use of advanced CFD techniques, where properties like specific heat, viscosity, and speed of sound are carefully defined for each working fluid.

Another important issue in CFD simulations is the accurate modelling of turbulence, which significantly influences ejector flow predictions. Turbulence impacts the mixing process, shockwave formation, and overall flow stability (Pope, 2000). As the flow inside the ejector becomes more complex, particularly in supersonic regimes, turbulence models become essential for capturing the detailed flow behaviour. Turbulence modelling is particularly important in ejector simulations, where high-velocity and compressible flow, characterised by large Reynolds numbers, dominate. Understanding the transition from laminar to turbulent flow and selecting the appropriate turbulence model is critical for ensuring accurate ejector design and performance.

2.2 Turbulence Modelling Approaches

In ejectors, the fluid flow is typically turbulent, in which velocity and pressure fluctuations occur initiating a process where kinetic energy, mass, and momentum are transferred from larger eddies to smaller ones through nonlinear interactions (Pope, 2000). Larger eddies extract energy from the mean flow, continuously breaking down into smaller eddies until all energy is dissipated as heat. This process, known as the energy cascade, is essential for understanding turbulence and its effects on fluid dynamics. Figure 2.13 shows the so-called energy spectrum, where turbulent kinetic energy is plotted against the angular wavenumber. The angular wavenumber is defined as(Pope, 2000):

$$\kappa = \frac{2\pi}{L_\Delta} \tag{2.10}$$

In equation (2.10), L_Δ represents the eddy length scale, which is the key parameter in describing the size of the turbulent structures. Understanding the variation of eddy sizes is essential for grasping the turbulence behaviour, particularly in the context of the energy cascade. According to Figure 2.13, The energy cascade process can be divided into three distinct regions (Pope, 2000):

- Region I (energy-containing range): This region consists of the largest eddies, with their size limited by the flow geometry. Due to this dependence on geometry, large eddies are assumed to be anisotropic and predictable.
- Region II (inertial subrange): Here, smaller eddies dominate, and they are influenced by the diffusive action of molecular viscosity. The eddies exhibit a more random behaviour, and they are independent of the viscosity.
- Region III (dissipation range): This region consists of the smallest eddies, where viscous effects dominate and convert the kinetic energy of the eddies into heat.

High Re Regions II and III are considered part of the universal equilibrium range, where the eddies are isotropic (Souza et al., 2011).

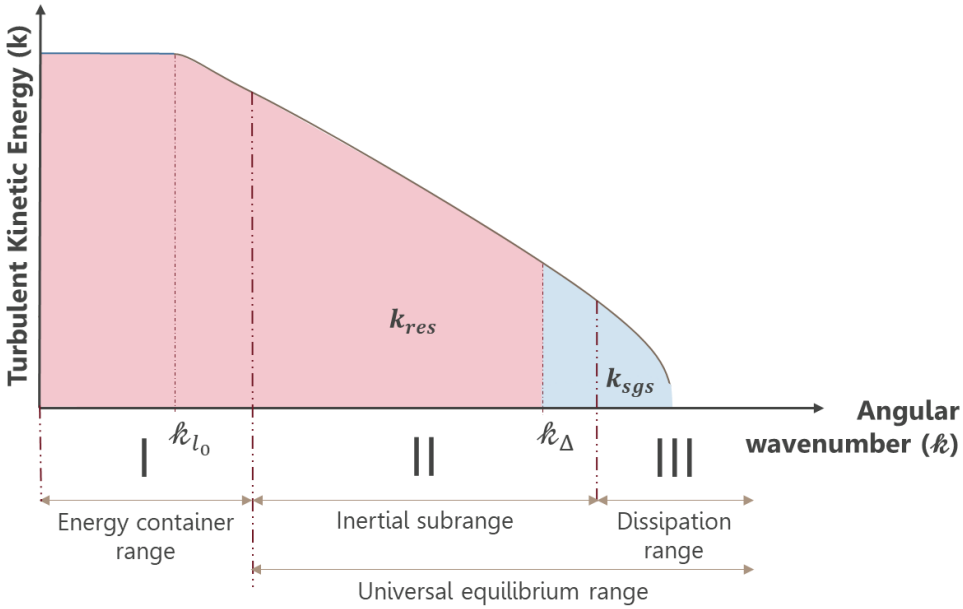


Figure 2.13 – Idealized isotropic turbulent kinetic energy spectrum as a function of wavenumber κ. I: Largest turbulent eddies; II: Inertial subrange; III: Dissipative range, representing the smallest eddies.

Several turbulence models are available in the literature (Wilcox, 2006; Davidson, 2015), and many share the same underlying principles, while being tailored to specific flow characteristics and applications (Ciofalo, 2022). These models aim to mathematically describe turbulence by completing the underlying fluid flow governing equations. Accuracy and computational cost are generally the major concerns during the selection between the available turbulence models.

2.2.1 Reynolds Averaged Navier-Stokes (RANS) for Ejector Flow Simulations

As mentioned earlier, turbulent flows are characterized by chaotic fluctuations, and their complexity requires sophisticated modelling techniques. The governing Navier-Stokes equations become particularly challenging to solve when turbulence is present (Pope, 2000). In engineering practice, Reynolds Averaged Navier-Stokes (RANS) approach is widely used to simulate a wide range of turbulent flows, including those in boundary layers, jets, and complex geometries. RANS models are particularly suitable for steady-state simulations where computational resources are limited. In fact, RANS models are often used for ejector flow simulations, the most frequently used ones are discussed below.

- Spalart-Allmaras Model:

It is a one-equation model that describes turbulence by an additional scalar transport equation for the kinematic eddy viscosity. Initially developed for aerodynamic applications, such as flow over wings (Wilcox, 2006), this model does not require wall functions, as it models turbulence directly near the wall. However, this requires a fine near-wall mesh, increasing the computational cost. For further details, Malalasekera (2007) provides a thorough analysis of this model.

- k-ε Models:

The k-ε models describe turbulence using two additional scalar transport equations(two-equation model): one for turbulence kinetic energy (k) and another for dissipation rate (ε) (Versteeg and Malalasekera, 2007). These models are commonly used for fully turbulent flows where molecular viscosity effects are negligible. Wilcox (2006) pointed that the k-ε models limited utility for flows involving high curvature or rotational effects.

  - Standard k-ε model: This is the original version, suitable for general turbulent flows. It is less accurate for flows where high local acceleration occurs.
  - ReNormalization Group k-ε (RNG k-ε) model: the RNG technique was initially developed within the context of quantum field theory. It was later adapted to study velocity fluctuations described by the Navier-Stokes equations, driven by a Gaussian random force. This approach is based on the systematic elimination of smaller scales and the calculation of renormalised transport coefficients (Yakhot and Orszag, 1986). However, it may perform worse than the standard version for certain configurations, such as in cases where the flow involves geometric convergence (Versteeg and Malalasekera, 2007).
  - Realizable k-ε model: It incorporates the Schwartz inequality for turbulent shear stress (Shih et al., 1995). This model improves numerical convergence at the cost of somewhat increased computational effort (Besagni et al., 2015).

For a comprehensive comparison of the Spalart-Allmaras, Standard k-ε, RNG k-ε, and Realizable k-ε models applied to complex turbulent flow simulation with strong pressure gradients, separation, and shocks interactions, the reader is referred to Kim et al. (1999).

- k-ω Models:

The k-ω models are also two-equation models having an additional scalar transport equation for the turbulence kinetic energy (k) and another for the specific dissipation rate (ω). These models are particularly effective near walls, without requiring wall functions. These models are known for having good accuracy in model boundary layers transition, particularly with high-pressure gradients.

  - Standard k-ω Model: It performs well in simulations near walls and under high-pressure gradients (Menter, 1994). However, it can suffer from freestream sensitivity, particularly for the ω value outside the boundary layer (Menter, 1994). This sensitivity can lead to overpredicted turbulence in the freestream, which may reduce accuracy in scenarios involving external flows or flows with significant separation.
  - Shear Stress Transport (SST) k-ω model: This model combines the advantages of the k-ε and k-ω models by introducing a cross-diffusion term, improving accuracy in both near-wall and far-field zones (Wilcox, 2006). It has been validated under different flow conditions, including adverse pressure gradients (Wilcox, 2006; Argyropoulos and Markatos, 2015).

- Transition Shear Stress Transport (T-SST) Model

The T-SST model incorporates the strengths of the k-ε and k-ω models. It is a four-equation model having a scalar transport equation for: turbulent kinetic energy (k), specific dissipation rate (ω), intermittency (γ) and the transition momentum thickness Reynolds number ($\widetilde{Re}_{\theta t}$). This model is particularly effective at capturing the transition regions at near boundaries and in free jets (Majchrzyk et al., 2022).

- Reynolds Stress Model (RSM)

The RSM offers a more advanced approach by directly resolving the Reynolds stresses without applying the Boussinesq hypothesis (Bartosiewicz et al., 2005). This model involves solving seven transport equations in 3D simulations (and five in 2D) (Tashtoush et al., 2019), providing greater accuracy in complex anisotropic turbulence scenarios (Bartosiewicz, et al. 2005). Despite its accuracy, the RSM is computationally expensive and often suffers from numerical convergence issues (Besagni and Inzoli, 2017).

The RANS models discussed here are essential tools for simulating turbulent ejector flows. Each model offers a distinct balance of accuracy, computational cost, and applicability depending on the specific flow characteristics. While simpler models, like the Spalart-Allmaras model, are computationally more cost-efficient, more advanced models, such as the RSM, may provide better accuracy for complex flows. Selecting the most adequate RANS model depends on the specific requirements of the simulation, such as the complexity of the ejector geometry and the turbulence regime.

2.2.1.1 Literature Review of RANS Models Applied to Ejector Flow Dynamics

Studies on ejector flow simulations using RANS models have produced mixed results, often depending on the turbulence model used and the assumptions about the working

fluid. Bartosiewicz et al. (2005) compared the performance of the Standard k-ε, Realizable k-ε, RNG k-ε, Standard k-ω, SST k-ω, and RSM models in simulating a 3D air supersonic ejector, assuming thermodynamics and transport properties constant. For predicting the axial pressure profile, the SST k-ω model showed the highest accuracy, though it began to under-predict pressure recovery after some shock peaks. The RNG k-ε model, with its constants adapted from experimental measurements, provided excellent agreement with the data for the axial pressure profile, showing an error margin of 10% for expansion and between 35% and 50% for compressions. Furthermore, the SST k-ω model performed better in modelling stream mixing, leading the authors to conclude that this model offered the closest alignment with experimental results.

Similarly, Hemidi et al. (2009) conducted simulations on supersonic air ejectors using constant thermodynamics and transport properties assumption in 2D axisymmetric models. They compared the Standard k-ε and SST k-ω models against experimental data, focusing on entrainment rate and pressure distribution. The Standard k-ε model provided better overall agreement with experimental results, particularly under on-design conditions, where it achieved a deviation of less than 10% for entrainment rate. However, despite the good global performance predictions, the local flow structures differed significantly between the models, illustrating that accurate global predictions do not necessarily reflect local flow dynamics.

In a more comprehensive evaluation, Varga, Soares, et al., (2017) assessed six turbulence models (Standard k-ε, Realizable k-ε, RNG k-ε, Standard k-ω, SST k-ω, and Transition SST) using steam as the working fluid. Density was calculated using the ideal gas law, while other properties were considered constant. Their study focused on the COP and critical backpressure. Among the k-ω models, the SST k-ω performed the best, particularly in double-choking mode, though all models tended to under-predict critical backpressure. The T-SST model achieved the highest accuracy, with an average error of 4% for COP and 1.4% for critical backpressure, offering a balanced solution for ejector flow simulations under various conditions. The authors also found that adapting the constants of the Standard k-ε improved COP prediction accuracy, reducing the maximum error to 8% and the average error to 4%. However, this came at the cost of reduced accuracy in predicting critical backpressure, making the model less effective under near-critical conditions.

In a broader analysis, Besagni and Inzoli (2017) compared seven RANS models, including Spalart-Allmaras, Standard k-ε, RNG k-ε, Realizable k-ε, Standard k-ω, SST k-ω, and RSM. Using steam ejectors and assuming ideal gas behaviour, they found that the SST k-ω model achieved the most accurate results, with a maximum relative error of 10% for the entrainment ratio, while also providing reliable predictions of shock wave position and pressure recovery. In contrast, the RSM model performed well in some cases but faced convergence issues at higher outlet pressures. The Standard k-ε model was the least accurate, with a maximum error of 24.5% for entrainment ratio. The Spalart-Allmaras model, while computationally efficient, showed reduced accuracy at higher pressures, particularly for pressure recovery predictions. Overall, the SST k-ω model was recommended for future studies due to its balance of accuracy and computational efficiency, especially for supersonic ejectors.

In another study, using ideal gas assumptions for density and real gas properties for other variables, Yang, X. et al. (2012) examined the performance of steam ejectors with five different nozzle designs. The turbulence models evaluated included standard k-ε,

RNG k-ε, and Realizable k-ε. The Realizable k-ε model provided the most accurate prediction for the wall static pressure profile, with a deviation of 1.5% for the entrainment ratio, while the RNG k-ε model showed the largest error at 7.5%. All models underestimated the critical backpressure, with the Realizable k-ε showing the smallest deviation of around 6%.

Zhu et al. (2009) evaluated the impact of turbulence models on the performance of R141b ejectors, using the ideal gas laws for density and real gas properties for other variables. The study compared the Realizable k-ε, RNG k-ε, and SST k-ω models, concluding that the RNG k-ε model offered the best accuracy for both entrainment ratio and critical backpressure, although no specific error metrics were provided.

When transitioning to real fluid properties, including fluid density, and complex ejector behaviours, Lin et al. (2013) investigated the performance of a variable geometry ejector using R134a in a multi-evaporator refrigeration system. Real gas properties of R134a were used in the simulations, and the Standard k-ε, RNG k-ε, and SST k-ω models were compared with experimental results. The SST k-ω model outperformed the others in flow rate predictions, with maximum and average errors of 9.3% and 4.4%, for the secondary flow rate, respectively. By contrast, the RNG and Standard k-ε models showed larger errors, exceeding ±10% in some operating conditions.

Yan, J. et al. (2012) studied an air-cooled ejector cooling system with R134a and real gas properties. Initially, the Standard k-ε, Realizable k-ε, and RNG k-ε models showed poor agreement with experimental data, with errors reaching up to 80% for the entrainment ratio. However, after calibrating the Standard k-ε model using the experimental results, the entrainment ratio error was reduced to 7.8%, with an average error of 4.5%.

For two-phase real gas flows, Haida et al. (2018) performed a numerical investigation of a CO_2 two-phase ejector, assessing the k-ε Realizable, SST k-ω, T-SST, and RSM models. The results showed that all models predicted wall temperatures near the suction chamber and pre-mixer within 3 K of experimental values. However, the k-ε Realizable and SST k-ω models showed significant deviations of up to 20 K in the constant-area section and just before the mixing zone. In contrast, the T-SST model provided more accurate predictions near the diffuser, with temperature differences below 1 K. In terms of entrainment ratio, the T-SST model had an error of 2%, while the k-ε Realizable model slightly outperformed it with an error of 1%. The SST k-ω and RSM models under-predicted the entrainment ratio, with errors of around 6.5%. The authors concluded that the T-SST model offered the best overall performance for predicting both wall temperature distribution and entrainment ratio.

Table 2.3 summarizes the performance of RANS models in ejector simulations based on these studies. While RANS models are frequently used for ejector flow simulations, their accuracy depends heavily on the turbulence model chosen and the flow conditions. The most accurate predictions of local flow structures were achieved when RANS models were calibrated with experimental data, indicating that initial experimental work is often necessary for precise local property predictions. However, advanced models such as LES are increasingly being explored to address the limitations of RANS models in capturing unsteady flows (Holgate et al., 2019). In ejectors, high-Reynolds-number turbulence significantly impacts performance, making accurate turbulence modelling critical for predicting local flow structures and optimising design (Zaheer, S. Q. et al., 2018).

Table 2.3 – Summary of RANS Model Performance in Ejector Simulations.

Each tested model is marked with an "x". The main results from each study are presented, showing the best-performing models for specific properties. "ER" stands for entrainment ratio; "COP" refers to the coefficient of performance in refrigeration cycles; "CBP" is the critical back pressure; "PP" is the pressure profile; "PR" refers to pressure recovery after shocks; "WTP" is the wall temperature profile; " SMFR" refers to the secondary mass flow rate prediction and "SWP" is the shock wave position. Models marked with an asterisk (*) had their constants calibrated with experimental results. "2D" indicates an axisymmetric simulation.

Study	Working Fluid	Geom.	Fluid Assumption	Model Performance Notes							
				SA	k-ε	Real. k-ε	RNG k-ε	k-ω	SST k-ω	T SST	RSM
Bartosiewicz et al. (2005)	Air	3D	constant properties		x	x	*SWP	x	SWP		x
Hemidi et al. (2009)	Air	2D			ER < 10%				ER ~10-20%		
Varga, Soares, et al. (2017)	Steam	2D	density - ideal gas; others - constant		*COP ~4%	x	x	x	COP ~4%, CBP ~1.4%	x	
Besagni and Inzoli (2017)	Steam	2D	Ideal gas	x	x	x	x	x	ER < 10%, SWP, PR		x
Yang, X. et al. (2012)	Steam	3D	density - ideal gas; others - real fluid		x	PP, ER ~1.5%, CPB ~6%	ER ~7.5%				
Zhu et al. (2009)	R141b	2D				x	ER CBP		x		
Lin et al. (2013)	R134a	2D	Real fluid properties		x		x		SMFR<9.3%		
Yan, J. et al. (2012)	R134a	2D			*ER < 7.8%	x	x				
Haida et al. (2018)	R744	3D	Real fluid, two-phase			ER ~1%			x	WTP, ER ~2%	x

2.2.2 Large Eddy Simulation (LES) in Ejector Turbulence Modelling

Large Eddy Simulation (LES) is a more advanced method for simulating turbulent flows, directly resolving (typically at least 80%) the larger, energy-containing eddies, while modelling the smaller eddies using specialised subgrid-scale (SGS) models (Pope, 2000). LES offers greater accuracy compared to RANS models because it captures the dynamics of the larger eddies, which are primarily responsible for momentum and energy transfer in turbulent flows (Davidson, 2015). This makes LES particularly effective for modelling complex flow phenomena such as shockwave interactions, turbulent mixing, and flow separation, all of which are critical to ejector performance. However, the enhanced accuracy of LES comes at the cost of increased computational demand, as it requires a finer grid resolution to effectively resolve larger eddies (Pope, 2000). The choice between RANS and LES depends on the specific flow characteristics and the computational resources available.

LES was first introduced by Smagorinsky (1963) and is particularly effective at capturing the large-scale structures that dominate turbulent dynamics. The core principle behind LES is the separation of turbulent eddies into resolved and subgrid scales, based on spatial filtering. This filtering process is applied to the Navier-Stokes equations, resulting in a set of equations that describe the behaviour of the resolved scales (Pope, 2000). The influence of smaller, unresolved eddies is represented through subgrid scale (SGS) models.

Several filtering strategies are employed in LES, including Fourier, Gaussian and Box filters (Aldama, 1990; Launder and Sandham, 2002; Jiang, X. et al., 2010). While the Fourier space filter is computationally accurate, it is demanding and impractical for most engineering applications (Jiang, X. et al. 2010). Instead, Gaussian and Box (or grid) filters are more feasible options, especially when combined with finite volume methods. Gaussian filters are reasonably compact in both physical and wavenumber spaces, allowing for a smooth attenuation of eddies across both domains (Pope, 2000). In contrast, box filters do not provide a precise attenuation of eddies in terms of their wavenumbers. However, they grant a clear representation of the spatial average of the filtered function within the filter domain. Box filter truncate eddies whose scales exceed half the filter width, effectively eliminating information from larger eddies. This characteristic makes box filters practical for LES in large-scale engineering applications (Jiang, X. et al., 2010). Further details on the filtering process are provided in Chapter 3.

Table 2.4 summarizes the advantages, disadvantages, and best applications of these commonly used filtering strategies in LES.

Table 2.4 – Overview of filtering strategies in LES: advantages, disadvantages, and best applications.

Filter Type	Advantages	Disadvantages	Best Applications
Fourier	Accurate in physical and wavenumber spaces	High computational cost	Rarely used in engineering simulations
Gaussian	Smooth attenuation across physical and wavenumber spaces	Requires careful tuning	Finite volume methods, smooth flows
Box / Grid	Simple to implement, effective physical transitions	Lacks smoothness in wavenumber space	Finite volume methods, engineering simulations

2.2.2.1 Subgrid Scale models

Subgrid-scale (SGS) models, which represent the dynamics of the unresolved eddies, play a crucial role in the accuracy of LES simulations. Smagorinsky (1963) first developed a subgrid-scale model based on the conservation equations of mass, momentum, and energy to predict turbulent dynamics of atmospheric circulation. Lilly (1967) later enhanced the model by identifying an inertial subrange and adjusting constants, resulting in the Smagorinsky-Lilly model, which remains widely used.

Germano, et al. (1991) introduced a significant advancement by developing a dynamic algorithm that adjusts the coefficients of the Smagorinsky-Lilly model in real-time. This allows the model to adapt to varying flow conditions, especially near-wall regions and during transitions between laminar and turbulent flows. By eliminating the need for wall-damping functions, this dynamic approach improved accuracy. Lilly (1992) further refined the method by applying least squares to minimise the difference between closure assumptions and resolved stresses extending the model's applicability. This technique is now known as the Dynamic Smagorinsky-Lilly Model.

Scale-similarity models, proposed by Bardina, et al. (1983), assume that interactions between resolved and subgrid scales occur primarily among the smallest resolved eddies and the largest SGS eddies. While Smagorinsky models generally correlate well with observed SGS stresses, direct application to general flows often requires modifications, such as the addition of eddy-viscosity terms for complex turbulence behaviour (Launder and Sandham, 2002).

Recent advances in SGS modelling have focused on improving local velocity prediction and addressing the limitations of traditional models. One approach involves refining the approximation of unresolved scales to ensure that their effects on larger, i.e. resolved eddies, are captured more accurately. Boris, et al. (1992) proposed a concept called monotonically integrated large-eddy simulation (MILES), integrating SGS stresses into numerical dissipation to stabilise computations. However, the benefit of this approach depends on the numerical schemes used, which can lead to variations in the SGS stress predictions.

Ghosal et al. (1995) further developed this concept by introducing an additional transport equation for the kinetic energy, significantly enhancing model accuracy for a broader range of inhomogeneous flows. Kim et al. (1997) introduced the Lagrangian Dynamic Kinetic Model (LDKM), which demonstrated strong agreement with computational and experimental data for a variety of wall-bounded turbulent flows, including turbulent plane Couette, recirculating, and separated flows.

Nicoud and Ducros (1999) proposed the Wall-Adapting Local Eddy Viscosity (WALE) subgrid-scale model, which is particularly suited for complex geometries. WALE adjusts eddy viscosity to reflect local flow conditions, making it effective at capturing near-wall behaviour, including transitions from laminar to turbulent flow in scenarios such as pipe flow.

Near-wall turbulence presents significant challenges for LES due to the fine grid resolution and small-time steps required to resolve the small turbulent scales near the wall. For high Reynolds number flows, this becomes computationally prohibitive (Pope, 2000). As a result, LES is typically applied to low Reynolds number flows or cases without significant wall boundary layers (Launder and Sandham, 2002).

As the Reynolds number increases, the boundary layer becomes thinner relative to the overall domain size, making the near-wall region narrower and requiring higher grid resolution (Shur et al., 2008). To address this challenge, a hybrid approach applies RANS in the near-wall region, where viscous effects dominate, and LES in the outer part of the boundary layer. This method, known as Wall-Modelled LES (WMLES), helps reduce computational costs while still capturing the essential flow dynamics (Shur et al., 2008). Although WMLES does not fully eliminate the scaling effects of higher Reynolds numbers, it significantly improves computational efficiency for high-Reynolds-number simulations (Armenio et al., 2010).

Despite some challenges in predicting near-wall quantities, such as skin-friction coefficient sensitivity, WMLES has demonstrated strong performance in simulating outer-layer turbulence when spatial discretisation is properly executed (Armenio et al., 2010). WMLES also addresses the "log layer mismatch" issue in hybrid RANS-LES methods by smoothing the transition between the logarithmic velocity profile in RANS and the LES-resolved outer flow (Shur et al., 2008). This mismatch occurs when the logarithmic velocity profile in the near-wall region, predicted by RANS, does not smoothly transition into the LES-resolved outer flow. As a result, WMLES is particularly effective for wall-bounded flows, where unsteady inflow conditions are critical.

By combining WMLES with Embedded LES (ELES), computational costs are reduced by confining the LES region to critical areas of the flow domain, while applying RANS to less critical regions. This strategy allows WMLES to extend LES to high Reynolds numbers efficiently. However, one limitation of WMLES is its difficulty in reducing eddy viscosity to zero for constant shear flows when using the modified Smagorinsky model in the LES zone (Shur et al., 2008). This leads to inaccuracies when simulating transitional flows and excessive eddy viscosities in separating shear layers. To address this, the WMLES S-Ω formulation was developed, which considers both the strain rate and vorticity magnitude when computing SGS turbulent viscosity (μ_{SGS}) (Ivanov and Zasimova, 2018).

Mousavi et al. (2021) examined the pseudo-shock structure in a convergent-divergent duct using LES and various SGS models. They observed that the Smagorinsky-Lilly and WALE models required significantly more computational time than WMLES, with a computational time ratio of approximately 1:3, due to the reduced grid cells needed by WMLES.

Considering the balance of superior accuracy and computational efficiency demonstrated by WMLES, particularly in confined flows with shock trains, this thesis adopts the WMLES S-Ω model. The reduced computational demand and reliable performance of WMLES make it well-suited for simulating the complex flow inside the ejector.

2.2.2.2 Subgrid Length Scale

Determining the optimal relationship between the subgrid length scale and grid spacing is particularly complex in anisotropic computational grids, which are commonly encountered in wall-bounded flows. In such simulations, finer grid spacing is typically applied perpendicular (normal) to the wall to accurately capture flow gradients near the boundary. Additionally, in cases involving near-wall modelling, the grid spacing parallel to the wall may be larger than the spacing perpendicular to it. This differs from the typical LES approach, where the grid spacing is usually more uniform. In traditional LES, subgrid-scale eddies are expected to be resolved uniformly, which would justify a more evenly

distributed grid spacing to resolve the turbulent structures adequately. However, this non-uniform grid spacing near the wall requires more adaptable SGS models to capture turbulent flow near the boundary with greater accuracy.

Traditionally, the filter length scale in LES has been calculated from the cubic root of the cell volume, as described by Schumann (1975):

$$\Delta_{SGS} = \sqrt[3]{V}. \tag{2.11}$$

This methodology, however, relies solely on the maximum cell dimensions, which has proven insufficient for accurately capturing wall-bounded turbulence, particularly near the wall, where grid anisotropy becomes a significant issue. Shur et al. (2008) compared a LES simulation, which employed the filter length scale defined by equation (2.11), with direct numerical simulation (DNS) results for channel flow. Their findings indicated that this methos overestimates the near wall velocity. As a result, Shur et al. (2008) emphasised the importance of ensuring that the filter length scale is adaptative near the wall to improve accuracy.

Given the significant impact of wall-proximity effects, it's logical to refine the subgrid length scale by considering both cell dimensions and the distance from the wall (Shur et al., 2008). For instance, in WMLES models, the subgrid scale must account for the reduction in grid spacing normal to the wall, while also addressing the wall-parallel spacing, particularly in high Reynolds number flows. Shur et al. (2008) proposed a modified filter length scale calculation to address grid anisotropies in wall-modelled flows. This method considers the maximum edge length of the computational cell (for a rectilinear hexahedral cell), the wall-normal grid distance, and the wall distance, providing a more accurate representation of the local flow dynamics

To further enhance near-wall modelling, van Driest damping technique (Pope, 2000), often employed in RANS models, is used to diminish eddy viscosity near-wall. This technique helps reduce excessive turbulence dissipation near walls, where the velocity gradient is excessive, thus improving the accuracy of the simulation. Details about the use of the van Driest damping technique in the WMLES is discussed in Chapter 3, section 3.4.2.

2.2.2.3 Case Studies and Applications in Ejector Flow Simulations

LES has been shown to be an effective tool for capturing the turbulent structures that significantly influence the mixing processes in ejectors. By directly resolving large eddies while modelling smaller ones, LES allows for detailed insights into the mixing dynamics without the excessive computational cost associated with fully resolving all turbulent scales (Ferziger et al., 2020).

For instance, Fang et al., (2018) investigated the impact of oblique shockwaves on supersonic mixing layers, observing the formation of hairpin vortices that reduce vorticity thickness and enhance mixing through intensified energy transport and convection. Further supporting evidence from Jiang, Z. et al. (2022) emphasizes how oblique shockwaves significantly increase mixing and turbulence in supersonic flows. Their DNS study confirmed the impact of compressibility on shock wave and turbulence boundary layer interaction, resulting in enhanced in flow compressibility and higher turbulent intensity.

In addition to shockwave interactions, understanding vortex structures within turbulent ejector flows has been essential for predicting and controlling flow dynamics. Vortex

structures play a crucial role in the exchange of momentum between the outer and core regions of the flow (Jeong and Hussain, 1995). Specifically, in turbulent jet flows, the examination of vortex dynamics provides key insights into how momentum is transferred between different regions of the flow, which is fundamental to the mixing processes in ejectors (Bandyopadhyay et al., 1990).

To capture these vortex structures, Q-criterion visualisation is commonly employed in LES simulations. The Q-criterion is a method used to identify regions of vorticity and coherent structures in turbulent flows (Ren, X. et al., 2022). By highlighting areas where the vorticity dominates over the strain rate, Q-criterion enables the clear visualisation of vortex cores, making it particularly useful in the analysis of complex flows like ejectors. This technique helps to resolve and analyse small-scale vortices and turbulent structures that are essential for understanding the dynamics within ejectors, as demonstrated by Ren, X. et al. (2022). Their study reinforced the ability of LES, coupled with Q-criterion visualisation, to provide accurate predictions and detailed insights into ejector performance by capturing the intricate flow structures that are missed by simpler models like RANS.

Despite the strengths of LES, its use in ejector flow simulations remains relatively limited, with few studies published in recent years. Medeiros et al. (2014) applied LES to a steam ejector but reported discrepancies between experimental Mach number profiles and LES results, attributed primarily to time-averaging of unsteady effects. Bouhanguel et al. (2015) applied LES to a supersonic air ejector to explore flow instabilities, although their study, being preliminary, did not fully resolve the numerical challenges associated with supersonic ejectors at high Mach and Reynolds numbers. However, their work demonstrated that LES outperformed RANS in capturing instabilities, such as those caused by jet deceleration and shear layer formation, visualising and tracking these instabilities through to complete mixing.

More recently, Croquer et al. (2022) used LES to model a rectangular supersonic air ejector, demonstrating the method's capability to visualise large-scale turbulent structures such as those in shear mixing layers and diffusers. Their study also identified the influence of minor geometric imperfections in the domain, often neglected in RANS studies but captured in LES simulations. Similarly, (Gupta et al., 2022) applied LES to a rectangular air ejector, focusing on instabilities caused by the mixing of primary and secondary flows. Their findings emphasised the ability of LES to resolve flow structures not captured by RANS models, reinforcing the importance of LES for accurate predictions of complex flows. Furthermore, Ren, X. et al. (2022) employed LES to simulate a thermal vapour compressor, using Q-criterion visualisation techniques to capture small-scale vortices. The results reinforced the reliability of LES in modelling high-performance ejectors.

Although LES has shown promise, the published LES results applied to ejectors are limited to fluids behaving as perfect gases. For more complex flows, such as those involving non-ideal fluid behaviour or two-phase conditions, LES presents an extremely high computational cost. There is a lack of studies balancing turbulent modelling accuracy with computational feasibility in ejectors using real fluids or featuring complex geometries.

Hybrid approaches, such as ELES, have been explored to tackle these computational challenges in ejector flow simulations. ELES combines the strengths of LES and RANS, by applying LES in critical flow regions that require detailed turbulence resolution, and

RANS in less critical areas. This method improves computational efficiency without sacrificing accuracy in the most important regions. For example, Zaheer, Q. and Masud, (2017) applied ELES to the mixing section of a liquid ejector, using LES to model the turbulent mixing and RANS for the rest of the flow. The outlet mass flow rates were compared with experimental data, for three different primary inlet pressures (with the same secondary inlet pressure), obtaining a maximum error of 1.9%. However, local flow variables were not analysed.

Considering these findings, ELES has emerged as a promising method for ejector simulations, balancing high-resolution turbulence modelling with computational efficiency. ELES selectively applies LES to critical regions, such as the mixing section in ejectors, while using RANS for the rest of the domain, improving the accuracy and practicality of ejector simulations. The following section will explore in greater detail how ELES can be effectively implemented to simulate complex ejector flows.

2.2.3 Embedded LES (ELES) Modelling for Complex Ejector Flows

The simulation of turbulent flows within ejectors presents significant challenges due to their intricate geometries and the physics. ELES modelling is well-suited for such cases, offering a balance between computational efficiency and accuracy. By embedding LES in critical flow regions, where turbulence structures dominate, and employing RANS in areas where the flow is more uniform and less complex. ELES approach allows for the detailed resolution of turbulence structures in specific zones without the computational costs of a full-domain LES.

In an ELES model, the simulation domain is divided into distinct RANS and LES zones. RANS is typically used in regions with relatively stable flows, such as the primary nozzle of an ejector, where RANS equations provide a sufficiently accurate representation of the flow. In contrast, LES is applied to regions with complex turbulent structures, such as the nozzle exit, mixing chamber, and constant-area sections of the ejector. This strategic division ensures that computational resources are focused on the areas where detailed turbulence modelling is most needed (Ferziger et al., 2020).

The critical aspect of ELES is the interface between LES and RANS regions, as it must ensure a seamless transition between the two modelling approaches. There are two primary methods for coupling RANS and LES in such simulations: unified and segregated modelling approaches (Fröhlich and Terzi, 2008).

Unified modelling allows for a smoother transition between RANS and LES regions without a clearly defined boundary (implicit interface). The transition is usually governed by the local grid resolution and overall flow properties (Peng, 2022). This method avoids abrupt changes in flow characteristics at the interface, but it requires careful tuning to ensure a consistent representation of the flow across the domain. While unified interfaces offer flexibility, they fall outside the scope of this thesis. For a more comprehensive review of implicit interface methods, refer to Fröhlich and Terzi (2008).

Segregated modelling, conversely, defines a clear boundary (explicit interface) between the RANS and LES regions, ensuring that each model is applied only within its designated area. This method provides a clean division of the flow domain, with each subdomain independently solved using distinct sets of transport equations. The interface acts as a junction between the two models. However, the abrupt transition between RANS and LES can present challenges in accurately transferring turbulent properties, particularly

when matching turbulent stresses and length scales across the interface. For example, without proper adjustments, mismatches in turbulent kinetic energy across the boundary can lead to inaccuracies in predicting flow separation and reattachment (Spalart et al., 1997).

As shown in Figure 2.14, various techniques can be applied to model these interfaces. Given that the ELES model uses an explicit interface, the focus of this thesis is on explicit interface modelling in line with the segregated approach.

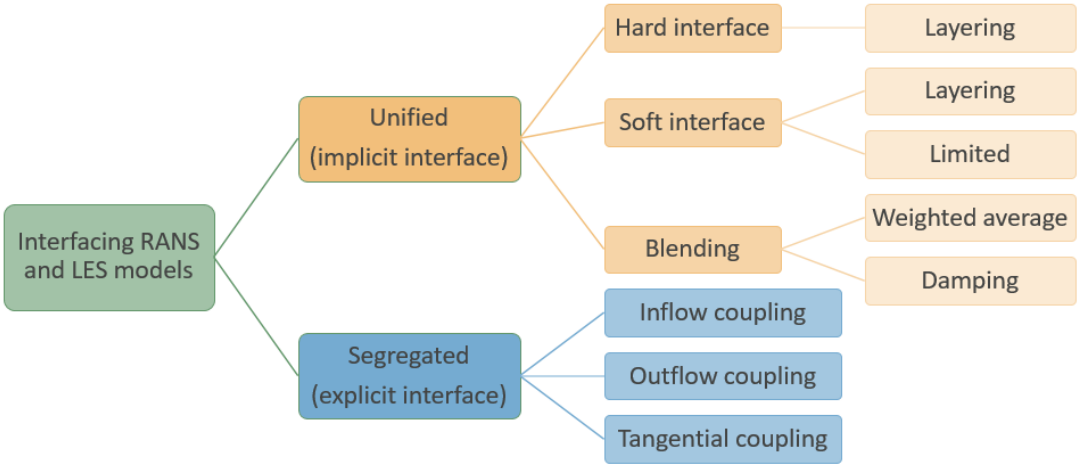


Figure 2.14 – Different approaches to resolving eddies in turbulent flows (*adapted from* Fröhlich and Terzi (2008)).

The segregated coupling method relies on internal boundary conditions that define which regions are subjected to either RANS or LES. Figure 2.15 illustrates this concept, depicting the different interfaces in ELES. The positioning of the LES region relative to the RANS region introduces various limitations and considerations, which necessitate meticulous attention and mitigation. These concerns will be discussed in detail in the following paragraphs.

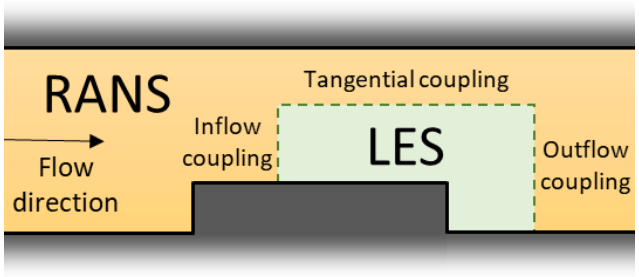


Figure 2.15 – Schematic representation of interface between LES and RANS regions in ELES.

In the inflow coupling region (see Figure 2.15), the transfer of flow properties from RANS to LES requires attention to prevent the emergence of artificial transition zones within the LES domain (Fröhlich and Terzi, 2008). This region is often referred as the "grey area", and it is characterized by underdeveloped resolved turbulent stresses (Mockett, 2018). This grey area arises from weak natural instabilities in the RANS region and the conversion of turbulent viscosity from RANS to LES. As a result, there is a mismatch in turbulent stress development, leading to two main issues: the log-layer mismatch phenomenon and under-prediction of wall shear stress (Yang, X. I. A. et al., 2017). One way to ensure a smooth transition is by adding turbulent fluctuations at the RANS-LES

interface. These fluctuations mimic natural turbulence and help maintain the continuity of turbulent structures as they move into the LES region. Various techniques can be applied to generate turbulent inflow fluctuations, including precursor simulation results (Jarrin et al., 2006) or flow databases tailored to specific conditions (Schlüter et al., 2005). Fourier transforms are also used as a tool to decompose periodic fluid flow behaviour into sinusoidal component. However, Fourier transform-based methods are limited to cartesian and equidistant grids, making them impractical for complex geometries (Kraichnan, 1970; Klein et al., 2003). Another approach is the Vortex Method, which is relatively inexpensive and accurate for generating inflow fluctuations at the RANS-LES interface (Mathey et al., 2006).

The Vortex Method adds a perturbation to a specified mean velocity profile by imposing a fluctuating vorticity field. It also ensures that the generated inflow turbulence is solenoidal (divergence-free), what prevents the creation of artificial sources or sinks of mass, which could otherwise distort the flow field (Leonard and Chua, 1989; Ogami, 2003). This method has been validated in studies involving high Reynolds numbers and geometrically complex flows. For example, Mathey et al. (2006) applied the Vortex Method to turbulent mixing simulations, and Leonard and Chua (1989) demonstrated its efficiency in capturing turbulent boundary layers. By employing this method, the study enhances the accuracy of inflow conditions in the LES domain, which is essential for capturing complex ejector flow dynamics. Given its proven capability to generate physically realistic turbulence and its effectiveness in maintaining flow consistency, the Vortex Method was selected in this study to ensure accurate inflow conditions in the LES domain.

For outflow coupling, mean flow data from LES is transferred back to RANS. In steady-state simulations, LES provides only mean flow data to RANS, but in cases involving unsteady data it is crucial that these fluctuations exit smoothly without reflecting back into the LES domain, which would otherwise compromise simulation accuracy (Holgate et al., 2019). While this study does not utilise outflow coupling, more details on this method can be found in Schlüter et al. (2005) and Holgate et al. (2019).

Finally, tangential coupling, which occurs when RANS and LES streamline directions align, remains underreported in the literature (Quéméré and Sagaut, 2002; Fröhlich and Terzi, 2008). This technique is relevant when RANS computes only mean flow properties, and innovative solutions are needed to address discontinuities at the interface. However, this method was not used in the current study.

2.2.4 Near-Wall Treatments for turbulent flows

Wall-bounded turbulent flows are significantly influenced by the presence of walls, because large gradients of the flow variables develop in their vicinity. Therefore, suitable description of turbulence near solid surfaces is essential and has a great impact on the prediction accuracy independently whether RANS or LES methods are applied. In RANS, handling the near-wall region often requires distinct methodologies such as the wall function law or the near-wall model approach (Ferziger et al., 2020). The wall function law utilises empirical correlations to approximate the mean velocity profile in the near-wall region, assuming that the total shear stress equals the wall shear stress. It employs a logarithmic velocity profile, which simplifies computations but can lead to less precise predictions near solid boundaries. In contrast, the near-wall model extends the turbulence model right up to the wall, resolving the steep velocity gradients more

accurately. While this approach improves flow representation, it requires a much finer numerical mesh near the wall, increasing computational demand (Mockett, 2018).

Experimental results have demonstrated that the near-wall region of fully developed turbulent flow can be divided into distinct layers depending on the dominating mechanisms of turbulence in each region. Figure 2.16 illustrates these layers as a function of the dimensionless wall distance (y^+). Understanding this layered structure is crucial for accurately modelling turbulent flow near solid boundaries using both RANS and LES approaches.

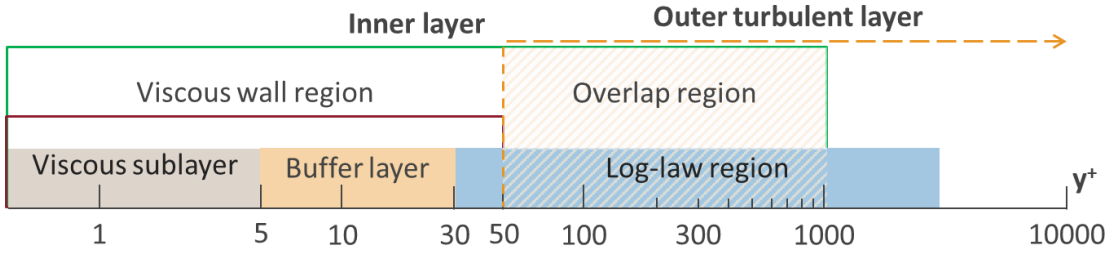


Figure 2.16 – Schematization of the wall regions in terms of y⁺ (adapted from Pope (2000)).

The first layer, nearest to the wall, is called the viscous sublayer. Here, the flow is essentially laminar and the velocity profile is nearly linear with a constant velocity gradient (U.S. Department of Energy, 1992). Consequently, the shear stress at the wall becomes:

$$\tau_w = \frac{\mu \cdot u}{\Delta y} \tag{2.12}$$

In equation (2.12), Δy is the wall distance, and μ the dynamic viscosity.

By making some flow variables non-dimensional, the characterisation of the turbulent boundary layer becomes more generalised. The most common adimensional scales are the shear or friction velocity (u_τ), the dimensionless distance from the wall (y^+), and the characteristic velocity (u^+). These non-dimensional variables are defined as:

$$u_\tau = \sqrt{\frac{\tau_w}{\rho}}, \tag{2.13}$$

$$y^+ = \frac{\Delta y \cdot \rho \cdot u_\tau}{\mu}, \tag{2.14}$$

$$u^+_{visc} = \frac{u}{u_\tau}. \tag{2.15}$$

Concerning Figure 2.16, the buffer layer ($5 < y^+ < 30$) is a transition zone between the laminar and turbulence-dominated regions. No well-established mathematical formulation exists for this region, often referred to as the blending region. Both RANS and LES have their unique approaches and challenges in modelling this region. Specific approaches for handling the blending region in this work are detailed in Chapter 3, section 3.3.6 for RANS and 3.4.4 for LES. Beyond $y^+ = 30$, both experimental data and DNS have confirmed the validity of the logarithmic law (Salim and Cheong, 2009; Kudela, 2011; Ferziger et al., 2020), which is expressed as:

$$u_{log}^{+} = \frac{1}{\kappa} ln(y^{+}) + B. \tag{2.16}$$

In equation (2.16), κ is the von Kármán constant and B an empirical constant. Recent investigations have concluded that the logarithmic law is not universal; some variations depend on the Reynolds number and flow conditions (Ferziger et al., 2020). It is important to determine the empirical constants B in Equation (2.16) for a specific problem (Salim and Cheong, 2009).

Additionally, the displacement thickness (δ^*) and momentum thickness (γ) are important measures in the context of boundary layer flows (Pope, 2000). The displacement thickness is defined by the integral (Kundu et al., 2012a):

$$\delta^*(x) = 2 \cdot \int_0^{\mathrm{R}} r \cdot \left(1 - \frac{\overline{u(x)}}{\overline{u_\infty(x)}}\right) dr \tag{2.17}$$

This represents the hypothetical distance that the wall would need to be displaced outward under ideal frictionless conditions, to maintain the same mass transport rate as in the actual case (Kundu et al., 2012a). Similarly, the momentum thickness (γ) quantifies the reduction in momentum flux due to the presence of the boundary layer and is defined as (Kundu et al., 2012a):

$$\gamma(x) = 2 \cdot \int_0^{\mathrm{R}} r \cdot \frac{\overline{u(x)}}{\overline{u_\infty(x)}} \cdot \left(1 - \frac{\overline{u(x)}}{\overline{u_c(x)}}\right) dr \tag{2.18}$$

In equations (2.17) and (2.18), $\overline{u_\infty(x)}$ is the free-stream velocity, and R is the total radius of the section at x.

In LES, traditional near-wall treatments are generally not required, as larger turbulence scales are resolved directly (Pope, 2000). However, for high Reynolds number flows, this becomes computationally prohibitive (Pope, 2000). As a result, the WMLES approach emerges as a compromise, where the near-wall region is modelled to reduce computational burden. Details about this model can be found in Section 3.4.2.

2.3 Multi-fluid dynamics

Modelling multi-fluid dynamics is essential for understanding and predicting the behaviour of two-phase flows, especially in complex systems like ejectors. Based on predefined assumptions, multiphase models must solve the governing equations for multiphase flow and track the equilibrium between the different phases. Several models are commonly used for this purpose.

2.3.1 Two-phase flow modelling in ejector

In two-phase flow ejector systems, two-phase flow modelling is crucial for predicting performance. The Homogeneous Equilibrium Model (HEM) is frequently employed due to its simplicity. This model assumes that thermodynamic equilibrium is maintained between the phases at all points, meaning that both phases share the same temperature and pressure (Ringstad et al., 2020). Additionally, the phases are perfectly mixed, having the same velocity and being in mechanical equilibrium (Angielczyk et al., 2019).

A more refined approach is the Homogeneous Relaxation Model (HRM), which allows for a relaxation process towards equilibrium. Unlike HEM, HRM introduces a finite relaxation

time, representing the gradual progression of the phases towards thermodynamic balance. (Bilicki and Kestin, 1990). This model is more adaptable to varying conditions in ejector flows, as the relaxation term can be empirically adjusted to fit different ejector configurations.

The Mixture Model further enhances the representation of two-phase flows by calculating the thermodynamic properties as a mass-weighted average of each phase (Ringstad et al., 2020). This model is particularly useful for capturing smooth variation of fluid density and predicting key parameters like the entrainment ratio and the motive mass flow (Giacomelli et al., 2019). However, Giacomelli et al. (2019) concluded that the convergence time was ten times higher compared to the HEM scheme, for ejector flow simulation. Despite this, recent versions of the mixture model have shown high accuracy in predicting the primary mass flow rate, with a errors under 2%, though accuracy diminishes at lower primary flow pressures (Ringstad et al., 2020).

The Delayed Equilibrium Model (DEM) offers another approach by considering three phases: saturated vapour, saturated liquid, and metastable liquid. While DEM assumes pressure equilibrium between all phases, it introduces thermal non-equilibrium, where the metastable liquid may have a higher temperature than the saturated liquid and vapour (Ringstad et al., 2020).

Finally, the Two-Fluid Model (TFM) treats each phase independently, solving a separate set of governing equations for each (Ishii and Hibiki, 2006). This model allows for a more detailed representation of non-equilibrium conditions by including interaction terms between phases, such as momentum exchange and velocity slip. The TFM approach is particularly useful for capturing velocity non-equilibrium, where each phase has its own velocity field, making it suitable for ejector simulations where phase interactions are complex and dynamic (Ishii and Hibiki, 2006). However, this model also introduces greater computational complexity due to the need to solve multiple sets of equations.

In systems where non-equilibrium between phases is considered, the non-equilibrium in some properties like pressure (often neglected in most models), velocity, temperature (can be neglected if the mesh resolution allows each cell to contain only one phase), and chemical potential are carefully evaluated. Only the mixture model and TFM allow the application of non-equilibrium momentum, where each phase has its velocity field. Other models may include additional equations to account for velocity non-equilibrium by adding an extra equation for velocity slip between the phases (Yazdani et al., 2012). Nevertheless, studies show that velocity non-equilibrium often has only a minor effect on the global performance of ejectors (Ringstad et al., 2020).

It is worth noting that the present published work showed that none of these models can predict the secondary mass flow rate with high accuracy. Errors often exceed 20%, mainly because this flow rate depends heavily on the turbulence of the mixing, the local velocity vector, and the momentum interaction between phases (Ringstad et al., 2020). In contrast, the motive mass flow rate is more accurately predicted, as it primarily depends on the primary flow pressure and temperature.

Based on the literature review, it can be concluded that while alternative models to HEM may provide better accuracy under specific flow conditions, they typically require prior calibration and/or demand increased time and computational resources. For these reasons, HEM will be employed for RANS modelling.

2.3.2 LES two-phase flow modelling

In recent years LES has gained attention as a powerful tool for investigating two-phase flows. LES is particularly effective for cases involving highly dispersed phases, where larger eddies dominate the flow dynamics. In such cases, it is common to solve for only one phase without any two-way coupling between the phases and the interface (Labourasse et al., 2007). This approach has been widely applied to particle-laden flows and sprays, where the particles are often smaller than the Kolmogorov scale, thus requiring detailed turbulence resolution. However, the computational cost remains a significant challenge (Kamin et al., 2023).

Schmitt and Ducruix (2023) demonstrated that LES coupled with HEM could accurately simulate coaxial cryogenic flames. Their study showed that even with the simplifying assumptions of HEM, LES produced reasonable results when the grid resolution was appropriate. This coupling enables LES to handle complex scenarios where both turbulence and phase interactions play crucial roles while maintaining computational feasibility.

For RANS, in an ejector two-phase flow, HEM has shown that it can provide accurate results without the need for calibration, making it simpler and less computationally intensive. Despite these successes, HEM cannot account for surface tension and atomisation, which may lead to inaccuracies in highly dispersed or complex flows (Schmitt and Ducruix, 2023). However, these limitations are balanced by the model's simplicity and its ability to simulate flows in ejectors with reasonable accuracy, particularly when high computational efficiency is required. Therefore, for two-phase flow ejector modelling, HEM presents a computationally feasible and effective solution, even for LES.

Chapter 3

Big whorls have little whorls,
Which feed on their velocity;
And little whorls have lesser whorls,
And so on to viscosity.
Lewis Fry Richardson (1922)

Mathematical model development

In this chapter, the fundamental equations governing turbulent flows are presented, including the Navier-Stokes equations, along with the associated turbulence models. First, a two-fluid model is introduced, in which each fluid phase is independently treated under thermodynamic non-equilibrium. This model is then applied to two cases: single-phase flow and two-phase flow. For the two-phase flow, thermodynamic equilibrium is assumed, resulting in the well-known Homogeneous Equilibrium Model. Subsequently, the Favre averaged and filtered governing equations are discussed, representing the developed Reynolds-Averaged Navier-Stokes (RANS) and Large Eddy Simulation (LES) models. To assist the reader, Appendix A presents the mathematical conventions applied in this document.

3.1 Thermodynamic property considerations

The evaluation of fluid properties in the single-phase ejector flow simulations was based on the database published by the National Institute of Standards and Technology (NIST), Thermodynamic and Transport Properties of Refrigerants and Refrigerant Mixtures Database Version 9.1 (REFPROP v9.1) (Lemmon et al., 2013). This database included a wide spectrum of common fluids and refrigerants, as the case of the fluid employed for the single-phase simulation: $C_3H_2F_4$, commercially known as R1234ze(E) from the hydrofluoroolefin (HFO) group. For additional information regarding the NIST REFPROP database refer to Thol and Lemmon (2016).

For the two-phase ejector flow simulations, carbon dioxide was used as the working fluid. The database for the two-phase CO_2 was created specifically for this thesis. It has two independent variables as inputs, with the output being a list of various thermodynamic properties. To generate the necessary property table, the software EES (F-Chart Software, 2020) was utilized. For each phase (liquid and gas), EES employs the equation of state (EoS) developed by Span and Wagner (1996) for CO_2 to compute each thermodynamic property, excluding thermal conductivity and viscosity. Thermal conductivity was determined using the method proposed by Vesovic et al. (1990), while viscosity was calculated following the approach described by Fenghour et al. (1998). For a more detailed discussion on the two-phase property table generation, the reader is referred to Section 3.2.2.

3.2 The Governing equations of fluid flow

The governing equations are based on three conservation laws of physics: continuity, Newton's second law, and the first and second laws of thermodynamics (Versteeg and Malalasekera, 2007). The particular form of these equations may vary, depending on the

underlying assumptions of the model (Versteeg and Malalasekera, 2007). In an initial approach, it is assumed that thermodynamic quantities remain unaffected by the local velocity field, implying separate compressible and unsteady velocity fields for each fluid phase (Linga and Flåtten, 2019). Since the flow under study involves two phases, the equations representing a two-fluid flow model are as follows:

$$\frac{\partial(\alpha_p\rho_p)}{\partial t}+\frac{\partial(\alpha_p\rho_p u_{p,j})}{\partial x_j}=K_p \tag{3.1}$$

$$\frac{\partial(\alpha_p\rho_p u_{p,i})}{\partial t}+\frac{\partial(\alpha_p\rho_p u_{p,i}u_{p,j})}{\partial x_j}= = -\frac{\partial(\alpha_p p_p)}{\partial x_i}+\frac{\partial \alpha_p\tau_{p,ji}}{\partial x_j}+p_{int}\frac{\partial \alpha_p}{\partial x_i}+u_{int,i}K_p+M_p \tag{3.2}$$

$$\frac{\partial(\alpha_p\rho_p E_p)}{\partial t}+\frac{\partial(\alpha_p\rho_p u_{p,j}E_p)}{\partial x_j}=-\frac{\partial q_{p,j}}{\partial x_j}-\frac{\partial(\alpha_p p_p u_{p,j})}{\partial x_j}+\frac{\partial(\alpha_p u_{p,i}\tau_{p,ji})}{\partial x_j}+ +p_{int}u_{int,i}\frac{\partial \alpha_p}{\partial x_i}-p_{int}I_p+\left(\mu^*_{int}+\frac{1}{2}u^2_{int,i}\right)K_p+u_{int,i}M_p+H_p \tag{3.3}$$

In equations 3.1 to 3.3, the subscript int denotes the interface between the phase properties and p each phase. These equations must be written twice: one for the liquid phase ($p=l$) and once for the vapour phase ($p=g$). Additionally, the momentum equation in (3.2) is divided into three components, corresponding to the x ($i=1$), y ($i=2$), and z ($i=3$) directions.

Each phase exhibits distinct pressure (p_p), temperature (T_p), chemical potential (μ^*_p), and velocity ($\vec{u}_p$). The terms $K_p, M_p,\ I_p$ and H_p are source terms that account for the progression towards equilibrium during the mixing process between the phases. These source terms correspond to different transfer processes, as outlined below:

- Mass transfer relaxation is given by equation (3.4) and it is applied when there is a difference in chemical potential between phases, resulting in a mass transfer from the phase with a higher chemical potential to the one with a lower potential for $\mathcal{K}\geq 0$.

$$\mathcal{K}=\frac{K_g}{\mu^*_l-\mu^*_g}=-\frac{K_l}{\mu^*_l-\mu^*_g} \tag{3.4}$$

  The chemical potential for the phase p (μ^*_p) is defined as (Demirel and Gerbaud, 2019):

$$\mu^*_p=\left(\frac{\partial G}{\partial N_p}\right)_{T,P,N_{m(m\neq p)}} \tag{3.5}$$

  Where N_p is the number of moles for phase p, and m is the other fluid phase.

- Momentum transfer defines the progression toward velocity equilibrium, driven by velocity differences between phases. The interface friction is defined as expressed in equation (3.6). It involves the transfer of momentum from the higher velocity to the lower velocity phase for $\mathcal{M}\geq 0$.

$$\mathcal{M}=\frac{M_g}{u_l-u_g}=-\frac{M_l}{u_l-u_g} \tag{3.6}$$

- The volume transfer process progresses towards mechanical equilibrium due to pressure differences between phases, resulting in expansion or compression, as described by the pressure relaxation equation (3.7), where $\wp \geq 0$ ensures that the phase with lower pressure compresses and the phase with higher pressure expands.

$$\wp = \frac{I_g}{p_g - p_l} = -\frac{I_l}{p_g - p_l} \tag{3.7}$$

- The heat transfer relaxation mechanism, characterized by equation (3.8), is driven by temperature differences between phases. By setting $\mathcal{H} \geq 0$, the heat is transferred from the hotter phase to the colder one.

$$\mathcal{H} = \frac{H_g}{T_l - T_g} = -\frac{H_l}{T_l - T_g} \tag{3.8}$$

A two-fluid model requires a transport equation for the volume fraction (α_p). This equation incorporates an advection term governed by the interface velocity ($u_{int,i}$). Additionally, the movement of the interface between phases is driven by pressure differences. Thus, the transport equation for the volume fraction can be formulated as follows (Linga and Flåtten, 2019):

$$\frac{\partial \alpha_g}{\partial t} + u_{int,i}\frac{\partial \alpha_g}{\partial x_i} = \wp\left(p_g - p_l\right) \tag{3.9}$$

In equation (3.9), $\alpha_g + \alpha_l = 1$ with $\alpha \in (0,1)$.

The energy equation (3.3) defines the fluid's specific energy (E) as the sum of internal (e) and kinetic energies. Deriving the transport equation for the specific internal energy requires obtaining the transport equation for kinetic energy. This involves multiplying the momentum equation (3.2) by the velocity vector and incorporating a mass transfer relation, as described by Linga and Flåtten (2019):

$$\begin{aligned}\frac{\partial\left(\frac{\alpha_p\rho_p u_{p,i}u_{p,i}}{2}\right)}{\partial t} + \frac{\partial\left(\frac{\alpha_p\rho_p u_{p,i}u_{p,i}u_{p,j}}{2}\right)}{\partial x_j} &= -u_{p,i}\frac{\partial\left(\alpha_p p_p\right)}{\partial x_i} + u_{p,i}\frac{\partial \alpha_p \tau_{p,ji}}{\partial x_j} + \\ &+ u_{p,i}p_{int}\frac{\partial \alpha_p}{\partial x_i} - \frac{1}{2}u_{p,i}^2 K_p + u_{p,i}u_{int}K_p + u_{p,i}M_p\end{aligned} \tag{3.10}$$

By subtracting the kinetic energy equation (3.10) from the energy equation (3.3), the transport equation for internal energy can be obtained:

$$\begin{aligned}\frac{\partial\left(\alpha_p\rho_p e_p\right)}{\partial t} + \frac{\partial\left(\alpha_p\rho_p u_{p,j}e_p\right)}{\partial x_j} &= -\frac{\partial q_{p,j}}{\partial x_j} - \alpha_p p_p\frac{\partial u_{p,j}}{\partial x_j} + \alpha_p\tau_{p,ji}\frac{\partial u_{p,i}}{\partial x_j} + \\ &+ p_{int}\left(u_{int} - u_{p,i}\right)\frac{\partial \alpha_p}{\partial x_i} - p_{int}I_p + \left(\mu_{int}^* + \frac{1}{2}\left(u_{int} - u_{p,i}\right)^2\right)K_p + \\ &+ \left(u_{int} - u_{p,i}\right)M_p + H_p\end{aligned} \tag{3.11}$$

In equation (3.11), $\tau_{p,ji}$ is the viscous stress tensor given by:

$$\tau_{p,ji} = \mu_p\left(\frac{\partial u_{p,i}}{\partial x_j} + \frac{\partial u_{p,j}}{\partial x_i}\right) + \varsigma_p\,\delta_{ij}\frac{\partial u_{p,k}}{\partial x_k} \tag{3.12}$$

In (3.12) i, j, and k represent the indices in the Einstein summation notation, δ_{ij} denotes the Kronecker delta ($\delta_{ij} = 1$ if $i = j$ and $\delta_{ij} = 0$ if $i \neq j$) (Versteeg and Malalasekera,

2007) and ς_p represents the longitudinal viscosity or second viscosity for the phase p. This latter requires calibration with experimental data (Bosch, 2023; Sharma and Kumar, 2023). It expresses the relation between shear viscosity (μ_p) and bulk viscosity (ψ_p) as:

$$\varsigma_p = -\frac{2}{3}\cdot \mu_p + \psi_p \tag{3.13}$$

To derive the enthalpy equation, it is necessary to add a pressure term to the internal energy equation (3.11), resulting in the transport equation for enthalpy (Versteeg and Malalasekera, 2007):

$$\begin{aligned}\frac{\partial(\alpha_p\rho_p h_p)}{\partial t} - \frac{\partial(\alpha_p p_p)}{\partial t} + \frac{\partial(\alpha_p\rho_p u_{p,j} h_p)}{\partial x_j} = -\frac{\partial q_{p,j}}{\partial x_j} + u_{p,j}\frac{\partial(\alpha_p p_p)}{\partial x_j} + \\ +\alpha_p\tau_{p,ji}\frac{\partial u_{p,i}}{\partial x_j} + p_{int}(u_{int} - u_{p,i})\frac{\partial \alpha_p}{\partial x_i} - p_{int}I_p + \\ +\left(\mu^*_{int} + \frac{1}{2}(u_{int} - u_{p,i})^2\right)K_p + (u_{int} - u_{p,i})M_p + H_p\end{aligned} \tag{3.14}$$

3.2.1 Single-phase flow

The governing equations for single-phase flow can be derived from equations 3.1 to 3.3, by considering only single-phase and $\alpha_p = 1$, as a result, the same equation can be written as (Versteeg and Malalasekera, 2007):

$$\frac{\partial \rho}{\partial t} + \frac{\partial(\rho u_j)}{\partial x_j} = 0 \tag{3.15}$$

$$\frac{\partial(\rho u_i)}{\partial t} + \frac{\partial(\rho u_i u_j)}{\partial x_j} = -\frac{\partial p}{\partial x_i} + \frac{\partial \tau_{ji}}{\partial x_j} \tag{3.16}$$

$$\frac{\partial(\rho E)}{\partial t} + \frac{\partial(\rho u_j E)}{\partial x_j} = -\frac{\partial q_j}{\partial x_j} - \frac{\partial(p u_j)}{\partial x_j} + \frac{\partial(u_i\tau_{ji})}{\partial x_j} \tag{3.17}$$

These partial differential equations describe the conservation of mass, momentum, and energy in the fluid. The energy equation (3.17) quantifies the rate of change of energy in the fluid due to heat transfer, pressure, and viscous dissipation. The first term on the right-hand side of equation 3.17, represents the net rate of heat transfer to the fluid particle due to heat flow, in most cases, can be modelled using Fourier's law of heat conduction expressed as (Versteeg and Malalasekera, 2007):

$$q_j = -\kappa\frac{\partial T}{\partial x_j} \Rightarrow -\frac{\partial q_j}{\partial x_j} = \frac{\partial}{\partial x_j}\left(\kappa\frac{\partial T}{\partial x_j}\right) = \frac{\partial(\kappa\,\nabla T)}{\partial x_j} \tag{3.18}$$

By replacing the specific energy (E) with the sum of internal (e) and kinetic energies ($(u^2 + v^2 + w^2)/2$), rearranging terms, and introducing the definition of the specific enthalpy (h), the energy equation (3.17) can be rewritten as:

$$\frac{\partial}{\partial t}\left[\rho\left(e + \frac{u_i u_i}{2}\right)\right] + \frac{\partial}{\partial x_j}\left[\rho u_j\left(h + \frac{u_i u_i}{2}\right)\right] = \frac{\partial}{\partial x_j}\left(\kappa\frac{\partial T}{\partial x_j}\right) + \frac{\partial(u_i\tau_{ji})}{\partial x_j} \tag{3.19}$$

3.2.2 Two-phase flow

When the mass, momentum, volume and heat transfer between phases occur rapidly enough, the flow can achieve thermodynamic equilibrium at each instance (Banasiak and Hafner, 2011), thereby extending to equilibrium between phases. By making this assumption, the model simplifies as follows:

- Mechanical equilibrium: is achieved with an infinitely large pressure relaxation factor ($\wp \to \infty$), resulting in uniform pressures between the gas and liquid phases ($p_g = p_l \equiv p$);
- Thermal equilibrium: is reached instantaneously, with $\mathcal{H} \to \infty$ and equal temperatures between gas and liquid phases ($T_g = T_l \equiv T$);
- Chemical equilibrium: is represented by the chemical relaxation parameter $\mathcal{K} \to \infty$ and equal chemical potentials between gas and liquid phases ($\mu_g^* = \mu_l^* \equiv \mu^*$);
- Velocity equilibrium: is denoted by $\mathcal{M} \to \infty$, resulting in equal velocities between gas and liquid phases ($\vec{u}_g = \vec{u}_l \equiv \vec{u}$).

This assumption culminates in the instantaneous mixing of the phases, which is the premise of the Homogeneous Equilibrium Model (HEM) (Angielczyk et al., 2019). Consequently, the continuity, momentum, specific internal energy and enthalpy equations for thermodynamic equilibrium can be written as:

$$\frac{\partial \rho}{\partial t} + \frac{\partial \left(\rho u_j\right)}{\partial x_j} = 0 \tag{3.20}$$

$$\frac{\partial (\rho u_i)}{\partial t} + \frac{\partial \left(\rho u_i u_j\right)}{\partial x_j} = -\frac{\partial p}{\partial x_i} + \frac{\partial \tau_{ji}}{\partial x_j} \tag{3.21}$$

$$\frac{\partial (\rho e)}{\partial t} + \frac{\partial \left(\rho u_j e\right)}{\partial x_j} = -p\frac{\partial u_j}{\partial x_j} + \tau_{ji}\frac{\partial u_i}{\partial x_j} + \frac{\partial}{\partial x_j}\left(\kappa \frac{\partial T}{\partial x_j}\right) \tag{3.22}$$

$$\frac{\partial (\rho h)}{\partial t} - \frac{\partial p}{\partial t} + \frac{\partial \left(\rho u_j h\right)}{\partial x_j} = u_j\frac{\partial p}{\partial x_j} + \tau_{ji}\frac{\partial u_i}{\partial x_j} + \frac{\partial}{\partial x_j}\left(\kappa \frac{\partial T}{\partial x_j}\right) \tag{3.23}$$

Typically, the energy equation for modelling two-phase ejector flow is expressed in terms of enthalpy, as shown in Equation (3.23) (Ringstad et al., 2020). Under the steady-state assumption, time-dependent terms become negligible, leading to the elimination of the first and second terms on the left-hand side of equation (3.23). However, in transient simulations, these terms must be modelled explicitly. To mitigate potential errors associated with this additional modelling step and to reduce computational costs, this study employs the internal energy equation (3.22) for the energy balance. Furthermore, as will be demonstrated later, this approach enables the explicit consideration of pressure work and dilatation effects, which are not accounted for when using the enthalpy-based formulation.

For the HEM consideration, the thermodynamic properties in the model are derived from the individual liquid and vapour phase properties and their relative fractions. For example, the mixture density (ρ) is determined as the weighted sum of the densities of each phase and their respective volume fractions (α_p) as:

$$\rho = \rho_g \cdot \alpha_g + \rho_l \cdot \alpha_l \tag{3.24}$$

In equation (3.24), α_g and α_l are the vapour and liquid volume fractions, respectively.

In a homogenous two-phase flow, the pressure and temperature are not independent. Nevertheless, all thermodynamic and transport properties must be determined from two independent properties. For the internal energy equation, the pressure and internal energy were selected as the independent variables. Other properties, such as density, specific enthalpy, specific entropy, specific heat, viscosity, and thermal conductivity, were obtained as weighted averages with the vapour quality ($\boldsymbol{x}$) being the weighing factor such that:

$$\boldsymbol{x} \cdot \varphi_g + (1 - \boldsymbol{x}) \cdot \varphi_l = \varphi_m \tag{3.25}$$

For the speed of sound, a different approach was implemented. For single-phase flow, the speed of sound is obtained by:

$$c = \left(\frac{dp}{d\rho}\right)^{0.5} \tag{3.26}$$

In a two-phase flow, the speed of sound also depends on the surface tension between phases (Brennen, 2005). However, since pressure equilibrium is assumed, the surface tension is considered to be very small (Ishii and Hibiki, 2006), and thus, effectively negligible for this analysis. Therefore, in this context, the speed of sound is modelled using Brennen's (2005) approach, which considers homogeneous equilibrium (instantaneous heat transfer between phases) and homogeneous frozen responses (no heat transfer between phases) as special extreme cases of model validity. By neglecting the surface tension, the speed of sound for a two-phase flow model simplifies to the same expression found in equation (3.26), aligning with Brennen's model under these specific assumptions, resulting in:

$$\frac{1}{c^2} = \frac{\rho}{p} \cdot \left[\alpha_g \cdot \left((1 - \epsilon_g) \cdot f_g + \epsilon_g \cdot g_g\right) + \alpha_l \cdot \left((1 - \epsilon_l) \cdot f_l + \epsilon_l \cdot g_l\right)\right] \tag{3.27}$$

Here, f and g are functions of the thermodynamic properties of the two phases and are functions of the thermodynamic properties of the fluid. These functions can be expressed as:

$$f_g = \left(\frac{\partial \ln \rho_g}{\partial \ln p}\right)_s \quad f_l = \left(\frac{\partial \ln \rho_l}{\partial \ln p}\right)_s$$

$$g_g = \left(\frac{\partial \ln \rho_g}{\partial \ln p}\right)_e + \left(1 - \frac{\rho_g}{\rho_l}\right) \cdot \left(\frac{h_l}{h_g - h_l} \cdot \frac{\partial \ln h_l}{\partial \ln p} + \frac{\partial \ln(h_g - h_l)}{\partial \ln p} - \frac{p}{(h_g - h_l) \cdot \rho_g}\right)_e \tag{3.28}$$

$$g_l = \left(\frac{\partial \ln \rho_l}{\partial \ln p}\right)_e + \left(\frac{\rho_l}{\rho_g} - 1\right) \cdot \left(\frac{h_l}{h_g - h_l} \cdot \frac{\partial \ln h_l}{\partial \ln p} - \frac{p}{(h_g - h_l) \cdot \rho_l}\right)_e$$

According to Brennen (2005), it is common practice to approximate f_g by the inverse of the specific heat ratio for the gas, which results in $f_g \approx 1$, while f_l is approximated to zero. Substituting these values into equation (3.27) leads to:

$$\frac{1}{c^2} = \frac{\rho}{p}\left[\alpha_g \cdot \left((1 - \epsilon_g) + \epsilon_g \cdot g_g\right) + (1 - \alpha_g) \cdot \epsilon_l \cdot g_l\right] \tag{3.29}$$

To determine the liquid index (g_l), there are some models available in the literature. According to Brennen (2005), for example, g_l can be determined as a function of the pressure and critical pressure (p_{crt}) from:

$$g_l = 2.11 - \epsilon_g \left(\frac{p}{p_{\mathrm{crt}}}\right)^{-0.566} \tag{3.30}$$

Figure 5.22 shows g_g and g_l as a function of pressure for CO_2. As can be seen in the figure, the vapour index (g_g) remains close to 1 and varies very little with pressure, consistent with typical assumptions (Giacomelli et al., 2019).

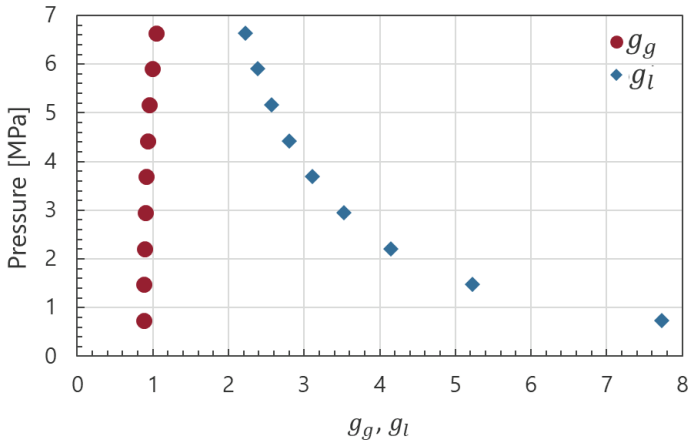


Figure 3.1 – CO_2 typical values for vapour index (g_g) and liquid index (g_l) as a function of pressure (Brennen, 2005).

Regarding ϵ_g and ϵ_l in equation (3.29), these variables represent the fractions of vapour or liquid that exchange heat with each other. The fractions $(1-\epsilon_g)$ and $(1-\epsilon_l)$ are assumed to be insulated and isentropic. In contrast, heat transfer occurs instantaneously between phases for ϵ_g and ϵ_l due to their close proximity. As the vapour volume fraction (α_g) approaches 1, the term involving ϵ_l becomes negligible, corresponding to a dispersed liquid phase in a vapour flow. Therefore, ϵ_l is more significant in cases with low vapour volume fractions or bubbly flows, where the interacting liquid fraction is comparable to the vapour volume fraction. Similarly, ϵ_g can be approximated by $\epsilon_g \approx (1-\alpha_g)$ and $\epsilon_l \approx \alpha_g$ to represent their magnitudes.

Another important property is the bulk viscosity (ψ). This property quantifies a fluid's resistance to volume changes, including both reversible and irreversible aspects. It is influenced by the isentropic bulk modulus, representing the fluid's stiffness concerning adiabatic and reversible volume change (Sharma and Kumar, 2023). To understand the bulk viscosity, one should look at the definition of the stress tensor ($\sigma_{ji} = \tau_{ji} - p\delta_{ji}$) in the momentum equation (3.2) (Bosch, 2023). The translational motion of particles is captured by the mechanical pressure (p_{m}), derived from the average normal stress as follows (Di Nucci et al., 2020):

$$p_{\mathrm{m}} = -\frac{1}{3}(\sigma_{xx} + \sigma_{yy} + \sigma_{zz}) \tag{3.31}$$

Replacing the normal stress tensor in equation (3.31), the mechanical pressure can be defined as:

$$p_{\mathrm{m}} = -\psi \frac{\partial u_k}{\partial x_k} + p \tag{3.32}$$

The introduction of bulk viscosity into the energy equation in fluids is needed to account for the discrepancy between the non-equilibrium (p_{m}) and equilibrium pressures (p). Assuming a zero bulk viscosity implies that the mechanical pressure consistently matches the thermodynamic pressure, regardless of the system's dynamics. This suggests that viscous forces remain unaffected by the rate of expansion or compression (Sharma and Kumar, 2023), which might not be the case for compressible flows. For the CO_2 ejector flow, the zero bulk viscosity assumption is inadequate due to both the flow characteristics and the fluid properties. Compressible flow, involving phenomena like wave-front spreading, fluid expansion and compression, and sound attenuation, according to the available literature, requires the consideration of the second viscosity (Guo and Zhang, 2001; Meier et al., 2005; Fanourgakis et al., 2012). Additionally, CO_2 is a polyatomic fluid, emphasizing the significance of the bulk-to-shear viscosity ratio, which is as high as 3,828 for 300 K (Sharma and Kumar, 2023).

To quantify CO_2 bulk viscosity, a number of researchers used a model derived from the Boltzmann equation (Zuckerwar and Ash, 2006):

$$\psi = \frac{2(d-3)}{d^2} \cdot p \cdot \mathrm{t} \tag{3.33}$$

In equation (3.33), d represents the number of molecular degrees of freedom (according to Fang et al. (2019) for CO_2 $d = 5$), and t denotes the relaxation time. It is noted t requires experimental data to avoid numerical instabilities. Fang et al. (2019) examined how including or excluding bulk viscosity affects pressure and vapour quality distributions in a CO_2 converging-diverging flashing nozzle. They considered two different relaxation times (10^{-5} s and 5×10^{-6} s) and found that numerical instabilities arose for relaxation times greater than 10^{-5} s. Their investigation reported marginal deviations in pressure and vapour quality near the nozzle's throat due to varying expansion rates. However, these variations did not significantly affect the initiation point of the fluid flashing. Consequently, bulk viscosity shows a minimal influence on the CO_2 flow behaviour within a supersonic converging-diverging nozzle. Nevertheless, it is crucial to acknowledge that more significant effects may emerge under conditions of intense compression or expansion, such as in shock waves (Bosch, 2023). Given the numerical instabilities associated with bulk viscosity and the challenges in selecting suitable relaxation time, the term related to bulk viscosity was omitted for the developed model.

3.3 Favre Averaging description of the governing equations of turbulence

Compressible turbulent flows pose unique challenges due to the intrinsic interaction between turbulence and compressibility effects. While laminar flow can be accurately described by the Navier-Stokes equations, turbulent compressible flow introduces fluctuations that significantly influence the wall shear stress. The stochastic and anisotropic nature of turbulence complicates the direct description of flow properties. Solving the Navier-Stokes equations via DNS is still remote (Ceci et al., 2022) for ejector flow analysis due to the high friction Reynolds numbers and system complexity. Instead, averaging and filtering techniques are necessary to effectively apply the ELES approach. This section focuses on introducing the Favre averaging principle for the Navier-Stokes

equations used in the developed model, mitigating the challenges that are associated with modelling additional unknown terms in turbulent flow descriptions.

Favre averaging implies the decomposition of the flow property terms into a density-weighted time-averaged term ($\tilde{\varphi}$) and a fluctuating term (φ''). The mean (mass-weighted time-averaged) flow property is defined as (Wilcox, 2006):

$$\tilde{\varphi} = \frac{1}{\bar{\rho}} \lim_{t\to\infty} \int_{t_0}^{t_0+t} \rho(\vec{x},t) \cdot u_i \cdot (\vec{x},t) dt \tag{3.34}$$

In equation (3.34) the overbar denotes a Reynolds-averaged property. Consequently, it is possible to establish the equality:

$$\overline{\rho\varphi} = \bar{\rho}\tilde{\varphi} + \overline{\rho\varphi''} \tag{3.35}$$

In equation (3.35), by definition, the second term of the right side is zero, however, is important to note that:

$$\overline{\varphi''} = \frac{\overline{-\rho'\varphi'}}{\bar{\rho}} \tag{3.36}$$

The equation (3.36) is different from zero.

More information about the averaging process rules can be found in Appendix B.1.

3.3.1 Favre averaged continuity equation

Applying the Favre averaging procedure to the mass conservation equation results in:

$$\frac{\partial\bar{\rho}}{\partial t} + \frac{\partial\left(\bar{\rho}\tilde{u}_j\right)}{\partial x_j} = 0 \tag{3.37}$$

Details about the averaging process can be found in Appendix B.2.1.

3.3.2 Favre averaged momentum equation

Applying the Favre averaging procedure to Newton's second law results in:

$$\frac{\partial(\bar{\rho}\tilde{u}_i)}{\partial t} + \frac{\partial\left(\bar{\rho}\tilde{u}_i\tilde{u}_j\right)}{\partial x_j} + \frac{\partial\left(\overline{\rho u_i'' u_j''}\right)}{\partial x_j} = -\frac{\partial\bar{p}}{\partial x_i} + \frac{\partial\overline{\tau_{ji}}}{\partial x_j} \tag{3.38}$$

The averaging process for the left side of equation (3.38) is detailed in Appendix B.2.2.

In the momentum equation (3.38), the term $\overline{\tau}_{ji}$ represents the sum of the laminar-like stress gradients for the mean motion term ($\tilde{\tau}_{ji}$) and apparent stress gradients ($\overline{\tau''}_{ji}$) due to the transport of momentum by turbulent fluctuations and deformations attributed to the fluctuations term (Anderson et al., 2020). The first term can be modelled using Boussinesq's assumption, and by neglecting the contribution of the bulk viscosity term this can be described as:

$$\tilde{\tau}_{ji} = \mu\left(\frac{\partial\tilde{u}_i}{\partial x_j} + \frac{\partial\tilde{u}_j}{\partial x_i}\right) - \frac{2}{3}\delta_{ij}\left(\mu\,\frac{\partial\tilde{u}_k}{\partial x_k}\right) \tag{3.39}$$

Several authors claim that the contribution of the molecular viscosity term ($\overline{\tau''}_{ji}$) to the equation is significantly smaller when compared to the Reynolds stresses tensor

($-\overline{\rho u_i'' u_i''}$), therefore the former is often neglected (Anderson et al., 2020). For the Reynolds stresses tensor term, this is usually modelled considering the eddy-viscosity assumption (C. Chen et al., 1991; Wilcox, 2006) as:

$$-\overline{\rho u_i'' u_j''} = -\overline{\rho}\widetilde{u_i'' u_j''} \approx \mu_T \left(\frac{\partial \tilde{u}_i}{\partial x_j} + \frac{\partial \tilde{u}_j}{\partial x_i}\right) - \frac{2}{3}\delta_{ij}\left(\mu_T \frac{\partial \tilde{u}_k}{\partial x_k} + \overline{\rho} k\right) \tag{3.40}$$

For subsonic flow, the term $\overline{\rho} k$ would vanish, and in case of incompressible flow, the term $\mu_T \, \partial \tilde{u}_k / \partial x_k$ would be zero. However, this is not the case for ejector flow simulations, which involve complex, compressible, and supersonic conditions. Thus, the Favre averaged momentum equation applied is given by:

$$\frac{\partial(\overline{\rho}\tilde{u}_i)}{\partial t} + \frac{\partial(\overline{\rho}\tilde{u}_i\tilde{u}_j)}{\partial x_j} = -\frac{\partial \overline{p}}{\partial x_i} - \frac{\partial\left(\overline{\rho u_i'' u_j''}\right)}{\partial x_j} + \frac{\partial \tilde{\tau}_{ji}}{\partial x_j} \tag{3.41}$$

In equation (3.40), μ_T is the eddy viscosity, or turbulent viscosity. An adequate approximation for this variable is to consider (Pope, 2000):

$$\mu_T = \overline{\rho} \cdot \mathcal{u}_T \cdot l_T \tag{3.42}$$

In equation (3.42) $\mathcal{u}_T$ and l_T correspond to a velocity and length scales that are specified according to the turbulence model adopted.

3.3.3 Favre averaged energy equation

For single-phase flow, the averaged energy equation is expressed as:

$$\frac{\partial(\overline{\rho}\widetilde{E})}{\partial t} + \frac{\partial(\overline{\rho}\widetilde{E})}{\partial x_j} = \frac{\partial(\kappa_{\text{eff}}\widetilde{T})}{\partial x_j} - \frac{\partial(\tilde{u}_j\overline{p})}{\partial x_j} + \frac{\partial\left(\tilde{u}_i \tau_{ji_{eff}}\right)}{\partial x_j} \tag{3.43}$$

Details about the origin of equation (3.43) can be found in Appendix B.2.3.

In equation (3.43) the left side is the total energy substantive derivative, where the density-averaged total energy is defined as:

$$\widetilde{E} \equiv \widetilde{e} + \frac{\tilde{u}_k \tilde{u}_k}{2} + k \tag{3.44}$$

In equation (3.44) the turbulent kinetic energy is defined as:

$$k = \frac{\widetilde{u_k'' u_k''}}{2}. \tag{3.45}$$

The first term of the right side of the equation (3.43) is the thermal diffusivity and considers the laminar and turbulent terms, the second term is the pressure work and the last is the laminar and turbulent viscous term. The expressions for effective conductivity (κ_{eff}) and effective stress tensor ($\tau_{ji_{eff}}$) depend on the turbulent model applied.

For two-phase flow, the Favre averaged internal energy equation can be expressed as:

$$\frac{\partial(\overline{\rho}\widetilde{e})}{\partial t}+\frac{\partial\left(\overline{\rho}\widetilde{e}\,\tilde{u}_j\right)}{\partial x_j}+\frac{\partial\left(\overline{\rho e'' u_j''}\right)}{\partial x_j}=\left[-\overline{p}\frac{\partial\tilde{u}_j}{\partial x_j}-\overline{p}\frac{\partial\overline{u_j''}}{\partial x_j}\right]-\left[\overline{p'\frac{\partial u_j''}{\partial x_j}}\right]+\\+\left[\tilde{\tau}_{ji}\frac{\partial\tilde{u}_i}{\partial x_j}+\overline{\tau_{ji}\frac{\partial u_i''}{\partial x_j}}\right]+\left[\frac{\partial}{\partial x_j}\left(\kappa\frac{\partial\widetilde{T}}{\partial x_j}\right)\right] \tag{3.46}$$

Details about the averaging process for equation (3.46) can be found in Appendix B.2.4.

For equation (3.46), the mean flow properties are straightforward to resolve; however the terms involving the velocity fluctuation (u_j'') require modelling. The third term on the left side of the equation (3.46) represents turbulence diffusivity, which can be modelled using the turbulent transport of a scalar (e). According to Anderson et al. (2020) it can be written as:

$$-\overline{\rho e''\overline{u''}}=-\overline{p}\widetilde{e''\overline{u''}}=\Gamma_T\nabla\widetilde{e}\,. \tag{3.47}$$

In equation (3.47), Γ_T represents the turbulent or eddy diffusivity, known as the ratio between the turbulent viscosity (μ_T) and the turbulent Prandtl number (σ_T). The latter is usually taken at constant (Versteeg and Malalasekera, 2007). Thus, the turbulent diffusivity term can be rewritten in equation (3.46) as:

$$\frac{\partial\left(\overline{\rho e''u_j''}\right)}{\partial x_j}=\frac{\partial}{\partial x_j}\left(-\frac{\mu_T}{\sigma_T}\frac{\partial\widetilde{e}}{\partial x_i}\right) \tag{3.48}$$

On the right side of equation (3.46), the terms are grouped with square parentheses. The first group describes the pressure work. These terms refer to the work performed by the fluid due to pressure-induced volume variations, the first related to the mean flow ($\tilde{u}_j$) and the second to the fluctuation ($\overline{u_j''}$), and the last needs to be modelled.

The term $\overline{u_j''}$ quantifies the compressibility effects arising from variations in density, representing the difference between unweighted and density-weighted averages of the velocity field (Ristorcelli, 1993). The model for predicting $\overline{u_j''}$, developed by Ristorcelli (1993) for wall bounded flow with $Ma = 4.5$, is commonly used in two-phase flow simulations as it satisfies the Galilean invariance (Wilcox, 2006). Despite not being validated with experimental data, this is the model applied in this study with certain simplifications proposed by the same author. Considering the specific characteristics of the flow under analysis and the limitations of the model, $\overline{u_j''}$ was computed under the assumption of anisotropic flow with small mean velocity gradients, as follows:

$$\overline{u_i''}=\Psi\,\widetilde{u_j''u_k''}\cdot\frac{\partial\overline{\rho}}{\partial x_k}\cdot\frac{1}{\overline{\rho}} \tag{3.49}$$

In equation (3.49), Ψ is a relaxation scale that is determined by:

$$\Psi=\frac{Ma_T k}{\varepsilon_s+Ma_T\cdot(\mathcal{P}/\bar{\rho}-\varepsilon_s)} \tag{3.50}$$

In equation (3.50), ε_s denotes the solenoidal turbulent kinetic energy dissipation, which is defined later in this section, and Ma_T represents the turbulent Mach number that is defined by:

$$Ma_T = \frac{\sqrt{2k}}{\overline{c}}. \tag{3.51}$$

This variable serves as a measure of compressibility by quantifying the ratio between turbulent velocity fluctuations and the local speed of sound (Sarkar, S. et al., 1993). Essentially, it indicates the degree to which compressibility influences turbulence within the flow field. Additionally, $\mathcal{P}$ denote the specific turbulent kinetic energy production.

Recalling the Favre averaged energy equation (3.46), the second group on the right side is the pressure dilatation. This term describes how fluctuating pressure influences the volume change within a fluid. Sarkar (1992) found through simulations and theoretical analyses that the pressure dilatation correlation for compressible flows can be written as:

$$\overline{p' \frac{\partial u_i''}{\partial x_i}} = \overline{\rho} \cdot Ma_T \cdot |2k| \cdot \left[\alpha_2 \cdot \frac{\partial \tilde{u}_i}{\partial x_j} \cdot b_{ij} + \frac{8}{3} \cdot \alpha_4 \cdot Ma_T \cdot \frac{\partial \tilde{u}_i}{\partial x_i} \right] + \alpha_3 \cdot \overline{\rho} \cdot \varepsilon_s \cdot Ma_T^2 \tag{3.52}$$

In equation (3.52), b_{ij} is the normalized anisotropy tensor given by:

$$b_{ij} = \frac{\widetilde{u_i'' u_j''}}{2k} - \frac{\delta_{ij}}{3} \tag{3.53}$$

Sarkar (1992) claimed that this correlation offers a reasonable approximation for weakly inhomogeneous flows unbounded, provided that the changes in flow properties, such as velocity and pressure, are observed over time intervals larger than the acoustic time scale ($t_{acustic}$), that is given by:

$$t_{acustic} = \frac{Ma_T \cdot k}{\varepsilon_s} \tag{3.54}$$

Additionally, the author emphasized the significance of the pressure dilatation term in the overall balance of turbulent kinetic energy in compressible flows, especially in high-speed flows. This means that the term plays a crucial role in understanding how turbulent energy is distributed and dissipated in these flows. Later, Sarkar, S. et al. (1993) calibrated the model using DNS data to account for the effects of isotropic turbulence and homogeneous shear, covering a range of turbulent Mach numbers (Ma_T) from 0.2 to 0.6. The study resulted in constants: $\alpha_2 = 0.15$, $\alpha_3 = 0.20$ and $\alpha_4 = 0$. Introducing these constants into equation (3.52) leads to:

$$\overline{p' \frac{\partial u_i''}{\partial x_i}} = -0.15 \cdot \mathcal{P} \cdot Ma_T + 0.2 \cdot \overline{\rho} \cdot \varepsilon_s \cdot Ma_T^2 \tag{3.55}$$

The third square parenthesis on the right side of equation (3.46) holds the viscous terms, the first is related to the laminar flow and the second describes the viscous effects in turbulent flows under the Favre averaged framework. This can be approximated as the sum of the solenoidal (ε_s) and dilatational (ε_d) dissipation rates, given by (Wilcox, 2006):

$$\overline{\tau_{ji} \frac{\partial u_i''}{\partial x_j}} = \overline{\rho} \cdot (\varepsilon_s + \varepsilon_d) \tag{3.56}$$

These dissipation terms can be expressed as:

$$\varepsilon_s = \beta^* \cdot \omega \cdot k \tag{3.57}$$

$$\varepsilon_d = \xi^* \cdot f(Ma_T) \cdot \varepsilon_s \tag{3.58}$$

In equation (3.57), β^* is a coefficient considering compressibility effects that is given by:

$$\beta^* = \beta_i^* \left[1 + \xi^* \cdot f(Ma_T)\right] \tag{3.59}$$

The coefficients β_i^* and ξ^* act as closure coefficients for the compressibility corrections and take values of 0.09 and 1.5, respectively (Wilcox, 2006).

The function $f(Ma_T)$ captures the influence of compressibility, given by:

$$f(Ma_T) = \begin{cases} 0 & Ma_T \leq Ma_{T0} \\ Ma_T^2 - Ma_{T0}^2 & Ma_T > Ma_{T0} \end{cases} \tag{3.60}$$

The value of Ma_{T0} determines the threshold turbulent Mach number at which boundary-layer properties remain unchanged by compressibility adjustments and it is usually taken at 0.25 (Wilcox, 2006). It's worth noting that for incompressible flows, the turbulent Mach number is zero (Sarkar, S. et al., 1993) and values greater than unit are considered unrealistic (Zeman, 1993).

The last term on the right-hand side of Equation (3.46) is associated with thermal diffusivity, which depends on the temperature gradient. However, maintaining model stability during the simulation proved challenging, frequently leading to divergence. To mitigate this issue, the dependency on the temperature gradient was removed by reformulating its expression.

The temperature gradient was decomposed into contributions from internal energy and pressure variations, expressed through the total differential of $\nabla\widetilde{T}$:

$$\nabla\widetilde{T} = \left(\frac{\partial\widetilde{T}}{\partial e}\right)_p \nabla\widetilde{e} + \left(\frac{\partial\widetilde{T}}{\partial p}\right)_e \nabla\overline{p} \tag{3.61}$$

In this decomposition, the first term on the right-hand side represents a diffusive term for internal energy. Consequently, the diffusive term is not solely governed by turbulent or eddy diffusivity, as previously described in Equation (3.48). Incorporating the presented considerations, the Favre-averaged internal energy equation (3.46) can be rewritten as:

$$\frac{\partial(\overline{\rho}\widetilde{e})}{\partial t} + \frac{\partial\left(\overline{\rho}\widetilde{e}\,\tilde{u}_j\right)}{\partial x_j} - \frac{\partial}{\partial x_j}\left(\left(\frac{\mu_T}{\sigma_T} + \kappa\left(\frac{\partial\widetilde{T}}{\partial e}\right)_p\right)\frac{\partial\widetilde{e}}{\partial x_i}\right) = \dot{S}_1 + \dot{S}_2 + \dot{S}_3 \tag{3.62}$$

In equation (3.62) has three source terms, each representing distinct physical contributions. The first term, $\dot{S}_1$, corresponds to heat diffusion due to pressure variations. The second term, $\dot{S}_2$, accounts or the work done by normal stress. Lastly, $\dot{S}_3$ represents the combined effects of work due to viscous stresses and the dissipation of the turbulent kinetic energy. These individual sources terms have the following forms:

$$\dot{S}_1 = \frac{\partial}{\partial x_j}\left(\kappa \cdot \frac{\partial\overline{p}}{\partial x_i} \cdot \left(\frac{\partial\widetilde{T}}{\partial p}\right)_e\right) \tag{3.63}$$

$$\dot{S}_2 = -\overline{p}\frac{\partial\tilde{u}_i}{\partial x_i} - \overline{p}\frac{\partial}{\partial x_i}\left(\Psi\,\widetilde{u_j''u_k''}\frac{\partial\overline{\rho}}{\partial x_k} \cdot \frac{1}{\overline{\rho}}\right) - \left(-0.15 \cdot \mathcal{P} \cdot Ma_T + 0.2 \cdot \overline{\rho} \cdot \varepsilon_s \cdot Ma_T^2\right) \tag{3.64}$$

$$\dot{S}_3 = \tilde{\tau}_{ji}\frac{\partial\tilde{u}_i}{\partial x_j} + \overline{\rho} \cdot 0.09 \cdot \omega \cdot k \cdot \left(1 + 1.5\, f(Ma_T)\right)^2 \tag{3.65}$$

Finally, after completing the averaging process, the developed Homogeneous Equilibrium Model based on the internal energy equation (HEM-e) can be compared to the conventional Homogeneous Equilibrium Model using the enthalpy-based energy equation (HEM-h) proposed by Smolka et al. (2013). The primary distinction lies in the explicit treatment of pressure dilatation and pressure work in HEM-e, which are critical for accurately modelling high-speed and compressible flows, as well as the dilatation dissipation of TKE. In contrast, HEM-h does not account for these effects explicitly; instead, they are indirectly represented through the turbulent dissipation term using the Boussinesq hypothesis. For further details, refer to Appendix C.

3.3.4 Closure equations for the governing equations

The averaged Navier-Stokes equations alone are not sufficient to fully resolve the flow field. Additional transport equations are needed to describe the transport properties of turbulence. There are several models available, a review of these existing turbulence models can be found in Ringstad et al. (2020) work. In this thesis, the k-ω SST model has been chosen, for its capability to accurately predict transonic and moderate supersonic flow behaviour (Mazzelli et al., 2015). The model demonstrates satisfactory performance for various flow conditions, including those with adverse pressure gradients and transonic shock waves, commonly observed in ejector flows.

This section introduces the turbulence transport equations and discusses the considered simplifications to these equations. The turbulent kinetic energy (TKE) equation has the form of:

$$\frac{\partial(\overline{\rho}k)}{\partial t}+\frac{\partial\left(\overline{\rho}k\tilde{u}_j\right)}{\partial x_j}=\left[-\overline{\rho u_j'' u_i''}\frac{\partial\tilde{u}_i}{\partial x_j}\right]+\left[-\overline{\tau_{ji}\frac{\partial u_i''}{\partial x_j}}\right]+\left[-\overline{u_i''}\frac{\partial\overline{p}}{\partial x_i}+\overline{p'\frac{\partial u_i''}{\partial x_i}}\right]+ \\ +\left[-\frac{\partial\left(\overline{u_i''p'}\right)}{\partial x_i}+\frac{\partial\left(\overline{u_i''\tau_{ji}}\right)}{\partial x_j}-\frac{\partial}{\partial x_j}\left(\overline{u_j''\frac{\rho u_i'' u_i''}{2}}\right)\right] \tag{3.66}$$

For more details regarding the derivation of equation (3.66), refer to Appendix B.2.5.

The right-hand side in equation (3.66) is grouped into five terms within square parentheses. The first term is the TKE production ($\mathcal{P}$), describing the rate at which turbulence kinetic energy is generated, typically through shear stresses or other turbulent fluctuations (Wilcox, 2006) given by:

$$\mathcal{P}=-\overline{\rho u_j'' u_j''}\frac{\partial\tilde{u}_\iota}{\partial x_j}=\mu_T\left(\sqrt{2\,\widetilde{S}_{ij}\,\widetilde{S}_{ij}}\right)^2 \tag{3.67}$$

$\mathcal{P}$ takes a positive value for all flow cases. $\widetilde{S}_{ij}$ represents the mean strain rate, defined as:

$$\widetilde{S}_{ij}=\frac{1}{2}\left(\frac{\partial\tilde{u}_i}{\partial x_j}+\frac{\partial\tilde{u}_j}{\partial x_i}\right) \tag{3.68}$$

The second group is the turbulent dissipation rate. This term quantifies the dissipation of kinetic energy due to fluid turbulence. This term is modelled according to equation (3.56), with the key distinction that β_i^* could not be a constant. β_i^* definition depends on the turbulent model selected and the software used to model.

The third group in equation (3.66) includes two pressure terms: pressure work and dilatation. The pressure work, the first term of the group, requires modelling $\overline{u_i''}$ (see equation (3.49)) and the pressure dilation (the second term) can be represented by equation (3.52).

According to Wilcox (2006), the fourth group in equation (3.66) can be modelled as:

$$-\frac{\partial\left(\overline{u_i''p'}\right)}{\partial x_i}+\frac{\partial\left(\overline{u_i''\tau_{ji}}\right)}{\partial x_j}-\frac{\partial}{\partial x_j}\left(\overline{u_j''\frac{\rho u_i''u_i''}{2}}\right)\equiv\frac{\partial}{\partial x_j}\left[\left(\mu+\frac{\mu_T}{\sigma_T}\right)\frac{\partial k}{\partial x_j}\right] \tag{3.69}$$

In equation (3.69) the first term is the pressure diffusion. This term characterizes the momentum transport arising from pressure gradients within the fluid, detailing how pressure influences fluid motion in different directions. The pressure-diffusion term lacks a direct analogy, and in the absence of definitive experimental data, it is typically endured together with the turbulent transport term (Wilcox, 2006).

The second term corresponds to the turbulent molecular diffusion. This phenomenon is associated with the chaotic motion of the molecules within the fluid, leading to the enhanced mixing of the different fluid layers. Turbulent molecular diffusion significantly contributes to the overall transport of mass, momentum, and energy in turbulent flows, thereby enhancing mixing and influencing the distribution of properties within the flow (Wilcox, 2006).

The last term represents the turbulent transport of TKE, which is carried out by turbulent eddies and fluctuations. It encompasses the advection and diffusion of turbulence kinetic energy within the flow field (Wilcox, 2006).

Reorganizing equation (3.66) and applying the modelled terms, the turbulent kinetic energy transport equation can be expressed as:

$$\frac{\partial(\overline{\rho}k)}{\partial t}+\frac{\partial\left(\overline{\rho}k\tilde{u}_j\right)}{\partial x_j}-\frac{\partial}{\partial x_j}\left[\left(\mu+\frac{\mu_T}{\sigma_T}\right)\frac{\partial k}{\partial x_j}\right]=\mu_T\left(\sqrt{2\,\widetilde{S}_{ij}\,\widetilde{S}_{ij}}\right)^2-\\-\overline{\rho}(\varepsilon_s+\varepsilon_d)+\dot{S}_{1_{TKE}}+\dot{S}_{2_{TKE}} \tag{3.70}$$

In equation (3.70), the source terms are defined as:

$$\dot{S}_{1_{TKE}}=-\Psi\,\widetilde{u_j''u_k''}\frac{\partial\overline{\rho}}{\partial x_k}\frac{1}{\overline{\rho}}\frac{\partial\overline{p}}{\partial x_i} \tag{3.71}$$

$$\dot{S}_{2_{TKE}}=-0.15\cdot\mathcal{P}\cdot Ma_T+0.2\cdot\overline{\rho}\cdot\varepsilon_s\cdot Ma_T^2 \tag{3.72}$$

The specific dissipation rate of turbulent kinetic energy for the SST k-ω model is given by Wilcox (2006) as:

$$\frac{\partial}{\partial t}(\overline{\rho}\omega)+\frac{\partial}{\partial x_j}\left(\tilde{u}_j\overline{\rho}\omega\right)-\frac{\partial}{\partial x_j}\left[\left(\mu+\frac{\sigma\overline{\rho}k}{\omega}\right)\frac{\partial\omega}{\partial x_j}\right]=\\=-\overline{\rho u_i''u_j''}\frac{\alpha\omega}{k}\frac{\partial\tilde{u}_i}{\partial x_j}-\beta\overline{\rho}\omega^2+\frac{\sigma_d\overline{\rho}}{\omega}\frac{\partial k}{\partial x_j}\frac{\partial\omega}{\partial x_j} \tag{3.73}$$

On the left side of equation (3.73), the third term corresponds to the effective specific dissipation rate diffusivity. This is a measure of the effective rate of turbulent energy dissipation per unit mass, considering the combined effects of molecular viscosity and turbulence.

The right side of equation (3.73) has three terms: the first is the turbulence specific dissipation rate production, which refers to the generation or creation of TKE per unit mass due to turbulent processes in a fluid flow. The second term is the turbulence specific dissipation rate dissipation, which represents the rate at which TKE is lost or dissipated per unit mass, due to viscosity and turbulent effects. The last term is the cross-diffusion modification. This term involves a blending factor that adjusts the model's behaviour near solid boundaries, adopting values suitable for the k-ω model, and gradually transitions to values similar to those used in k-ε in other regions of the flow. This blending ensures that the turbulence model accurately reflects the effects of turbulence in different regions of the flow domain.

3.3.5 Turbulence scales for RANS

Kolmogorov introduced three scales to represent the smallest scales in turbulent flow, known as the Kolmogorov scales: the length scale l_η, the velocity scale u_η and the time scale t_η. These scales are universally determined by the turbulent kinetic energy dissipation rate (ε) and the viscosity (μ) (Pope, 2000). They are defined as:

$$l_\eta = \left(\frac{\mu^3}{\overline{\rho}^3 \varepsilon}\right)^{1/4} \tag{3.74}$$

$$u_\eta = \left(\frac{\varepsilon \cdot \mu}{\overline{\rho}}\right)^{1/4} \tag{3.75}$$

$$t_\eta = \left(\frac{\mu}{\overline{\rho}\varepsilon}\right)^{1/2} \tag{3.76}$$

Where the turbulent kinetic energy dissipation rate is given by (Pope, 2000):

$$\varepsilon = \frac{\mu}{\overline{\rho}} \cdot \left(\frac{u_\eta}{l_\eta}\right)^2 \tag{3.77}$$

The Kolmogorov length scale (l_η) is the product of the Kolmogorov velocity scale and time scale. Similarly, the turbulent length scale (l_T) is the product of the turbulent velocity scale (u_T) and time scale (t_T):

$$l_T = u_T t_T \tag{3.78}$$

For the SST k-ω turbulence model, the turbulent velocity and time scales can be defined as:

$$u_T = \sqrt{k} \tag{3.79}$$

$$t_T = \frac{k}{\varepsilon} \tag{3.80}$$

Since RANS simulations represent the average flow, the turbulent scales (denoted with the subscript T) will always be larger than the Kolmogorov scales. The eddy viscosity (μ_T) term for the k-ω SST turbulence model can be defined as (Wilcox, 2006):

$$\mu_T = \frac{\overline{\rho} \cdot k^2}{\varepsilon} \tag{3.81}$$

According to Wilcox (2006), the turbulent kinetic energy dissipation can be approximated by the solenoidal dissipation, so the eddy viscosity can be rewritten as:

$$\mu_T = \frac{\overline{\rho} \cdot k}{\beta^* \cdot \omega} \tag{3.82}$$

3.3.6 RANS Near-Wall Treatment

In turbulent flow modelling, adequate mathematical description of the flow variables near solid walls has a high impact on the simulation quality. This accuracy is strongly influenced by the numerical mesh density, particularly in capturing near-wall effects. A key parameter in this context is the dimensionless wall distance (y^+). Ideally, y^+=1 is desirable; however achieving this can be challenging in simulations involving intricate geometries and high Reynolds numbers. The use of wall formulations helps address this difficulty by ensuring a smoother transition between the viscous sublayer and the log-law region. These formulations aim to minimize errors in wall boundary conditions, ensuring accurate predictions of wall shear stress and heat flux while reducing sensitivity to near-wall mesh resolution. Accordingly, an appropriate wall shear stress model is required. In this study, the wall-shear stress (τ_w) is defined as:

$$\tau_w = \overline{\rho}_{\tan} \cdot u_\tau \cdot u^* \tag{3.83}$$

In equation (3.83), the subscript tan refers to the wall-adjacent cell centroid and u^* is the dimensionless velocity (or alternative velocity scale).

The friction velocity and the alternative velocity scale are expressed as:

$$u_\tau = \frac{U_{\tan}}{\left[\left(u^+_{\text{visc}}\right)^{-4} + \left(u^+_{\log}\right)^{-4}\right]^{1/4}} \tag{3.84}$$

$$u^* = \left[\left(\mu_{\tan} \cdot \left|\frac{\Delta U_{tan}}{\Delta y}\right| + \left(0.09^{1/2} \cdot \overline{\rho}_{\tan} \cdot k_{\tan}\right)\right)\frac{1}{\overline{\rho}_{\tan}}\right]^{1/2} \tag{3.85}$$

In equations (3.84) and (3.85), $U_{\tan}$ represents the mean velocity tangent to the wall at the wall-adjacent cell centroid. The dimensionless velocity for the viscous sublayer (u^+_{visc}) and the logarithmic region ($u^+_{\log}$) are defined as:

$$u^+_{\text{visc}} = y^+ \tag{3.86}$$

$$u^+_{\log} = \frac{1}{\kappa}\ln[9.793 \cdot \max(y^+, 0.2)] \tag{3.87}$$

In equations (3.86) and (3.87), κ is the von Kármán constant and y^+ is expresses as:

$$y^+ = \frac{\Delta y \cdot \overline{\rho}_{\tan} \cdot u^*}{\mu_{\tan}} \tag{3.88}$$

Where Δy denotes the distance from the wall at the wall-adjacent cell centroid (tan).

A zero-flux boundary condition for the TKE is considered. This is applied from the logarithmic region until the wall. This formulation results in the following expression for the TKE production term:

$$\mathcal{P} = \mu_{\log}\left(\frac{\tau_w}{\mu_{\tan}}\frac{\partial u^+}{\partial y^+}\right)^2 \tag{3.89}$$

Leading to:

$$\mathcal{P}_{visc} = \frac{\overline{\rho}_{\tan}\cdot k_{\tan}}{\omega_{\tan}}\left(\frac{\tau_w}{\mu_{\tan}}\right)^2 \tag{3.90}$$

$$\mathcal{P}_{log} = \frac{\tau_w^2}{\mu_{tan}}\frac{\partial u_{log}^+}{\partial y^+} \tag{3.91}$$

The dimensionless velocity for the logarithmic region is given by:

$$\frac{\partial u_{\log}^+}{\partial y^+} = \begin{cases}(\kappa\cdot y^+)^{-1} & y^+ > 0.2\\ 0 & y^+ < 0.2\end{cases} \tag{3.92}$$

The blended function for the production term is:

$$\mathcal{P}_w = \left(\mathcal{P}_{\text{visc}}^{-1} + \mathcal{P}_{\log}^{-1}\right)^{-1} \tag{3.93}$$

The transport equation at the wall for the specific dissipation rate is expressed as:

$$\omega_w = \frac{\overline{\rho}_{\tan}(u^*)^2}{\mu_{\tan}}\omega_w^+ \tag{3.94}$$

In equation (3.94), ω_w^+ represents the dimensionless blended specific dissipation rate at the wall, calculated as:

$$\omega_w^+ = \omega_{\text{visc}}^+\left[1 + \left(\frac{\omega_{\log}^+}{\omega_{\text{visc}}^+}\right)^{1.3}\right]^{1/1.3} \tag{3.95}$$

$$\omega_{\text{visc}}^+ = \frac{2}{\beta_i\cdot(y^+)^2} \tag{3.96}$$

$$\omega_{\log}^+ = \frac{1}{\sqrt{\beta_\infty^*}}\frac{du_{log}^+}{dy^+} \tag{3.97}$$

Regarding temperature, the Kader (1981) blending method between the viscous sublayer and the logarithmic law of the wall was employed to compute the characteristic wall temperature (T^+). This is expressed as:

$$T^+ \equiv \frac{(T_w - T_{tan})\cdot\overline{\rho}\cdot c_p\cdot u^*}{\dot{q}} = e^{\Gamma}\cdot T_{\text{visc}}^+ + e^{\frac{1}{\Gamma}}\cdot T_{\log}^+ \tag{3.98}$$

In equation (3.98), T_w is the temperature at the wall, $T_{\tan}$ is the temperature at the wall-adjacent cell centroid and q_w is the wall heat flux.

3.4 Formulation of the large eddy simulation model

This section discusses the equations for large eddy simulations (LES), building upon the governing equations discussed in Section 3.2. While the fundamental equations remain unchanged, modifications are necessary for LES, in particular, filtering the equations to distinguish between resolved and modelled eddies.

3.4.1 Filtering Processes for LES

Filtering processes serve as mathematical tools to distinguish between resolved and subgrid scale (SGS) turbulent motions. In turbulent flow simulations, the diversity in length and time scales pose challenges (Pope, 2000). However, filtering operations relieve this by selectively removing small scales from the Navier-Stokes equations' solutions. This not only reduces computational load but also enhances simulation efficiency. Here, the core principles of filtering processes for LES are examined regarding common methodologies and implications for resolving turbulent flows. Understanding these particularities is crucial for effectively implementing LES for ejector simulations.

The complexity of turbulent flow largely arises from the energy cascade, where eddies progressively break down until kinetic energy dissipates into internal energy. While RANS models can simulate this phenomenon, LES advances by resolving eddies to the dimensions of the computational grid cells (Pope, 2000). For the small eddies, energy dissipation occurs instead of being transmitted to smaller eddies. Figure 3.2 represents a simple schematic of this process. In this figure Δ_{cell} characterises the mesh size, and A, B, C and D denote different size eddies. Eddies A, B and C are larger than the mesh size and are therefore resolved, with the energy cascade terminating at eddy C. The energy contained in eddy C is dissipated as heat, while eddy D, being smaller than the mesh resolution, remains unresolved. Although eddy D is not explicitly modelled, it still influences the resolved flow by exerting a resistive force or stress, ultimately leading to the dissipation of energy from larger resolved structures.

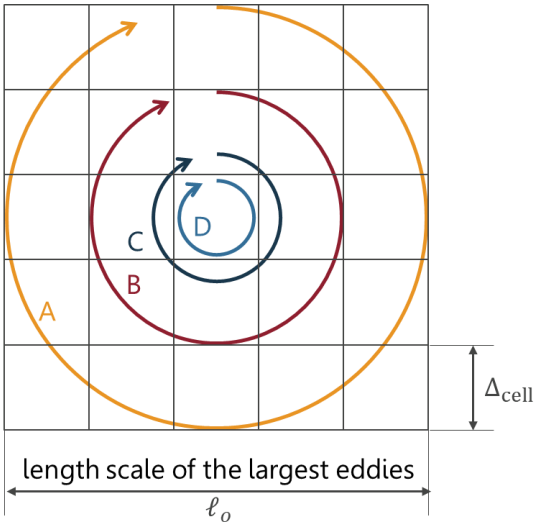


Figure 3.2 – Schematic of different eddy sizes and mesh resolution. Δ_{cell} is the characteristic cell dimension size. A, B and C represent eddies larger than the mesh size, and D is an eddy smaller than the mesh size.

To illustrate the filtering process, consider a hypothetical scenario where a random scalar function $\varphi(x_1, x_2, x_3)$ is defined in the real numbers' domain. Assume a homogeneous filter function G, which defines the scale of the resolved eddies and satisfies a normalization condition (Pope, 2000; Anderson et al., 2020) such that:

$$\iiint_{\mathcal{D}} \left[\prod_{i=1}^{3} G_i(x_i - x_i')\right] dx_1' dx_2' dx_3' = 1 \tag{3.99}$$

In equation (3.99), x_i represents the position vector of a point in space where the filtered value is calculated, while x_i' denotes the coordinates of a point within the integration region around x_i, where the filter is applied. Figure 3.3 provides a schematic representation of a grid cell, identifying the position of x_i (the cell centre) and a random x_i' within the integration region.

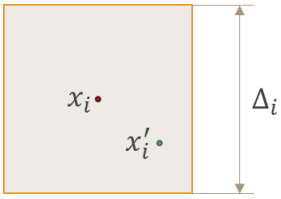


Figure 3.3 – Schematic representation of a grid cell, where x_i is the cell centre, x_i' is one of the integrations points and the coloured area is the integration region.

Therefore, the filtered scalar $\tilde{\varphi}(x_1, x_2, x_3)$ on the computational domain ($\mathcal{D}$) can be defined as:

$$\tilde{\varphi}(x_1, x_2, x_3) \coloneqq G\varphi \coloneqq \iiint_{\mathcal{D}} \left[\prod_{i=1}^{3} G_i(x_i - x_i')\right] \varphi(x_1', x_2', x_3')\, dx_1' dx_2' dx_3' \tag{3.100}$$

In equation (3.100), $\tilde{\varphi}$ represents the resolved scale for the scalar function. The filter function $G_i(x_i, x_i')$ uses a cut-off length (Δ_i), which is applied to the points x_i' to compute the weighted average that defines the filtered value $\tilde{\varphi}$. Various filtering functions have been developed, including Fourier space, Gaussian, and box filters (Jiang, X. et al., 2010). In this study, an unstructured box filter is applied, which can be written as (Jiang, X. et al., 2010):

$$G_i(x_i - x_i') = \begin{cases} \Delta_i^{-1}, & |x_i - x_i'| \leq \Delta_i/2 \\ 0, & otherwise \end{cases} \tag{3.101}$$

The cut-off box size (Δ_i) is equivalent to the mesh size, meaning that scales smaller than the local cell size are eliminated from $\tilde{\varphi}(x_i)$. This constraint, imposed by the finite-volume discretization, results in the following filtering operation:

$$\tilde{\varphi}(x_i) = \frac{1}{V} \iiint_{x_i - \Delta_i/2}^{x_i + \Delta_i/2} \varphi(x_i')\, dx_i' \tag{3.102}$$

In equation (3.102), V denotes the computational cell volume (Aldama, 1990). As shown in Figure 3.2, the impact of eddies smaller than C is not accounted for in $\tilde{\varphi}(x_i)$ (Pope, 2000). To compensate for this, the energy cascade process is mimicked by artificially increasing viscosity through the SGS stress (τ_{ji}^{SGS}). Consequently, the SGS model applies a force proportional to the velocity gradient of the resolved eddies, effectively dissipating their energy while modelling the effects of smaller ones. Conversely, not using a subgrid scale model leads to an overestimation of kinetic energy, allowing unresolved eddies to persist within the grid. This unresolved component is referred to as the sub-filtered (φ'), meaning that any scalar field φ can be decomposed as (Pope, 2000):

$$\varphi = \tilde{\varphi} + \varphi' \tag{3.103}$$

Applying the filtering function to the continuity and momentum equations yields:

$$\frac{\partial \rho}{\partial t} + \frac{\partial (\overline{\rho}\tilde{u}_i)}{\partial x_i} = 0 \tag{3.104}$$

$$\frac{\partial (\overline{\rho}\tilde{u}_i)}{\partial t} + \frac{\partial \left(\overline{\rho}\tilde{u}_j\tilde{u}_i\right)}{\partial x_j} = \frac{\partial}{\partial x_j}\left[-\overline{p}\delta_{ij} + \widetilde{\tau}_{ji} - \tau_{ij}^{SGS}\right] \tag{3.105}$$

In equation (3.105), $\widetilde{\tau}_{ji}$ represents the stress tensor due to molecular viscosity, defined as:

$$\widetilde{\tau}_{ji} = \mu\left[\left(\frac{\partial \tilde{u}_i}{\partial x_j} + \frac{\partial \tilde{u}_j}{\partial x_i}\right) - \frac{2}{3}\,\delta_{ij}\frac{\partial \tilde{u}_k}{\partial x_k}\right] \tag{3.106}$$

Equation (3.105) is different from the Favre averaged momentum equation due to differences between the filtered product $\overline{\rho}\widetilde{u_i u_j}$ and the product of the filtered velocities $\overline{\rho}\tilde{u}_i\tilde{u}_j$. This difference is known as the residual stress tensor:

$$\tau_{ji}^{R} = \left(\overline{\rho}\widetilde{u_j u_i}\right) - \left(\overline{\rho}\tilde{u}_j\tilde{u}_i\right) \tag{3.107}$$

The SGS kinetic energy is represented as (Pope, 2000):

$$k^{SGS} \equiv \frac{\tau_{kk}^{R}}{2} \tag{3.108}$$

Since $\widetilde{u_i u_j}$ cannot be directly derived from the filtered local velocities ($\tilde{u}_i$), this leads to an incomplete system of equations. Consequently, proper modelling of the SGS stress tensor (τ_{ji}^{SGS}) becomes imperative, as discussed below:

$$\tau_{ji}^{SGS} \equiv \tau_{ji}^{R} - \frac{1}{3}\tau_{kk}^{R}\delta_{ij} \tag{3.109}$$

Replacing the residual stress tensor in equation (3.109), the SGS stress tensor can be expressed as:

$$\tau_{ij}^{SGS} \equiv -2\mu_{SGS}\left(\widetilde{S}_{ij} - \frac{1}{3}\widetilde{S}_{kk}\delta_{ij}\right) + \frac{2}{3}\overline{\rho}k_{SGS}\delta_{ij} \tag{3.110}$$

In equation (3.110), the resolved large-scale strain rate ($\widetilde{S}_{ij}$) is defined as the gradient of the resolved velocity field $\tilde{u}_i$:

$$\widetilde{S}_{ij} = \frac{1}{2}\left(\frac{\partial \tilde{u}_i}{\partial x_j} + \frac{\partial \tilde{u}_j}{\partial x_i}\right) \tag{3.111}$$

This results in unclosed filtered momentum equations, requiring closure through the modelling of the SGS stress tensor. The effectiveness of this closure is governed by the SGS viscosity (μ_{SGS}). An excessively high value of μ_{SGS} results in eddy breakdown and a significant drop in kinetic energy. Conversely, the absence of μ_{SGS} results in inadequate subgrid stress, permitting eventual, despite slow, breakdown of eddies slightly larger than the mesh size, thereby maintaining high kinetic energy levels (Ciofalo, 2022). Recalling Figure 2.13 from Section 2.2, the inertial subrange and dissipation range are characterized by eddies whose size is dictated by the diffuse movement of molecular viscosity, leading to a more random behaviour of vortices (Pope, 2000). Consequently, these eddies can be considered isotropic, simplifying the model complexity, and allowing μ_{SGS} to be represented as a single scalar value. The μ_{SGS} calculation depends on the SGS model applied.

For the single-phase flow case, the LES energy equation is similar to the Favre averaged form. There is a difference however in the treatment of the modelled terms, particularly the subgrid scale effects. The LES formulation of the energy equation for a single-phase flow case is as follows:

$$\frac{\partial(\overline{\rho}\widetilde{E})}{\partial t}+\frac{\partial(\overline{\rho}\widetilde{E}\,\tilde{u}_j)}{\partial x_j}=\frac{\partial}{\partial x_j}\left((\kappa+\kappa_{SGS})\frac{\partial\widetilde{T}}{\partial x_j}\right)-\frac{\partial(\tilde{u}_j\overline{p})}{\partial x_j}+\frac{\partial(\tilde{u}_i\widetilde{\tau}_{ji})}{\partial x_j}-\frac{\partial(\tilde{u}_i\tau_{ij}^{SGS})}{\partial x_j} \tag{3.112}$$

Equation (3.112) accounts for various factors affecting the energy dynamics in the fluid, including pressure work, thermal diffusion (comprising both turbulent and subgrid scale contributions) and viscous effects (both resolved and subgrid scale). The SGS thermal conductivity is derivate from Sutherland law and is calculated as (Quéméré and Sagaut, 2002):

$$\kappa_{SGS}=\frac{\mu_{SGS}\cdot c_p}{\sigma_{SGS}} \tag{3.113}$$

In equation (3.113), σ_{SGS} represents the subgrid Prandtl number, typically assigned a value of 0.85 (Doehring et al., 2021).

Such as in the single-phase case, the energy equation for the two-phase flow has a similar structure to the Favre averaged formulation. However, for LES the source terms are divided into resolved ($\dot{S}$) and modelled ($\dot{S}^{SGS}$) components, addressing both large and small-scale (subgrid scale) turbulent effects, respectively. The energy equation then can be written as:

$$\frac{\partial(\overline{\rho}\widetilde{e})}{\partial t}+\frac{\partial(\overline{\rho}\widetilde{e}\,\tilde{u}_j)}{\partial x_j}-\frac{\partial}{\partial x_j}\left(\left(\frac{\mu_{SGS}}{\sigma_t}+\kappa\left(\frac{\partial\widetilde{T}}{\partial e}\right)_p\right)\frac{\partial\widetilde{e}}{\partial x_i}\right)=\dot{S}_1+\dot{S}_2+\dot{S}_2^{SGS}+\dot{S}_3+\dot{S}_3^{SGS} \tag{3.114}$$

The source terms in equation (3.114) for the resolved eddies are:

$$\dot{S}_1=\frac{\partial}{\partial x_j}\left(\kappa\cdot\frac{\partial\overline{p}}{\partial x_i}\cdot\left(\frac{\partial\widetilde{T}}{\partial p}\right)_e\right) \tag{3.115}$$

$$\dot{S}_2=-\overline{p}\frac{\partial\tilde{u}_i}{\partial x_i} \tag{3.116}$$

$$\dot{S}_3=\tilde{\tau}_{ji}\frac{\partial\tilde{u}_i}{\partial x_j} \tag{3.117}$$

The source terms for the SGS correspond to those in Favre averaged source terms in the energy equation (see equation (3.62)). Among these, the velocity-pressure gradient correlation term ($\dot{S}_2^{SGS}$) is often ignored in LES due to its increased computational complexity and minimal impact, as most of the energy is contained in the larger scales (Jiang, X. et al., 2010). For this reason, it was omitted in the developed ejector model. The term $\dot{S}_3^{SGS}$, which accounts for turbulent kinetic energy dissipation in the subgrid scale, is computed as follows:

$$\dot{S}_3^{SGS}=\frac{C_\varepsilon\cdot\overline{\rho}\cdot(k^{SGS})^{\frac{3}{2}}}{L_\Delta} \tag{3.118}$$

In equation (3.118) C_ε is a constant with a typical value of 0.916, as suggested in the literature (Kazuo Sone et al., 2001; Sone and Menon, 2003; Jiang, X. et al., 2010). The length scale L_Δ represents the length of the eddy, further discussed in the next section.

3.4.2 Subgrid Length Scale

As previously discussed in Section 2.2.2, the WMLES S-Ω model (Ivanov and Zasimova, 2018) is based on a modified subgrid length scale approach proposed by Shur et al. (2008). The filter length scale (Δ_{SGS}) depends on the mesh size, and is determined by the following function:

$$\Delta_{SGS} = \min[\max(0.15 \cdot d_w, 0.15 \cdot h_{max}, h_{wn}), h_{max}] \tag{3.119}$$

Figure 3.4 presents a schematic view of the mesh grid, identifying view with the identification of the different variables in equation (3.119): the shortest distance of the cell centre to the wall (d_w), the maximum cell edge length (h_{max}) and the wall-normal grid distance (h_{wn}).

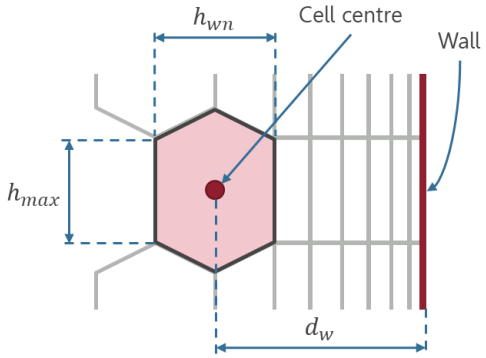


Figure 3.4 – Schematic of a grid mesh with the identification of the shortest distance of the cell centre to the wall (d_w), the maximum cell edge length (h_{max}) and the wall-normal grid distance (h_{wn}).

Considering the van Driest damping technique (Shur et al., 2008), the subgrid scale eddy viscosity (μ_{SGS}) is calculated as:

$$\mu_{SGS} = \overline{\rho} \cdot L_\Delta^2 \cdot \left|\widetilde{S}_{ij} - \widetilde{\Omega}_{ij}\right| \cdot \left\{1 - exp\left[-\left(\frac{y^+}{25}\right)^3\right]\right\} \tag{3.120}$$

In equation (3.120), $\widetilde{S}_{ij}$ and $\widetilde{\Omega}_{ij}$ represent the strain rate and the vorticity magnitude, respectively. The vorticity magnitude is defined as:

$$\widetilde{\Omega}_{ij} = \frac{1}{2}\left(\frac{\partial \tilde{u}_i}{\partial x_j} - \frac{\partial \tilde{u}_j}{\partial x_i}\right) \tag{3.121}$$

The length scale (L_Δ) in equation (3.120) is computed using the formulation proposed by Shur et al. (2008):

$$L_\Delta = \min(\kappa \cdot d_w, 0.2 \cdot \Delta_{SGS}) \tag{3.122}$$

In equation (3.122), κ is the von Kármán constant. Finally, the subgrid scale turbulent kinetic energy (k^{SGS}) is determined by the standard Smagorinsky model (Ciofalo, 2022):

$$k^{SGS} = \left(\frac{\mu_{SGS}}{\rho L_\Delta}\right)^2 \tag{3.123}$$

3.4.3 Turbulence scales for LES

As presented in Section 3.3.5, the turbulent length scale (l_T) is defined as the product of the turbulent velocity scale (u_T) and the turbulent time scale (t_T), as given by equation (3.78). For LES, these scales are defined as follows (Bardina et al., 1980):

$$u_T = \frac{\mu_{SGS}}{\rho \cdot \mathrm{L}_\Delta} \tag{3.124}$$

$$t_T = \frac{\rho \cdot L_\Delta^2}{\mu_{SGS}} \tag{3.125}$$

Since LES resolves larger eddies while modelling smaller-scale turbulence, it is expected that the turbulent scales in LES remain larger than the Kolmogorov scales.

3.4.4 LES Near-Wall Treatment

The near-wall treatment implemented in the LES region of the ejector model follows the methodology proposed by Kader (1981). This approach accounts for different flow regimes near the wall, including the laminar sublayer, the logarithmic region, and an appropriate transition in the buffer region. The general formulation for the wall shear stress (τ_w) is given by:

$$\tau_w = \overline{\rho}_{\tan} \cdot u_\tau^2 \tag{3.126}$$

The friction velocity (u_τ) depends on the y^+ value, which is determined by the near-wall mesh resolution. If the wall-adjacent cell centroid lies within the viscous sublayer, the friction velocity is given by:

$$u_\tau = \sqrt{\frac{U_{\tan} \cdot \mu_{\tan}}{y \cdot \overline{\rho}_{\tan}}} \tag{3.127}$$

For a coarser mesh, where the wall-adjacent cell centroid falls within the logarithmic region, the velocity distribution is obtained from:

$$u_\tau = U_{\tan}\left[\frac{1}{\kappa} ln(9.793 \cdot y^+)\right]^{-1} \tag{3.128}$$

In equation (3.128), the non-dimensional wall distance (y^+) is defined as:

$$y^+ = \frac{\Delta y \cdot \overline{\rho}_{\tan} \cdot u_\tau}{\mu_{\tan}} \tag{3.129}$$

If the wall-adjacent cell centroid lies within the buffer region, a blending function is used to smoothly transition between the viscous and logarithmic formulations:

$$u_\tau = e^{\Gamma} u_{\tau,\mathrm{visc}} + e^{1/\Gamma} u_{\tau,\log} \tag{3.130}$$

In equation (3.130) the term $u_{\tau,\mathrm{visc}}$ and $u_{\tau,log}$ are determined using equations (3.127) and (3.128), respectively, and the blending function (Γ) is given by:

$$\Gamma = -\frac{0.01(y^+)^4}{1 + 5y^+} \tag{3.131}$$

3.4.5 Interface between RANS and LES zones

As discussed previously in Section 2.2.3, an Embedded LES (ELES) Modelling approach was used for the ejector flow simulations. The chosen coupling method for the ELES model was a segregated approach with separate inflow and outflow interfaces. This method was implemented because it is known that local variables are reasonably well simulated using the Favre principle. The simulation domain was divided into separate RANS and LES zones, coupled by clearly defined boundaries. The RANS approach was applied to the primary nozzle, where the flow is relatively stable and well-represented by RANS equations. The LES approach was used for the mixing chamber and the constant sections, where complex turbulent structures and mixing phenomena are dominant. The LES approach provides a more detailed representation of the flow dynamics, essential for capturing the intricate interactions between the motive and entrained flows. Effective management of the interfaces between the RANS and LES zones is crucial to ensure a seamless transition and accurate simulation results, as highlighted by findings in the literature (Fröhlich and Terzi, 2008).

Figure 3.5 shows a schematic representation of one of the simulated ejectors, illustrating the flow regions where the LES (red zone) and RANS (blue zone) models were applied. The motive and entrained inlet chamber, as well as the diffuser, were excluded to reduce computational costs, depicted as grey zones in the figure. The inflow interface is indicated by a red dashed line for the secondary flow and a grey dashed line for the motive flow. The outflow interface is identified by a yellow double dashed line at the end of the constant area section. This ELES approach, with its strategic division of the simulation domain and careful management of interfaces, provides a robust framework for accurately simulating the complex flow dynamics within the ejector. The choice of using RANS for the stable regions and LES for the turbulent mixing regions ensures a detailed and computationally efficient simulation.

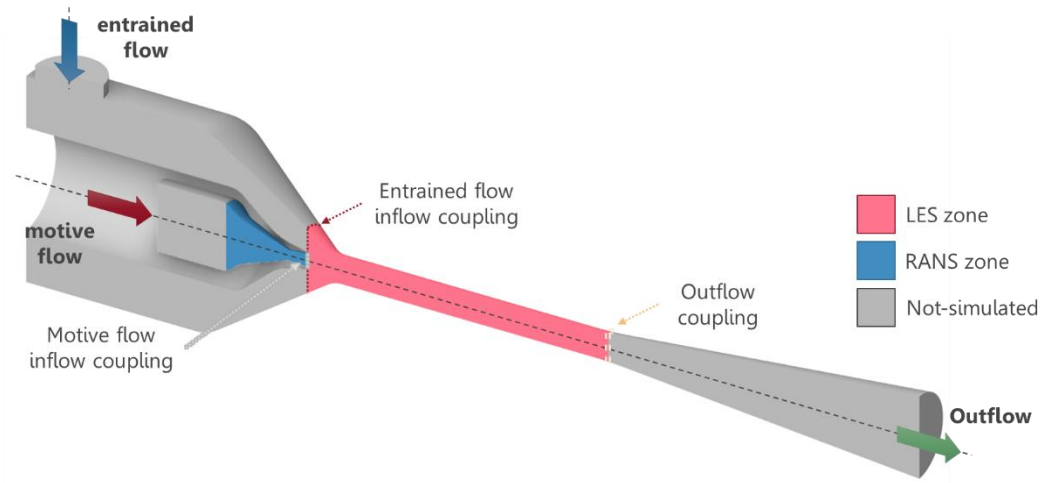


Figure 3.5 – Schematic representation of the ejector simulated in this work, identifying the LES and RANS zones in the ELES, and the not-simulated zones. The inflow interface is depicted by a dashed red and grey line, while the outflow interface is indicated by a yellow double dashed line.

At the RANS-LES interface, an adequate coupling method was needed to effectively transfer inflow and outflow data between the models. To impose a time-dependent inlet condition, the vortex method proposed by Sergent (2002) was applied. This approach introduces perturbations to a specified mean velocity profile by imposing a fluctuating vorticity field within a two-dimensional plane orthogonal to the streamwise direction,

specifically at the interface separating the RANS zone from the LES zone. The vortex method operates within a Lagrangian framework, where the system evolves with the fluid. In two dimensions, its governing equation is expressed as follows (Sergent, 2002; Jiang, X. et al., 2010):

$$\frac{\partial(\rho\omega_i)}{\partial t} = \mu\frac{\partial}{\partial x_i}\left(\frac{\partial\omega_i}{\partial x_i}\right) \tag{3.132}$$

In this method, each vortex i is characterized by its position vector $\vec{x}_j(t)$, size (ξ), and circulation (Γ_j), with spatial distribution given by η_j. The overall vorticity field is typically the sum of all vortices j, described as:

$$\omega(\vec{x},t) = \sum_{j=1}^{N} \Gamma_j(t)\,\eta_j\left(\left|\vec{x}-\vec{x}_j\right|,t\right) \tag{3.133}$$

In equation (3.133), the spatial distribution of the vortex j follows a Gaussian-type distribution (Jiang et al., 2010):

$$\eta_j(\vec{x}) = \frac{1}{2\pi\xi^2}\left(2e^{-\frac{|\vec{x}|^2}{2\xi^2}}-1\right)2e^{-\frac{|\vec{x}|^2}{2\xi}} \tag{3.134}$$

Due to the assumption of transversal periodicity, the circulation parameter Γ_j depends solely on the vortex height in the injection plane. This parameter is directly influenced by the local turbulent kinetic energy (k_j), which determines the intensity of the introduced vortices. The circulation parameter is computed using the following expression (Sergent, 2002):

$$\Gamma_j = 4\sqrt{\frac{\pi\cdot\mathcal{S}\cdot k_j}{3\cdot\boldsymbol{N}\cdot[2\cdot\ln(2)-3\cdot\ln(2)]}} \tag{3.135}$$

Here, $\mathcal{S}$ denotes the inlet cross-sectional area and $\boldsymbol{N}$ the number of vortices. Through the Biot-Savart law and numerical manipulation, the discretized velocity field is expressed as (Mathey et al., 2006):

$$\vec{u}(\vec{x}) = \frac{1}{2\pi}\sum_{j=1}^{N}\Gamma_j\frac{\left(\left(\vec{x}_j-\vec{x}\right)\times\vec{z}\right)}{\left|\vec{x}-\vec{x}_j\right|^2}\left(1-e^{-\frac{\left|\vec{x}-\vec{x}_j\right|^2}{2\xi^2}}\right)e^{-\frac{\left|\vec{x}-\vec{x}_j\right|^2}{2\xi^2}} \tag{3.136}$$

In equation (3.136), $\vec{z}$ represents the unit vector in the streamwise direction. The local vortex size (ξ), i.e. the vortex radius, is determined through a turbulent mixing length hypothesis, calculated from a known profile of mean turbulence kinetic energy and mean dissipation rate at the inlet:

$$\xi = \frac{C_\mu^{\frac{3}{4}}k^{\frac{3}{2}}}{2\varepsilon} \tag{3.137}$$

To ensure the vortex remains within resolved scales, the minimum value of ξ is constrained by the local grid size. This grid size is determined by the number of vortices ($\boldsymbol{N}$), which is defined as (Gerasimov, 2016):

$$\boldsymbol{N} = \frac{n}{4}. \tag{3.138}$$

In equation (3.138), n represents the number of cell faces in the injection plane. The vortex method accounts for velocity fluctuations normal to the streamwise direction, with the circulation sign of each vortex undergoing random alterations at each characteristic time scale. This time scale corresponds to the duration required for a two-dimensional vortex, transported by the mean flow velocity in the boundary normal direction, to travel 100 times its mean characteristic 2D size (Mathey et al., 2006). To replicate the effect of these vortices on the streamwise velocity field, a simplified linear kinematic model was employed. This approach preserves the spatial coherence of the vortices while remaining independent of the characteristic time scale (Mathey et al., 2006). If the mean streamwise velocity $\tilde{u}_i$ is treated as a passive scalar, the resulting fluctuation (u_i''), due to the transport of $\tilde{u}_i$ by the planar fluctuating 2D velocity field computed by the vortex method (v_i''), can be modelled as follows:

$$\vec{u}'' = -\vec{v}'' \cdot \vec{g}'' \tag{3.139}$$

In equation (3.139), $\vec{g}$ represents the unit vector aligned with the mean inlet velocity gradient ($\nabla\tilde{\vec{u}}$).

For any LES simulation, it is good practice to use a prior RANS simulation as the initial condition. In an embedded LES approach, the existing RANS solution is suspended within the LES zone. This means the LES model takes over, providing a more detailed representation of the flow dynamics in this region. At the interface where the flow transitions from the LES zone to the RANS zone, the RANS model resumes. Specifically, the prior RANS solution is used as the inlet condition for the downstream RANS region, ensuring a smooth transition between the two models and accurately capturing the flow dynamics across the entire domain. It is important to note that in the LES zone, the momentum equations are not influenced by the eddy viscosity from the previous RANS results; instead, the governing equations rely solely on the LES model's eddy viscosity. This distinction ensures consistency and accuracy in the simulation.

Chapter 4

Remember that all models are wrong;
the practical question is
how wrong do they have to be
to not be useful.
George Box (1987)

Model implementation and numerical considerations

This chapter focuses on the numerical considerations and implementation details for simulating ejectors using CFD. Adequate computational domain selection and meshing strategies are essential to ensure accurate and efficient simulations, particularly for supersonic turbulent flows. Special attention was given to capture shock waves, boundary layers, and complex turbulent structures accurately, while maintaining computational effort within reasonable.

This chapter covers the following topics:

- The discussion of the computational domain, meshing strategies, and boundary conditions for both RANS and LES simulations.
- The development and implementation of User-Defined Functions (UDFs), required for performing ejector flow simulations in FLUENT.
- The discussion of numerical considerations for RANS and LES, including solution methods, discretization schemes, and mesh assessment.

4.1 Computational domains for the numerical simulations

Two different ejectors were considered: a single-phase ejector using R1234ze(E) as the working fluid and a two-phase ejector using CO_2. The geometry of the R1234ze(E) ejector was adopted from previously published experimental studies, while the CO_2 ejector geometry was based on a prior experimental setup. The results from these experimental works serve as the foundation for validating the numerical models developed in this study, ensuring their accuracy and reliability.

4.1.1 Computational domain and boundary conditions for the RANS simulation of the R1234ze(E) ejector

For the R1234ze(E) ejector, a schematic representation of the device is shown in Figure 4.1. Seven pressure transducers and temperature sensors were installed within the ejector body. The pressure transducers were mounted on the ejector wall at the positions marked “P” in Figure 4.1. The temperature sensors were positioned perpendicular to the flow stream in glands, located at the same sections as the pressure transducers. The temperature sensors are identified as “T”.

Although not depicted in the figure, the test rig also included a pressure transducer and a temperature sensor at the motive chamber inlet, inside the suction chamber, and at the diffuser outlet. Further details about the experimental setup can be found in Appendix D.1 and in Śmierciew, Gagan, et al. (2017).

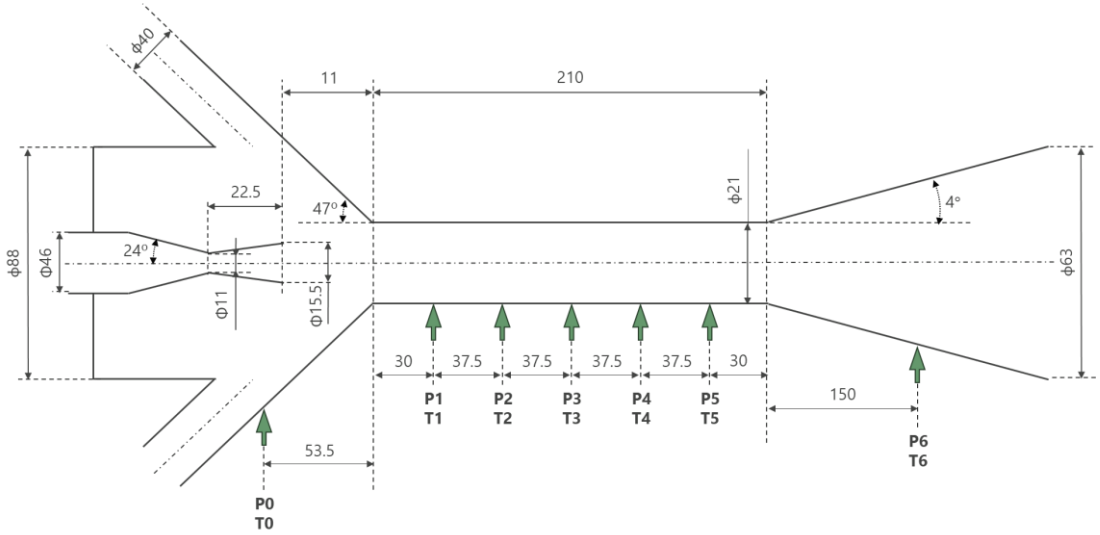


Figure 4.1 – Details of the R1234ze(E) ejector geometry in millimetres for the 3D simulation, indicating the positions of pressure transducers (P) and temperature sensors (T).

The domain was modelled and discretised using the SpaceClaim 2022 software (ANSYS Inc., 2022b). The actual geometrical details of the experimental device (shown in Figure 4.1) was maintained in the models with some minor changes. For instance, sharp edges were removed from the flow domain to prevent small-scale recirculation that could cause numerical instabilities, require excessively fine local meshing, and increase simulation times. The final flow domain for the R1234ze(E) ejector is shown in Figure 4.2.

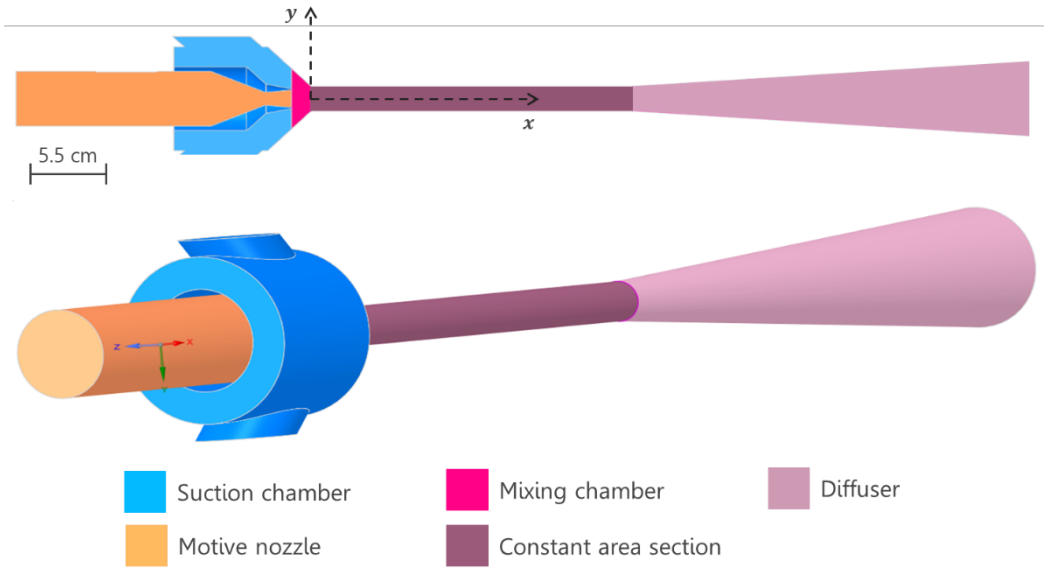


Figure 4.2 – R1234ze(E) ejector geometry: each colour corresponds to an ejector section. (a) Cut view of the domain (scale factor: 1:5.5). (b) 3D isometric view of the complete ejector.

To perform the RANS simulation, a 3D model of the ejector was utilised. However, to reduce computational costs and leverage the averaging properties of the RANS model, only half of the domain volume was simulated by introducing a symmetry plane, as illustrated in Figure 4.3. The total fluid volume in the ejector was calculated as 5.88×10^{-4} m³, with a corresponding ejector length of 0.739 m.

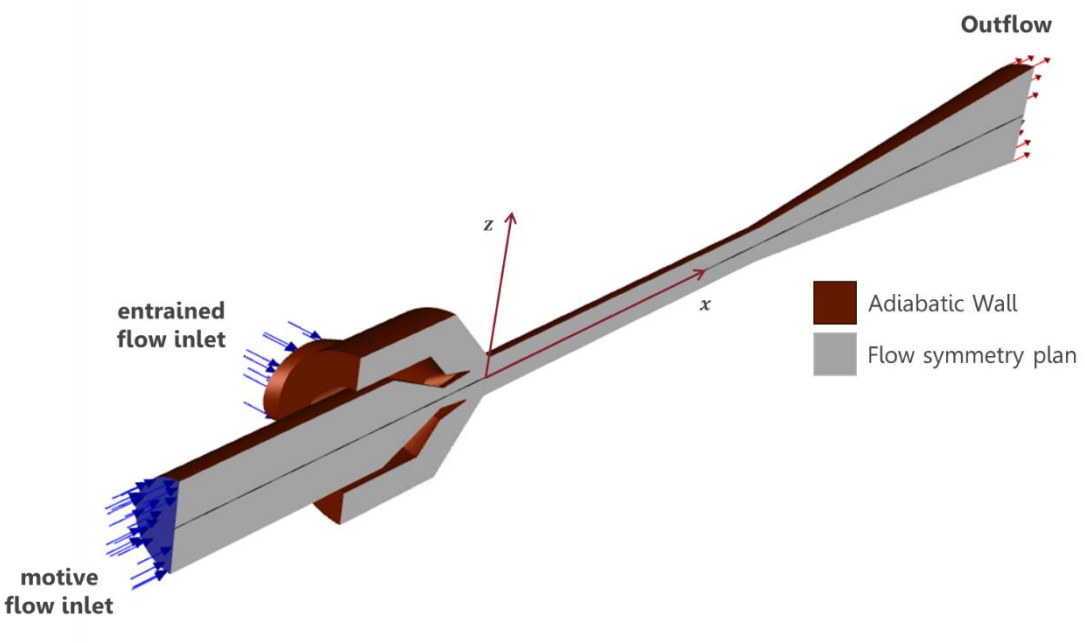


Figure 4.3 – R1234ze(E) ejector RANS simulation flow domain, each colour corresponds to different boundary type.

The simulation employed five distinct boundary conditions. For the inlets, Dirichlet boundary condition were applied, according to a fully developed flow assumption (Rapp, 2017). A pressure inlet type boundary condition was selected, with the static pressure and temperatures values specified based on the experimental measurements detailed in Section 5.1. For turbulence, turbulent intensity and hydraulic diameter were defined at the inlets. It should be noted that the inlet turbulence properties has neglectable impact on the ejector flow simulation results (Bodys et al., 2022), as turbulence generated on the inside of the ejector is much more significant than that occurring at the inlets. At the outlet, a pressure outlet boundary condition was applied, using the experimentally recorded static pressure value, as described in Section 5.1.

The ejector walls were considered adiabatic with a no-slip condition and zero roughness. This assumption was primarily adopted to reduce computational cost, as previous studies have shown that heat transfer through the ejector walls to the ambient has a negligible impact on overall ejector performance (Haida, et al., 2018a). However, non-adiabatic effects on interior walls can influence the fluid temperature distribution near critical regions, such as the converging-diverging nozzle and the suction nozzle. Nonetheless, for predicting mass flow rates, the adiabatic assumption was found to have minimal impact (Haida, et al., 2018a). To further reduce computational complexity without compromising accuracy, a symmetry plane was defined along the xz mid-plane. Additionally, interior surfaces were introduced at sensor locations to facilitate data extraction during post-processing.

4.1.2 Computational domain and boundary conditions for ELES

As previously discussed in Section 3.4, the entire flow domain was not simulated using LES due to computational resource limitations. To make the simulations more feasible, an ELES approach was adopted (further details are provided in Section 2.2.3). During the setup phase, it became evident that even this approach was insufficient, requiring the removal of non-critical sections of the domain. Figure 4.4 illustrates the computational domain, with the LES and RANS regions clearly identified by different colours.

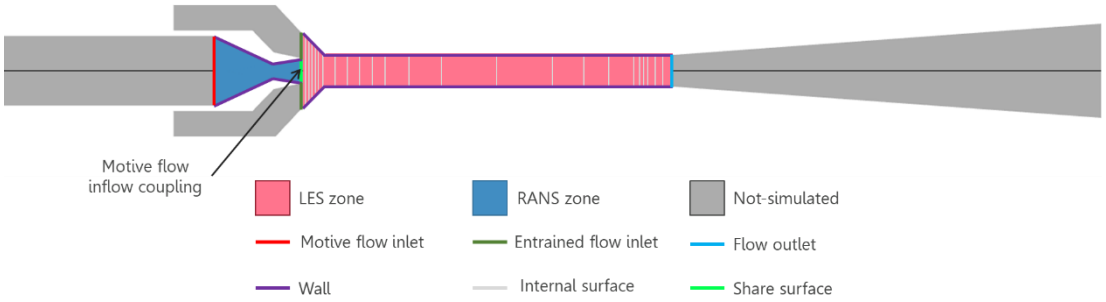


Figure 4.4 – R1234ze(E) ejector simulation flow domain, each colour corresponds to a different boundary type.

For the ELES simulation, a 3D model of the flow domain was created, covering both the LES and RANS regions shown in Figure 4.4. The total fluid volume of the domain was 1.28×10^{-4} m³, with the LES region accounting for approximately 76% of the total volume. The overall domain length was 0.308 m.

For the ejector inlets, a pressure inlet boundary condition was applied, with the total pressure, total temperature, and velocity direction profiles obtained from the precursor RANS simulation. Turbulence properties, including turbulent intensity and turbulent viscosity ratio, were also extracted from the RANS data and applied at the inlets. A pressure outlet boundary condition was specified at the ejector outlet, following the same methodology as the inlet boundaries. Further details on the precursor RANS simulation can be found in Section 5.1.

For the RANS/LES interface, an explicit shared surface was created with inflow coupling to ensure a smooth transition between the two regions. The vortex method was used to generate fluctuations at the interface; further details about this method are provided in Section 3.4.5. The ejector walls were assumed to be adiabatic with a no-slip condition and zero roughness. To facilitate post-processing and data analysis, interior surfaces were introduced at sensor locations and other regions of interest.

4.1.3 Computational domain and boundary conditions for the RANS simulation of the CO_2 ejector

The schematics of the CO_2 ejector are illustrated in Figure 4.5. Four pressure transducers are mounted on the ejector wall within the constant-area section, with their positions marked as "P" in Figure 4.5a). Seven temperature sensors are positioned perpendicular to the flow, housed in glands. Four of these sensors align with the pressure transducers, while three are in the diffuser section. The positions of the temperature sensors are

indicated as "T" in Figure 4.5a). Figure 4.5b) displays a real photography of the ejector, where the slots for the designed sensor placement are visible.

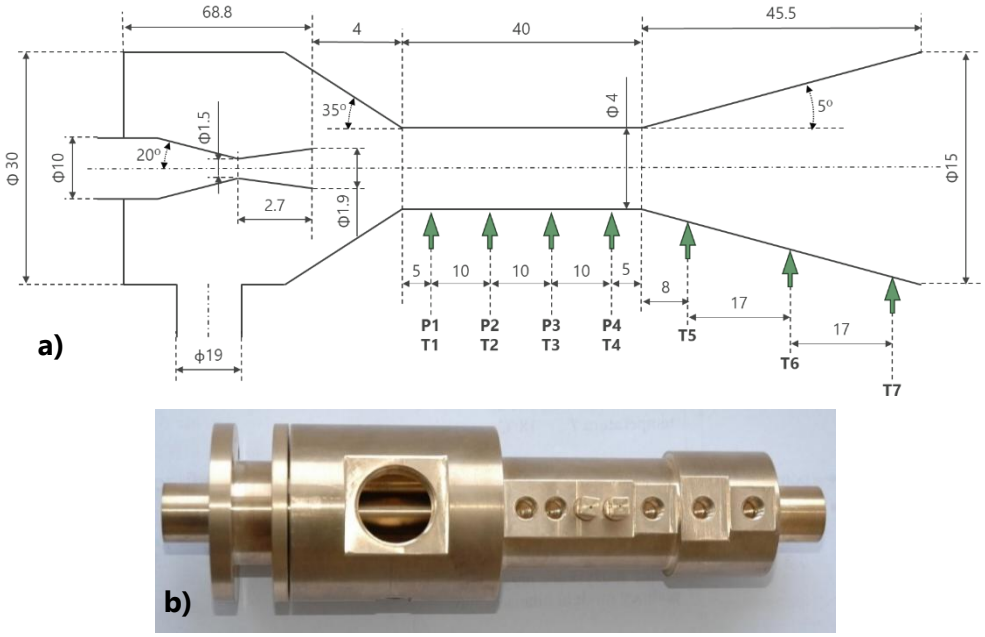


Figure 4.5 – (a) CO_2 ejector geometry (dimensions in mm) for the 3D simulation, indicating the positions of pressure and temperature sensors. (b) Ejector body showing sensor slots.

Upstream of the motive and entrained flow inlets, the test rig features a pressure transducer, a temperature sensor, and, for the motive flow, a flow meter. At the diffuser outlet, the setup includes a pressure transducer, a temperature sensor, and a Coriolis flow meter to measure the flow density. Additional details about the experimental setup are provided in Appendix D.2.

For the CO_2 ejector RANS simulations, both a 2D axisymmetric domain and a 3D symmetrical domain were employed. The flow domain was modelled and discretised using SpaceClaim 2022. Since the 2D axisymmetric model could not accurately represent the real entrained mass flow inlet, adaptations were necessary. The schematic of the adapted 2D ejector geometry is shown in Figure 4.6, with a total revolution area of 1.04×10^{-3} m².

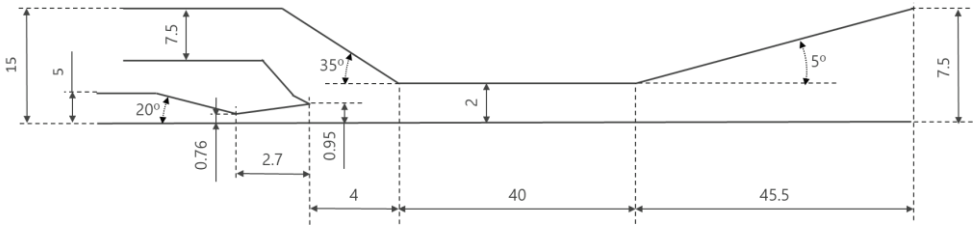


Figure 4.6 – CO_2 ejector geometry (dimensions in mm) for the 2D simulation.

For the 3D simulation, the experimental ejector geometry (Figure 4.5a)) was replicated with minor modifications, similar to those applied to the R1234ze(E) ejector model. The resulting 3D flow domain is depicted in Figure 4.7, where each ejector section is represented by a different colour. The total fluid volume for the 3D model was 1.31×10^{-5} m³.

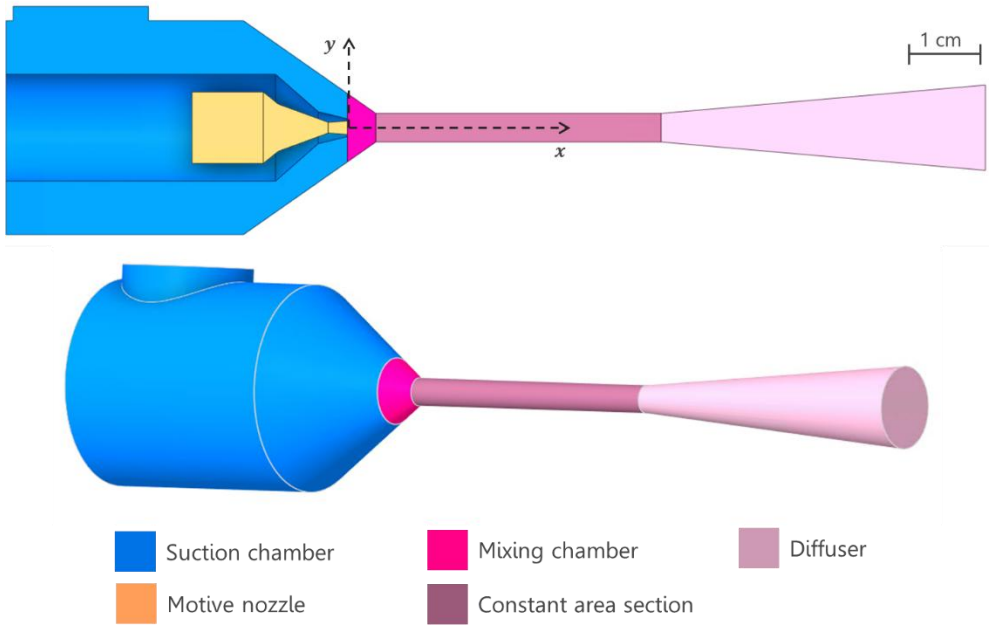


Figure 4.7 – CO_2 ejector geometry. Each colour corresponds to a specific ejector section: (a) Cross-sectional view of the domain (scale 1:1). (b) 3D isometric view of the complete ejector.

For both the 2D and 3D ejector models, as with the R1234ze(E) case, a fully developed flow assumption was applied at the inlets. A pressure inlet boundary condition was used, with the static pressure and internal energy values derived from experimental measurements. At the outlet, a pressure outlet boundary condition was implemented, utilising the experimentally recorded static pressure value. Detailed information about these boundary condition values is provided in Section 6.1.

The ejector walls were considered adiabatic, with a no-slip condition and zero roughness. Different from the 3D model, the 2D model has an axis boundary, while a symmetry plane was used in the 3D. These boundary condition setups are illustrated in Figure 4.8 for the 2D case and Figure 4.9 for the 3D case. Additionally, interior lines/surfaces were introduced to enable detailed data extraction and facilitate mesh refinement where necessary.

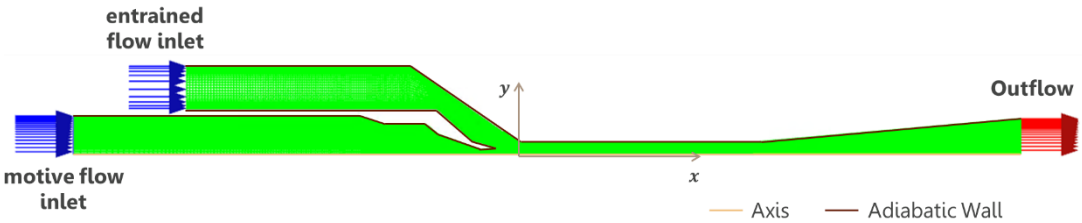


Figure 4.8 – 2D axisymmetric flow domain, and corresponding boundary conditions for the CO_2 ejector RANS simulation.

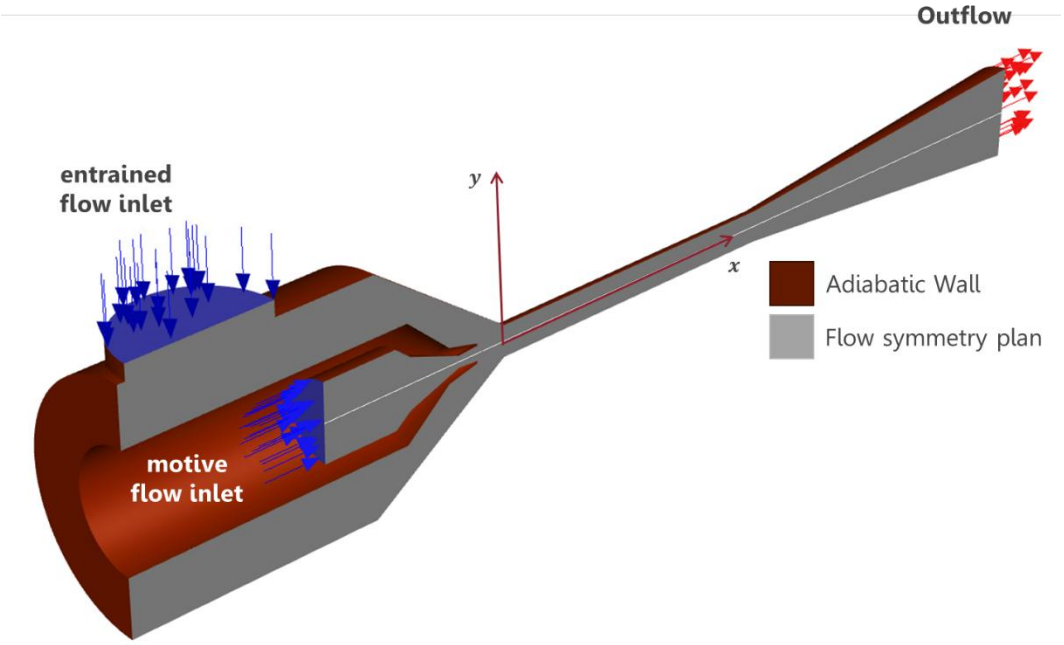


Figure 4.9 – 3D symmetrical flow domain, and corresponding boundary conditions for the CO_2 ejector RANS simulation

4.2 Meshing Strategy for Ejector Flow Simulations

A numerical mesh divides the computational domain into small, finite cells, approximating the continuous flow domain into discrete points. This discretisation enables the numerical solution of the governing equations. The quality of the numerical mesh plays a critical role in determining convergence behaviour, the model accuracy, and computation time cost. Employing an effective meshing strategy is essential, particularly for simulating complex flows involving transonic turbulent regimes, shock waves, boundary layer separation, expanding jets, phase changes, and other intricate phenomena.

Once the computational domains were defined, the numerical meshes were generated. Different meshing strategies were employed depending on the simulation type, with tailored approaches for 2D RANS, 3D RANS, and LES regions. To ensure clarity and relevance, this section presents descriptive examples of the meshing strategies used for each type of simulation, as well as the considerations and methods applied.

4.2.1 3D Mesh Generation and Optimization for R1234ze(E) ejector flow RANS simulation

The 3D mesh used for the ejector flow simulations was a hybrid mesh, combining structured and unstructured elements. Polyhedral cells were utilised for the flow core, while hexahedral cells were applied to the boundary layer to effectively capture wall-bounded flow phenomena.

The use of polyhedral cells in computational fluid dynamics has been widely recognised for its advantages. Lanzafame et al. (2013) reported that polyhedral meshes can reduce the required number of cells by one-third compared to tetrahedral meshes, without compromising simulation accuracy. Furthermore, polyhedral cells offer improved

numerical performance due to their greater number of neighbouring cells, which allows for better identification of dominant flow directions (Sosnowski et al. 2017). Their reduced sensitivity to cell stretching minimises interpolation errors and numerical diffusion, which is particularly beneficial for simulations involving complex geometries (Sosnowski et al. 2017). These characteristics result in faster convergence, enhanced numerical stability, and reduced computational costs, making polyhedral meshes ideal for resolving turbulent structures and shock waves efficiently.

Fluent 2022 R2 Mesh software (ANSYS Inc., 2022a) was employed to generate the 3D mesh for these simulations.

4.2.1.1 Surface Meshing and Refinement

In addition to physical boundaries such as inlets, outlets, and walls, internal surfaces and edges were defined at specific axial locations. Figure 4.4 depicts the symmetry plan for the 3D RANS mesh, identifying the internal surfaces and edge considered. These were included to facilitate the control of mesh density in those critical regions.

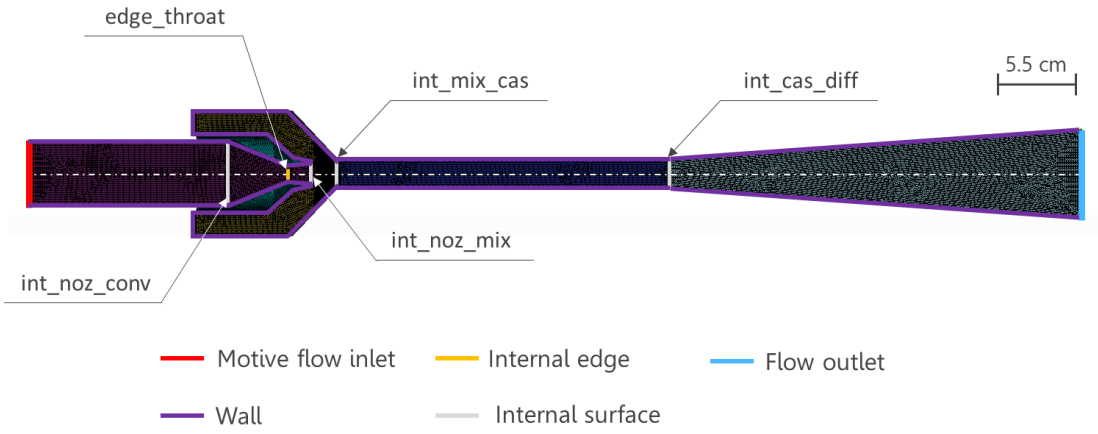


Figure 4.10 – R1234ze(E) ejector 3D RANS mesh with identification of boundaries.

4.2.1.2 Boundary Layer Resolution

Adequate boundary layer resolution is critical in wall-bounded flow simulation, as it defines the near-wall treatment and directly influences the accuracy of turbulence modelling (see Section 2.2.4). To optimise boundary layer generation, two different meshing methods were applied depending on the required resolution in each region.

For critical regions, the uniform offset method was employed to precisely control the first cell height, ensuring sufficient resolution of the boundary layer while satisfying flow conditions and turbulence model requirements. The boundary layer mesh growth rate was carefully set to maintain smooth transitions across mesh interfaces.

In less critical regions, where a coarser mesh was sufficient, the smooth transition method was used. This method computes the local initial height and total boundary layer thickness based on the underlying mesh, balancing computational efficiency with accuracy. As a result, boundary layer resolution varied across the ejector, requiring tailored first cell heights, boundary layer thicknesses, and smooth transitions between mesh regions. Figure 4.11 a) and b) present detailed views of the boundary layer mesh

at the transition between the constant-area section and the diffuser, illustrating the smooth interface between mesh zones.

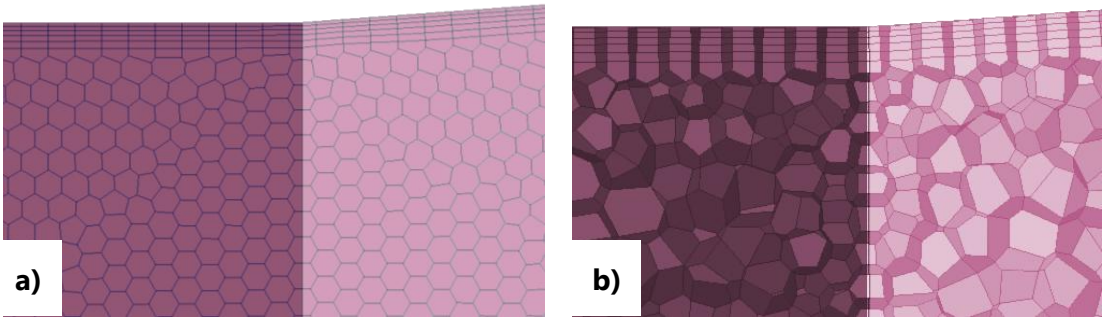


Figure 4.11 – Boundary layer in the ejector constant-area section interface with the diffuser: a) symmetry plan and b) xz-plan cut.

4.2.1.3 Mesh Quality base line

The mesh quality during the generation process held to the following criteria to ensure numerical stability and simulation accuracy:

- Maximum skewness: 0.65
- Minimum orthogonal quality: 0.25

These thresholds were selected based on best practices for CFD simulations involving transonic and turbulent flows with shock waves.

To confirm that the results were independent of mesh density, a mesh independence study was conducted. This study involved running simulations with progressively finer meshes and analysing the convergence of key global flow parameters, such as pressure and velocity distributions. The final mesh was selected after verifying that further refinements did not lead to significant changes in the results. This approach guarantees the reliability of the numerical predictions while maintaining computational efficiency. Details about the mesh independence study can be found in Section 4.4.5.1.

4.2.2 3D Hybrid Mesh Generation for ELES

The precursor RANS simulation results provide valuable insights into the required mesh size for a LES. By utilizing the RANS-derived turbulent kinetic energy (k_{RANS}) and dissipation rate ($\varepsilon_{\mathrm{RANS}}$), the integral length scale (L_{Δ}) can be estimated and with that, obtain a preliminary estimate for the local cell size required. To ensure that 80% of the turbulent kinetic energy (TKE) is resolved, the maximum characteristic cell dimension should satisfy the following condition (Pope, 2000):

$$\Delta_{\mathrm{cell}} \leq \frac{k_{\mathrm{RANS}}^{3/2}}{5 \cdot \varepsilon_{\mathrm{RANS}}} \tag{4.1}$$

4.2.2.1 LES mesh preliminary assessment

As described in Section 3.4, the subgrid viscosity in LES is influenced by mesh resolution. Adjusting the mesh impacts the underlying discretised equations, affecting the computed subgrid viscosity. Consequently, traditional mesh independence studies used in RANS are not applicable in LES simulations. Instead, alternative strategies must be

employed to evaluate mesh quality. Section 5.2.1 details the methodology used to assess mesh suitability for resolving large-scale eddies.

To identify zones requiring refinement, an indicator variable ($\boldsymbol{f}$) was defined using Equation (4.1) and implemented as a custom field function in ANSYS Fluent (ANSYS Inc., 2022a):

$$\boldsymbol{f} \geq \frac{k_{\mathrm{RANS}}^{3/2}}{\Delta_{\mathrm{cell}} \cdot \varepsilon_{\mathrm{RANS}}} \tag{4.2}$$

The RANS solution was interpolated onto the LES mesh, enabling the calculation of the $\boldsymbol{f}$-value across the domain. Figure 4.12 shows a visualisation of $\boldsymbol{f}$ values for the LES region. Red regions correspond to $\boldsymbol{f} \geq 5$, indicating areas where the mesh size is adequate for the 80% TKE resolution. As expected, higher refinement is needed near shock-prone areas.

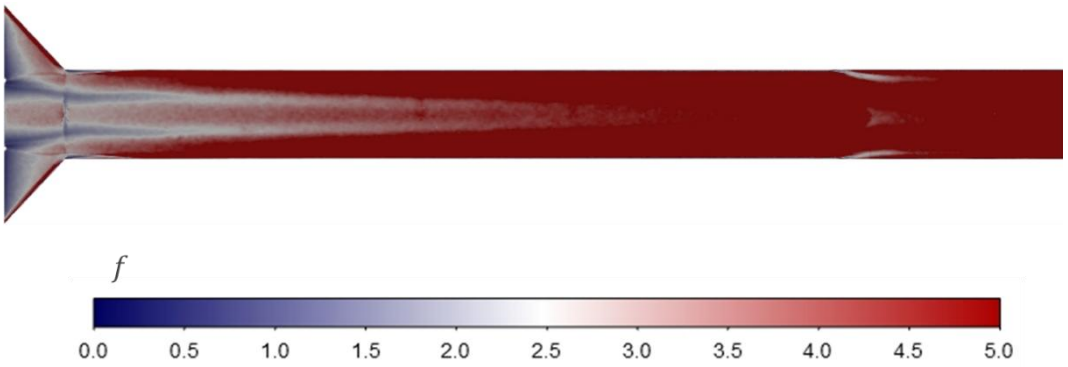


Figure 4.12 – Visualisation of the $\boldsymbol{f}$ –value in the LES region of a RANS R1234ze(E) simulation.

4.2.2.2 Surface Meshing and Refinement

The meshing strategy included both physical boundaries and internal boundaries, which were defined based on sensor and transducer locations from experimental validation and the $\boldsymbol{f}$-values from the precursor RANS simulation. Additionally, local volumes of influence were employed using the "body of influence" (BOI) tool in ANSYS Fluent. This tool enables targeted refinement in critical regions without unnecessarily increasing the total cell count. Figure 4.13 illustrates two distinct BOI zones (A and B) with different refinement levels, ensuring adequate mesh resolution in key areas.

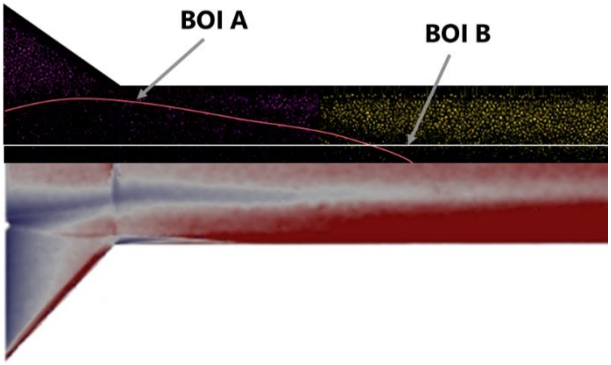


Figure 4.13 – Example of local refinement using the body of influence (BOI) tool.

For LES meshing, the aspect ratio (AR) of cells adjacent to walls is a critical parameter. Considering the variables identified on Figure 4.14, the AR is defined as:

$$AR = \frac{A}{B} \tag{4.3}$$

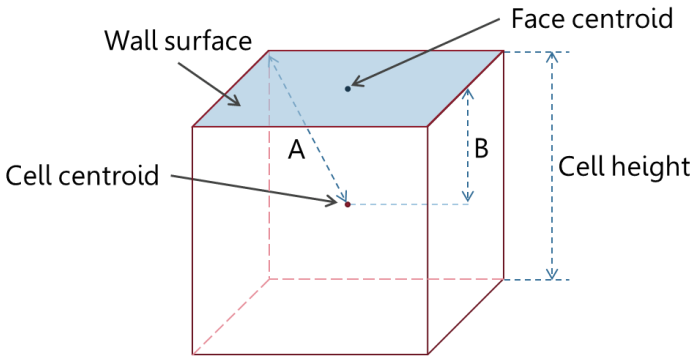


Figure 4.14 – Schematic representation of a cell adjacent to the wall, with dimensions A and B identified.

In critical regions, ideal AR values range from 0.5 to 2 (Gerasimov, 2016). Additionally, the ratio between the characteristic edge length (Δ_{wall}) of the wall-adjacent cell and its height should ideally be close to 1, although values below 10 are still acceptable (Gerasimov, 2016). The characteristic edge length of the wall-adjacent cell is given by:

$$\Delta_{wall} = \sqrt{A_{wall-surface}} \tag{4.4}$$

4.2.2.3 Boundary Layer Resolution

The WMLES S-Ω SGS model imposes specific requirements for boundary layer resolution (ANSYS Inc., 2015). These include:

$$N_x = 10 \tag{4.5}$$

$$30 \leq N_y \leq 40 \tag{4.6}$$

$$N_z = 20 \tag{4.7}$$

Where N_x, N_y and N_z represent the number of cells in the x, y and z directions.

The relationship between boundary layer thickness (δ) and cell dimensions is illustrated in Figure 4.15. For a cylindrical geometry with radius R:

$$\Delta_{cell,x} = \frac{\delta}{N_x} \tag{4.8}$$

$$\Delta\theta = \frac{\delta}{R \cdot N_z} \tag{4.9}$$

These equations help define the streamwise cell length ($\Delta_{cell,x}$) and angular size ($\Delta\theta$), ensuring sufficient resolution within the boundary layer while maintaining computational efficiency.

The mesh generation strategy for the ELES of the R1234ze(E) ejector balances computational efficiency with simulation accuracy. Insights from the precursor RANS simulation, combined with advanced meshing tools and best practices for LES boundary layer resolution, were applied to develop a robust and optimised mesh. This approach ensures the accurate capture of critical flow features, including shock structures,

boundary layer interactions, and turbulence, enabling high-fidelity ejector flow simulations.

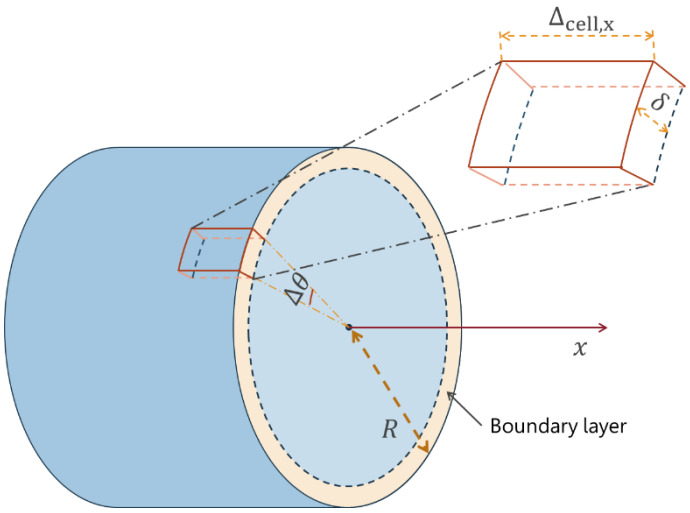


Figure 4.15 – Schematization of a cell adjacent to the wall.

4.2.3 2D Mesh Generation and Optimization for CO_2 two-phase ejector flow RANS simulation

The 2D mesh used for the ejector flow simulations was a structured quadrilateral grid, generated using SpaceClaim 2022 software (ANSYS Inc., 2022b). The quality indicators confirmed that the mesh was suitable for achieving high-accuracy simulations. For instance, the mesh aspect ratio was predominantly below 10, skewness values were less than 0.44, and orthogonal quality exceeded 0.74.

The mesh was divided into fourteen distinct blocks, enabling tailored mesh resolutions for specific zones of interest. The boundaries of each block were defined to control the number of divisions or element edge sizes, ensuring adequate resolution where needed. Figure 4.16 illustrates the axisymmetric 2D mesh and the different blocks.

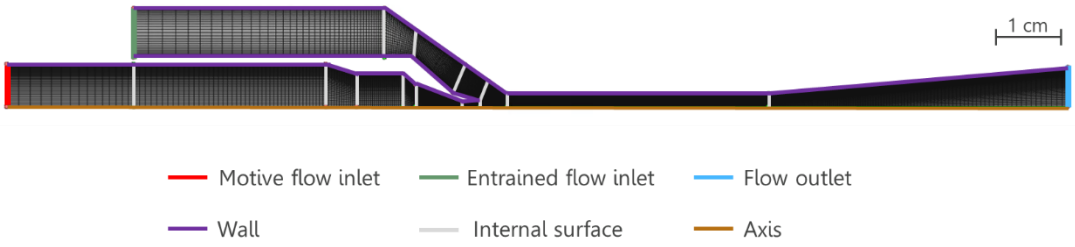


Figure 4.16 – Axisymmetric 2D mesh for the CO_2 ejector, with identification of blocks and boundaries.

For the boundary layer, the first cell height was carefully set to capture near-wall gradients accurately, and a smooth transition was ensured between the boundary layer and the core mesh. Details regarding the mesh independence study are provided in Section 4.4.5.2.

4.2.4 3D Mesh Generation and Optimization for CO_2 two-phase ejector flow RANS simulation

This mesh creation followed the same steps as the one presented for the 3D mesh of the R1234ze(E), as well as the boundary layer resolution and quality base line details. Yet, for the surface meshing and refinement, some differences need to be considered. Figure 4.17 depicts the symmetry plan for the 3D RANS mesh, showing the localization for the different internal surfaces considered.

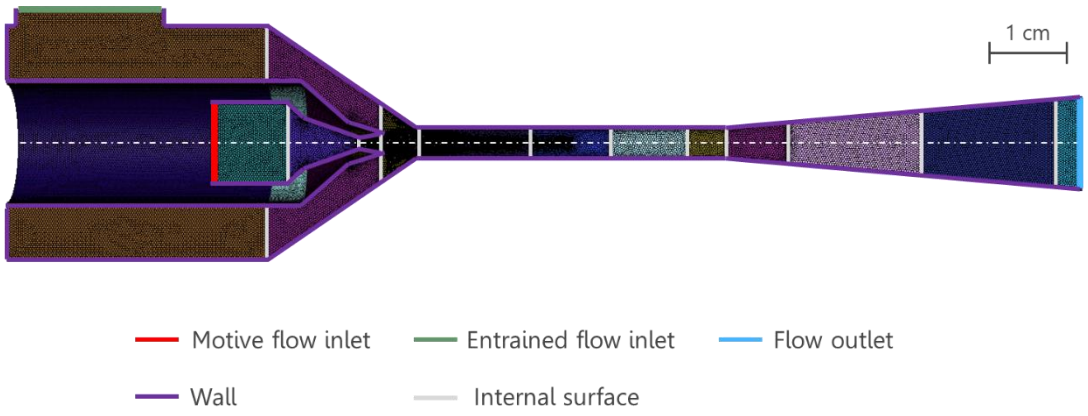


Figure 4.17 – CO2 ejector 3D RANS mesh with identification of boundaries.

Local refinement was applied using the "body of influence" (BOI) tool in ANSYS Fluent, allowing for enhanced resolution in targeted areas of interest. Four distinct BOI regions, labelled A to D, were defined to improve mesh accuracy in critical zones. Figure 4.13 illustrates an example of the BOI implementation for the CO_2 3D mesh.

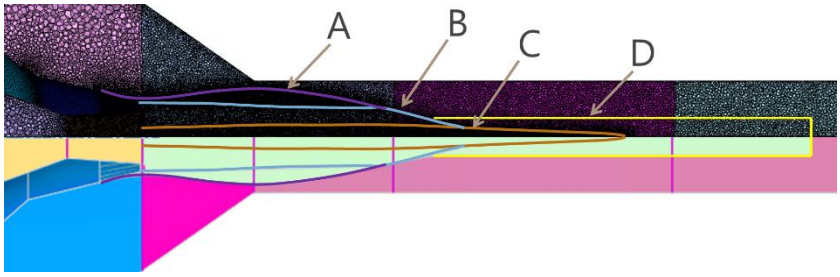


Figure 4.18 – Example of local refinement using the body of influence (BOI) tool for the CO_2 3D mesh.

4.3 Development and Application of User-Defined Functions (UDFs) for Ejector Simulation

In ANSYS FLUENT, non-standard models can be implemented via User-Defined Functions (UDFs), which are custom functions written in the C programming language. These UDFs are dynamically linked to the solver during runtime to extend or modify its capabilities. Within this thesis, multiple UDFs were developed to implement the mathematical models described in Chapter 3. This section details the UDFs created for evaluating CO_2 thermophysical properties and implementing the internal energy-based energy equation, as well as the enthalpy-based energy equation, for two-phase ejector simulations.

The internal energy-based model was designed to accommodate different working fluids. To simplify its implementation, the UDFs were divided into three main groups:

- User-Defined Real Gas Model (UDRGM): handles the computation of thermodynamic properties for real gases.
- User-Defined Functions – Homogeneous Equilibrium Model (UDF-HEM-e): implements the internal energy-based energy equation described in Chapter 3.
- User-Defined Functions – Homogeneous Equilibrium Model (UDF-HEM-h): implements the enthalpy-based energy equation described in Appendix C. The appendix also includes details about the integration of the HEM with UDFs.

It is also noteworthy that ANSYS FLUENT provides pre-defined terms and parameters tailored for turbulence models, which are directly integrated into the simulation setup. Specific details about the parameters and terms pre-defined in FLUENT and utilised in the turbulence modelling for this study can be found in Appendix E.

4.3.1 Header Configuration and Memory Allocation for UDFs in FLUENT

Both UDF groups share a common header file, which configures the model assumptions, constants, and memory allocation within FLUENT. The header file allows the user to:

- Select the coordinate system for computational model:
  - Cartesian (for 2D or 3D);
  - Cylindrical for axisymmetric (2D).
- Define the speed of sound calculation model[1];
- Set model constants:
  - turbulent Prandtl number for energy diffusivity: $\sigma_t = 0.85$;
  - pressure diffusivity constants: $\alpha_2 = 0.15$ and $\alpha_3 = 0.20$;
  - maximum turbulent Mach number for compressibility corrections: $Ma_{T0} = 0.25$;
  - compressibility corrections for kinetic energy dissipation: $\beta_i^* = 0.09$ and $\xi^* = 1.5$;
- Specify assumptions for velocity fluctuation averaging: options include anisotropic turbulence or equilibrium turbulence, with or without small mean velocity gradients (default).
- Enable or disable bulk viscosity effects, defining constants such as molecular degrees of freedom (disabled by default).
- Control turbulent kinetic energy (TKE) production limits, either as a constant or function.

In FLUENT, memory is allocated via User-Defined Memory (UDM) for storing custom variables and User-Defined Scalars (UDS) for adding transport equations. For this model,

[1] The model is prepared to work with one of five different methods to compute the speed of sound. The default method is described in Section 3.2.2 (Brennen, 2005), details about the other models can be found in Lund and Flatten (2010), Nguyen, Winter, and Greiner (1981), Ameur, Aidoun, and Ouzzane (2016) and Giacomelli, Mazzelli, and Milazzo (2018).

several UDMs were employed for storing intermediate values, post-processing data, or supporting calculations.

The standard energy equation in FLUENT was replaced by the internal energy transport equation, as defined in Equation (3.61). To implement this, a User-Defined Scalar (UDS) was created to represent the specific internal energy. Although no additional transport equations were strictly required, eight supplementary UDSs were introduced to support the model.

Three UDSs were allocated for each auxiliary variable ($S1_{\mathrm{aux_i}}$ and $S2_{\mathrm{aux_i}}$) to compute gradients and derivatives in the x, y, and z directions. Table 4.1 summarises these variables and their associated equations.

Table 4.1 – List of UDS defined.

Source 1	$S1_{\mathrm{aux_i}} = \kappa \cdot \frac{\partial \overline{p}}{\partial x_i} \cdot \left(\frac{\partial \tilde{T}}{\partial p}\right)_e$	Section 3.3.3 Equation (3.63)
Source 2	$S2_{\mathrm{aux_i}} = \overline{u_i''}$	Section 3.3.3 Equation (3.49)

While UDMs could have been used to store these variables, FLUENT lacks native macros to compute UDM derivatives. By associating these variables with UDSs and disabling their transport exchange, their gradients could be accessed as needed.

Additionally, UDSs were introduced for both density and temperature to address specific limitations in FLUENT. In the pressure-based solver, FLUENT does not natively provide density gradients via UDFs, requiring the creation of a dedicated UDS for density. Similarly, a UDS for temperature was added due to errors encountered when attempting to call the temperature gradient macro within the source term macro.

4.3.2 Implementation of a Real Gas Model Using UDRGM

The UDGRM is a function that incorporates specialised macros to define a custom real gas model. This model must include specific functions in a particular sequence, as summarised in Table 4.2. This table provides a concise summary of the function and purpose of each macro.

Table 4.2 – List of macros included in the UDRGM.

FluidProp_Setup	initialises the model and performs a basic quality check of property tables
FluidProp_density	returns the value of the correspond property, by performing a linear interpolation in the property table, using pressure and internal energy (UDS) as inputs
FluidProp_enthalpy	
FluidProp_entropy	
FluidProp_specific_heat	
FluidProp_mw	returns the fluid molecular weight, that is defined in the file header
FluidProp_speed_of_sound	returns the value of the correspond property, by performing a linear interpolation in the property table, using pressure and internal energy (UDS) as inputs
FluidProp_viscosity	
FluidProp_thermal_conductivity	

The UDRGM is designed for flexibility, allowing users to easily modify the file header to adapt the model for different fluids. For instance, Figure 4.19 shows the header for the CO_2 UDRGM developed in this work.

```
/* define fluid properties  */

char fluidname[3]= "CO2";    /* define the fluid name, between [] put the quantity of char in the name */

#define MW 44.01             /* fluid molecular weight */

#define pcrit 7377000.       /* fluid critical pressure in Pa */

#define numP 78              /* number of pressure points for the property table */
#define numU 461             /* number of internal energy points for the property table */
```

Figure 4.19 – Header of the UDRGM with property table details for CO_2.

Physical properties were determined by interpolation from property tables, as detailed in Section 3.2.2. The interpolation process adheres to the flow chart outlined in Appendix F. The tables were created based on predefined ranges of pressure and internal energy. Each entry was indexed by pressure (iP) and internal energy (iU). Saturation properties, including Gibbs free energy and entropy, were stored in separate tables for use in specific computations.

Table 4.3 outlines the external .txt files required for the thermodynamic property tables and specifies the data included in each column. The Properties.txt file contains comprehensive thermodynamic data, including pressure, internal energy, enthalpy, and other key properties. The Pressure.txt file lists saturation properties (e.g., saturated liquid and vapour internal energy, Gibbs free energy, entropy, and density) for each pressure value defined in the property table. Finally, the IntEnergy.txt file is a vector that includes all internal energy values used in the property table defined in Properties.txt.

Table 4.3 – External files with the thermodynamic table.

File name	Colum identification
Properties.txt	Line number, iP, pressure [Pa], iU, internal energy [J/kg], enthalpy [J/kg], temperature [°C], dynamic viscosity [Pa.s], density [kg/m^3], thermal conductivity [W/(K.m)], heat capacity [J/(kg.K)], speed of sound [m/s], entropy [J/(kg.K)], dTdu, dTdp
Pressure.txt	pressure [Pa], saturated liquid internal energy [J/kg], saturated vapour internal energy [J/kg], saturated liquid Gibbs free energy [J/kg], saturated vapour Gibbs free energy [J/kg], saturated liquid entropy [J/kg], saturated vapour entropy [J/kg], saturated liquid density [kg/m^3], saturated vapour density [kg/m^3]
IntEnergy.txt	internal energy [J/kg]

In the file Properties.txt, the values for $\left(\frac{\partial \tilde{T}}{\partial e}\right)_p$ and $\left(\frac{\partial \tilde{T}}{\partial p}\right)_e$, were included as auxiliary data for the diffusive term calculation. These values were computed for each set of pressure and internal energy using the finite difference method. The results were organised into a table to facilitate interpolation during the simulation process.

By default, a UDRGM in FLUENT relies on temperature and density as primary variables to calculate other thermophysical properties (ANSYS Inc., 2021a). However, in the developed model, pressure and internal energy are utilised as independent variables. Although temperature is not directly included as a primary variable in this approach, an

adjustment macro was created to compute the temperature field within the computational domain during each iteration. This macro determines the local temperature based on pressure and internal energy and computes both cell centre and cell face temperatures, ensuring accurate boundary condition application.

Some on-demand macros were integrated into the UDRGM to support post-processing and model validation. These macros verify whether the maximum and minimum pressure and internal energy values remain within the predefined property table limits. Additionally, they compute other properties such as vapour quality and saturated state properties.

4.3.3 Integration of the Homogeneous Equilibrium Model (HEM) with UDFs

When UDS is added in FLUENT, a transport equation for that scalar is automatically generated. To complement the UDS transport equation, FLUENT provides specific macros for defining the diffusivity term and source terms associated with the scalar. Figure 4.20 shows the internal energy transport equation (Equation (3.62)) along with the macros required to resolve its terms.

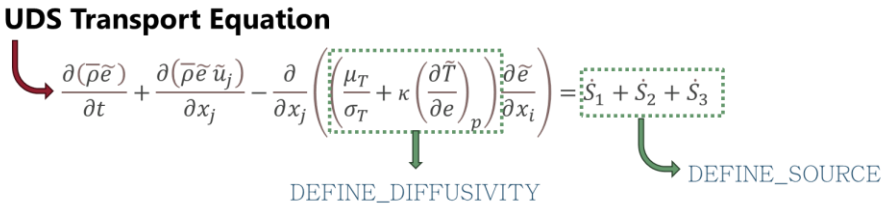
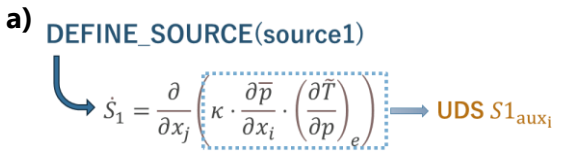


Figure 4.20 –Transport equation of the UDS internal energy, and identification of the model specific macros to compute the diffusivity term and sources.

The DEFINE_DIFFUSIVITY macro specifies the diffusivity for UDS transport equations. For this model, the diffusivity term was computed as presented in section 3.3.2 and described in equation (3.62).

In total, five source terms were defined for the RANS model in Section 3.3.3: three for the internal energy transport equation and two additional terms for the TKE transport equation, to account for pressure work and dilatation effects. For LES, two source terms were defined specifically for the internal energy transport equation. Figure 4.21 shows these source terms and their connection to the general-purpose macros used in the model.



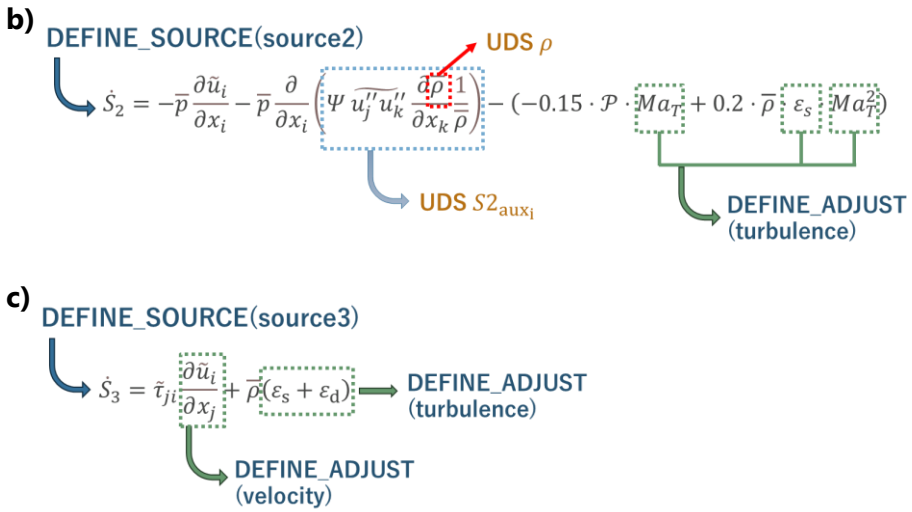


Figure 4.21 – Sources for the internal energy transport equation, with general-purpose macros and auxiliary UDSs: a) heat diffusion; b) work due to normal stresses; c) work due to viscous stresses and TKE dissipation.

The DEFINE_ADJUST macro adjusts or modify variables not directly passed as arguments to other macros. This was necessary for variables like the turbulent Mach number (Ma_T), the solenoidal and dilatational TKE dissipation rates (ε_s and ε_d). These values are updated during every iteration before solving the transport equations through the adjust_turbulence macro, which was implemented using the equations detailed in Section 3.3.3.

Additionally, for simulations programmed in cylindrical coordinates, variables such as velocity, velocity gradients, strain rates, and turbulent shear stress tensors are computed within another DEFINE_ADJUST macro. The adjust_velocity macro calculates these matrices, ensuring compatibility with the cylindrical coordinate system.

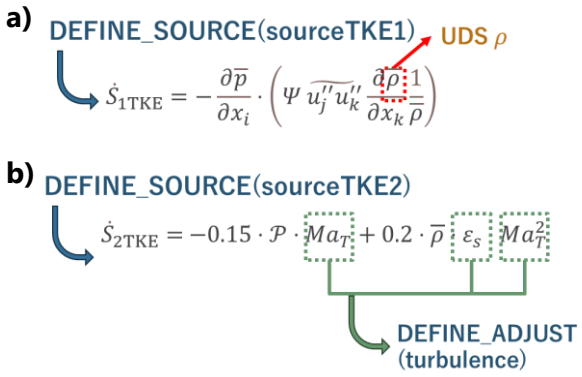


Figure 4.22 – Sources for TKE transport equation, with general-purpose macros and auxiliary UDSs: a) pressure dilatation; b) pressure work.

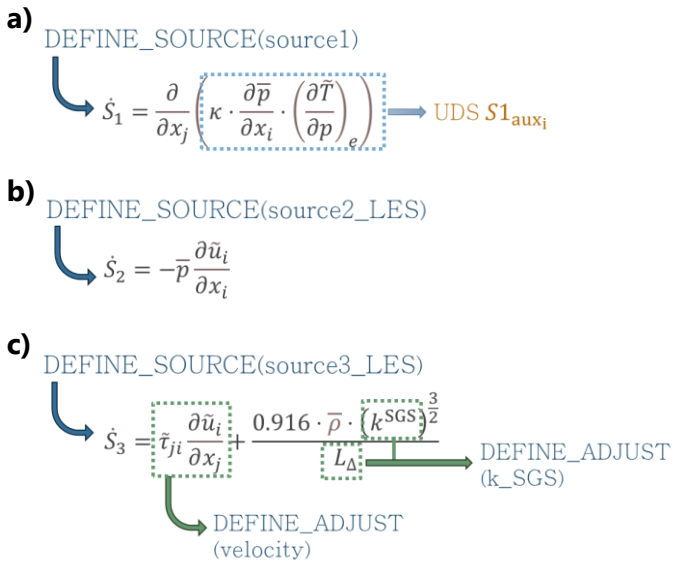


Figure 4.23 – Sources for the internal energy transport equation in LES, with general-purpose macros and auxiliary UDSs: a) heat diffusion; b) work due to normal stresses; c) work due to viscous stresses and TKE dissipation.

Figure 4.22 and 4.23 shows the sources for the TKE transport equation and the internal energy transport equation for LES region, respectively. While the same `DEFINE_ADJUST` macros were reused, a new macro (`adjust_kSGS`) was introduced to compute Subgrid Scale variables specifically for LES simulations.

To ensure the adiabatic wall assumption, the `adjust_wall_temperature` macro sets the outer layer wall temperature to match the cell-centre temperature of the nearest cell computational domain. As optional, two other macros were included based on specific simulation setups:

- `adjust_TKE_prod`: applies the production of TKE limit defined by the user in the header.
- `adjust_bulk_visc`: Computes bulk viscosity based on molecular degrees of freedom and relaxation time factors defined in the header.

Lastly, `DEFINE_ON_DEMAND` were implemented for optional execution, reducing computational overhead. These macros are executed only when triggered by the user, rather than being called during every iteration or time step. Some mandatories `DEFINE_ON_DEMAND` macros are required during initialization, depending on the simulation setup:

- For cylindrical coordinates: `define_coordinates` computes radial and angular coordinates for each cell centre.
- For LES, or ELES, simulation: `define_h_max`, `define_h_wn` and `define_d_w` determine mesh-related variables to compute SGS data.

4.4 Numerical considerations during the RANS ejector flow simulation

4.4.1 Flow Solver Algorithm for FLUENT energy equation

The governing equations (mass, momentum, and energy) are not sufficient on their own to fully resolve the flow. It is necessary to close these equations using an equation of state, which relates different thermodynamic fluid properties and ensures interdependency between pressure, density, and internal energy. This is extremely important in compressible flows, where pressure has both hydrodynamic meaning, associated to the velocity field, and thermodynamic significance, associated to temperature (Kundu et al., 2012b).

The density-based solver is particularly well-suited for compressible flows, as it efficiently handles the interactions between density, momentum, and energy equations during the solution process (Launder and Sandham, 2002). Figure 4.24 illustrates the iterative procedure for this solver. Initially, fluid properties are updated, followed by the calculation of density and internal energy fields. The pressure field is then determined by the equation of state (Boger, 2014). In FLUENT, when using the density-based solver, the turbulence and other scalar equations are solved afterward, followed by a convergence check (ANSYS Inc., 2021b).

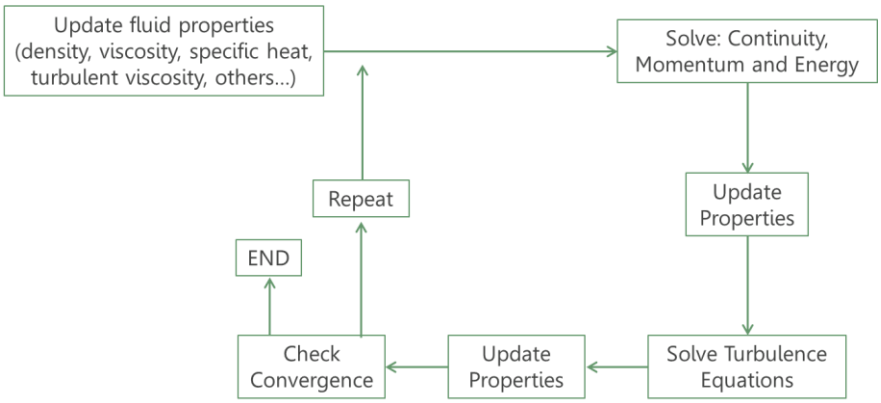


Figure 4.24 – Solution procedure for the density-based solver in FLUENT.

An alternative method is the pressure-based solver, originally developed for incompressible flows but applicable to compressible cases as well (Chorin, 1968). This algorithm first determines the pressure field by coupling the continuity and momentum equations, ensuring that the velocity field satisfies continuity (ANSYS Inc., 2021b). Other transport equations, such as energy and turbulence, are solved subsequently. In incompressible flows, the pressure field results from the velocity field, as there is no significant density variation. Additionally, because the energy equation is solved separately, pressure becomes independent of energy (and thus temperature) in such cases. The pressure-based solver can operate in either segregated or coupled modes, as illustrated in Figure 4.25.

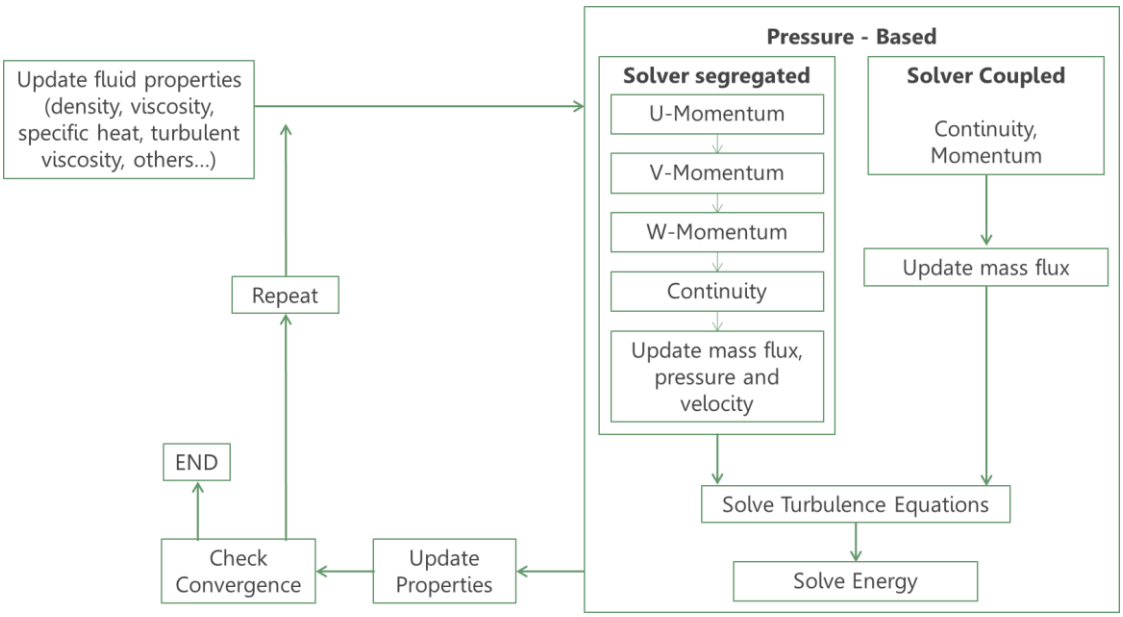


Figure 4.25 – Solution procedure for the segregated and coupled pressure-based solver in FLUENT.

In the segregated mode, the momentum and continuity equations are solved iteratively and separately. The pressure field is adjusted at each iteration to correct the velocity field until continuity is satisfied. Subsequent steps include solving turbulence and energy equations, updating fluid properties, and checking for convergence. While this approach is computationally efficient for low-speed flows, it may face stability challenges or slower convergence in high-speed compressible flows or cases with strong pressure-temperature coupling.

To address these limitations, the coupled mode solves the continuity and momentum equations simultaneously within a unified system, capturing their interdependence more effectively. Once the primary fields are resolved, turbulence and energy equations are addressed sequentially, followed by property updates and convergence checks. This approach improves convergence rates and stability, making it particularly suitable for ejector simulations and other cases where compressibility and shock interactions play a significant role.

For this study, the pressure-based solver was chosen due to its versatility and demonstrated effectiveness in handling flows with moderate to high compressibility. Its ability to couple continuity and momentum equations ensures mass conservation while accommodating compressibility effects through the energy equation (Launder and Sandham, 2002; ANSYS Inc., 2021b). Additionally, the solver's discretization scheme, based on the mass flux ($\rho\vec{u}$) through cell faces, maintains coupling between pressure and density fields, which is essential for accurately predicting the interaction between supersonic jets and subsonic recirculating flows.

Furthermore, this approach has been widely validated in previous studies on ejector flows[2], demonstrating its reliability and accuracy. While the density-based solver may offer advantages in certain highly compressible regimes, the pressure-based solver

[2] Some scientific studies that used pressure-based solver to model the ejector interior flow - (Yazdani et al., 2012; Smolka et al., 2013; Lucas et al., 2014; Giacomelli et al., 2016, 2019; Palacz et al., 2017; Giacomelli, Banasiak, et al., 2018; Giacomelli, Mazzelli, et al., 2018; Haida, et al., 2018b; Elbarghthi et al., 2020; Ringstad, 2023)

provides a robust and efficient framework for the range of operating conditions encountered in this work.

4.4.2 Flow Solver Algorithm for internal energy equation

As discussed in Chapter 3, the temperature-based energy equation in FLUENT was replaced with the internal energy-based formulation for the two-phase flow simulations. Figure 4.26 presents the modified solution procedure with FLUENT's pressure-based solver, incorporating the custom macros embedded in the UDF and UDRGM. A comparison with the typical FLUENT resolution algorithm (Figure 4.25) shows that the overall solution procedure remains largely unchanged. In this solver, the energy equation is traditionally calculated after the pressure, velocity, and turbulence fields are resolved. This sequence is maintained even when the energy equation is replaced with the internal energy-based formulation, ensuring consistency in the solution process.

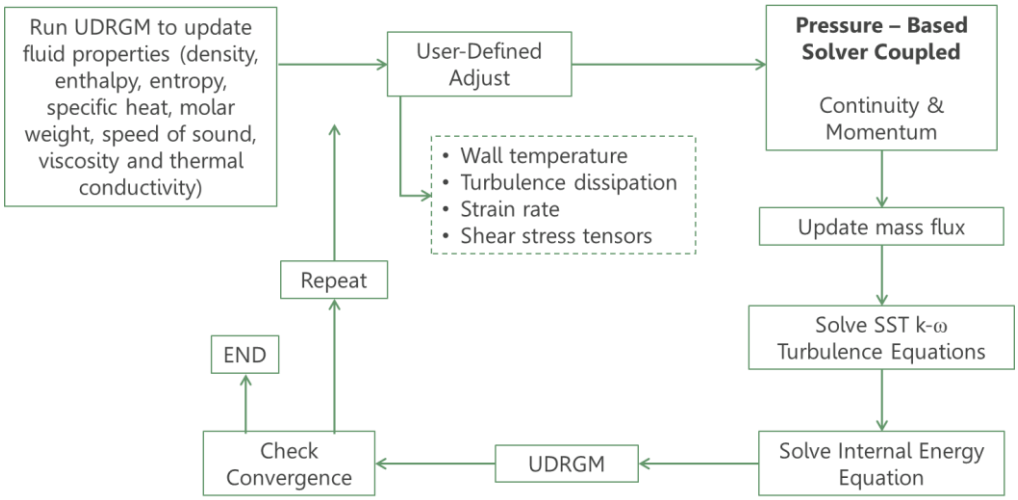


Figure 4.26 – Solution procedure for the coupled pressure-based solver in FLUENT using the internal energy-based energy equation and UDRGM.

While this study employs a pressure-based solver, it is worth noting that in a density-based scheme, replacing the energy equation with a scalar equation leads to partial decoupling from other transport equations. This occurs because, in density-based solvers, scalar equations are computed after the turbulence equations, unlike the energy equation, which is traditionally solved alongside the continuity and momentum equations. As a result, pressure becomes primarily dependent on fluid density and velocity fields, rather than being fully linked to thermodynamic variables such as temperature and internal energy. This aligns the solver's behaviour more closely with that of the pressure-based coupled solver.

4.4.3 Numerical Methods and Spatial Discretization

Table 4.4 presents each scheme applied to each variable in the CFD RANS models. The RANS simulations were performed under steady-state conditions, a common approach in studies of this type (Ringstad, 2023). It is important to note that the discretization scheme used in some simulation may differ from the one presented here, as it can influence simulation convergence time.

Table 4.4 – Discretization schemes used in the CFD models.

Solver	Pressure-Based
Pressure-Velocity Coupling	
Scheme	Coupled
Spatial Discretization	
Gradient	Least Squares Cell Based
Pressure	Second Order
Density	Second Order Upwind
Momentum	Second Order Upwind
Turbulent Kinetic Energy	Second Order Upwind
Specific Dissipation Rate	Second Order Upwind
Energy	Second Order Upwind

The gradients were evaluated using the least-squares cell-based method, which assumes a linear variation of the solution between adjacent cell centres. This approach provides accuracy comparable to the Green-Gauss node-based gradient method while offering superior performance over the Green-Gauss cell-based gradient method. Furthermore, the least-squares method has the added advantage of lower computational cost, making it well-suited for large-scale simulations (ANSYS Inc., 2021b).

For all variables, the advective schemes were discretised using the Second-Order Upwind Scheme. This technique achieves higher-order accuracy at cell faces by utilising a Taylor series expansion of the cell-centred solution around the cell centroid. As a result, it ensures robust capture of flow features and improved resolution in simulations (ANSYS Inc., 2021b).

4.4.4 Convergence Time and Criteria

The general convergence criteria were deemed satisfied when the following conditions were met:

- The relative residuals for all governing equations remained below 10^{-6}.
- The relative mass flow rate variation over at least 500 consecutive iterations was less than 0.1%.
- The net flux imbalance across the domain boundaries was kept below 1% of the smallest mass flow rate in the system.

For the RANS simulation using R1234ze(E) as the working fluid, these criteria were easily maintained, demonstrating stable and consistent convergence. However, in the CO_2 two-phase flow simulations, which employed two different HEM models (HEM-h and HEM-e) the convergence behaviour varied. The residuals for the HEM-h model proved more challenging to reduce. Specifically, the lowest residual for the continuity equation was 4×10^{-4}, while the streamwise velocity (u) achieved 1.5×10^{-6}, turbulent kinetic energy (TKE) 9×10^{-6}, and the specific dissipation rate of TKE 6×10^{-6}. Residuals for other variables (v, w and e) dropped below 10^{-6}.

For the HEM-e model, all residuals were below 10^{-6}, except for the continuity residual, which fluctuated around 9×10^{-6}. The relative mass flow rate variation criteria are summarized in Table 4.5.

Table 4.5 – Mass flow rate convergence criteria for 3D HEM-h and 3D HEM-e models.

	3D HEM-h	**3D HEM-e**
$\dot{m}_{\mathrm{pr}}$ **variation allowed**	0.1%	0.1%
$\dot{m}_{\mathrm{sec}}$ **variation allowed**	1%	0.1%
Iteration interval for verification	500	1 000

While both CO_2 two-phase models allowed a maximum variation of 0.1% for the motive flow rate, the HEM-h model was unable to maintain the same level of control for the entrained flow rate, which fluctuated by up to 1%, compared to the stricter 0.1% limit achieved by HEM-e. This demonstrates HEM-e's superior ability to resolve flow dynamics with greater precision. Additionally, the extended iteration interval for verifying mass flow rate fluctuations in HEM-e further emphasizes its stability and efficiency in achieving convergence.

These convergence criteria ensured the accuracy and reliability of the numerical results, minimising potential errors from residual instability or boundary condition imbalances. Such rigorous practices are crucial when simulating complex ejector flows to achieve high-trust and reproducible outcomes.

4.4.5 Mesh Independence Study

Achieving mesh independence is a critical step to ensure accurate CFD results. This section details the mesh independence study generated for the RANS simulations. First, the 2D mesh study for CO_2 is presented, focusing on the internal energy-based model. Next, the 3D mesh used for the ELES precursor RANS simulation is analysed.

The observation from existing studies reveals that mesh independence can be achieved with a wide range of mesh resolutions, depending on the specifics of the simulation setup. Based on the insights gained in this work, uniformly refining the mesh throughout the entire domain often results in inefficient use of computational resources. Coarser meshes in non-critical regions can yield similar levels of accuracy while reducing computational costs. Consequently, this study employed a strategic approach to mesh refinement, focusing on key areas of the ejector to balance computational efficiency with the accuracy of the results.

4.4.5.1 3D R1234ze(E) Mesh Independence Study

As described in Section 4.1.2, the simulation domain represents only half of the ejector geometry. The computational model was validated using experimental data from Kracik et al. (2018), as detailed in Section 5.1. The mesh independence study was conducted under Run 1 operating conditions, selected because, according to the authors, it is the only case where the 1D numerical simulation, ideal gas CFD simulation, and real-gas CFD simulation consistently identified a double-choke ejector flow regime (Kracik et al., 2018).

Meshes with cell counts ranging from 537×10^3 to 946×10^3 were tested, labelled A to F, from the coarsest to the finest. Table 4.6 summarises the key characteristics of these

meshes. The minimum and maximum surface cell sizes refer to the edge lengths of cells surfaces at the physical boundaries. The maximum length represents the largest distance between cell centroids in the entire domain, while the mixing chamber target specifies the intended cell size in that region. Local refinement was focused on limiting the edge cell size at the motive nozzle throat and controlling the maximum surface cell size at the constant-area section inlet.

For all meshes, the y^+ value was greater to 1. While y^+ values close to 1 are often desired for enhanced accuracy, they were computationally expensive and did not yield additional precision in this case. The near-wall model employed, as described in detail in Section 3.3.6, is compatible with higher y^+ values, ensuring reliable results without requiring extreme near-wall refinement.

Table 4.6 – Characteristics of the meshes tested for the 3D RANS R1234ze(E) simulation.

Mesh	Cell count	Cell size [mm]				Local refinement
		Min. Surf.	Max. Surf.	Max. Length	Mix. Cham. target	
A	536 837	0.5	1.2	1.704	-	No
B	728 267	0.55	1.05	1.413	-	No
C	785 964	0.5	1	1.389	-	No
D	825 377	0.5	1	1.360	0.5	Yes
E	902 184	0.5	0.95	1.349	0.5	Yes
F	946 170	0.5	0.925	1.271	0.5	Yes

Figure 4.27 illustrates the impact of mesh size on the motive ($\dot{m}_{\mathrm{pr}}$) and entrained ($\dot{m}_{\mathrm{sec}}$) mass flow rates. A decrease in both flow rates is observed when local refinement is introduced, with values stabilising for meshes E, F, and G. The differences between the maximum and minimum flow rates across the tested meshes are 3.8 g/s for the motive flow and 2.7 g/s for the entrained flow, corresponding to variations of 0.8% and 1.9%, respectively. These results indicate that the mass flow rates are nearly independent of mesh resolution, with variations remaining below 1% for the motive flow and under 5% for the entrained flow between the coarsest and finest meshes. Additionally, the entrainment ratio value variated between 0.30 and 0.29, confirming its independence from mesh resolution. This behaviour is consistent with trends reported in the literature (Smolka et al., 2013; Palacz et al., 2015).

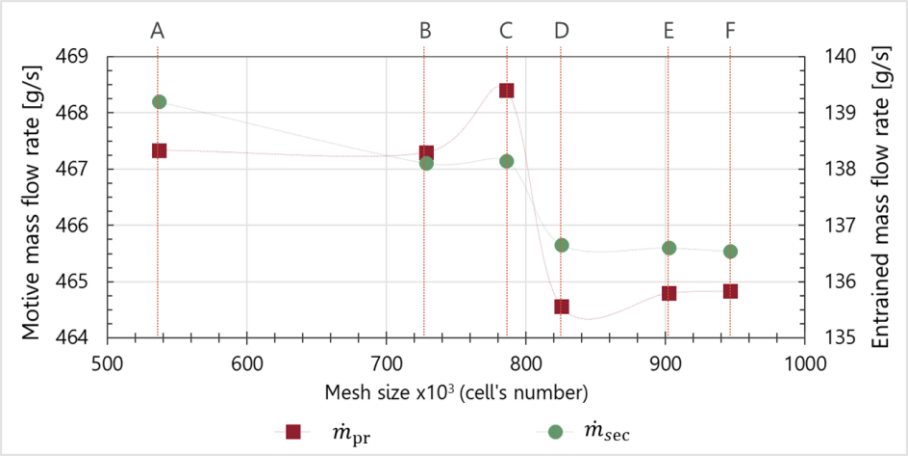


Figure 4.27 – Impact of the mesh size on the ejector inlet mass flow rates.

The static wall pressure for all six meshes was compared with experimental static wall pressure measurements, as shown in Figure 4.28a) and b). These plots focus on the region from the nozzle exit to the ejector outlet. Across all meshes, the intensity of the shock at the nozzle outlet was underpredicted. The final sensor in the constant-area section (P5 in Figure 4.1) is located before the pressure recovery, where the flow reaches the subsonic regime. However, the numerical results predicted a premature pressure recovery in the simulation for most meshes. Exceptions to this were observed with meshes C and E, which achieved pressure values closely matching the experimental data.

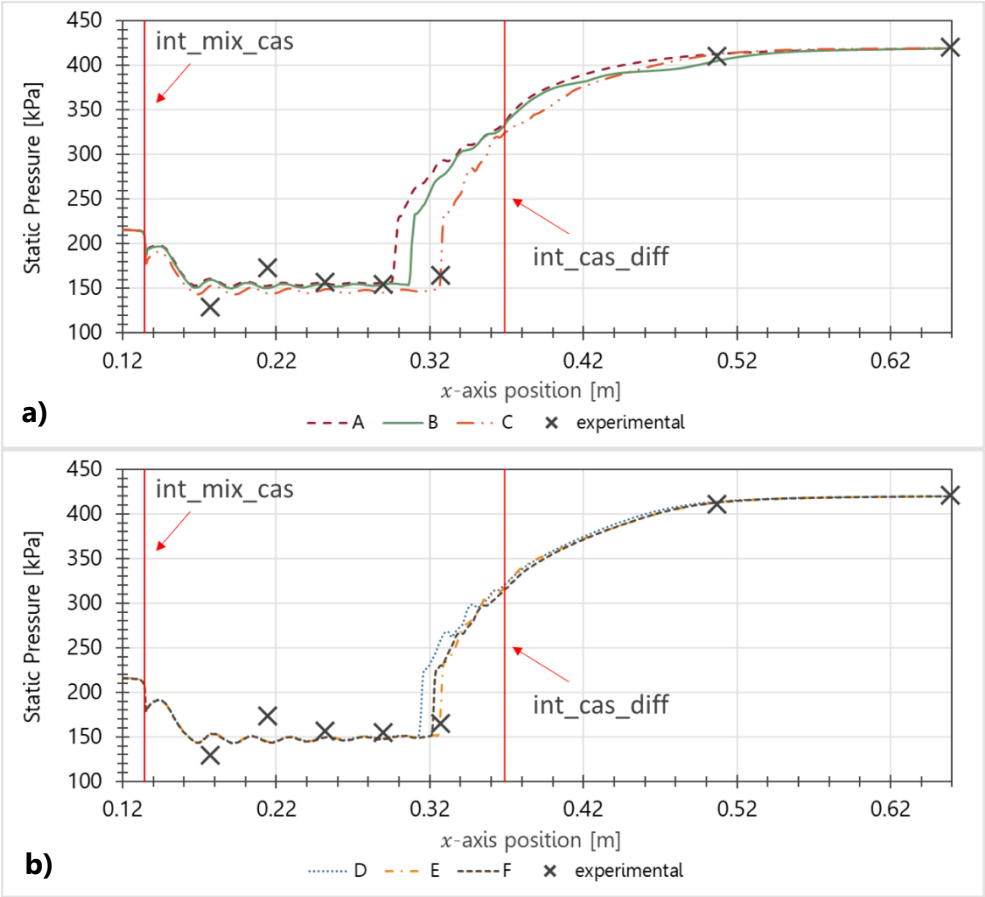


Figure 4.28 – Predicted static wall pressure using meshes a) A to C, and b) D to F vs experimental results for run 1.

Despite its accuracy, mesh E presented convergence difficulties for other operating conditions due to its density and computational requirements. Based on these results, Mesh C was selected for model validation and the LES precursor RANS simulation. Mesh C provided an optimal balance between computational efficiency and simulation accuracy, making it the most suitable choice for further analyses.

4.4.5.2 2D CO_2 Mesh Independence Study

The mesh sensitivity analysis was performed using experimental data, evaluating the influence of three key parameters: (1) radial division, (2) axial divisions, and (3) near-wall mesh sizing. The mesh independence assessment was based on variations in the predicted motive and entrained mass flow rates, ensuring that further refinements did not significantly impact the results.

To evaluate the impact of radial divisions (y-axis), four meshes were tested, ranging from $35x10^3$ to $107x10^3$ elements, while keeping the axial divisions constant. The primary mass flow rate was found to be insensitive to changes in the radial divisions. However, the secondary mass flow rate varied by up to -3.4% when comparing the coarsest and finest meshes. The mesh with $71x10^3$ elements, which showed only a 1% variation in the entrained mass flow rate, was selected as the baseline for further analysis.

The second phase of the analysis involved varying the number of axial divisions in the ejector from 50% to 150%, producing 10 different meshes. Both primary and secondary mass flow rates were influenced, with a maximum variability of 2%, as shown in Figure 4.29. It was observed that reducing the number of elements in the motive nozzle section led to an increase in the primary mass flow rate, which subsequently affected the entrained mass flow rate (Figure 4.30).

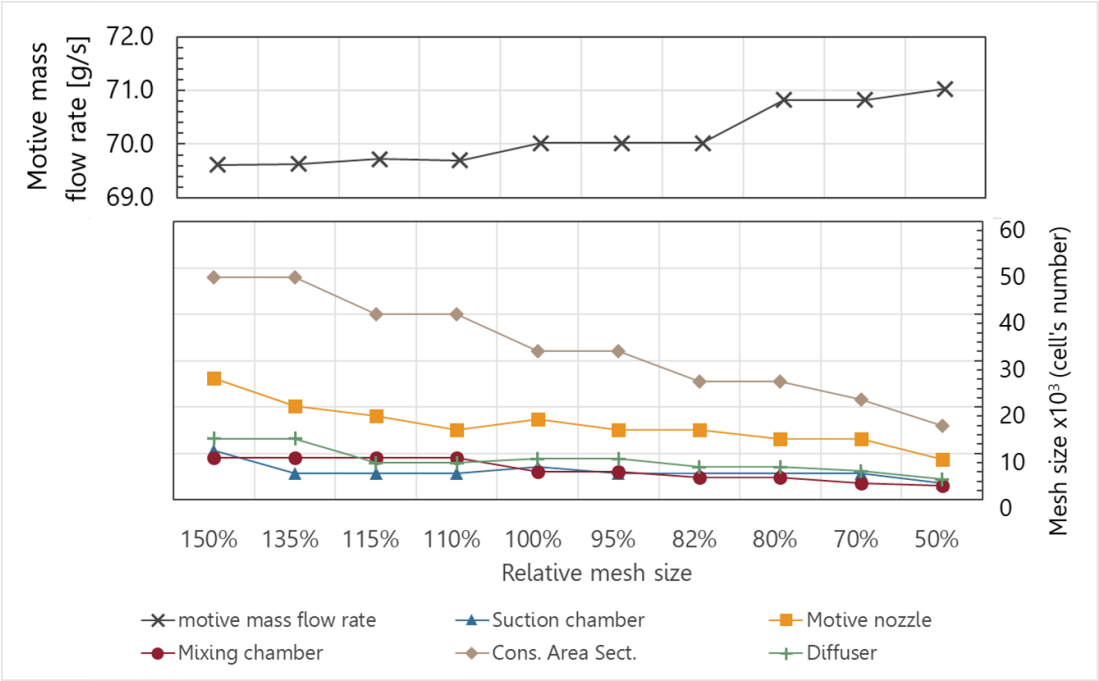


Figure 4.29 – Impact of mesh size on the ejector motive mass flow rate with varying axial divisions.

Reducing the number of axial divisions in the constant-area section led to a decrease in the entrained mass flow rate. However, this effect was primarily driven by variations in the primary mass flow rate rather than the mesh resolution in the constant-area section. The initial mesh size proved to be the most effective, showing minimal variability (approximately 0.5%) compared to the mesh with 150% more divisions. Additionally, it ensured faster convergence and reduced numerical instability during calculations.

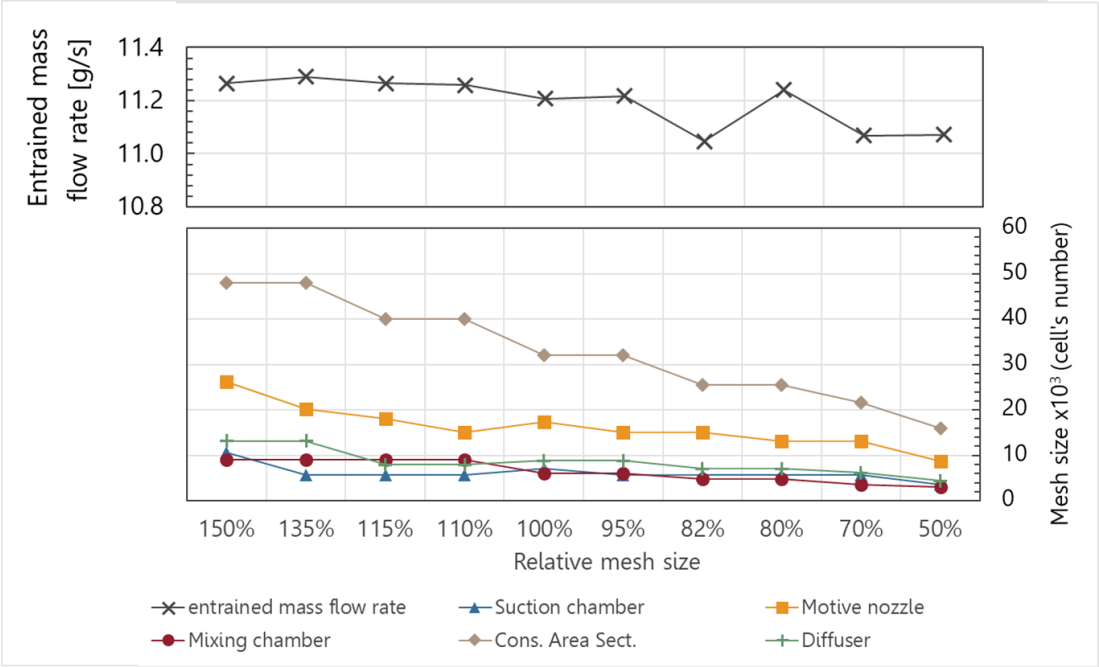


Figure 4.30 – Impact of mesh size on the ejector entrained mass flow rate with varying axial divisions.

A detailed study of the near-wall resolution (y^+) was performed by adjusting the cell height near the walls. The aim was to lower the y^+ values to comply with the SST k-ω turbulence model requirements ($y^+ \leq 1$), as recommended, while preserving overall mesh quality and cell count. In the primary nozzle, the y^+ value was reduced from 53 to 2, resulting in a negligible impact on the primary mass flow rate (0.03%). In the mixing and constant area sections, y^+ values were lowered from 20 and 15 to 1 and 3, respectively, leading to a 2.32% variation in the secondary mass flow rate. However, achieving y^+ values close to 1 proved challenging and led to prolonged convergence times and occasional failure to meet convergence criteria at different operating points. Consequently, a mesh with slightly higher y^+ values was selected, offering faster convergence, greater numerical stability, and keeping reliable simulation results.

4.4.5.3 3D CO_2 Mesh Independence Study

As outlined in Section 4.1.3, the simulation domain represents only half of the ejector geometry. The mesh independence study was conducted using the same operating conditions from the 2D mesh independence study. Meshes with cell counts ranging from 462×10^3 to $3\,498 \times 10^3$ were tested, labelled A to I in order of increasing refinement. Table 4.7 summarises the key characteristics of these meshes. To enhance local mesh refinement, four distinct bodies of influence (BOI), labelled A to D, were defined, as illustrated in Figure 4.18.

Except for Mesh A, all other meshes applied a target cell size of 0.60 mm and 0.05 mm for the motive nozzle's convergent and divergent sections, respectively. Mesh A, however, had a target cell size of 0.60 mm for the convergent and 0.50 mm for the divergent section.

For the surface mesh size, all meshes—except Mesh A—used minimum and maximum sizes of 0.025 mm and 0.30 mm, respectively. Mesh A applied a minimum cell size of 0.075 mm and a maximum of 1.5 mm. Specific maximum cell sizes were assigned to

different ejector zones, ensuring that wall and internal surfaces received tailored refinement.

As previously explained, similar to the approach for the 3D mesh in the R1234ze(E) simulation, achieving y^+ values close to 1 proved computationally expensive. However, the near-wall turbulence model employed ensures reliable results with the y^+ values achieved, minimising the need for excessive near-wall refinement.

Table 4.7 – Characteristics of the meshes tested for the 3D RANS CO_2 simulation.

Mesh	Cell count	BOI target size in mm			Boundary layer
		A+B	C	D	
A	461 884	-	-	-	BL1
B	923 523	-	-	-	BL2
C	1 074 172	0.15	-	-	BL2
D	1 450 823	0.05	-	-	BL3
E	1 584 124	0.05	0.035	0.10	BL3
F	1 845 467	0.05	-	-	BL2
G	1 869 582	0.05	0.030	0.10	BL3
H	2 329 087	0.05	0.030	0.10	BL3
I	3 498 288	0.025 (A) 0.05 (B)	0.030	0.10	BL4

Figure 4.31 illustrates the impact of mesh size on the motive ($\dot{m}_{\mathrm{pr}}$) and entrained ($\dot{m}_{\mathrm{sec}}$) mass flow rates. The differences between the maximum and minimum values are 0.5% for the motive flow and 3.9% for the entrained flow, suggesting that the mass flow rates are nearly independent of mesh resolution. Additionally, the difference in entrainment ratio remained below 4%.

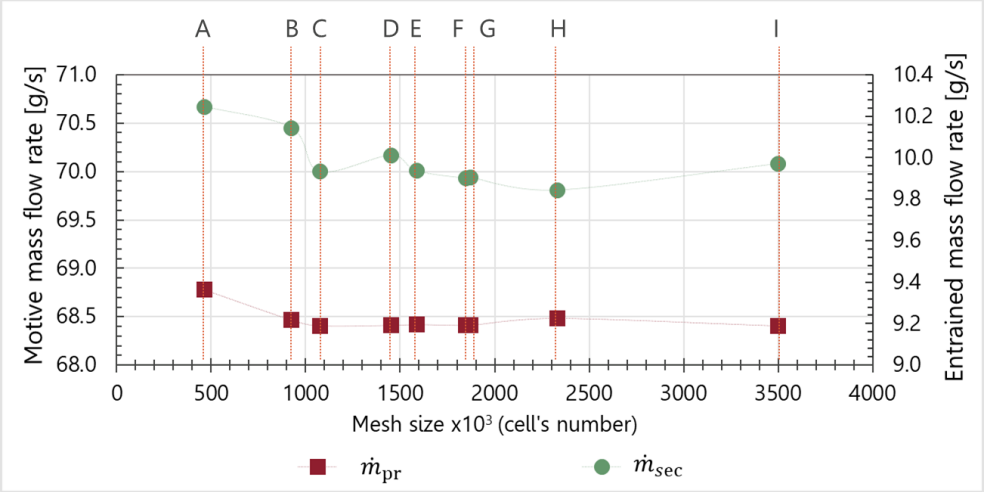


Figure 4.31 – Impact of the mesh size on the ejector inlet mass flow rates.

Figure 4.32 provides additional insights: panel (a) shows the motive mass flow rates, while panel (b) depicts the entrained mass flow rates, both with 1% error bars. The boundary layer resolution for each mesh is also identified, with BL1 corresponding to the highest y^+ values and BL4 the lowest.

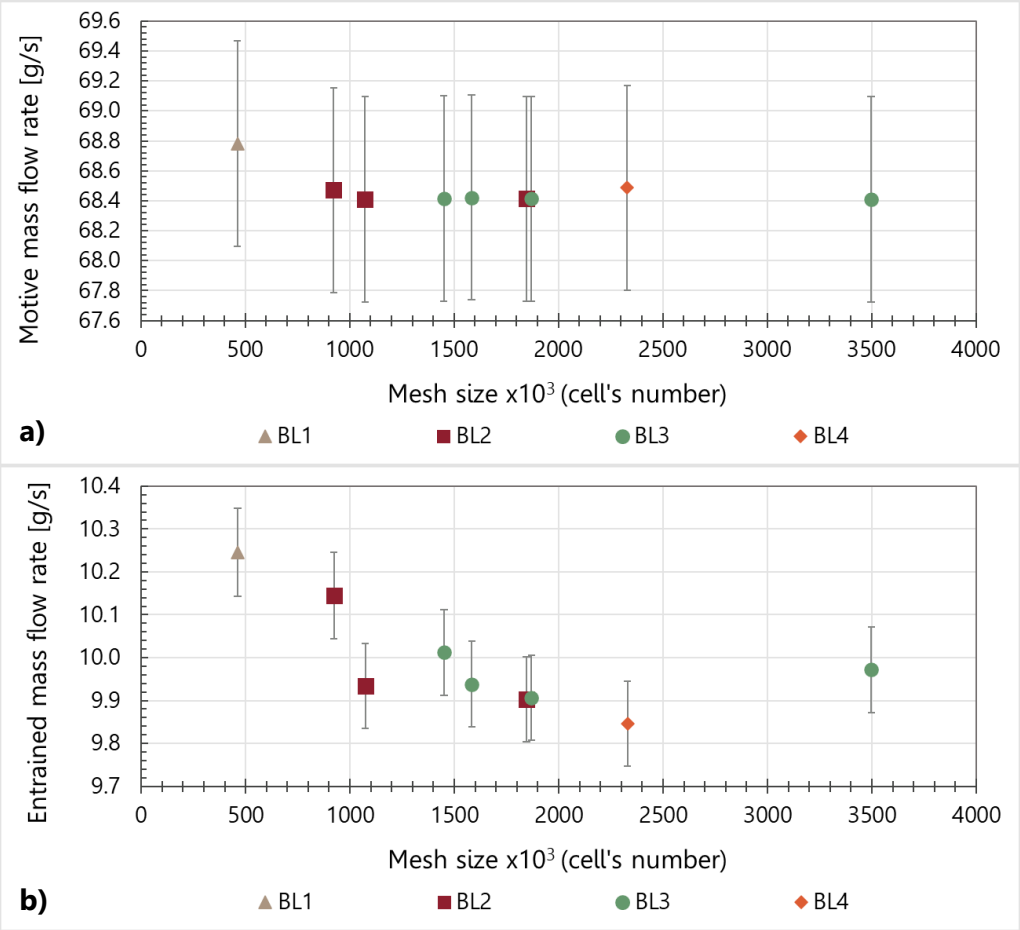


Figure 4.32 – Impact of the boundary layer resolution and mesh cell count on the ejector inlet mass flow rates.

Adding to the analysis of the data presented in Table 4.7, Figure 4.32b) reveals trends in the entrained flow rate associated with boundary layer resolution and local refinement. For BL2, an increase in the cell number correlates with a decrease in the entrained mass flow rate. This behaviour is influenced by the existence of the BOI, specifically the refinement near the motive jet at the primary nozzle exit. Similarly, for BL3, increasing the cell count also reduces the entrained mass flow rate; however, the refinement of BOI A (see Figure 4.18) resulted in a slight increase in the entrained flow rate.

For Mesh H, despite having the highest boundary layer resolution, the entrained mass flow rate remains within a 1% range of those observed for meshes E, F, and G. Furthermore, a comparison between meshes F and G indicates that the primary distinction lies in the boundary layer resolution, with Mesh G offering better detail. Nevertheless, the mass flow rate remains unchanged, suggesting diminishing returns on additional refinement in this context.

Since the experimental data used do not confirm a double-choke condition (details in Section 6.1), the static wall pressure predicted by the CFD model deviates significantly from the measured values. Therefore, rather than comparing the static wall pressure profile of the CFD with the experimental results, the static axial pressure profiles of the nine meshes were compared. These results are illustrated in Figure 4.33, where Figure 4.33a) presents data for meshes with BL1 and BL2, while Figure 4.33b) represents meshes with BL3 and BL4.

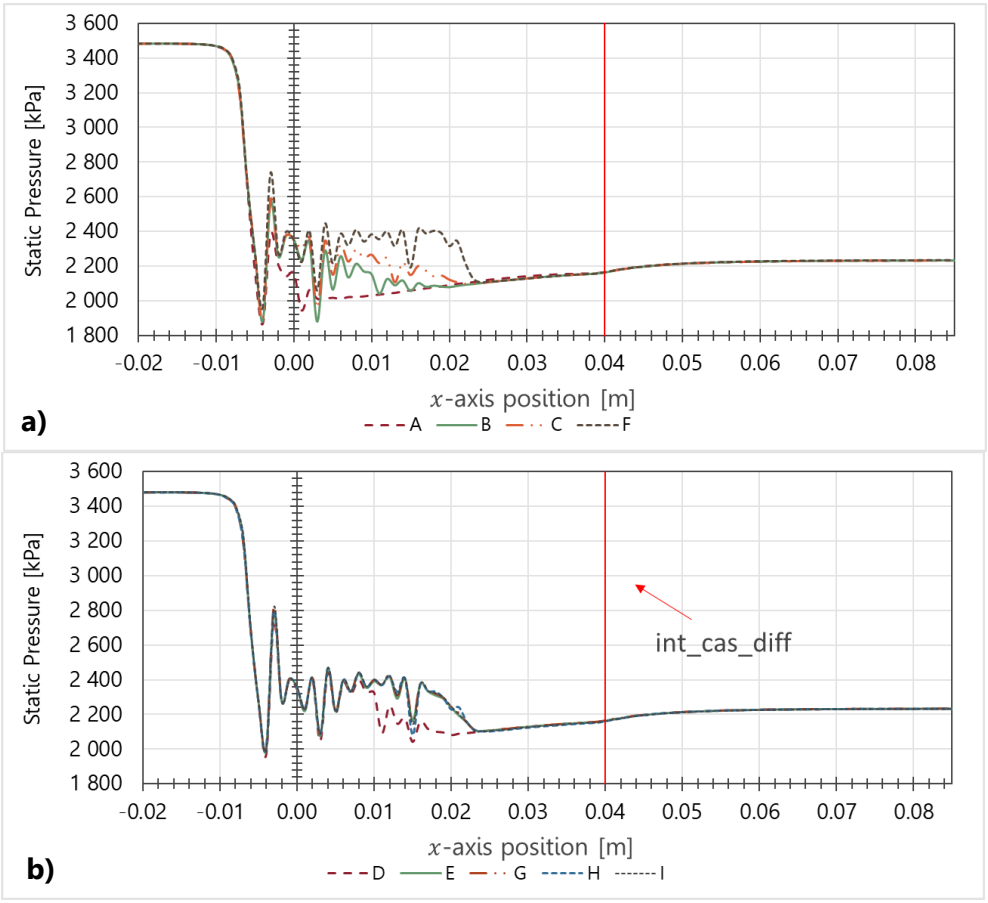


Figure 4.33 – Predicted static axial pressure profiles for a) meshes A, B, C, and F, and b) meshes D, E, G, H, and I.

In Figure 4.33a), it is evident that while the flow rate values align well, mesh A fails to capture the chain shock expected near the nozzle outlet, which is detected by the other meshes. In Figure 4.33b), despite having the same boundary layer resolution as meshes E, G, and I, mesh D exhibits a different pressure profile. This deviation shows the sensitivity of these details to the presence of the body of influence (BOI) near the nozzle outlet. Meshes E, G, H, and I show consistent pressure profiles. Since mesh E achieves similar accuracy to the more refined meshes while having a lower cell count, it is computationally less expensive, making it the preferred choice for further simulations.

4.5 Numerical considerations during the ELES ejector flow simulation

4.5.1 Numerical Methods and Time and Space Discretization for ELES

Table 4.8 presents the discretization scheme applied in the ELES. The pressure-based solver was selected for the flow solver algorithm, consistent with the justification presented in Section 4.4.1. SIMPLE algorithm was utilised as the iterative method due to its efficiency and ability to mitigate divergence issues during simulation.

As in the RANS simulations, gradients were evaluated using the Least-Squares Cell-Based method, and most variables were discretised using the Second-Order Upwind Scheme. However, the momentum equations required special consideration to ensure low numerical diffusion, a key requirement for ELES simulations (ANSYS Inc., 2015). Therefore,

the spatial discretisation for momentum was divided between the RANS and LES regions of the domain: the Second-Order Upwind Scheme was applied in the RANS region, while the Bounded Central-Differencing Scheme was used in the LES region to enhance accuracy and reduce numerical diffusion.

Table 4.8 – Discretization schemes used in the ELES.

Solver	Pressure-Based
Pressure-Velocity Coupling	
Scheme	SIMPLE
Spatial Discretization	
Gradient	Least Squares Cell Based
Pressure	Second Order
Density	Second Order Upwind
Momentum	RANS region: Second Order Upwind
	LES region: Bounded Central-Differencing
Turbulent Kinetic Energy	Second Order Upwind (only in RANS region)
Specific Dissipation Rate	Second Order Upwind (only in RANS region)
Energy	Second Order Upwind
Temporal Discretization	
Transient Formulation	Second Order Implicit

For temporal discretisation, the Second-Order Implicit Scheme was employed, maintaining a Courant number of 0.5 to balance computational stability and temporal resolution. For each time step, convergence was considered achieved when the relative residuals for momentum, energy, and turbulence equations fell below 10^{-6}, while for continuity, it was set at 10^{-4}. Results were recorded once a stable mass flow rate was achieved, ensuring the reliability of the simulation. Further details on the simulation results and their validation are discussed in Section 5.2.

4.5.2 ELES Mesh Assessment

To optimise the ELES, multiple candidates meshes were generated and evaluated to balance computational cost and accuracy. The precursor RANS simulation provided crucial insights, including the maximum characteristic cell dimension determined using equation (4.1). The final mesh selection was based on two main criteria: (1) the stability of the simulation during the initial iterations and (2) the time required to achieve stable mass flow rates. However, due to time constraints, it was not possible to exhaustively test all candidates meshes to fully assess convergence criteria or comprehensively evaluate the results.

The tested meshes ranged in size from 2 million to 5.97 million cells. Divergence issues encountered during preliminary tests necessitated adjustments to the boundary layer configuration in the LES zone, preventing adherence to the configuration proposed in Section 4.2.2.3. As a result, the boundary layer radial resolution was limited to 25 divisions (N_r). The final mesh consisted of approximately 4.07 million cells.

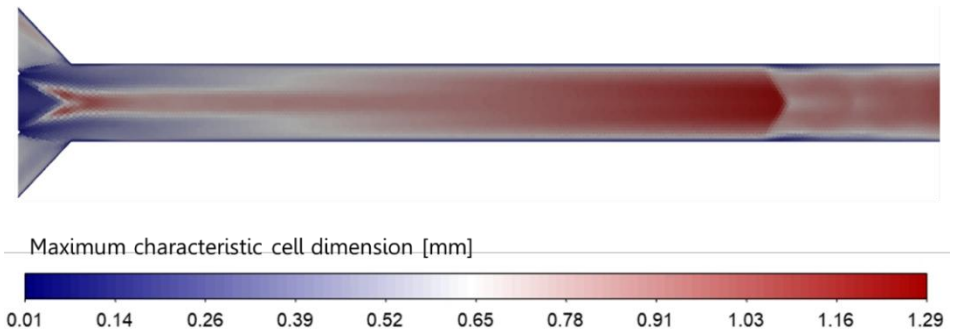


Figure 4.34 – Maximum characteristic cell size for LES mesh according to equation (4.1).

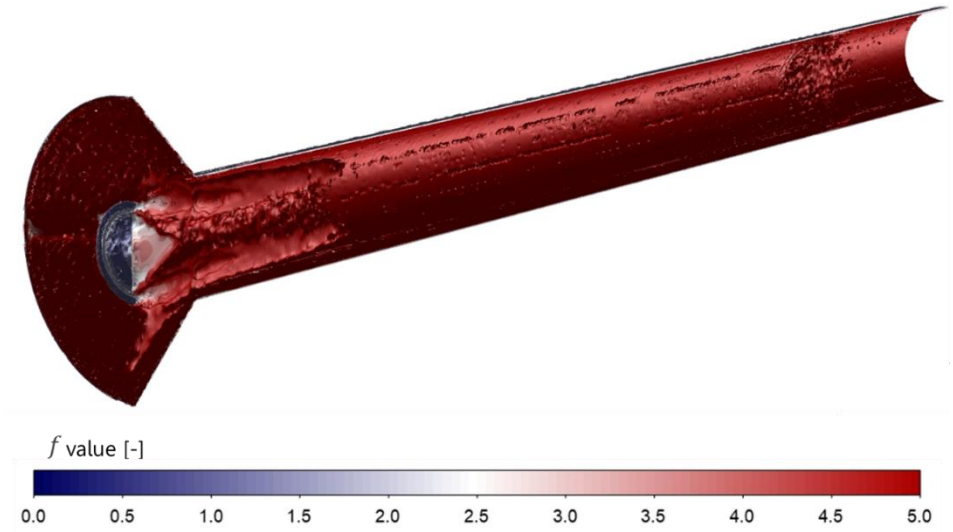


Figure 4.35 – Computed f-value distribution for the selected LES region of the ELES mesh.

An analysis of the f-value distribution, shown in Figure 4.35, highlights areas where further refinement would be beneficial. These include zones with high flow gradients, such as the mixing chamber, nozzle exit surface, primary jet, and near-wall regions. However, computational resource limitations restricted additional refinement in these areas. Despite this, most f-values were close to the target value of 5, suggesting that the selected mesh strikes a reasonable balance between the desired level of refinement and available resources.

While further refinement could enhance simulation accuracy, the selected mesh represents the optimal configuration achievable under the constraints of this study. Future work should prioritise refining the mesh in critical regions, such as the mixing chamber and nozzle exit, to better resolve turbulence and shock interactions. These improvements would likely increase the accuracy of flow predictions, particularly in areas critical to ejector performance.

Chapter 5

Turbulence is the graveyard of theories.

Hans W. Liepmann (1997)

R1234ze(E) ejector simulation results and discussion

This chapter presents the results of the single-phase ejector flow simulations. R1234ze(E) was considered a working fluid in all simulations. First, the RANS simulation results are validated using experimental data, followed by the discussion of the results using embedded large eddy simulations (ELES). Finally, the results obtained using the two modelling approaches are then compared and conclusions are taken.

5.1 Experimental Validation of the RANS CFD Model

The R1234ze(E) ejector flow simulations using the RANS model were conducted in a 3D domain representing half of the ejector, with details of the numerical mesh are provided in Section 4.2.1. Validation was performed using experimental data published by Kracik et al. (2018). The test rig, illustrated in Figure 5.1, was equipped with temperature sensors (denoted as T) and pressure transducers (denoted as p) strategically placed at critical locations, with a photograph of the test rig also included. Static pressure was measured using transducers with an accuracy of ±0.25%, while temperatures were recorded using RTDs. Mass flow rates were measured with Coriolis-type mass flow meters (FM in Figure 5.1), providing an accuracy of ±0.15%. During each experimental run, 100 readings were taken at a frequency of one per second under steady-state conditions, and the results were averaged for analysis. Additional details on the experimental methodology can be found in Appendix D.1, with further information available in Śmierciew et al. (2017).

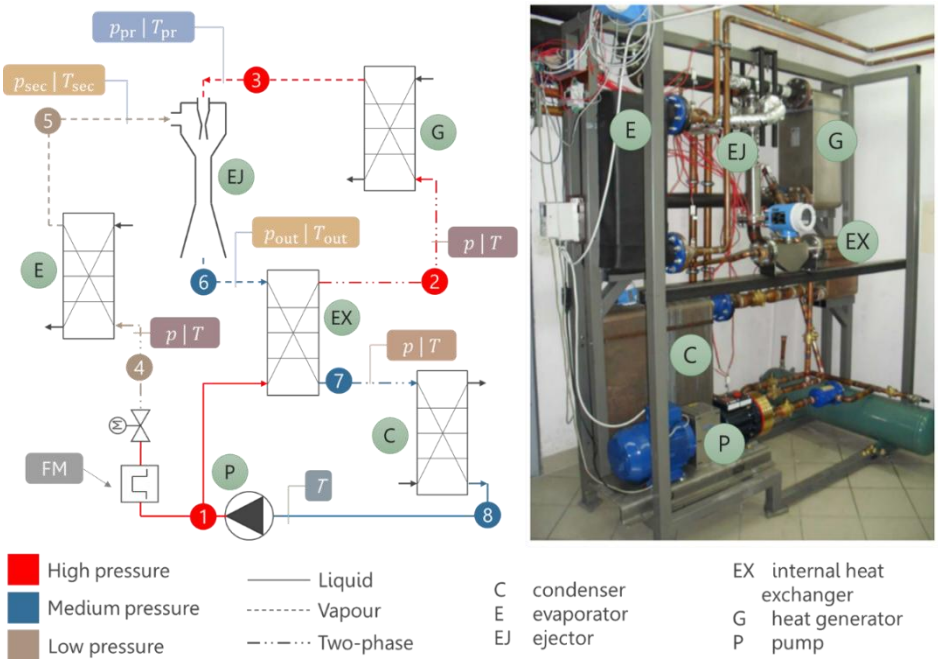


Figure 5.1 – Simplified diagram (left) and photo of the experimental rig (right) (Kracik et al., 2018).

Seven RANS simulations (run 1-7) were performed with the CFD model described in Section 3.3, considering single-phase flow without additional source terms in the turbulent kinetic energy transport equation. The boundary conditions, including predefined pressure and temperature at the ejector inlets and a specified outlet pressure, were selected based on the experimentally measured data by Kracik et al. (2018) and are summarised in Table 5.1. The RANS model was validated by comparing the computed motive and secondary mass flow rates, as well as the wall static pressures distributions, against experimental measurements.

Table 5.1 – Boundary conditions for the different RANS simulations.

Run	p_{pr} [kPa]	T_{pr} [K]	p_{sec} [kPa]	T_{sec} [K]	p_{out} [kPa]
1	1 174	338.3	215.9	278.9	419.6
2	1 180	335.1	210.4	284.0	479.3
3	1 170	335.5	203.4	281.8	503.3
4	1 165	337.2	207.2	279.5	508.5
5	1 179	338.1	255.5	283.4	541.3
6	1 182	338.2	265.3	284.1	551.5
7	1 205	341.7	320.0	284.9	611.5

The results for the primary mass flow rate ($\dot{m}_{\mathrm{pr}}$) are shown in Table 5.2. Due to the relatively small variation in the primary inlet conditions, the experimentally observed motive mass flow rates exhibited a deviation of 2.1%. The RANS simulations reflected a similar trend. As shown in Table 5.2, the computed values closely matched the experimental data, with maximum and average relative errors ($\delta_{\dot{m}_{\mathrm{pr}}}$) of 4.3% and 3.5%, respectively. Although the model exhibited a slight underprediction of $\dot{m}_{\mathrm{pr}}$, there results confirm that the RANS approach provides a reliable representation of the motive mass flow.

The predictions for the entrained mass flow rate ($\dot{m}_{\mathrm{sec}}$) are also shown in Table 5.2. while Runs 1 and 2 exhibited reasonable agreement with experimental data, significant discrepancies were observed in Runs 3 to 7. Previous validation studies indicate that secondary mass flow rates are generally predicted with lower accuracy than primary mass flow rates. For instance, Palacz et al. (2015) and Smolka et al. (2013) reported errors ranging from 20% to 40% in similar simulations. Moreover, the prediction error ($\delta_{\dot{m}_{\mathrm{sec}}}$) can be substantially higher when the ejector operates in single choking regime (Kracik et al., 2018). In the present study, the increased deviation in Runs 3 to 7 suggests that the model struggles to accurately capture the complex flow behaviour in these conditions.

Table 5.2 – Motive and entrained mass flow rate in g/s – experimental data vs CFD results.

Run	$\dot{m}_{\mathrm{pr-exp}}$ [g/s]	$\dot{m}_{\mathrm{pr-RANS}}$ [g/s]	$\delta_{\dot{m}_{\mathrm{pr}}}$	$\dot{m}_{\mathrm{sec-exp}}$ [g/s]	$\dot{m}_{\mathrm{sec-RANS}}$ [g/s]	$\delta_{\dot{m}_{\mathrm{sec}}}$
1	486	469	-3.4%	118	138	17.2%
2	493	472	-4.3%	118	134	13.6%
3	488	471	-3.5%	116	37	-68.2%
4	483	467	-3.4%	116	28	-76.1%
5	488	472	-3.3%	81	27	-67.0%
6	489	473	-3.3%	73	18	-75.3%
7	495	479	-3.3%	31	-25	-182.2%

For Runs 1 to 4, the primary inlet pressure varied by only 1.3%, and the secondary inlet pressure by 5.8%, both relatively small differences compared to the 17.5% variation in outlet pressure. While the experimental mass flow rates for these runs showed small variations, the CFD results consistently underpredicted the entrained mass flow rate by approximately 70% for Runs 3 and 4. This discrepancy suggests an underprediction of the critical back pressure by the RANS model.

The variation in the flow boundary conditions across runs leads to distinct flow regimes and variations in the relationship between motive and secondary flows, complicating the construction of a consistent performance curve that accurately represents the ejector's behaviour. Figure 5.2 approximates the ejector's operational curve by plotting the entrainment ratio (λ) against outlet pressure for both experimental and CFD results. However, differences in boundary conditions between runs make direct comparations challenging. The CFD results indicate that only Runs 1 and 2 operate in a double-choking regime, while the remaining runs likely involve single-choke operation. This conclusion is supported by the significant drop in λ observed in the CFD result for Run 3 where the predicted entrainment ratio is approximately one-quarter of the experimentally measured value. The underprediction of the critical back pressure in the simulations contributes to discrepancies in entrained flow rates, as single-choke operation is less accurately captured by the RANS model.

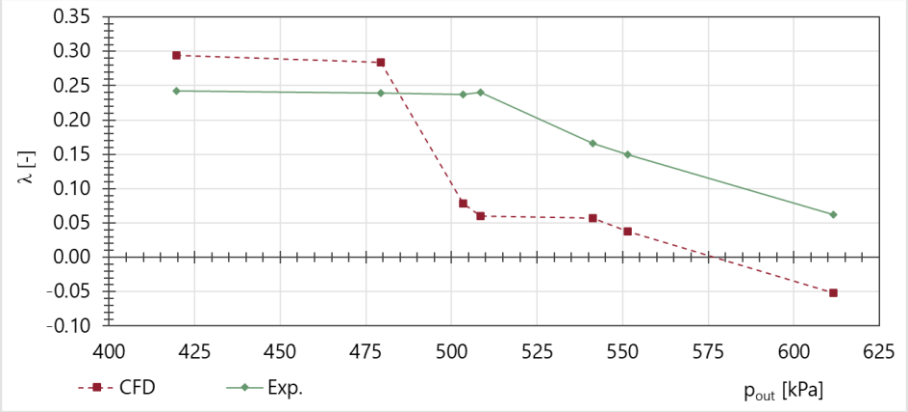


Figure 5.2 – The ejector entrainment ratio (λ) vs. outlet pressure for experimental data and CFD results (note: boundary conditions vary across runs).

The simulated pressure profiles along the ejector wall are shown in Figures 5.3 to 5.9. The axial location of each pressure transducer is described in Chapter 4, Figure 4.1. The dimensionless axial position (x/L) is defined as the ratio between the relative distance from the constant area section inlet (x=0) and the constant-area section length (L).

The results indicate that the CFD simulations overestimated the wall static pressure in the constant-area section but showed excellent agreement with the experimental data in the diffuser, particularly for pressure recovery. For sensor 6 (x/L=1.59), the maximum error for all runs was within 2%. Among the analysed cases, Run 1 exhibited the closest agreement between CFD predictions and experimental results, reflecting the model's higher accuracy under these specific conditions.

A closer analysis of the pressure profile for Run 1 (Figure 5.3), at the beginning of the mixing process, between x/L=0.18 and 0.34, the RANS model does not accurately simulate the oblique shock structure. At x/L=0.18, the model underestimates the shock intensity, resulting in an error of 24% for the wall static pressure, while at x/L=0.34, the overestimation is about 13%. These results reinforce the limitations of the RANS

turbulence model in accurately simulating the local flow structure, which is important for understanding the mixing process in ejector flow.

Further downstream, between x/L=0.50 and 0.66, with the absence of strong shock waves, RANS model performs well, with pressure prediction errors less than 1%. However, at x/L=0.82, the prediction error for the wall static pressure was as high as 49.3%. This result indicates a critical shortcoming of the RANS models in predicting the supersonic-to-subsonic transition, as the simulation foresees the final shock more upstream than it was observed experimentally. This discrepancy is likely due to the model's inability to resolve fine-scale turbulence and complex interactions between the shock and the boundary layer (Pope, 2000).

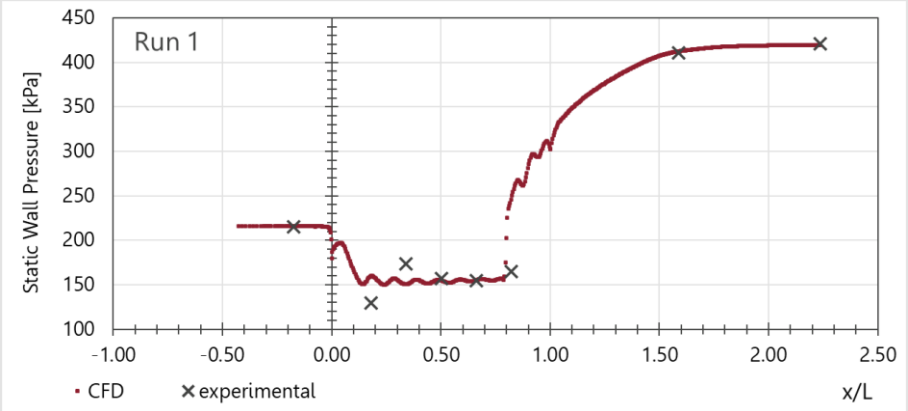


Figure 5.3 – Experimental wall pressure profile and CFD RANS results for Run 1.

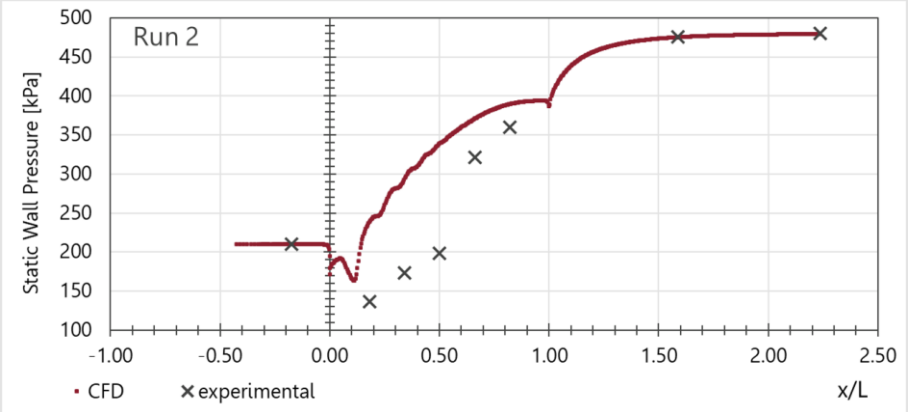


Figure 5.4 – Experimental wall pressure profile and CFD RANS results for Run 2.

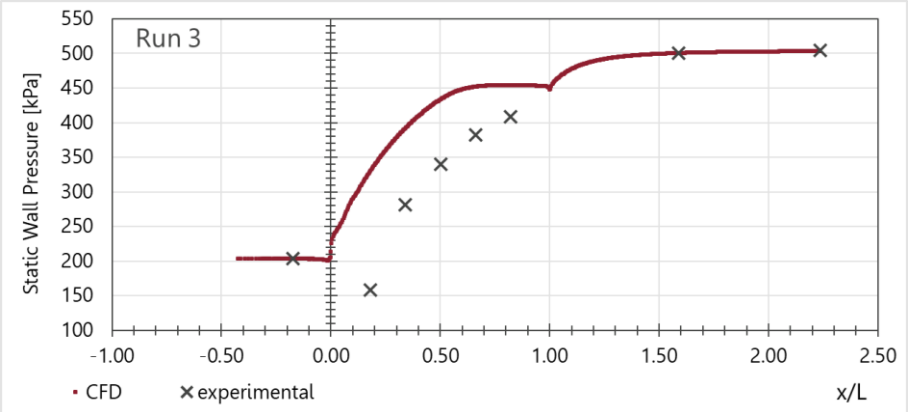


Figure 5.5 – Experimental wall pressure profile and CFD RANS results for Run 3.

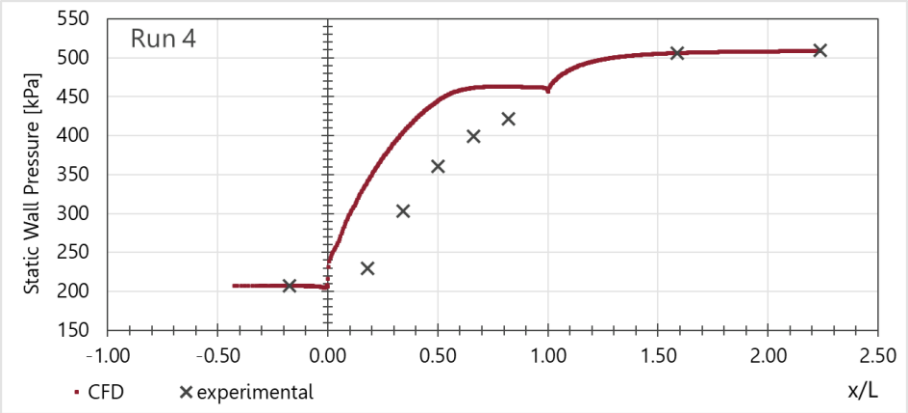


Figure 5.6 – Experimental wall pressure profile and CFD RANS results for Run 4.

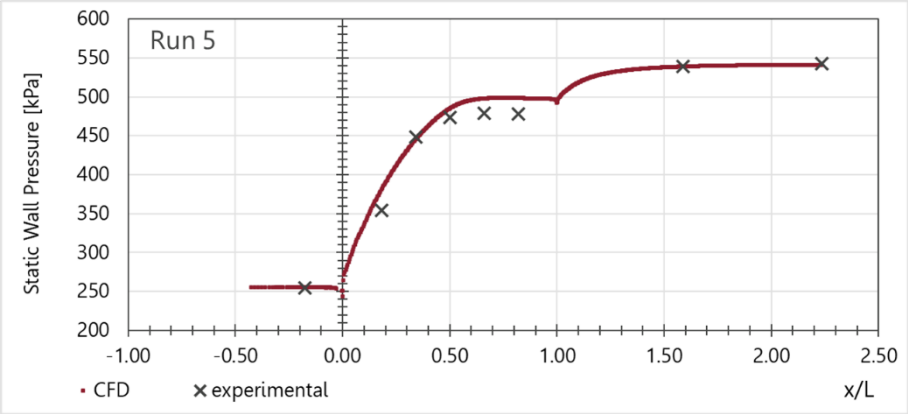


Figure 5.7 – Experimental wall pressure profile and CFD RANS results for Run 5.

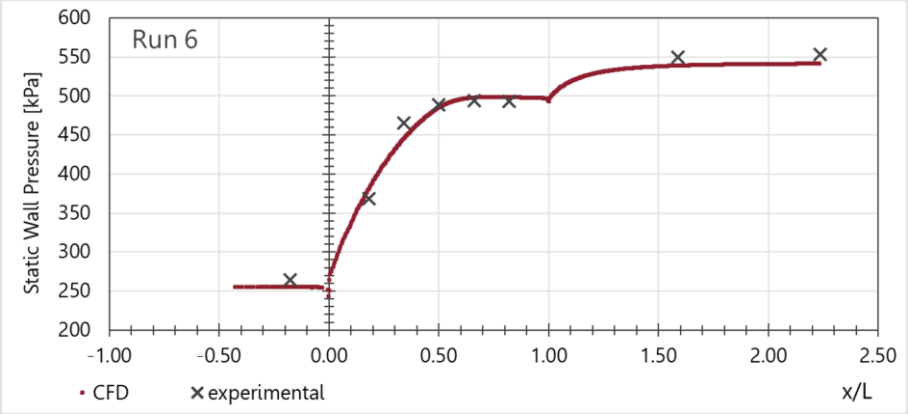


Figure 5.8 – Experimental wall pressure profile and CFD RANS results for Run 6.

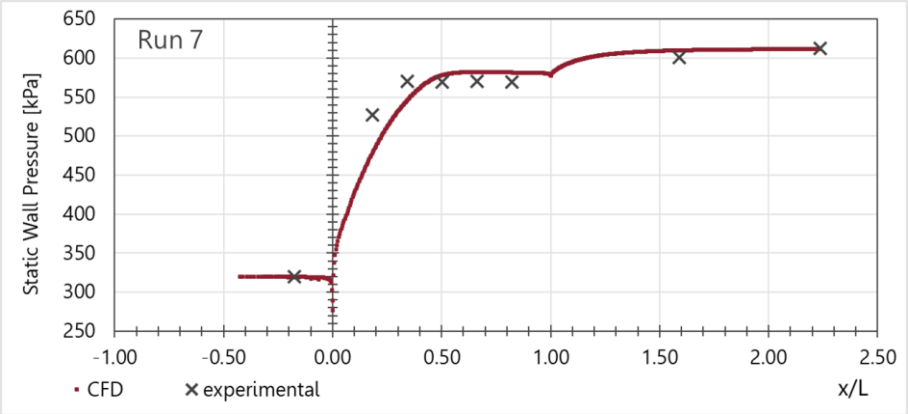


Figure 5.9 – Experimental wall pressure profile and CFD RANS results for Run 7.

During the experiments, the temperature was measured at seven axial positions inside the ejector; however, the radial position of the measurement points is not known. The experimental data were compared to the mass-weighted averaged, maximum and minimum simulated temperatures for each axial position, where the sensors were located to address this uncertainty. The results are shown in Figures 5.10 to 5.16.

The RANS model generally overestimated the temperature for most RTD locations across all experimental runs. However, distinct trends emerge depending on the operational regime. For Run 1, the simulated temperature profile underestimated the experimental measurements in the constant-area section, while in the diffuser and at the ejector outlet, the measured temperatures fell within the range of simulated values, as shown in Figure 5.10. In contrast, for Runs 2, 3, and 4, the model consistently overpredicted the temperature (Figures 5.11 to 5.13) and the wall static pressure (Figures 5.4 to 5.6). The RANS simulation exhibited significant improvement in temperature and pressure predictions for Runs 5, 6, and 7, where the results closely matched the experimental data. Further analysis suggests that Runs 3 to 7 correspond to a single-choke regime, as indicated by the lower motive mass flow rates compared to the maximum values observed in Runs 1 and 2 (see Table 5.2).

In a single-choked ejector, the flow structure downstream of the primary nozzle exit is fundamentally different from that of a double-choked ejector. In this regime, only the motive flow reaches a critical state, while the entrained flow remains subsonic. This absence of fully developed shock trains within the constant-area section results in more gradual variations in flow properties such as pressure and velocity, leading to a smoother and more uniform flow profile. The absence of strong shock interactions reduces the compressibility effects and the associated challenges for turbulence modelling. Without the complexities introduced by shock-boundary layer interactions, the RANS model can more accurately predict the wall static pressure and temperature distributions. Moreover, the reduced entrained mass flow rate in a single-choked ejector also impacts the mixing layer development. Weaker interaction between the motive and entrained streams generates less turbulence, particularly in the constant-area section. This reduction in turbulence intensity further simplifies the flow, allowing the RANS model to perform better, which often fails in high-shear and high-turbulence regions (Wilcox, 2006). This behaviour contrasts sharply with double-choke regimes, such as in Run 1, where the flow exhibits a more complex structure. In these cases, the presence of strong interacting shock trains, high turbulence levels, and supersonic-to-subsonic transitions introduces boundary layer instabilities and shear-layer interactions, leading to greater discrepancies between CFD predictions and experimental results.

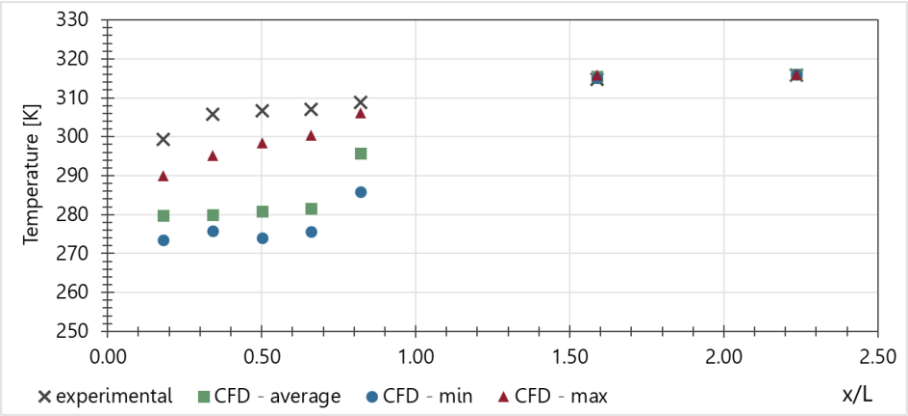


Figure 5.10 – Comparison of experimental and CFD temperature data obtained for Run 1.

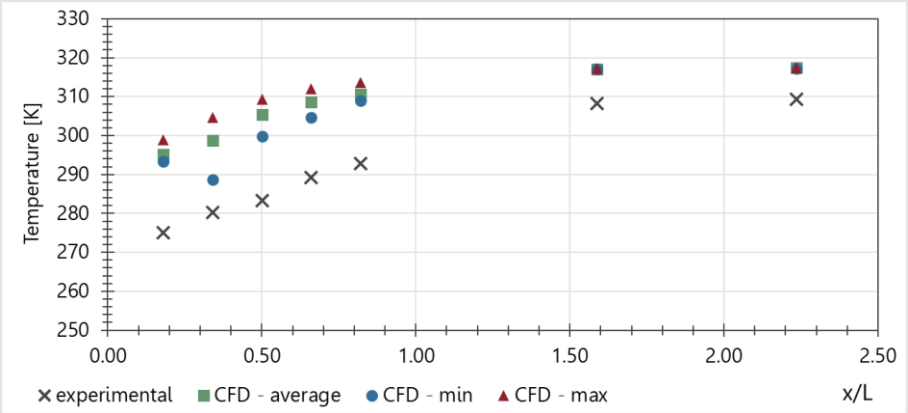


Figure 5.11 – Comparison of experimental and CFD temperature data obtained for Run 2.

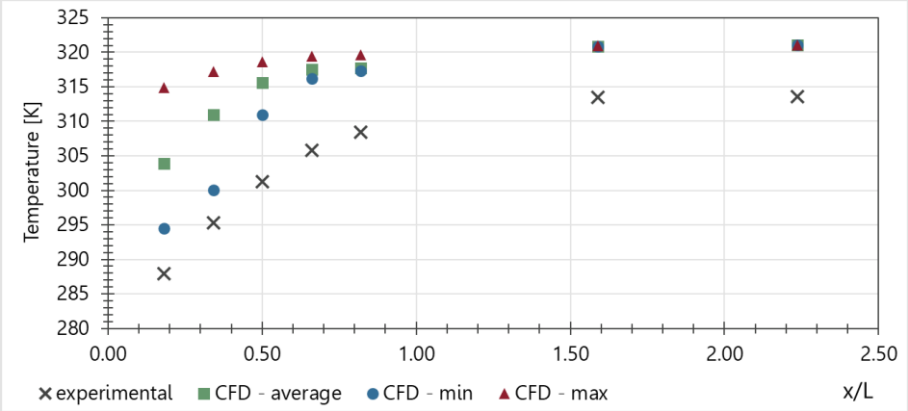


Figure 5.12 – Comparison of experimental and CFD temperature data obtained for Run 3.

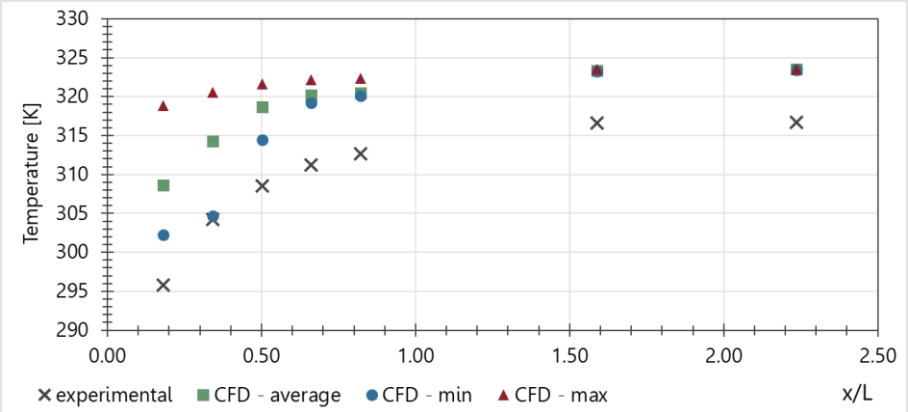


Figure 5.13 – Comparison of experimental and CFD temperature data obtained for Run 4.

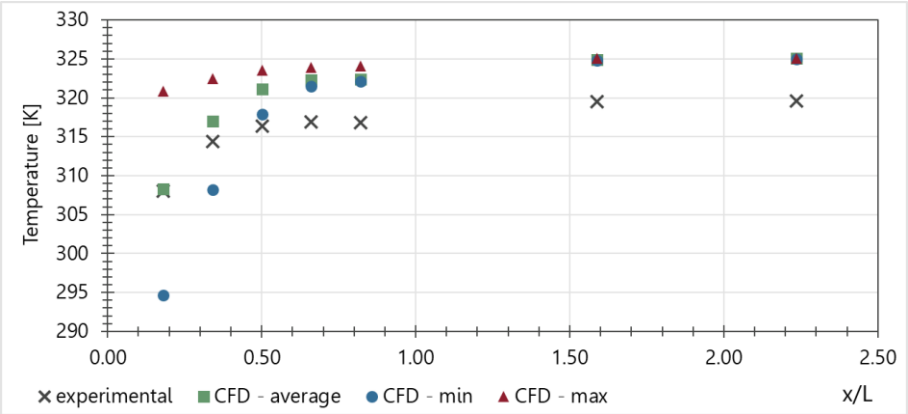


Figure 5.14 – Comparison of experimental and CFD temperature data obtained for Run 5.

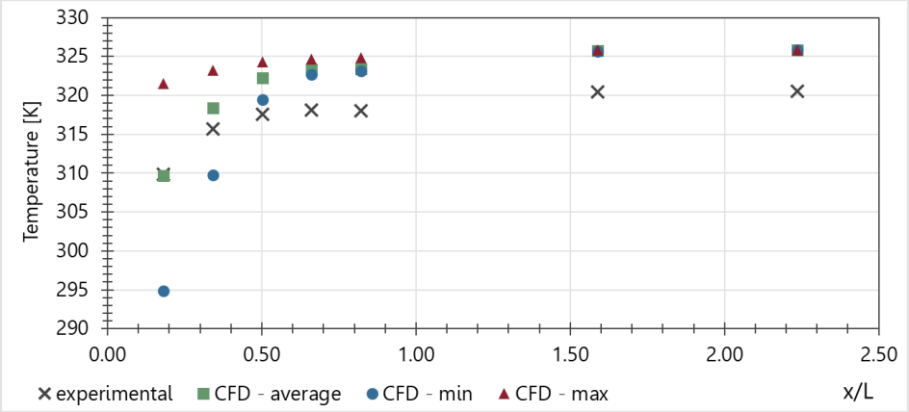


Figure 5.15 – Comparison of experimental and CFD temperature data obtained for Run 6.

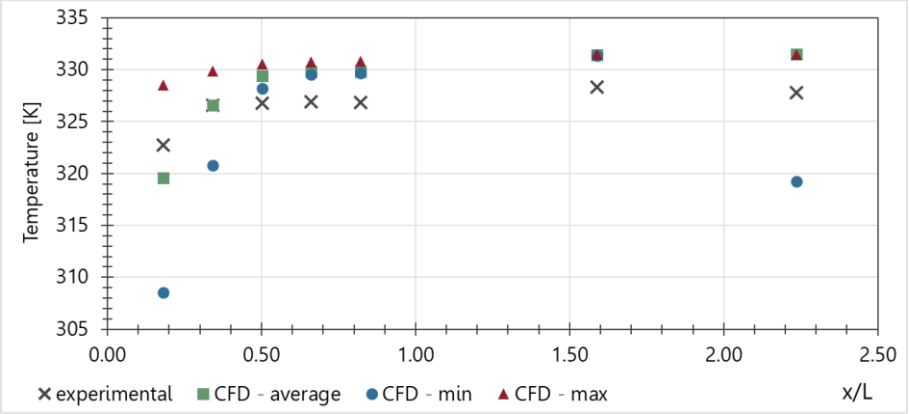


Figure 5.16 – Comparison of experimental and CFD temperature data obtained for Run 7.

The results from Runs 5, 6, and 7 underscore the limitations of the RANS approach in handling more complex flow regimes, such as double-choke operation, while demonstrating its effectiveness in simpler single-choke scenarios. In single-choke regimes, the absence of fully developed shock trains and reduced turbulence intensity allows the RANS model to deliver more accurate predictions for static wall pressure and temperature profiles. Conversely, for double-choke operation, as observed in Run 1, the intricate interplay of shock interactions, coupled with high levels of turbulence, exposes the inadequacies of the RANS model. Capturing these complexities requires more advanced turbulence modelling techniques, such as LES or hybrid RANS-LES.

It is also evident that while Run 1 is firmly in a double-choke regime, the other runs operate under varying flow conditions, potentially transitioning between single-choke and subcritical regimes. This variability complicates direct comparisons between experimental and simulated results, as the RANS model's predictive accuracy is highly sensitive to changes in Mach number, Reynolds number, and pressure ratios. Run 1 was selected as the baseline case for the subsequent ELES study because its flow dynamics distinctly demonstrate double-choke operation, characterized by supersonic flow in both the motive and secondary streams and a well-defined shock train structure. This makes it an ideal case for evaluating the enhanced predictive capabilities of ELES under complex flow conditions.

5.2 Results of the 3D Embedded LES

Figure 5.17 shows the 3D simulation domain for the LES region within the ELES model and the specific axial cross-sections analysed in detail. The full simulation domain is presented in Figure 4.4, while the axial positions of the pressure transducers and temperature sensors are detailed in Figure 4.1.

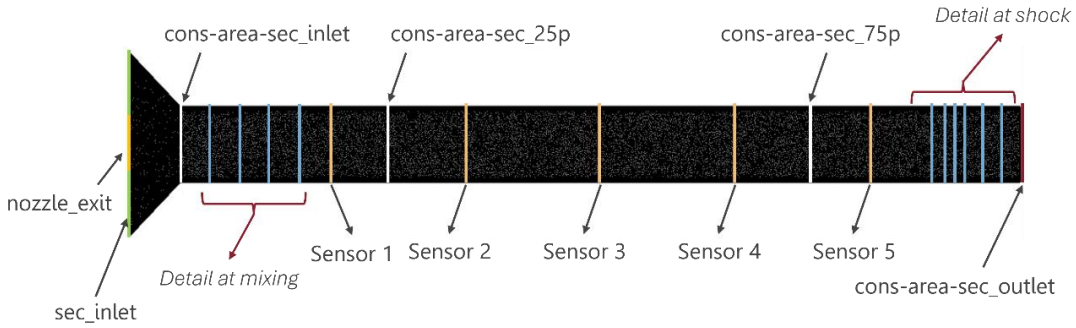


Figure 5.17 – Cross section view of the LES region in the 3D simulation domain with identification of the different sections for local result analysis.

Several time-consuming tests were carried out to find the most suitable combination of Courant number (C) and time step (Δt) to ensure numerical stability throughout the simulation. Based on these tests, a Courant number of 0.5 was selected, and the time step obtained from:

$$C = \frac{\overline{u}_{\mathrm{pr,RANS}} \cdot \Delta t}{\Delta_{cell}} \tag{5.1}$$

In this study, the cell length (Δ_{cell}) corresponds to the minimum mesh size, set at 0.5 mm. The velocity ($\overline{u}_{\mathrm{pr,RANS}}$=261 m/s) was defined as the mass-average velocity of the motive flow at the nozzle exit, as predicted by the RANS model. Based on these parameters, a time step size of 10^{-6} s was selected to satisfy the Courant number requirement. A detailed discussion of the test procedures to optimise these parameters is beyond the scope of this thesis. Instead, the focus is on the results obtained using the final optimised simulation setup.

As mentioned in Section 5.1, the boundary and initial conditions for the ELES simulations were derived from RANS model results. The nozzle exit plane, being an explicit interface between the RANS and LES region, was required for generating the perturbations necessary for inflow coupling. For this purpose, the Vortex Model was used. 596 vortices were introduced as a result of applying Equation (3.138). Figure 5.18 shows the evolution of the predicted mass flow rate with time. It can be seen that the calculated motive mass flow rate exhibited a transient behaviour during the early stages of the LES simulation. It took approximately 8×10^{-3} s for the amplitude of the oscillations to stabilise. Time-averaged properties were calculated after a stable mass flow rate was achieved.

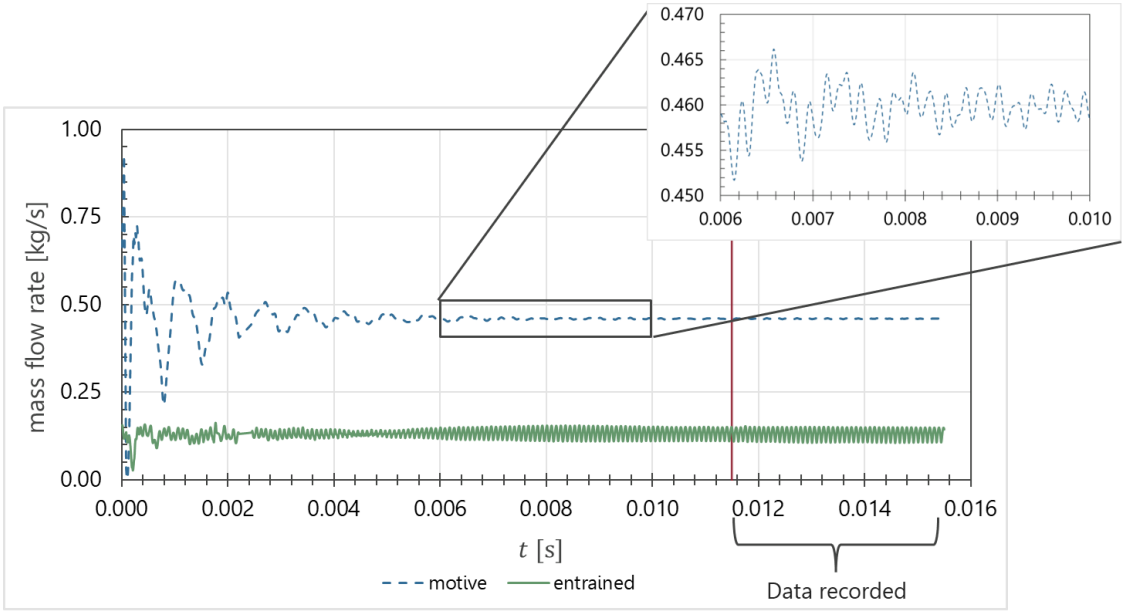


Figure 5.18 – Evolution of predicted mass flow rate over simulation time.

Data recording began at a flow time of 0.0115 seconds and concluded at 0.0155 seconds. The motive jet exited the primary nozzle with a mean axial velocity of 264 m/s. The total flow length, from the primary nozzle outlet to the constant-area section outlet, was 0.2345 m (L_{cas}). The characteristic flow-through time can be estimated from (Croquer et al., 2022):

$$t_{\mathrm{c}} = \frac{L_{\mathrm{cas}}}{\overline{u}_{\mathrm{pr,NXP}}} \tag{5.2}$$

In the simulated ejector t_{c} was estimated to be 8.9×10^{-4} s. Therefore, the time-averaged data is a result of approximately five flow-through cycles ($5t_{\mathrm{c}}$) in the LES domain. The simulation was performed on an HPC cluster, utilizing an average of four nodes, each with 16 cores. The exact CPU time required to obtain the results was not directly measured, the data recording process took approximately 41 days, with a total CPU runtime of around 145 days.

5.2.1 LES Mesh Validation: TKE Resolution

Before analysing the results from an LES simulation, it is necessary to verify the accuracy of the LES model by evaluating the turbulent kinetic energy (TKE) spectrum as a function of the wavenumber (κ), as defined in Equation (2.10). The total TKE (k) is expressed as:

$$k = k^{\mathrm{res}} + k^{\mathrm{SGS}} \tag{5.3}$$

In equation (5.3) k^{SGS} represents the subgrid scale TKE (see Equation (3.123)), and k^{res} denotes the resolved TKE, defined as:

$$k^{\mathrm{res}} = \frac{u_{\mathrm{RMS}}^2 + v_{\mathrm{RMS}}^2 + w_{\mathrm{RMS}}^2}{2} \tag{5.4}$$

The root-mean-square (RMS) axial velocity can be calculated from:

$$u_{\mathrm{RMS}} = \sqrt{\frac{1}{N} \cdot \sum_{i=1}^{N} (u_N - \overline{u})^2} \tag{5.5}$$

In equation (5.5), N represents the number of time instances. The root-mean-square velocities for the remaining velocity components in equation (5.4) can be calculated in a similar fashion.

Figure 5.19 illustrates the turbulent kinetic energy spectra at the central point (i.e., along the ejector axis, where r=0) for five different axial locations within the constant-area section of the ejector. The curves exhibit three distinct regions, identified based on significant changes in the slope of κ versus $E(\kappa)$. At approximately $\kappa \approx 10^4$, all the curves display a sudden increase in $E(\kappa)$. Up to this point, the eddies are anisotropic and predictable, representing scales that are not relevant for turbulence (Pope, 2000; Sengupta et al., 2024). Slightly beyond $\kappa \approx 10^5$, a sharp decline in $E(\kappa)$ is observed, more pronounced in some curves than in others. This decline is followed by a slope change, indicating that beyond this point, turbulence is predominantly modelled by the subgrid-scale (SGS) model. These observations suggests that the inertial subrange, for the five points analysed, lies within the range $10^4 < \kappa < 10^5$.

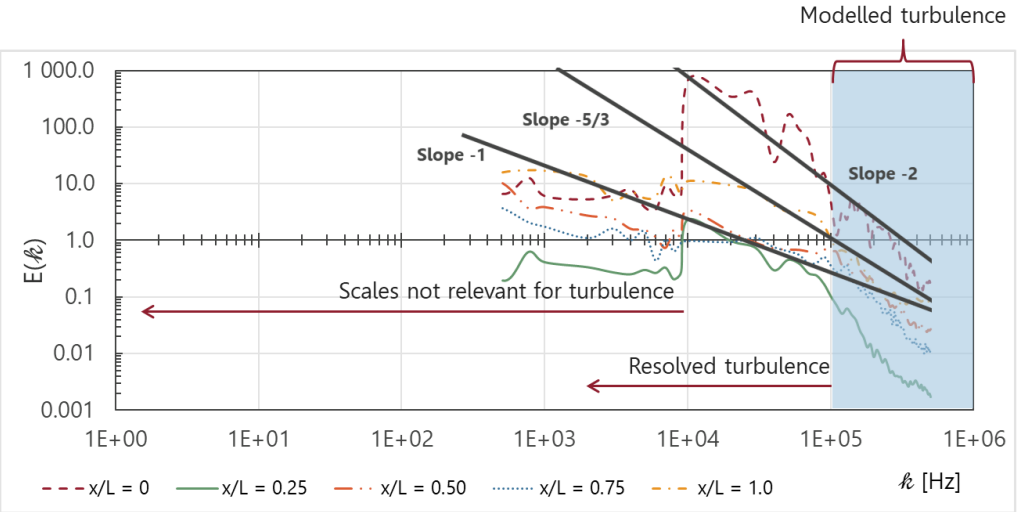


Figure 5.19 – Energy spectra of axial velocity fluctuations in the ejector axis for different x/L.

For incompressible flows, the slope of the energy spectrum in the inertial subrange is typically −5/3, as predicted by the Kolmogorov spectrum (Pope, 2000). However, in compressible supersonic flows, such as the one studied here, deviations occur due to alternative energy transfer mechanisms and the influence of shocks. These deviations remain less understood, as experimental data for such flows are limited, complicating the validation of theoretical models (Garnier et al., 2009; De Vanna et al., 2024).

In compressible flows, the kinetic energy spectrum is divided into dilatational and solenoidal components. The dilatational component generally exhibits a slope of −2 in the inertial subrange, reflecting the impact of compressibility. The solenoidal spectrum however, transitions through distinct phases depending on the flow dynamics (Garnier et al., 2009). In the quasi-supersonic phase, dominated by shock formation and interactions, the slope is approximately −2. Baroclinic vorticity production and mechanisms like vortex stretching and dilatation govern this phase. As shocks weaken in the post-supersonic phase, vortex interactions and the decay of vortical structures

dominate, leading to a slope closer to −1. Over time, the flow approaches a subsonic-like equilibrium state where shock effects diminish, and solenoidal dynamics decouple from compressible phenomena.

The reference slopes identified by Garnier et al. (2009) are indicated in Figure 5.19. Looking at the simulation results, the slope of the energy spectra curve is approximately −2 at the constant area section inlet (x/L=0), which is consistent with the dominant shock-driven dynamic disruption of the energy cascade for the solenoidal spectrum. Further downstream (x/L=0.75), the slope of the energy cascade is closer to −1, reflecting a shift to vortex-dominated dynamics and the decay of vortical structures. These results illustrate the interaction between shocks and vortices in shaping the energy spectrum at different ejector regions. While the spectral analysis helps to understand the flow dynamics, it is not suitable for evaluating mesh's capability to resolve the turbulent kinetic energy (TKE). In order to do that the percentage of resolved TKE ($\mathrm{TKE_{res}}$) was calculated using:

$$\mathrm{TKE_{res}} = \frac{k^{\mathrm{res}}}{k^{\mathrm{res}} + k^{\mathrm{SGS}}} \tag{5.6}$$

Figure 5.20 presents $\mathrm{TKE_{res}}$ for the mixing section of the ejector (x/L≤0), organised into three classes: $\mathrm{TKE_{res}}$ <40%, 40%<$\mathrm{TKE_{res}}$<80%, and $\mathrm{TKE_{res}}$ >80%. As expected, axial locations with resolved TKE below 40% are concentred near inlet boundaries, where flow variables resulted from RANS simulations. These findings suggest the need for mesh refinement in the mixing section and align with predictions based on the $\boldsymbol{f}$-value (see Figure 4.35). In contrast, for the constant area section (x/L>0), the resolved TKE consistently exceeded 80% across all analysed axial locations.

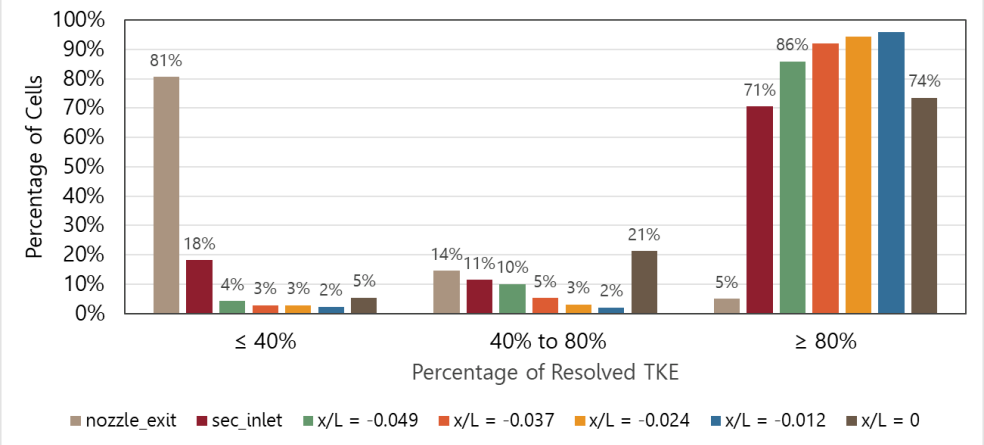


Figure 5.20 – Cell percentage vs resolved TKE for different axial locations in the ELES computational domain.

To better understand the potential for mesh refinement, Figure 5.21 shows a contour map of the percentage of resolved turbulent kinetic energy. White regions indicate areas where the resolved TKE is below 80%. It is evident from the figure that most of the ELES model in the ejector resulted in a TKE resolution of 80% or higher. The results also suggested that minor mesh refinement would be required in regions of elevated pressure gradients and near the centre line of the ejector. However, the primary aim of this study was to investigate the mixing process, and because of computational constraints, fewer cells were allocated near the axis. Future work will include additional simulations with improved mesh in these areas.

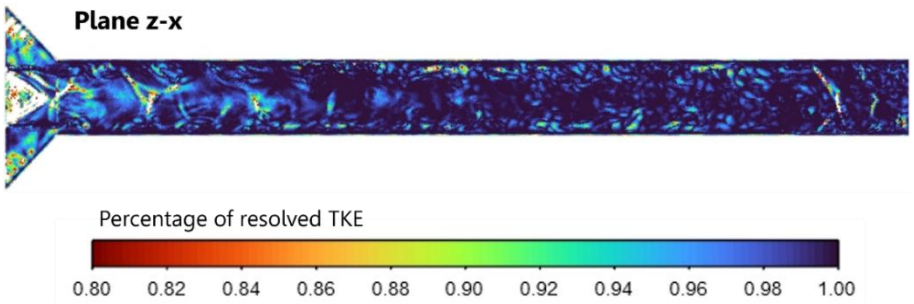


Figure 5.21 – Percentage of resolved turbulent kinetic energy in the LES section.

5.2.2 Discussion of the instantaneous flow field results

The results of the instantaneous flow field analysis were gathered for $t = 0.0155$ s, corresponding to a motive mass flow rate ($\dot{m}_{\mathrm{pr}}$) of 460.8 g/s, an entrained mass flow rate ($\dot{m}_{\mathrm{sec}}$) of 143.8 g/s, and an outflow of 620.9 g/s. The static pressure, temperature, and axial velocity fields for two streamwise planes are discussed, providing valuable insights into flow dynamics, including the development of mixing layers, shock interactions, and the transition from supersonic to subsonic regimes. Figure 5.22 shows the instantaneous static pressure field for the two streamwise planes. Both figures demonstrate a substantial degree of asymmetry in the static pressure distribution. Notably, beyond the axial position of sensor 3 (x/L>0.50), the pressure field becomes nearly homogeneous, which is frequently interpreted as the end of the mixing process (Zhdanov and Chorny, 2011; Zhu and Jiang, 2014).

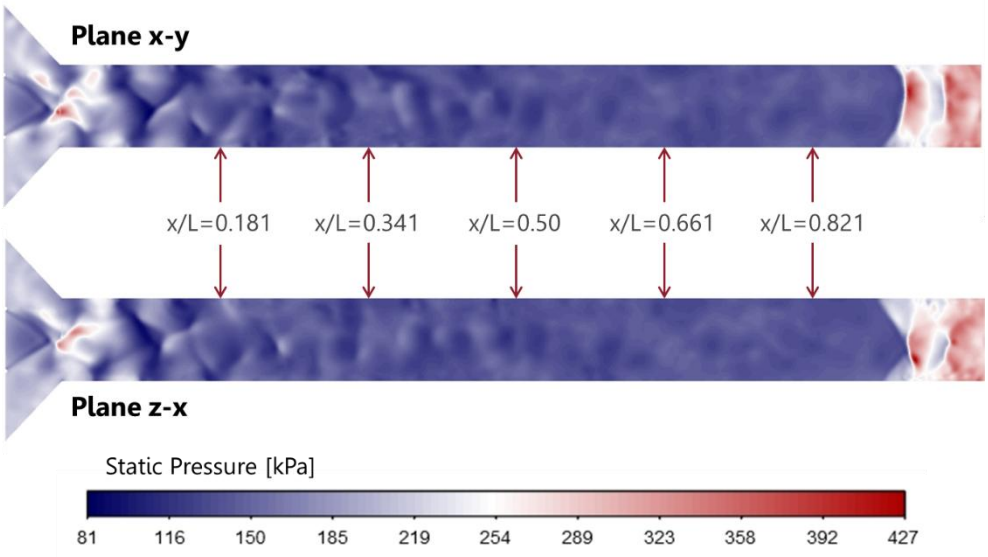


Figure 5.22 – Instantaneous static pressure field over two axial direction cross-section planes.

Figure 5.23 provides additional detail on the instantaneous static pressure distribution for two transversal planes in the constant-area section using the local pressure scale. It can be seen from the figure that a considerable variation of the static pressure was obtained for x/L=0, with higher pressures near the ejector axis. This is a result of the high-pressure motive stream exiting the nozzle, where the flow remains pressurized before undergoing expansion and mixing with the entrained flow. The pressure varied from about 140 kPa to 370 kPa. Further downstream, at x/L=0.50, the simulated pressure

distribution was much more uniform, ranging from 126 kPa to 156 kPa. This observation aligns well with the conclusions drawn from Figure 5.22.

It can also be observed in Figure 5.23 that, the pressure profile exhibits a certain degree of asymmetry, which was not predicted using the RANS model. However, for x/L≥0.50, after the shocks, the pressure variations within the section are relatively small. While the profile may not be fully symmetric, this asymmetry likely has minimal impact on the overall flow dynamics in this region.

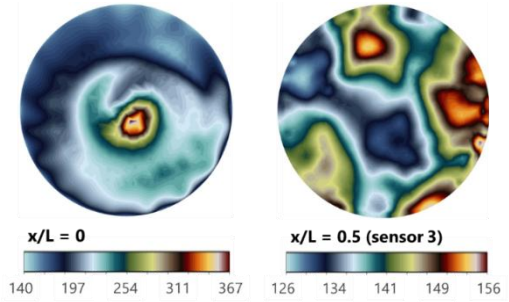


Figure 5.23 – Instantaneous static pressure field over two transversal planes within the constant-area section.

Figure 5.24 depict the static pressure variation within a cross section for different axial locations in the flow domain. It can be seen that the there is a considerable pressure variation near the entrance of the constant area section, the is due to the strong oblique shock waves resulting from the interaction of the primary and secondary streams. Further downstream, the shock waves diminish, and the mixing is completed. Near the entrance of the diffuser (x/L=0.92), the flow becomes subsonic, accompanied by a set of final shock waves, indicated by the larger pressure variations.

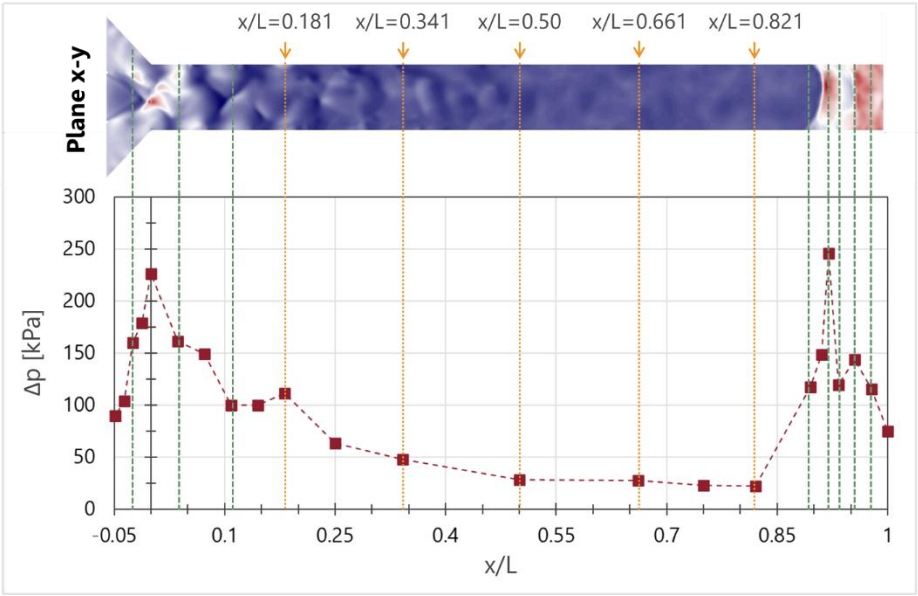


Figure 5.24 – Static pressure range at various sections represented in Figure 5.17.

Figure 5.25 presents the instantaneous static temperature field over two streamwise midspan planes, while Figure 5.26 shows the static temperature variation for different axial positions. The strong shock waves before the entrance of the constant area section (x/L<0), result in a significant temperature fluctuation. As the shock waves disappear further downstream, the temperature field becomes relatively uniform. At the second

shock, located at x/L=0.11, the minimum temperature increases significantly due to the compression effect, which reduces the temperature variation across the section and results in a smoother overall gradient downstream.

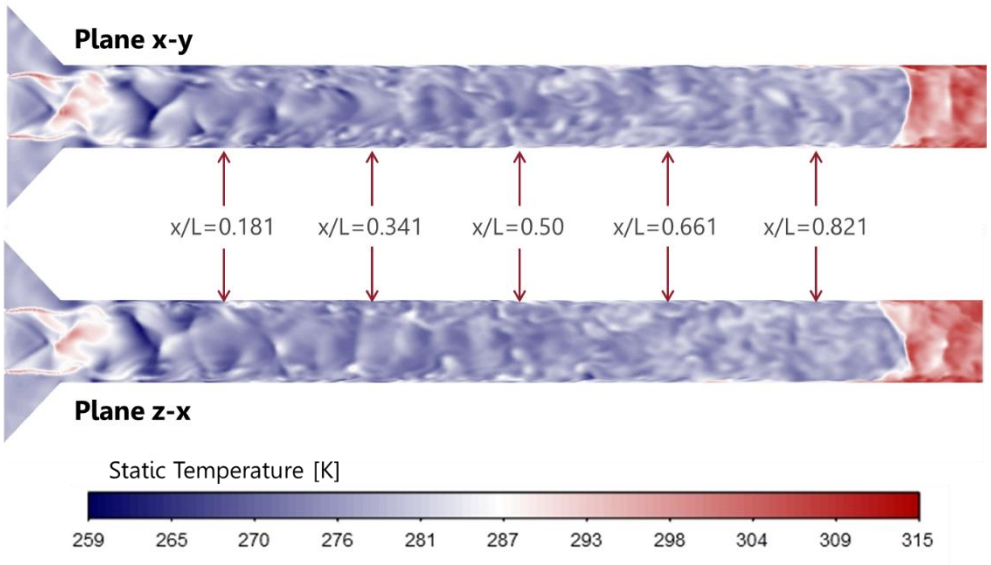


Figure 5.25 – Instantaneous static temperature field over two streamwise midspan plane.

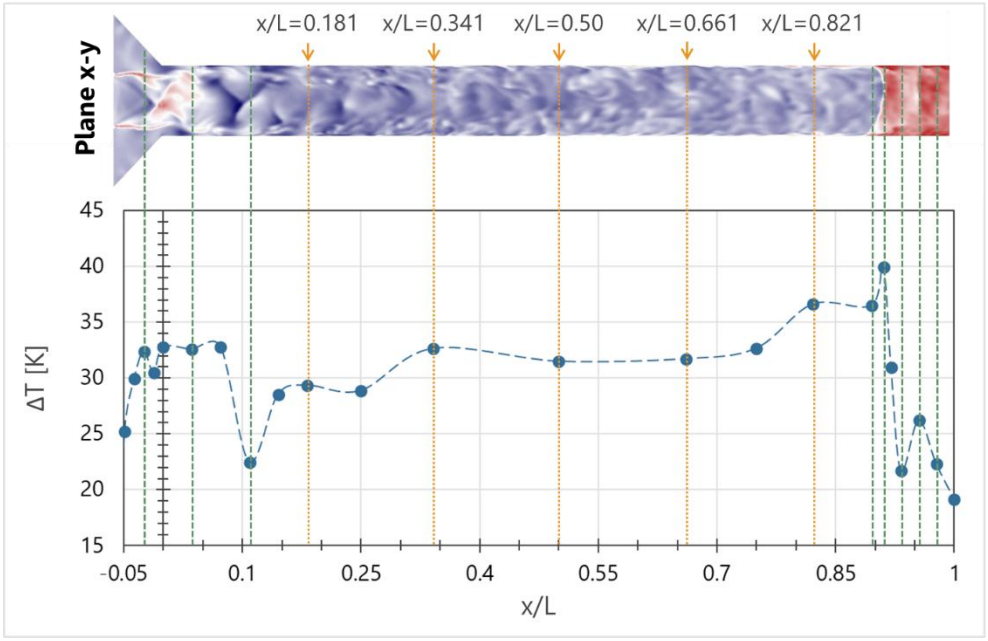


Figure 5.26 – Static temperature range at various sections represented in Figure 5.17.

Figure 5.27 illustrates density gradient magnitude contours, often referred to as pseudo-Schlieren images (Croquer et al., 2021), which provide insights into the flow structure, particularly the shock pattern. Dark regions indicate high-density gradients, corresponding to shock waves, while lighter areas represent lower density gradients. At the flow entrance, an oblique shock train is observed, a phenomenon characteristic of high Mach number flows or confined geometries (Sullins and McLafferty, 1992; Matsuo et al., 1999; Zhdanov and Chorny, 2011; Rao and Jagadeesh, 2014; Zhu and Jiang, 2014; Z. Chen et al., 2017; Karthick et al., 2018; Gupta et al., 2019; Gupta, Kumar, et al., 2022).

Further downstream, at the end of the constant-area section, a re-compression λ-shock train facilitates the transition to subsonic conditions.

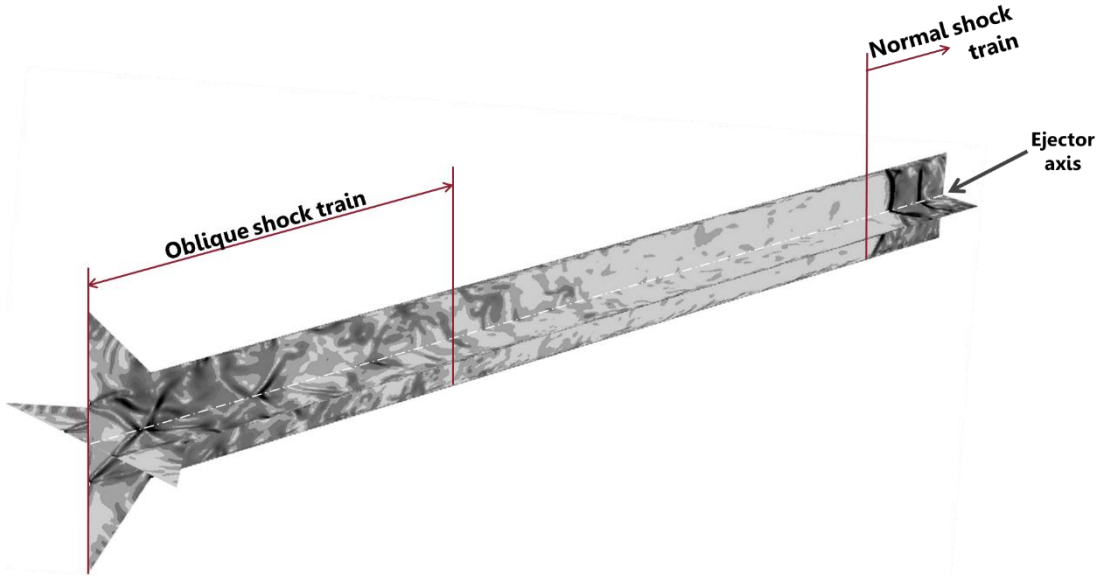


Figure 5.27 – Numerical pseudo-Schlieren images showing flow structure and shock identification in the flow domain.

Oblique shock trains are known to induce boundary layer separation, with the initial shock reflecting between duct walls and propagating downstream through alternating compression and expansion waves (Gnani et al., 2016). However, the pseudo-Schlieren images in Figure 5.28 do not explicitly show boundary layer separation, likely due to geometric constrains. The constant-area section has a diameter only 1.4 times larger than the primary nozzle diameter, and the short distance between the nozzle-exit and the entrance of the constant-area section restricts the mixing layer development. Despite this, vortex structures were detected near the wall, as indicated by the arrows in Figure 5.28. These observations suggest that the mixing layer merges with the boundary layer, accelerating the dissipation of the shock train (Zhdanov and Chorny, 2011; Zhu and Jiang, 2014).

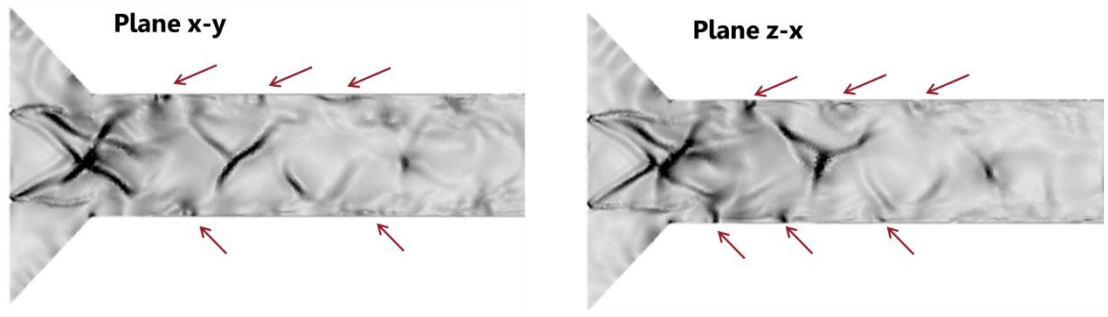


Figure 5.28 – Numerical pseudo-Schlieren images showing flow structure details at the primary nozzle exit, the arrow indicates the vortex structure present in the shear layer.

The double-choking operation of the ejector implies that the flow remains supersonic up to the end of the constant-area section. Figure 5.29 shows the density gradient in the vicinity of this region. It can be seen that some identifiable normal shocks are present, marking the transition from supersonic to subsonic flow. The profile of the first shock suggests the presence of a curved shock structure, which is consistent with observations of confined supersonic flows (Gnani et al., 2016). However, the planes used for pseudo-

Schlieren representation do not clearly capture the shapes of the subsequent shocks, requiring further investigation, for example by examining Mach number fields, to clarify their structure and dynamics.

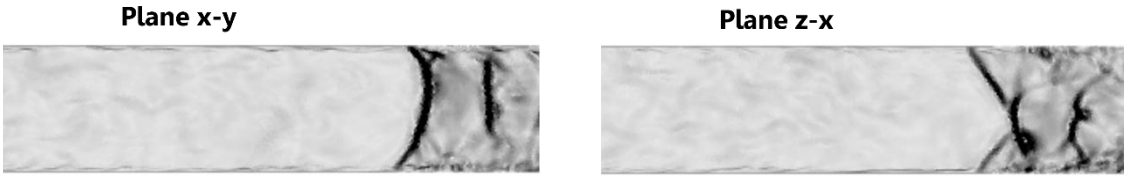


Figure 5.29 – Numerical pseudo-Schlieren images showing the flow structure after reaching subsonic conditions.

The Q-criterion, which identifies vortices by distinguishing between rotational and strain-dominated regions, provides a valuable tool for understanding vortical structures and the mixing process near the constant area inlet zone. It quantifies the difference between rotation and strain rates (Dubief and Delcayre, 2000). It can be used to identify vortices where the rotation rate exceeds the strain rate. This visualisation tool is adequate for identifying the mixing process and the onset of complete turbulence. Figure 5.30 illustrates the positive Q-criterion field, highlighting vortex structures in orange, overlaid on numerical pseudo-Schlieren images. As the oblique shock train dissipates energy, the flow becomes increasingly dominated by vortices, marking the transition to the turbulent mixing region. Additionally, the size of the vortex structures grows as the shock train diminish, leading to the growth of large-scale fully developed turbulent structures occupying the cross section of the duct.

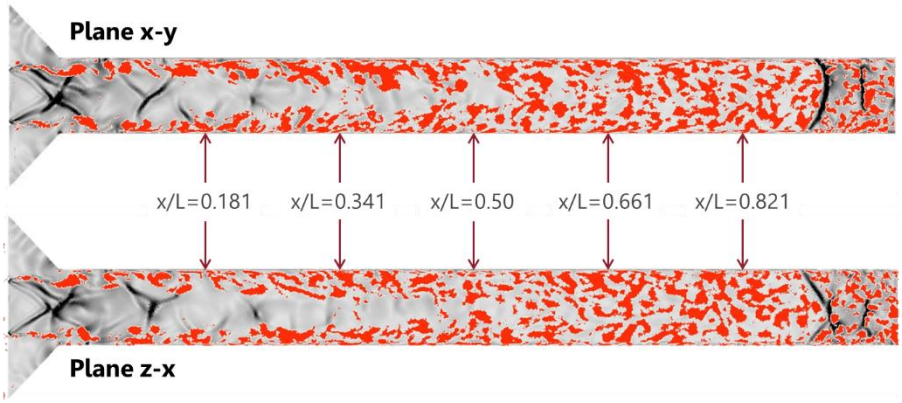


Figure 5.30 – Q-criterion contours showing vortex structures over two streamwise midspan planes, overlaid on numerical pseudo-Schlieren images.

Figure 5.31 further exploits the Q-criterion analysis where the contours are coloured by the rotational direction of the vortices, focusing on the domain entrance. Red and blue colours indicate opposing rotational directions, where red represents a rotation vector normal to the plane of the figure. Initially, the rotational direction of the vortices aligns predictably with the streamwise direction of the motive flow. However, as the shock train dissipates, the flow becomes increasingly chaotic, and the vortex rotation direction becomes irregular and unpredictable, further signifying the transition to a fully turbulent state.

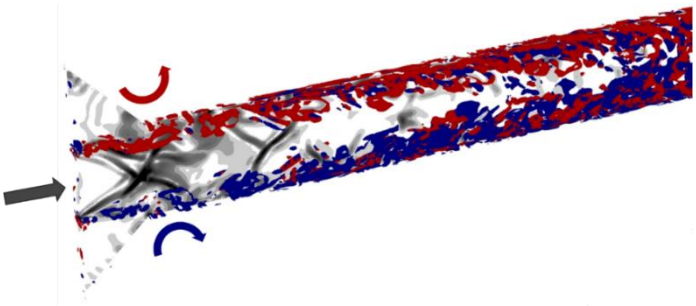


Figure 5.31 – Pseudo-Schlieren images overlaid with Q-criterion contours, showing vortex rotational direction near the domain entrance.

Pathikonda et al. (2021) investigated the turbulent mixing behaviour in a confined coaxial jet, where a high-momentum, low viscosity jet is injected into a lower-momentum, high viscosity co-flowing stream within a pipe. Using simultaneous high-resolution Particle Image Velocimetry (PIV) and Planar Laser-Induced Fluorescence (PLIF), the authors measured velocity and scalar concentration fields, while LES was employed to capture the three-dimensional flow structures. Their findings identified three distinct stages of flow development in the mixing region: (1) the formation of a thin shear layer (or mixing layer), (2) the subsequent growth and mixing of the jet, and (3) the transition to a fully turbulent pipe flow downstream. Figure 5.32 illustrates the simulated axial velocity field, clearly depicting the sharp mixing layer that separates the two streams. The termination of the oblique shock train marks the boundary of the non-mixed region, where its energy dissipates into large-scale turbulent structures, initiating the turbulent mixing region. These results indicate that the flow exiting the primary nozzle and entering the mixing section closely resembles a confined coaxial jet, as characterised by Pathikonda et al. (2021).

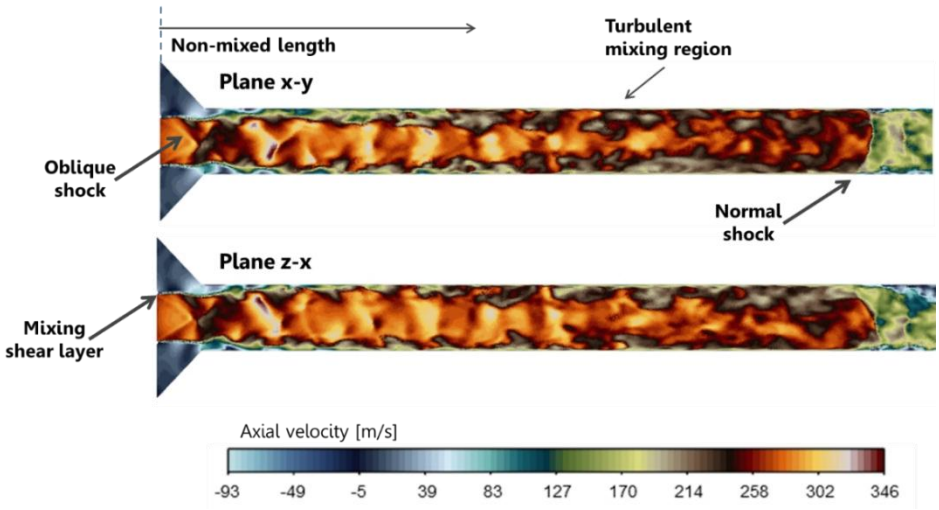


Figure 5.32 – Instantaneous axial velocity field over two streamwise midspan planes.

Figure 5.33 illustrates two midspan planes with Mach number contours, where the sonic line is marked in blue. Additionally, red vertical lines perpendicular to the flow were added to indicate sections where compound supersonic flow occurs. Yellow lines indicate zones of compound subsonic flow. The compound choke indicator (β) was calculated for each section using the choking criterion based on the compound-compressible flow theory for real gases using the formula (Croquer et al., 2021):

$$\beta = \sum \left[\frac{p_i \cdot A_i}{\rho_i \cdot u_i^2} \cdot \left(1 - Ma_i^2\right) \right] \tag{5.7}$$

In Equation (5.7), the subscript i refers to the properties of a specific cell. The flow is considered compound-subsonic when $\beta > 0$, compound-sonic when $\beta = 0$, and compound-supersonic when $\beta < 0$. In Figure 5.33 it is notorious that the sonic line rapidly approaches the wall near x/L=0.181 and attaches to the wall after the x/L=0.341. This observation indicates that the ejector operated under double-choking conditions, achieving a fully supersonic flow for x/L>0.34 in agreement with the Fabri-choking theory (Fabri and Siestrunck, 1958).

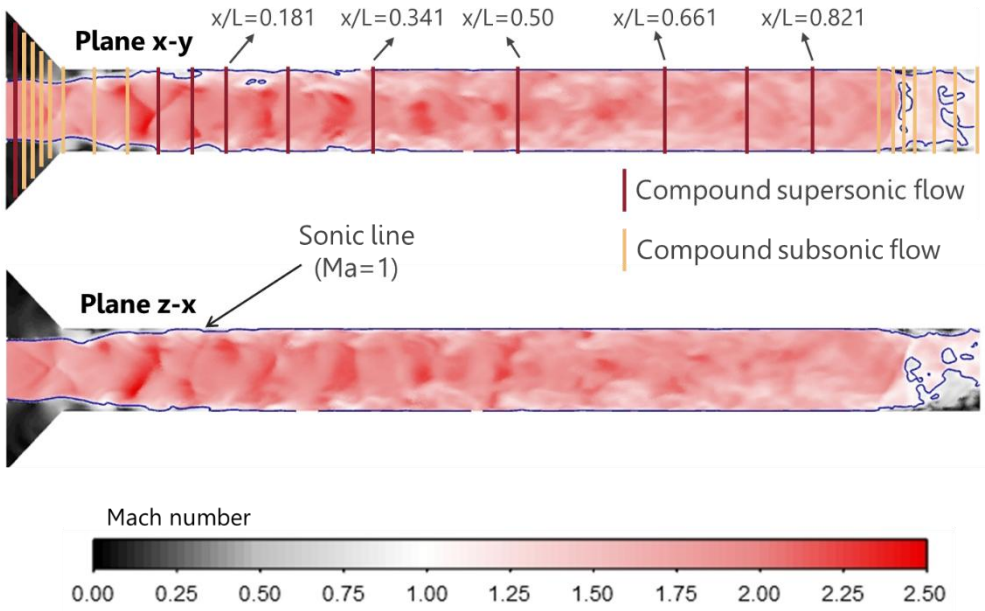


Figure 5.33 – Instantaneous Mach number field over two streamwise midspan planes, with the sonic line in blue. Vertical lines indicate the compound flow regime: red for compound supersonic flow and yellow for compound subsonic flow.

According to the compound-compressible flow theory, the flow can be classified as compound-supersonic at the entrance of the mixing section. However, this classification appears physically inconsistent since the entrained flow velocity is low. This contradiction arises because the nozzle exit velocity is significantly higher than the entrained flow velocity, while the pressure and density differences between the streams remain relatively small. Consequently, the calculated β value is negative, leading to an incorrect conclusion that flow is compound-supersonic type. This result demonstrates the limitation of the compound theory in accurately capturing flow physics in cases with large velocity disparities and, therefore, it should be applied with caution.

In the constant-area section of the ejector, the flow switches to the compound-supersonic regime x/L<0.181 and becomes compound-subsonic after x/L=0.821 and before the normal shock. According to Fabri-choking theory, however, the flow becomes fully subsonic only when the sonic line detaches from the wall that is the axial location of the first normal shock. This difference demonstrates the contrast between the two theories. Fabri-choking theory provides a more conservative assessment of the transition, defining double-choking operating conditions based solely on the supersonic nature of both streams and without considering the detailed local flow dynamics described by compound-compressible flow theory.

Recalling the shock structure analysis, the boundary layer separation at the initial oblique shock train is visible in Figure 5.33, as it is characterised by a local Mach number less than 1 (Karthick et al., 2017). As the shock train propagates downstream, the flow becomes fully supersonic and turbulent. It is evident from Figure 5.24 that most of the compression occurs through the first shock at x/L=0.92. Downstream of this point, the flow alternates between supersonic and subsonic states, as well as compressing and expanding, forming a subsonic bubble immediately after the shock. Here (x/L>0.92), the boundary layer becomes thicker, effectively acting as a nozzle that accelerates the flow. This phenomenon explains the switching between supersonic and subsonic flow. The process is inherently dissipative, thus the flow eventually stabilising as fully subsonic.

The agreement between these findings and experimental data on confined coaxial jets underlines the validity of the ELES approach in capturing the complex flow dynamics within the ejector. The ability of ELES to resolve transient features such as shocks, boundary layer interactions, and turbulence makes it a superior tool for studying mixing phenomena compared to RANS-based methods.

5.2.3 Discussion of the mean flow results

As mentioned before, time statistics were collected over $5t_c$ from stabilised simulation results. Figures 5.34 to 5.38 illustrate the mean streamwise velocity profile ($\overline{u}/\overline{u}_c$) normalised by the centreline velocity ($\overline{u}_c$), plotted against the normalised radius (r/R, where R represents the maximum local radius). These profiles are shown for different ejector sections. For each r/R value, the maximum $\overline{u}/\overline{u}_c$ was recorded, providing a detailed view of the velocity distribution at successive axial positions (x/L).

Figure 5.34 displays the velocity profiles for the mixing section. At the centre of the profile (r/R=0), a prominent maximum is observed, corresponding to the motive flow entrance (nozzle-exit). As the flow progresses (x/L>-0.037), the high-speed region shifts away from the ejector axis. This behaviour confirms the development of the mixing layer, where the momentum exchange between the motive and entrained flows occurs. At x/L=−0.024 and particularly at x/L=0, the contour of the mixing layer becomes evident, marking the shear layer between the two streams.

Figure 5.35 presents velocity profiles near the constant-area section inlet (0<x/L<0.181). The profile for x/L=0, previously shown in Figure 5.34, is included here for comparison across different ejector sections. Except for the profile at x/L=0.109, all velocity profiles exhibit two peaks, corresponding to the mixing layer. At x/L=0.109, the profile intersects an oblique shock, significantly altering its shape. A subtle asymmetry in the flow is also observed in Figure 5.35. For instance, at x/L=0.036, a secondary peak appears at r/R=−0.65, indicating that the flow is not perfectly axisymmetric. This asymmetry may result from boundary layer effects or slight imbalances in the interactions between the motive and entrained flow. The instantaneous pseudo-Schlieren images and the normalized time-averaged velocity profiles consistently characterise the shock structure. The sudden changes in velocity magnitude align with the observed shock positions, suggesting that the shock location remains relatively stable over time.

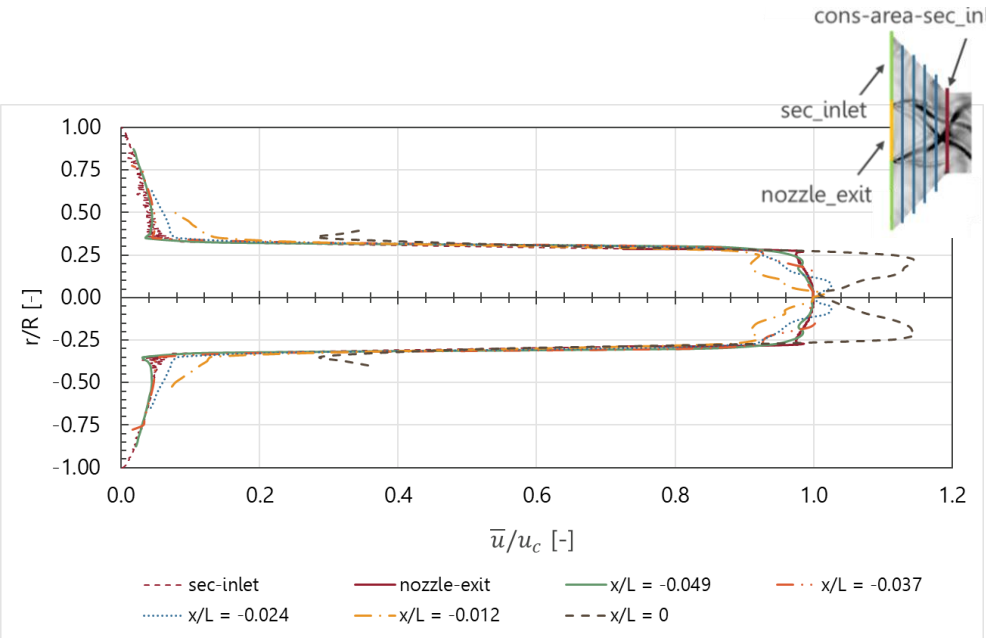


Figure 5.34 – Mean streamwise velocity profile normalised by the centreline velocity plotted against the normalised radius at different streamwise positions in the mixing section.

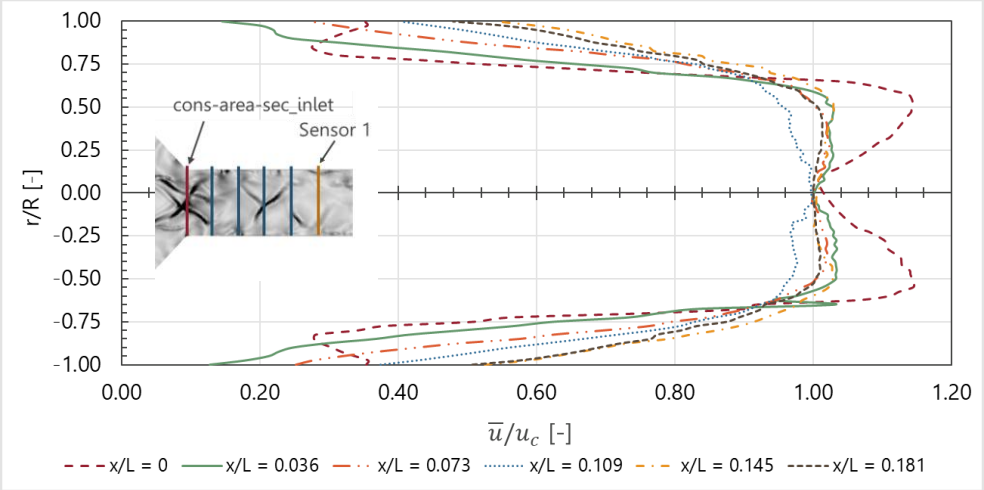


Figure 5.35 – Mean streamwise velocity profile normalised by the centreline velocity plotted against the normalised radius at different streamwise positions for the constant area section inlet until x/L=0.181.

For illustrative purposes, Figure 5.36 overlays the normalised mean streamwise velocity profile with the corresponding instantaneous pseudo-Schlieren images for the ejector cross-section at x/L=0. Similar behaviour was observed across other sections for x/L≤0.181. A mixing layer, marked with dashed red lines, can be identified in the pseudo-Schlieren image by its light grey region and in the velocity profile by the boundary of the red contours. Similarly, the oblique shock centre aligns in both pseudo-Schlieren image and the normalized mean velocity profile. The higher velocity observed in the profile corresponds to regions associated with the mixing layer or abrupt interactions with a shock structure, as indicated in the identified areas of the figure.

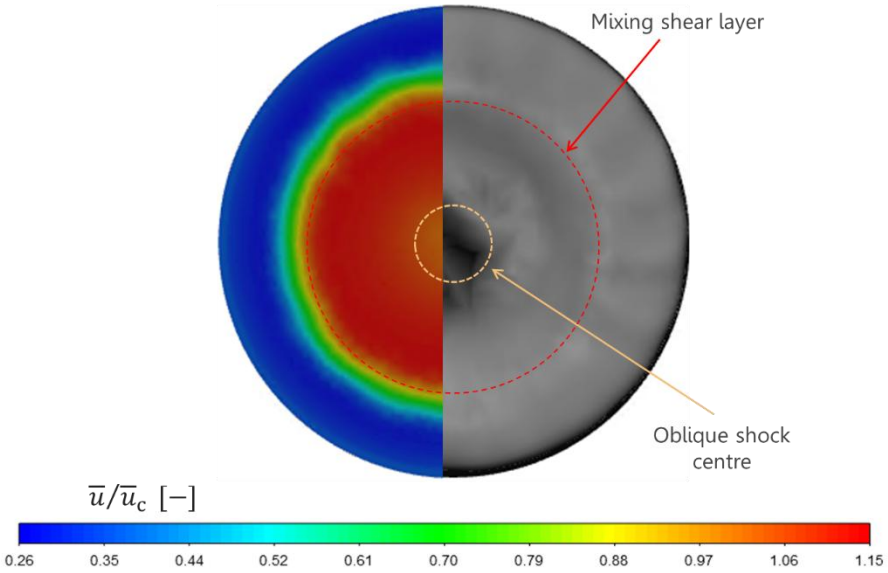


Figure 5.36 – Overlay of the normalised mean streamwise velocity profile and the instantaneous pseudo-Schlieren image for the ejector cross-section at x/L=0.

As the flow develops into the turbulent mixing region, the velocity profiles evolve into a smoother, bell-shaped form that is typical for fully developed turbulent flows. This transition is evident in Figure 5.37a) (from x/L=0.181 to x/L=0.5) and Figure 5.37b) (from x/L=0.661 to x/L=0.911). According to the pseudo-Schlieren images (see Figure 5.37c)), the normal shock starts at x/L=0.895. Nonetheless, the velocity profiles at x/L=0.895 and x/L=0.911 do not correspond to a steady shock position. This suggests that, unlike the oblique shock train, the normal shock position fluctuates over time.

Figure 5.38 shows velocity profiles from x/L=0.920 to the constant-area section outlet. Most profiles exhibit a smooth shape, except for x/L=0.978, suggesting the presence of a shock. This behaviour was not captured by the analysis of the instantaneous flow field (see Section 5.2.2). This suggests that the position of the shock wave is less predictable over time. Another notable detail is the near-the-wall velocity profile. In that region the velocity is maximum for x/L≤0.933 (near $\overline{u}/u_c \approx 0.62$) and then starts to decrease, indicating a disruption in the flow dynamics beyond this point. This disruption likely corresponds to the interaction between the boundary layer and the normal shock, which alters the near-wall velocity distribution. The observation suggests that while the shock's position in the bulk stream exhibits some instability, near-wall flow characteristics are more predictable over time, aligning with the analysis of the instantaneous flow field.

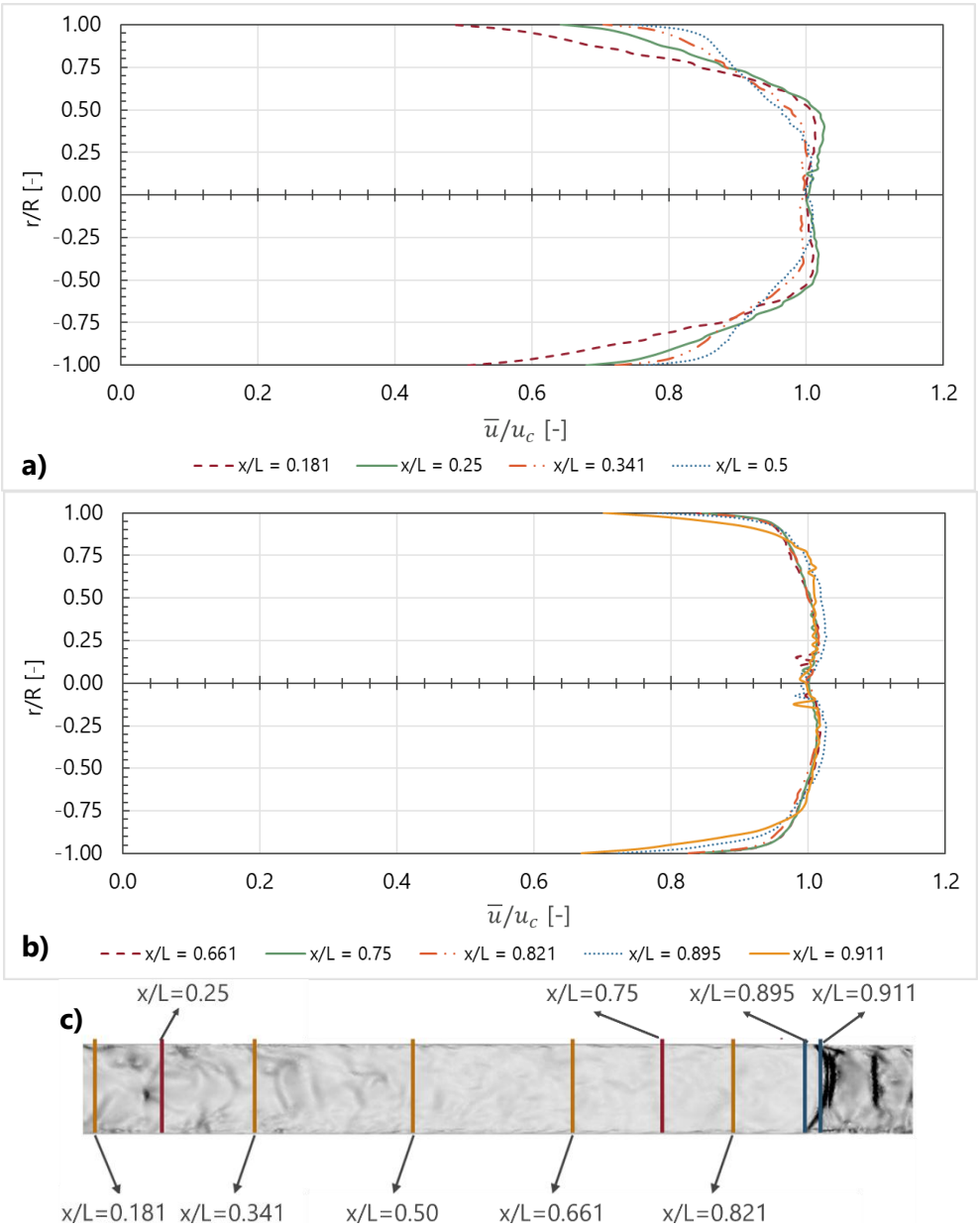


Figure 5.37 – Mean streamwise velocity profile normalised by the centreline velocity plotted against the normalised radius at different streamwise positions for the constant area section: a) for 0.181≤x/L≤0.50; b) for 0.661≤x/L≤0.911 and c) corresponding pseudo-Schlieren image.

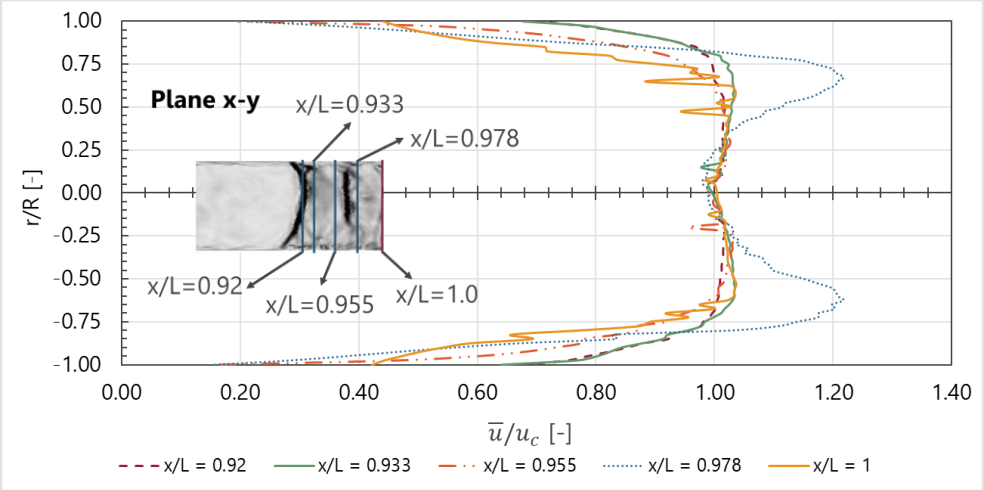


Figure 5.38 – Mean streamwise velocity profile normalised by the centreline velocity plotted against the normalised radius at different streamwise positions for x/L≥0.92.

Analysing the static pressure along the ejector length reveals some characteristic behaviour. Near the wall where the viscous forces dominate, a smoother static pressure profile was obtained when compared to the core region. Figure 5.39 illustrates this behaviour, where the pressure profile is normalized using the pressure value ($p_{c,0}$) for x/L=0. The core region profile ($p_c/p_{c,0}$) demonstrates alternating compression and expansion waves, which are stronger in the vicinity of the oblique and normal shocks and weaker in the turbulent mixing region. Although these compression and expansion waves are also noticeable near the wall, they are less pronounced than in the core region.

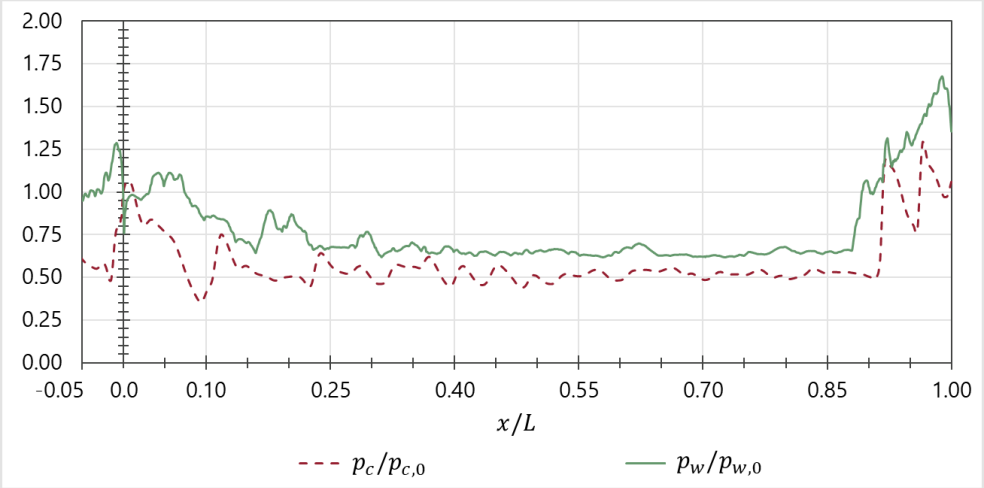


Figure 5.39 – Static pressure profile distribution along the mixing and constant area section; the dashed line represents the centreline pressure, and the solid line represents the wall pressure, both normalized with the corresponding x/L=0 pressure value.

The wall shear stress reaches a maximum at the entrance of the constant-area section, as depicted in Figure 5.40. This can be attributed to the sudden change in the wall-normal direction. It is followed by a sharp decrease and oscillations up to x/L=0.50. Downstream x/L=0.50, the wall shear stress gradually decrease as the flow enters the turbulent mixing region, until it reaches the normal shock (x/L=0.933), where a sudden drop in the wall shear stress is observed.

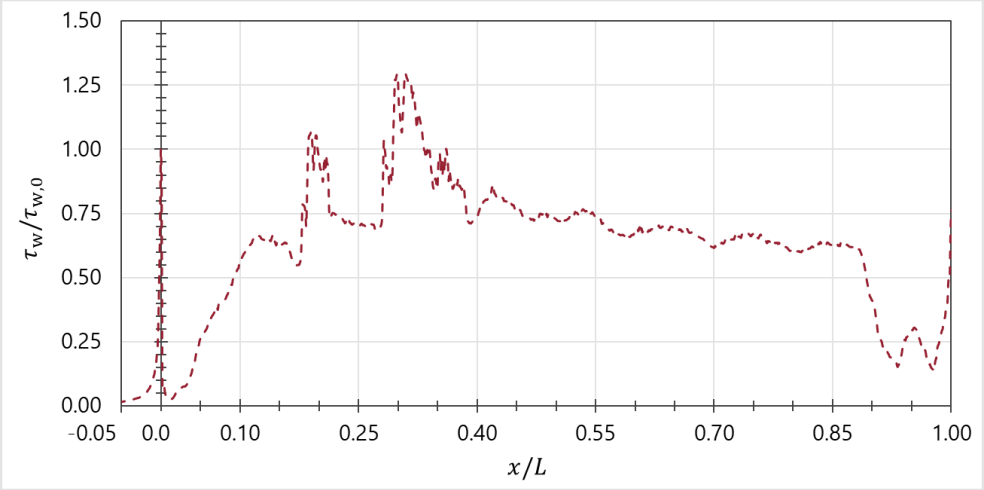


Figure 5.40 – Wall shear stress profile distribution along the mixing and constant area sections, normalized with the x/L=0 value.

A relatively stable accelerating flow velocity profile was observed from the entrance of the constant area section to x/L=0.50, near the wall. This stability persists until the normal shock, where the velocity decreases abruptly. The combined effect of the velocity variation and the wall shear stress induces variations in the thickness of the viscous sublayer. These variations are reflected in the displacement thickness (δ^*), which is shown in Figure 5.41. The relative displacement thickness (δ^*/R) decreases as the flow enters the constant area section, exhibiting oscillations due to the oblique shock train. This trend continues until x/L=0.50. Beyond this point, the displacement thickness decreases slightly as it approaches the normal shock.

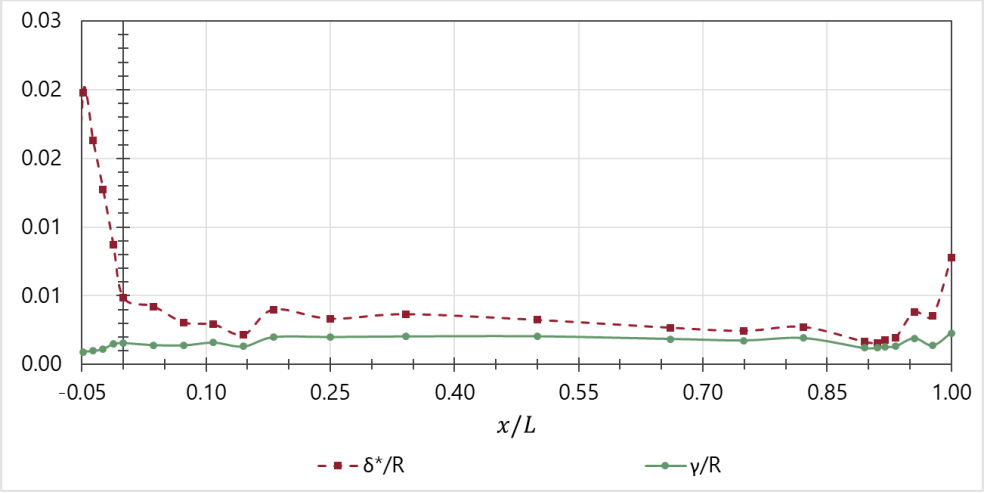


Figure 5.41 – Relative to the maximum radius displacement (dashed line) and momentum thickness (solid line).

The relative momentum thickness (γ/R) quantifies the momentum deficit induced by the boundary layer relative to the overall flow scale. Its value remains relatively constant throughout the domain, suggesting minimal changes in the momentum distribution near the wall. Consequently, the shape factor (δ^*/γ), depicted in Figure 5.42, shows an inverse behaviour of the relative displacement thickness. This indicates that the shape factor is

primarily governed by the changes in displacement thickness rather than the momentum thickness.

The discussion of the results above points out the non-equilibrium nature of the ejector flow during the mixing of the jets, due to the complex interactions between the shock wave structures and the boundary layer. The oscillatory behaviour in both the wall shear stress and displacement thickness reflects the flow's response to successive shock-induced compression and expansion events. The stabilization of these quantities for x/L>0.50 suggests that the flow begins to respond to the geometric and dynamic constraints imposed by the constant area section.

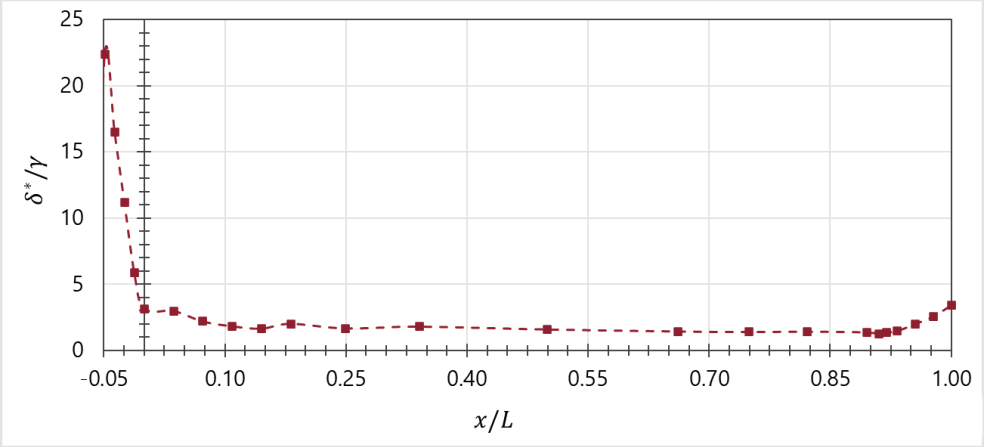


Figure 5.42 – Shape factor (δ^*/γ) distribution.

5.2.4 Mixing layer evolution during the mixing process

The root-mean-square (RMS) of the radial velocity fluctuation profile provides valuable insights into the evolution of the mixing layer along the ejector domain. The radial velocity is particularly important because it captures the cross-stream interactions and the spread of the mixing layer, reflecting the energy exchange and turbulence generated as the motive and entrained streams interact. By quantifying the intensity of these velocity fluctuations, the RMS profiles helps to identify the regions where strong turbulence is generated, offering a detailed understanding of how the two streams mix and evolve within the ejector.

Figure 5.43 illustrates the contours of instantaneous radial velocity fluctuations in a streamwise midplane. The characteristic diamond-shaped oblique shock train structure at the onset of the mixing process is indicated in the Figure 5.43b). This structure extends to approximately halfway into the constant area section (x/L=0.5). The contours also reveal other distinct flow features, such as the mixing layer between the streams and the wall shear stress, as pointed out in Figure 5.43b), both crucial for understanding the mixing dynamics.

The mixing process can be further studied by analysing the RMS radial velocity fluctuations distribution at a given axial position. By performing this analysis, the development of the mixing layer, including its growth rate, thickness, and interaction with the boundary layer can be studied. Figure 5.44 presents the normalised radial RMS velocity fluctuation ($\sqrt{(\overline{u_r}'')^2}/u_c$) profiles for the mixing chamber and constant-area section. In Figure 5.44a), the profiles have two maximums corresponding to the oblique

shock position. These peaks occur because the oblique shock waves create a radial pressure gradient, which intensifies the velocity fluctuations in the radial direction. At x/L=−0.049, a small local maximum can be identified near r/R=-0.80, indicating a secondary fan. The secondary fan results from the interaction between the near-wall secondary flow and the developing mixing layer. The secondary flow enhances turbulence near the boundary, producing localized velocity fluctuations that are characteristic of this region.

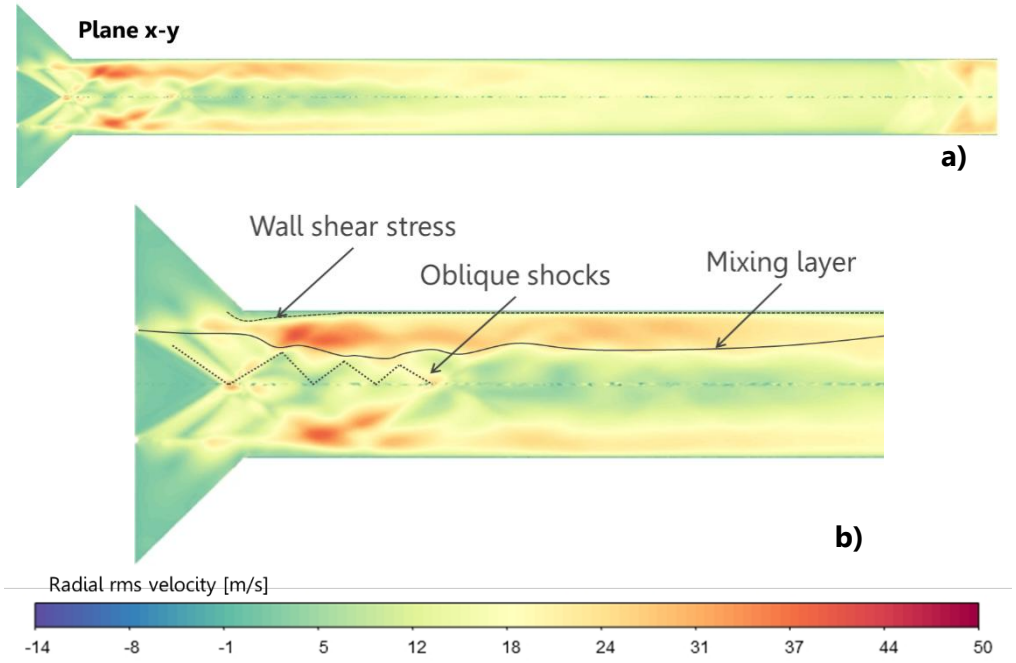


Figure 5.43 – Contours of instantaneous radial velocity fluctuations in a streamwise midplane: a) covering the mixing chamber and constant-area section; b) a zoomed-in view of the mixing chamber and constant-area entrance, identifying the wall shear stress, oblique shocks and mixing layer positions.

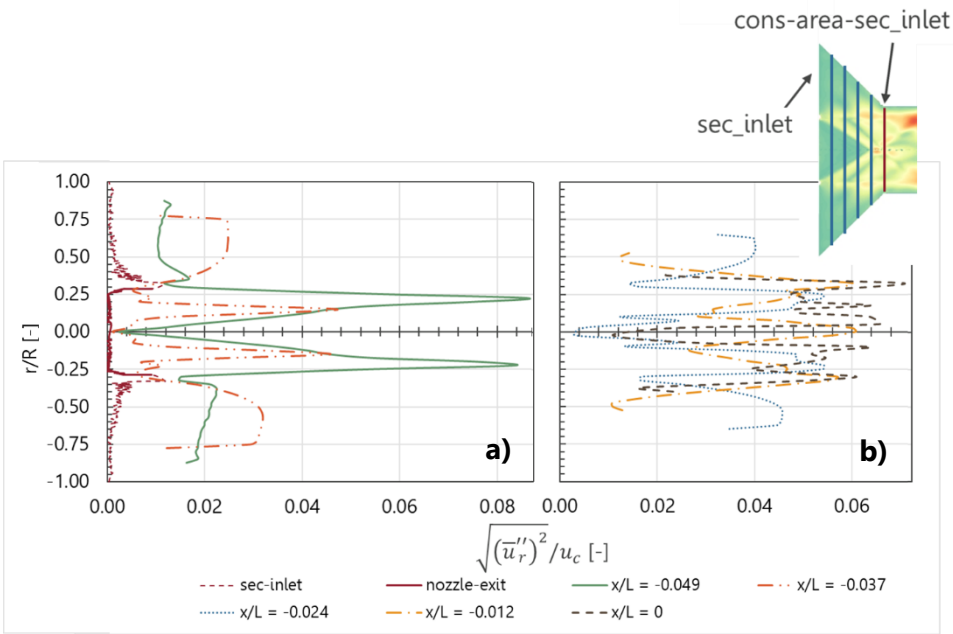


Figure 5.44 – Profiles of the normalised radial RMS velocity fluctuation at different locations in the mixing section: a) for the mixing section entrance and x/L≤-0.037; b) for -0.024≤x/L≤0.

Figure 5.45 shows the normalised radial RMS velocity fluctuation profiles near the entrance of the constant-area section. Downstream x/L=0, the profiles exhibit two distinct maxima defining the location of the shear layers (or mixing layer). At x/L=0.036, the normalised radial RMS velocity fluctuation was the highest due to the strong oblique shock in this section. The shock creates significant velocity gradients and enhance turbulence, amplifying the magnitude of velocity fluctuations in the mixing layer. Beyond x/L=0.109, the boundary layer effect becomes apparent by a hump-like variation of the curve in Figure 5.45b). The radial RMS velocity fluctuation magnitude increases through the shock partially mitigating the boundary layer's influence on the profiles.

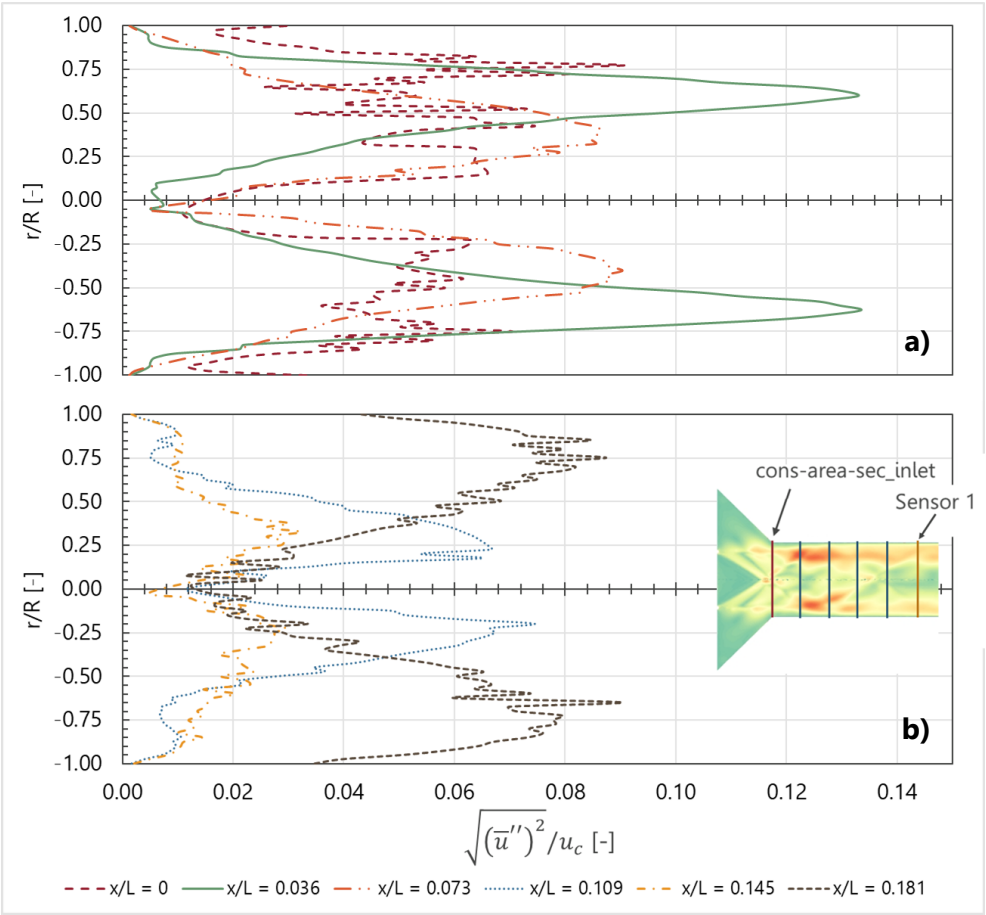


Figure 5.45 – Profiles of the normalised radial RMS velocity fluctuation at different locations in the mixing section: a) for 0≤x/L≤0.073; b) for 0.109≤x/L≤0.181.

Further downstream (x/L>0.25), the magnitude of the radial RMS velocity fluctuation decreases from a maximum of ≈0.145 at x/L=0.25 to values near 0.10 at x/L=0.50. Additionally, the ratio between the maximum and minimum values decreases significantly, from 7 to 2, indicating a pronounced profile shape readjustment, as shown in Figure 5.46a). This trend reflects the growth and expansion of the mixing layer and its interaction with the developing boundary layer along the ejector walls. In the second half of the constant-area section (x/L > 0.5), depicted in Figure 5.46b), the profile takes on the characteristic shape of a fully turbulent mixing region, with a maximum near the ejector axis. At this stage, the mixing of the primary and secondary streams is complete, resulting in fully turbulent flow concentrated around the ejector axis.

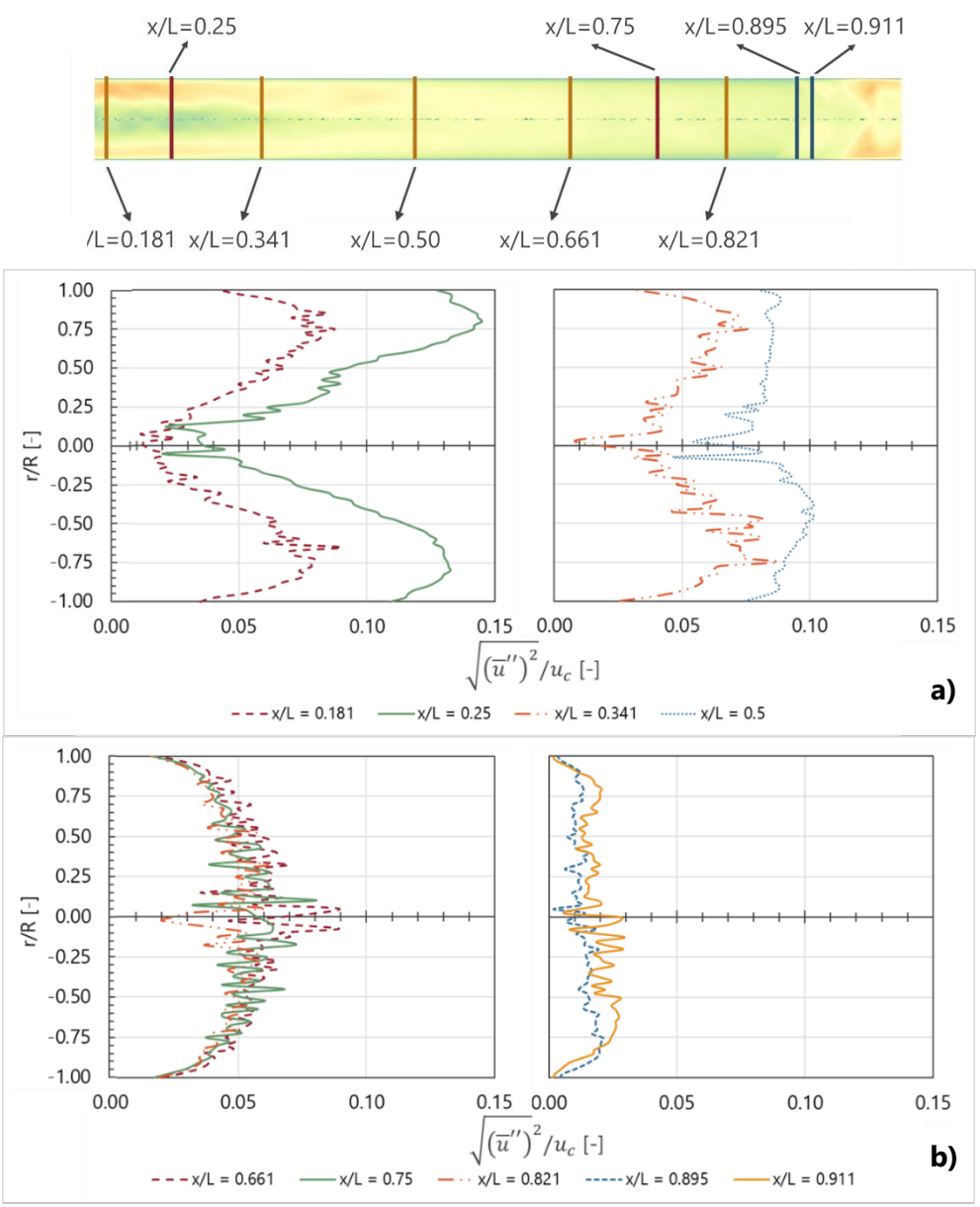


Figure 5.46 – Profiles of the normalised radial RMS velocity fluctuation at different locations in the mixing section: a) for 0.181≤x/L≤0.5; b) for 0.661≤x/L≤0.911.

As it was mentioned before, the final shocks occur at about x/L=0.895, from where the flow becomes subsonic. As it was the case for the mean streamwise velocity profile, the time-averaged RMS radial fluctuation velocity profile predict the mean shock position different from the analysis of the instantaneous data (see Figure 5.38). This difference indirectly demonstrates the unsteady nature of the axial location where the flow becomes subsonic, in contrast to the relatively steady oblique shock train in the ejector mixing section. Looking at the data in Figure 5.47, start of the normal shock train is approximately at x/L=0.955. At this location, the RMS radial fluctuation velocity profile exhibit two maximums (r/R=-0.775 and 0.875). Downstream of the shock, the flow is asymmetric, and the magnitude of fluctuation increases several local maxima and minima indicating more chaotic turbulent eddies.

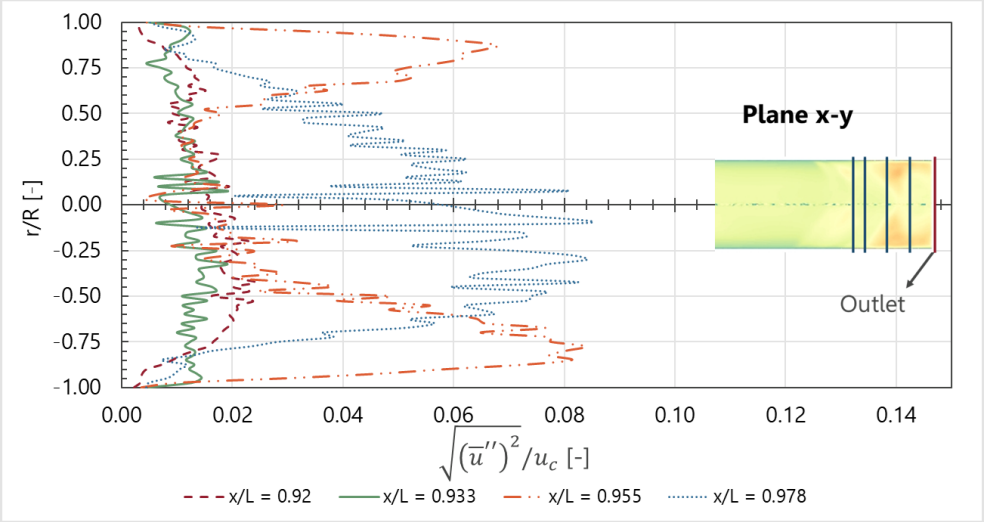


Figure 5.47 – Profiles of the normalised radial RMS velocity fluctuation at different locations in the mixing section for 0.920≤x/L≤0.978.

The RMS velocity fluctuation profiles provide a detailed understanding of the mixing layer evolution within the ejector. In the mixing section, the fluctuations revealed the contribution of oblique shocks and secondary flows in turbulence generation. In the constant-area section, the profiles demonstrated the progressive transition from shear-dominated mixing to fully turbulent flow. Finally, near the normal shock region, the RMS velocity fluctuation profiles result from the interaction between shocks and turbulence, terminating in a chaotic subsonic flow and fully mixed streams. These findings agree with the expected behaviour of an ejector operating under double-choking conditions.

5.3 Comparison of the ELES results with experimental data

Figure 5.48 shows the experimental static wall pressure data from x/L=0.181 (sensor 1) to x/L=0.821 (sensor 5) and the simulation results using the RANS and ELES models. The experimental data in the figure was obtained from Run 1 in Figure 5.3. Figure 5.48 includes a grey coloured shaded band corresponding to the range of the instantaneous static pressure predictions by the ELES model. It can be seem from the figure that the time-averaged pressure profiles obtained with the RANS and ELES models had similar shapes, except for the axial location corresponding to $x/L > 0.8$. Here, the RANS model predicts a rapid pressure increase, while the ELES predict the fluid recompression starting at about $x/L \approx 0.9$, which is in better agreement with the experimental data.

The ELES model captured the flow transition more accurately with better agreement with the experimental data than the RANS model. This can be attributed to the ELES model's ability to resolve fine-scale turbulence and capture the complex interactions between shock waves, the mixing layer, and the boundary layer. In contrast, the RANS model, using simplified models to describe the Reynolds stress terms, lacks accurate mathematical formulation of the transient and localised phenomena dominating these flow regimes.

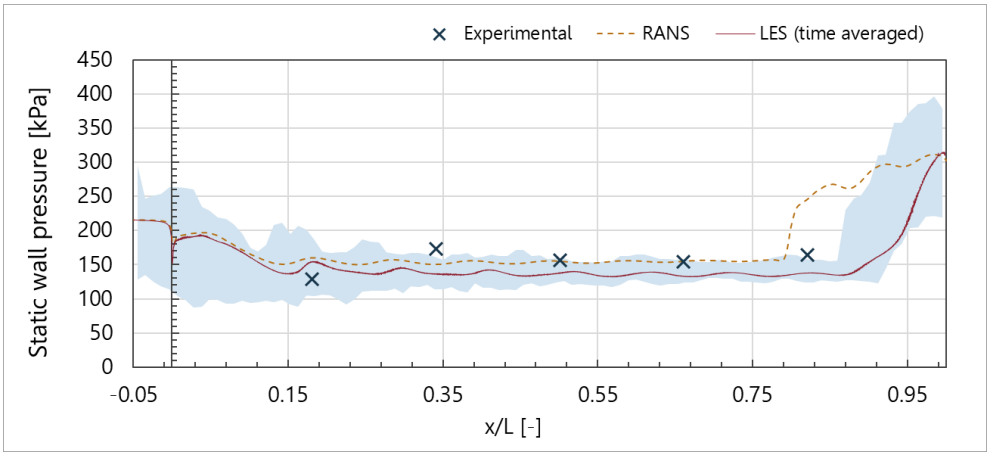


Figure 5.48 – Comparison of static wall pressure profiles through the mixing and constant-area sections for RANS, LES, and experimental data. The shaded area represents the range of LES instantaneous results.

Due to data storage limitations during the embedded large eddy simulation, recording the local temperature data for all mesh points within the domain was not plausible. Therefore, only the wall temperature data was stored for comparison with the experimentally measured temperature profiles. Additionally, time-averaged static wall temperature data for the ELES simulation was not explicitly calculated or stored during the simulation setup, which restricted post-processing options. Figure 5.49 presents the experimental static temperature measurements at different axial locations during Run 1 (see Figure 5.10), along with the static wall temperature results from the RANS model. The LES instantaneous data are represented as a shaded band to encompass the instantaneous wall temperature values. At the constant-area section inlet (x/L=0), the smallest temperature range is observed, with a 2% difference between the maximum and minimum values. As the flow evolves, the temperature range increases, reaching its maximum at x/L≈0.2, where ΔT reaches 43°C, representing a 16% increase relative to the minimum temperature. This significant fluctuation is attributed to the complex flow interactions and compressibility effects associated with the shocks in that region. Beyond this point, the temperature amplitude decreases steadily, reaching a minimum near x/L≈0.9, before showing a slight increase associated with the normal shock in this region. The data shows that both the RANS and ELES models slightly but consistently underestimated the experimentally recorded wall temperatures. However, the overall temperature range along the wall predicted by the simulations aligns well with the experimental measurements across all axial positions. Thus, one may conclude that the ELES model describes the ejector temperature profile closer to the observations when compared to the RANS model.

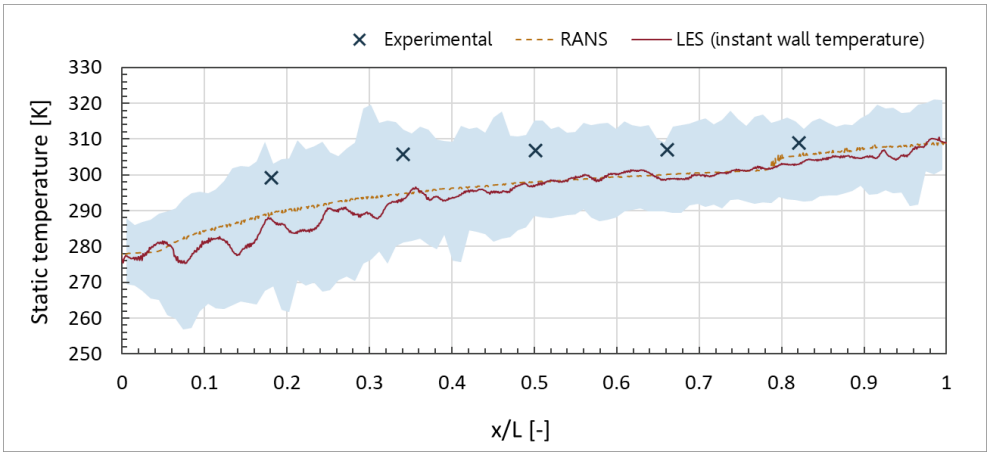


Figure 5.49 – Comparison of static temperature profiles through the mixing and constant area sections for RANS, ELES, and experimental results. The shaded area represents the variation range of ELES instantaneous results.

The ELES model results indicate that static pressure variations are less pronounced than temperature variations, particularly in the turbulent mixing zones where mixing is already complete (for x/L>0.5). This phenomenon is likely related to the correlation between the kinetic energy of the eddies and the internal energy of the flow. In single-phase flows, the kinetic energy of turbulent eddies is converted into internal energy through viscous dissipation leading to temperature fluctuations. Since no latent energy transfer is involved in a single-phase flow, the energy exchange is accompanied with the temperature variations.

Due to the transient nature of the LES approach, flow properties are expected to fluctuate over time. To assess this variability, Table 5.3 compares the experimental motive mass flow rate with the predicted values from the RANS and ELES models. For the ELES results, the average, maximum, and minimum values are presented. It can be seen from the table that both models underestimated the motive mass flow rate with a relative error of about 3-5%, with only a small difference between the two approaches. In fact, these results were somewhat expected, because the motive flow rate is determined by the primary nozzle throat section and the primary nozzle inlet conditions. Since the flow in the primary nozzle was modelled in both simulation cases using the RANS approach, the motive flow rates resulted in very similar values (within 2%).

Table 5.3 – Motive mass flow rate in g/s – experimental data vs simulation results for Run1.

Run	$\dot{m}_{pr}$ **[g/s]**		$\delta_{\dot{m}_{pr}}$
Experimental	486		-
RANS	468		-3.6%
ELES	Max.	466	-4.1%
	Aver.	460	-5.4%
	Min.	452	-7.1%

The entrained mass flow rate in the ejector is primarily influenced by the mixing process within the mixing chamber and constant-area section, as well as the backpressure at the outlet. In the ELES simulation, the outflow is set based on the constant-area section outlet pressure from the precursor RANS simulation. However, as shown in Figure 5.48, the RANS model consistently overestimates pressure values, likely resulting in an overestimation backpressure in the ELES setup. This may correspond to a non-double-choke regime in the LES simulation, which might explain the observed variability and

discrepancies in the entrained mass flow rate. The entrained mass flow rate fluctuated between 0.105 and 0.156 kg/s, with an average value of 0.133 kg/s. As summarised in Table 5.4, the average entrained mass flow rate predicted by ELES resulted in a smaller relative error ($\delta_{\dot{m}_{sec}}$=12%) when compared to RANS ($\delta_{\dot{m}_{sec}}$=17%).

Table 5.4 – Entrained mass flow rate in g/s – experimental data vs simulation results for Run1.

Run	$\dot{m}_{sec}$ [g/s]	$\delta_{\dot{m}_{sec}}$
Experimental	118	-
RANS	138	17%
ELES	133	12%

The instability of the entrained mass flow rate may result from the overestimated backpressure (i.e. constant-area section outlet pressure), preventing the ejector from stabilising in a double-choke regime. Extending the LES domain to include the diffuser section could address this issue by capturing downstream flow dynamics more effectively, potentially improving the accuracy of entrained mass flow rate predictions.

5.4 Comparison of the ELES and RANS model flow field results

In this section, local flow properties are compared between the RANS simulation, used as precursor to the ELES, and the ELES results. Figure 5.50 illustrate the instantaneous static pressure field for the LES region alongside the RANS simulation results. It was found that the RANS simulation predicted a maximum pressure of 468 kPa at x/L=0.835. The ELES approach resulted in a maximum pressure of 412 kPa at x/L=0.965, which is considerably smaller that the RANS case. Similarly, the LES also resulted in a lower minimum pressure than RANS (81 kPa vs 128 kPa). The ELES approach, by resolving a broader range of turbulent scales, captures the gradual dissipation of the shock and the associated turbulence-shock interactions. This enables a more accurate representation of the normal shock and post-shock flow dynamics, resulting in lower maximum pressures and a more extended shock structure compared to the RANS model. From Figure 5.50, three key observations can be made. First, as expected, the pressure distribution in the RANS simulation is more homogeneous in the constant-area section, reflecting its time-averaged approach. Second, both RANS and ELES agree on the location of the first oblique shock which is also consistent with experimental findings (see Figure 5.50). Finally, the RANS simulation showed a wall pressure recovery just before x/L=0.821. Additionally, the RANS pressure profile along the ejector length exhibits axial symmetry, that is not the case for the LES results.

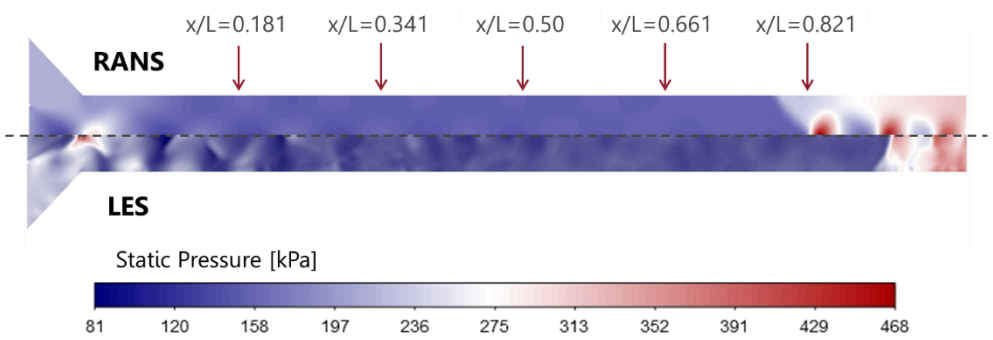


Figure 5.50 – RANS and LES region instantaneous static pressure field.

Figure 5.51a) and b) present the static temperature fields for the LES region and the RANS simulations. Figure 5.51a), a common temperature scale is used for direct comparison, while Figure 5.51b) has no scale to emphasize local variations. It was observed that the field minimum and maximum temperatures were comparable between the two simulations. The RANS simulation showed a temperature range from 272 K to 310 K, while LES from 259 K to 315 K. For the RANS simulation, the temperature field remains stable throughout the constant-area section, after the stronger oblique shock train at its entrance. Also, at any transversal section, it is evident that the temperature varies radially, increasing gradually from the ejector axis toward the wall (most visible in Figure 5.51b)), while in LES, the temperature variation is independent of the radial position, reflecting the unpredictable and heterogeneous nature of turbulence. At the entrance of the constant-area section (x/L<0), the first oblique shock introduces significant local temperature variations, approximately 30°C for RANS and 36°C for ELES. However, in Figure 5.51a), the shock train is less distinct in the RANS results, whereas in Figure 5.51b), its structure is more visible, though with reduced intensity. For the normal shock train at the end of the mixing process, the RANS simulation reveals a near wall region of high temperature, with its thickness increasing along x/L, representing the gradual and predictable evolution of the subsonic region surrounding the shock train (Gnani et al., 2016). In contrast, the LES simulation also shows near-wall regions of high temperature, but these regions lack the predictable form seen in RANS, exhibiting more heterogeneous characteristics.

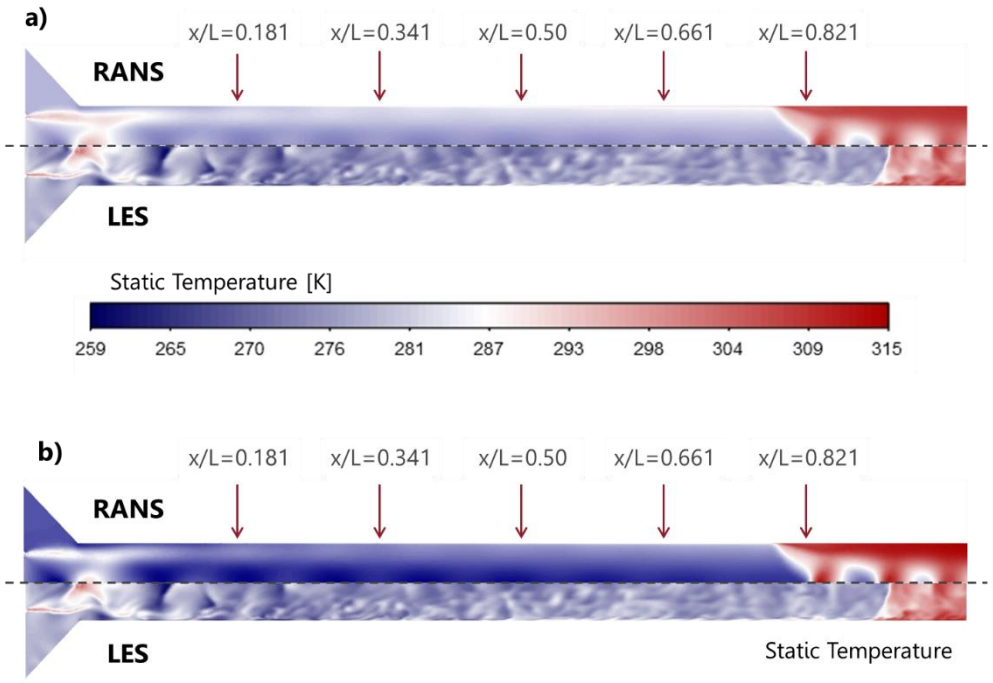


Figure 5.51 – RANS and LES region instantaneous static temperature field: a) using the same temperature scale for both results; b) without scale.

Figure 5.52 illustrates the axial velocity field for both RANS and LES simulations. LES results reveals a broader velocity range (from −55 m/s to 345 m/s) compared to RANS (from −48 m/s to 292 m/s). Within the constant-area section, the RANS velocity field shows a straightforward radial dependence, with maximum velocities at the axis and minimum velocities near the wall. Conversely, LES captures finer details, reflecting local turbulence and flow instabilities. At the end of the constant-area section, the velocity

field confirms that the shock train initiates earlier in the RANS simulation. In this region, the flow separates into two distinct zones as it interacts with the wall, thickening the boundary layer.

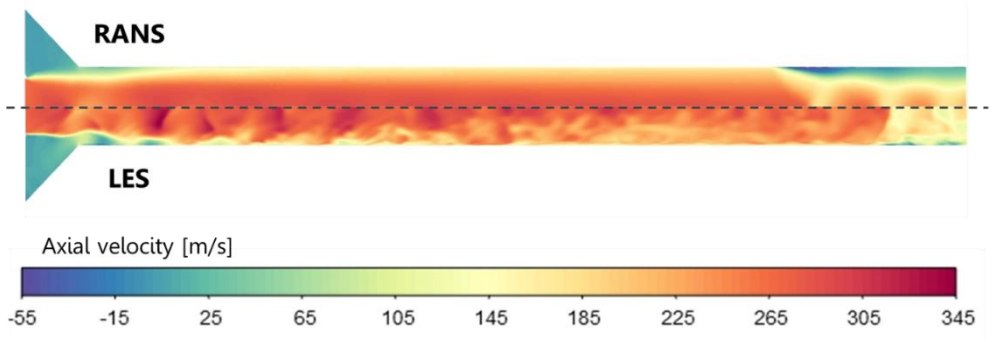


Figure 5.52 – RANS and LES region instantaneous axial velocity field.

Figure 5.53 presents the Mach number field for both RANS and LES simulations, providing deeper insights into the shock phenomena. The sonic line is marked in blue, while vertical lines, coloured red and yellow, indicate compound-supersonic and compound-subsonic flow regimes, respectively.

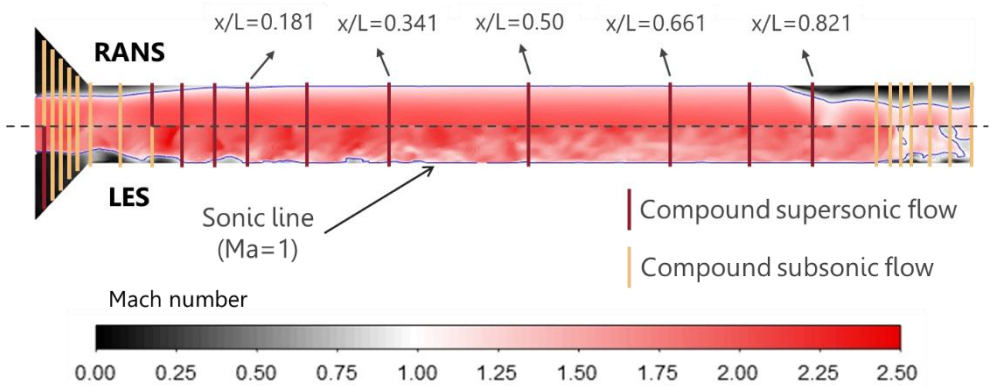


Figure 5.53 – Instantaneous Mach number field for the RANS and LES region, with the sonic line in blue. Vertical lines indicate the compound flow regime: red for compound-supersonic flow and yellow for compound-subsonic flow.

According to Fabri-choking theory, the RANS simulation predicts a supersonic flow regime immediately after x/L=0.181, though in the ELES model, supersonic flow is observed only for x/L>0.341. Additionally, compound-compressible flow theory indicates that the RANS model predicts compound-supersonic flow further upstream compared to ELES. Both simulations agree that the supersonic-to-subsonic transition occurs around x/L=0.821, although Fabri-choking theory suggests an earlier transition in RANS, as indicated by the static wall pressure recovery. Regarding Mach number distribution, RANS predicts a maximum of 2.05 from the nozzle-exit up to approximately x/L=0.8, while the minimum remains nearly constant at Ma=0.9 between x/L≈0.2 and x/L≈0.8. In contrast, the LES predicts a higher peak of 2.5 at x/L=0.080, decreasing oscillatory to approximately Ma=2 near x/L≈0.915, with a minimum fluctuating around Ma=0.5. This underscores the ability of LES to resolve finer flow details, including higher velocity gradients and more intense shock dynamics. Furthermore, the RANS Mach number distribution indicates the presence of an effective throat caused by local thickening of

the boundary layer, a feature more pronounced in RANS due to its inability to fully resolve the shock-boundary layer interactions.

In summary, while the RANS model provides reasonable predictions in regions where the flow is less influenced by shocks, its performance deteriorates significantly in regions dominated by strong shock interactions and the supersonic-to-subsonic transition. The observed differences, particularly in the prediction of shock positions and local flow properties, highlight the limitations of RANS. The ELES approach has demonstrated its capacity to simulated complex ejector flows. By capturing fine-scale turbulence and shock-boundary layer interactions, LES offers more accurate predictions of critical parameters such as wall pressure, Mach number profiles, and the supersonic-to-subsonic transition.

Chapter 6

Thermodynamics is a funny subject.
The first time you go through it, you don't understand it at all.
The second time you go through it, you think you understand it,
except for one or two small points.
The third time you go through it, you know you don't understand it,
but by that time, you are so used to it, it doesn't bother you anymore.
Arnold Sommerfield (1950)

CO_2 ejector simulation results and discussion

This chapter presents the results of two-phase flow ejector simulations conducted using two different modelling approaches. The analysis begins with a 2D axisymmetric model based on the enthalpy-based energy equation (HEM-h), originally developed by Smolka et al. (2013). This well-established model has been extensively validated in the literature (Palacz et al., 2015; Smolka et al., 2016; Ringstad, 2023). Simulations were performed for three different operating conditions, providing a benchmark for the internal energy-based approach developed in this thesis. Subsequently, the ejector was simulated in 3D using the same HEM-h framework to assess the influence of dimensionality on flow behaviour. Building on this, the internal energy-based energy equation (HEM-e) developed in this thesis was applied to the same 3D ejector model, allowing for a direct comparison between the two approaches. Finally, additional studies examined the impact of specific features of the HEM-e model on the simulation results. Experimental data were used as boundary conditions for all simulations to ensure consistency and facilitate validation. This methodology provides a comprehensive understanding of each model's capabilities and limitations in predicting ejector performance.

6.1 Experimental results and definition of the boundary conditions for the CO_2 models

A test rig was previously operated to investigate the performance of a two-phase CO_2 ejector, and the corresponding experimental data was collected by a professor from Bialystok University of Technology, Poland, and provided for this study. The schematics of the experimental setup is shown in Figure 6.1, while the ejector geometry is detailed in Section 4.1.3. To monitor system variables such as temperature, pressure, mass flow rate, and density at different locations, the test rig was equipped with multiple sensors and transducers. Temperature measurements were obtained using calibrated Type-T thermocouples with an accuracy of ±0.4 K and mutual deviations below ±0.1 K. Pressure was recorded using transducers with an accuracy of ±0.25%. Coriolis mass flow meters measured the flow rates and fluid densities, with uncertainties of ±0.1% for liquids and ±0.5% for gases regarding flow rate, and ±0.5 kg/m³ for density. The experimental setup included three auxiliary loops: two thermal load loops for the evaporators (E) and a cooling loop for the condenser (C) (see Figure 6.1). Each loop was instrumented by mass flow meters and temperature sensors positioned at the heat exchanger inlets and outlets.

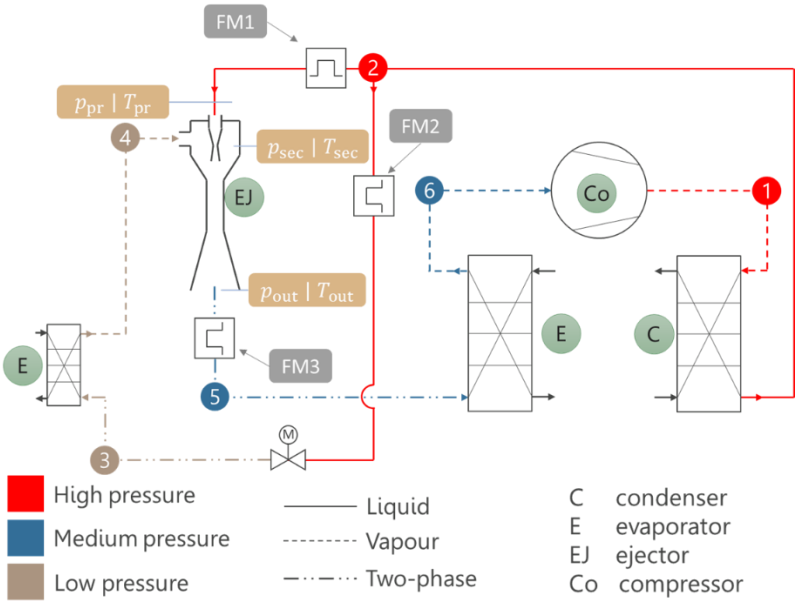


Figure 6.1 – Simplified diagram of the experimental rig.

Experimental data were collected for tree different operation conditions and used to evaluate the CFD models developed in the thesis. Table 6.1 summarises the recorded inlet and outlet conditions for Runs 1, 2, and 3. While Runs 1 and 2 exhibit similar conditions with minor variations, Run 3 shows significant differences, particularly in suction chamber and diffuser outlet pressures. The lower suction chamber pressure in Run 3 (1 732 kPa vs. ~2 012 kPa in Runs 1 and 2) leads to a higher entrained mass flow rate (1.23 g/s compared to 0.52 g/s and 0.41 g/s). Also, the diffuser outlet pressure is considerably lower in Run 3 (1 961 kPa vs. ~2 233 kPa in Runs 1 and 2). These observations confirm that the ejector did not operate in a double-choke regime during the tests.

Table 6.1 – Results obtained during the experimental.

	Run	p [kPa]	T [K]	ρ [kg/m^3]	$\dot{m}$ [g/s]
Nozzle motive inlet	1	3 483	271.75	992	71.1
	2	3 474	271.85	991	70.8
	3	3 451	271.05	995	74.0
Suction chamber inlet	1	2 012	268.25	-	0.522
	2	2 013	268.85	-	0.409
	3	1 732	266.55	-	1.23
Diffuser outlet	1	2 233	264.25	292	-
	2	2 227	264.75	288	-
	3	1 961	262.85	204	-

To verify the thermodynamic states at the experimental data points, the property functions of EES (F-Chart Software, 2020) for CO_2 were used. For a pure substance like CO_2, only two independent properties are required to define its thermodynamic state. At the motive nozzle inlet, CO_2 was in a subcooled liquid state, thus pressure, temperature and density are independent properties, so any two could be used to verify the third. However, measured temperatures were significantly higher, by 7 to 10ºC, than those predicted by EES when using experimental pressure and density values (Table 6.1). This

discrepancy results indicated that at least one of the measured variables did accurately represent the fluid state at the primary inlet.

Given the experimental setup, pressure and density were considered the most reliable and were therefore used as boundary conditions at the primary inlet in the CFD model. At the ejector outlet, experimental pressure and density were also applied, while for the entrained flow, pressure and temperature data were used due to the lack of additional information. Depending on the CFD model, enthalpy and internal energy values were required at the ejector boundaries. These were computed using EES with the Span and Wagner (1996) equations of state. Table 6.2 summarises the boundary conditions applied in the CFD simulations.

Table 6.2 – Boundary conditions for the different RANS simulations, includes enthalpy (h) and internal energy (e) values computed using EES with Span and Wagner (1996) EoS.

	Run	p [kPa]	T [K]	ρ [kg/m³]	h [kJ/kg]	e [kJ/kg]
Nozzle motive inlet	1	3 483	-	992	-332.3	-335.9
	2	3 474	-	991	-331.8	-335.3
	3	3 451	-	995	-333.7	-337.1
Suction chamber inlet	1	2 012	268.25	-	-52.5	-94.9
	2	2 013	268.85	-	-51.8	-94.4
	3	1 732	266.55	-	-49.8	-93.1
Diffuser outlet	1	2 233	-	292	-301.7	-309.3
	2	2 227	-	288	-301.1	-308.8
	3	1 961	-	204	-292.3	-301.9

6.2 Experimental validation of the 2D axisymmetric benchmark ejector model

Simulations were performed with the 2D ejector model in axisymmetric coordinates considering the boundary conditions presented in Table 6.2. The model was based on the HEM-h approach, and the ejector geometry and numerical mesh are shown in Figure 4.6 and Figure 4.16. Computed motive mass flow rates were compared with experimental data in Table 6.3, showing a maximum relative error of 5.7% and an average error of 3.1%. Previous studies (Palacz et al., 2015; Haida, et al., 2018b) reported that the accuracy of the HEM in predicting motive mass flow rates declines significantly for inlet pressures below 5.9 MPa, with errors as high as 33%. Since the pressures in this study were below this threshold, the obtained accuracy can be considered very good.

Table 6.3 – Motive Mass Flow Rate Comparison (Experimental vs CFD Results).

Run	$\dot{m}_{\mathrm{pr-exp}}$ [g/s]	$\dot{m}_{\mathrm{pr-RANS}}$ [g/s]	$\delta_{\dot{m}_{\mathrm{pr}}}$
1	71.1	70.0	-1.5%
2	70.8	69.4	-2.0%
3	74.0	69.8	-5.7%

In contrast, the entrained mass flow rates demonstrated significant deviations between the experimental and CFD results, as presented on Table 6.4. The simulated entrained flow rates were approximately 20 times higher than the experimental values. This greatly exceeds the typical error range of 20%–40% reported in the literature for ejectors operating in the double-choking regime (Smolka et al., 2013; Palacz et al., 2015). Such discrepancies suggest that the experimental data may not represent double-choked ejector flow conditions but rather single-choked flow conditions.

Table 6.4 – Entrained Mass Flow Rate Comparison (Experimental vs CFD Results).

Run	$\dot{m}_{sec-exp}$ [g/s]	$\dot{m}_{sec-RANS}$ [g/s]	$\delta_{\dot{m}_{sec}}$
1	0.522	11.2	2 049%
2	0.409	11.6	2 744%
3	1.23	12.1	882%

Simulated profiles and experimental wall pressure date for the constant-area section of the ejector are presented in Figure 5.3. Sensor locations are described in Section 4.1.3 and the axial positions are relative to the constant-area section inlet (x=0). The experimental pressure data includes an error estimate of ±2%. Looking at the figure it is clear that CFD simulations underestimated the static wall pressure (by about 5%), particularly in the initial region of the constant-area section (x<8.2 mm). As the primary and secondary streams begin to mix, the experimental data indicate a slow wall pressure increase with a not very obvious maximum near the diffuser inlet (x=40 mm). The data (experimental and CFD) do not indicate a shock wave in the constant area section. The high entrained mass flow rates predicted by the CFD model likely contribute to the lower static wall pressure values when compared to experimental data.

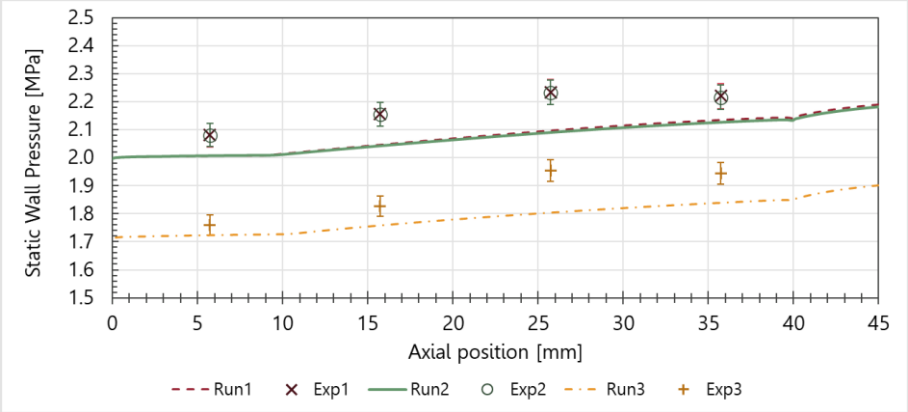


Figure 6.2 – Comparison of experimental wall pressure profile with CFD HEM-h results for Runs 1, 2, and 3 in the constant area section of the ejector.

The experimental and simulated static temperature profiles are shown in Figure 6.3. Measurements were taken at seven axial positions with an uncertainty of ±0.4 K. Significant radial temperature variations (9°C to 24°C) were simulated near the constant-area section inlet, primarily due to differences in state properties between the primary and secondary flows before mixing. For Runs 1 and 2, mixing began from about x=8.2 mm, while for Run 3, it started later at x = 10 mm. Downstream of these points, the oscillations in temperature profiles were caused by shock wave interactions. For x>25 mm, the simulated axial temperature profiles became uniform, indicating complete mixing of the primary and secondary flows. Runs 1 and 2 produced nearly identical results due to similar test conditions, whereas Run 3 exhibited delayed mixing due to differences in the secondary flow's inlet conditions and lower outlet pressure. Despite these variations, the simulations consistently indicated that mixing was completed at similar axial locations across all runs, aligning well with experimental observations.

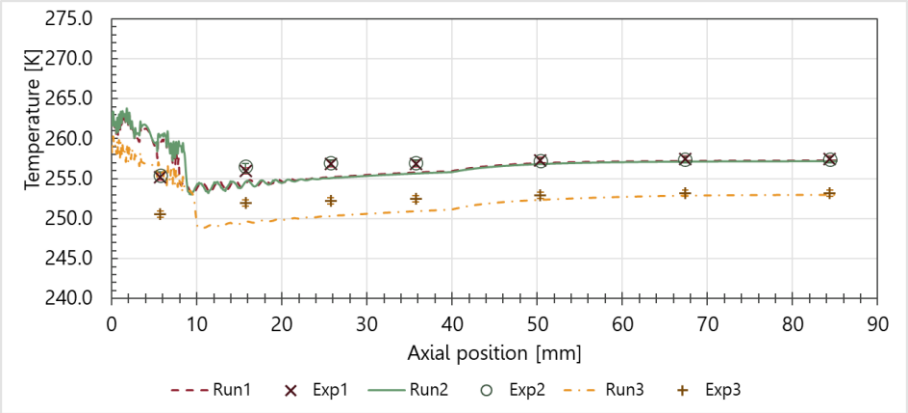


Figure 6.3 – Comparison of experimental and simulated static axial temperature profiles for Runs 1, 2, and 3.

6.3 Discussion of the 2D axisymmetric and 3D CFD model results for the HEM-h formulation

The results discussed in this section were obtained using the HEM-h model, where both 2D and 3D approaches numerically represent the same ejector. Details of the numerical meshes can be found in Section 4.2.3 for the axisymmetric case and in Section 4.2.4 for the 3D case. Besides dimensionality, a considerable difference between the 2D and 3D models lies in how the secondary flow enters the domain. In the 2D case, the secondary stream enters axially, while in the 3D model, it enters radially, better reflecting the experimental ejector design. The data presented in this section were obtained using the boundary conditions for Run 1, as described in Table 6.2.

The static pressure distribution in the mixing chamber and constant-area section is shown in Figure 6.4. The top half presents the results for the 3D and the bottom half for the 2D approaches. Both models predict an oblique shock train in the primary jet stream near the axis, extending through the first half of the constant-area section. The 2D model exhibits longer shock periods, resulting in a more elongated shock train compared to the 3D simulation. Additionally, the shocks in the 2D case appeared weaker, as evidenced by smaller pressure jumps between shocks.

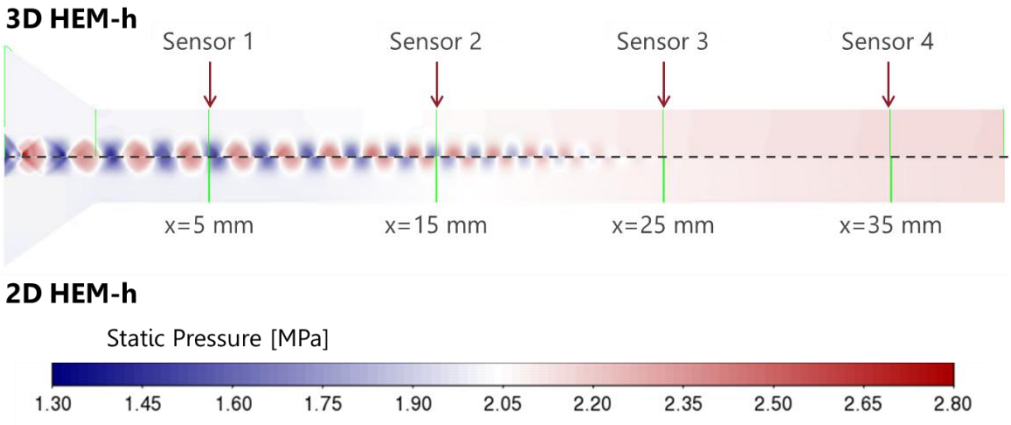


Figure 6.4 – Static pressure field on the symmetry plane in the mixing chamber and constant-area section for the 2D and 3D models.

Figure 6.5 shows the centre line static pressure profile for the mixing chamber and constant-area section. The results indicate that the 2D simulation produced slightly lower static pressure and weaker shock intensities compared to the 3D model. For x>25 mm, i.e., downstream of sensor 3, the flow enters the turbulent mixing regime, where both models show close agreement in the predicted pressure values.

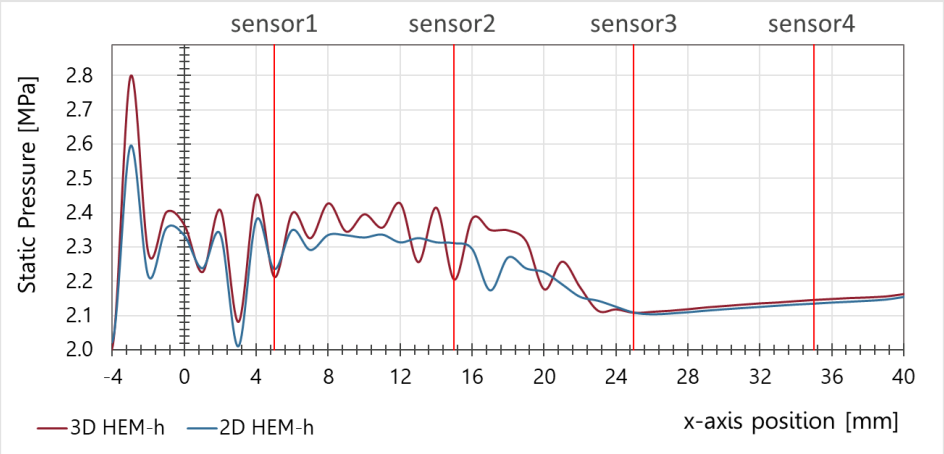


Figure 6.5 – Static pressure along the ejector axis in the mixing chamber and constant-area section for the 2D and 3D models.

Figure 6.6 presents the radial pressure distribution for the 3D model at four axial positions: to the constant-area section inlet (x=0 mm) and the locations of sensors 1, 2, and 3. At the mixing chamber inlet, the secondary flow exhibits nearly uniform pressure, with variations within 0.12%, justifying the omission of the pressure profile for this section. The selected axial positions capture key flow characteristics, including the shock train and the turbulent mixing process. At the constant-area section inlet, the pressure difference between the maximum and minimum values is approximately 10% of the maximum pressure, indicating substantial radial pressure gradients at this location. Further downstream, at x=5 mm and x=15 mm, the pressure profiles show a gradual reduction in these variations, with increasing pressure uniformity. By x=25 mm, the pressure variations have diminished significantly to less than 0.10%, indicating that the shock train's influence is declining, and the flow is transitioning toward a more stable mixing regime.

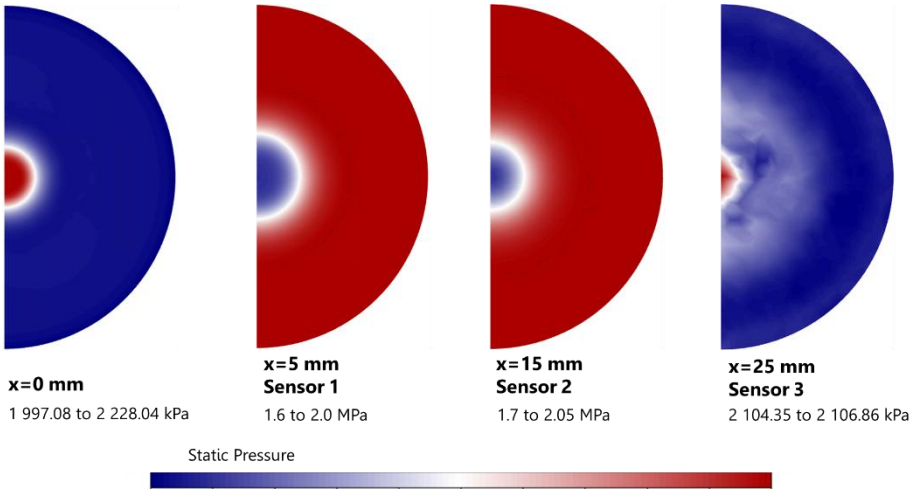


Figure 6.6 – Static pressure at transversal sections:(constant-area section inlet (x=0 mm) and sensor positions 1, 2, and 3, each with a different pressure scale.

As discussed in Section 6.2, the HEM-h 2D model underpredicted the experimental wall pressure profiles. Given the similar magnitude of the results between the 2D and 3D models (see Figure 6.5), it is reasonable to conclude that the 3D model also underestimated the static wall pressure. Despite this, the simulated axial temperature distributions show good agreement with experimental data, as illustrated in Figure 6.7. This figure compares the axial temperature profiles predicted by the 2D and 3D models with the experimental measurements. For x<20 mm, both models exhibit an oscillating temperature pattern due to the presence of strong shock waves. The 3D simulation predicts a wider temperature variation, consistent with the corresponding pressure profiles.

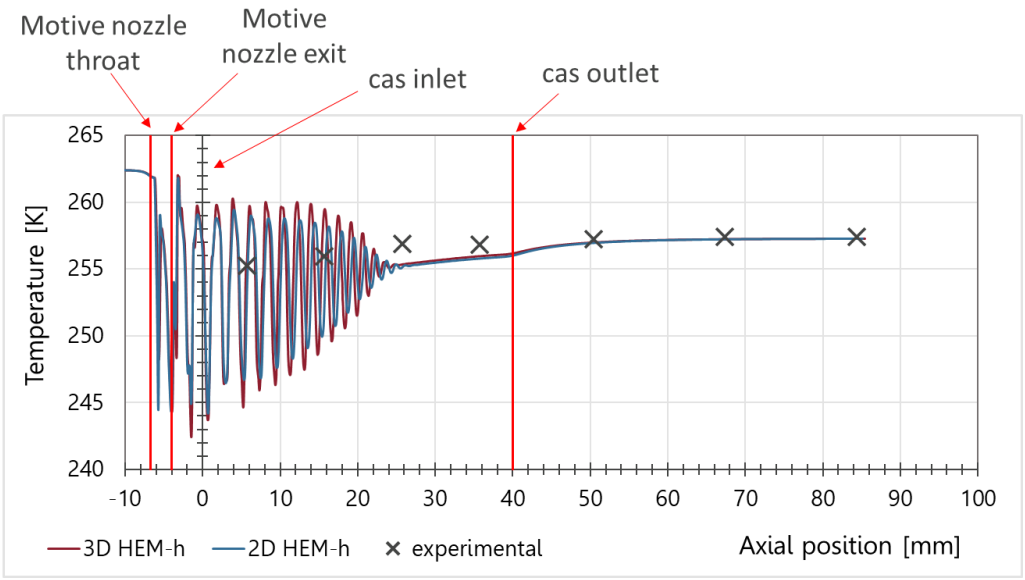


Figure 6.7 – CFD-predicted static temperature along the ejector axis compared to experimental measurements.

The predicted axial specific enthalpy profiles are shown in Figure 6.8. As expected, the fluid enters the primary nozzle with low enthalpy, which decreases during expansion, reaching its minimum at the nozzle exit. In the 2D model, within the mixing chamber and the first half of the constant-area section (x<25 mm), enthalpy remains nearly constant, influenced by oblique shock waves. Beyond x=25 mm, enthalpy increases along the centreline, reaching its maximum at the ejector outlet due to turbulent mixing and pressure recovery. The 3D model exhibited a similar profile until x=15 mm., where it showed a sudden enthalpy drop followed by a gradual increase. For 22 mm<x<44 mm, the 3D model predicted higher enthalpy values, after which the increase rate decreased, resulting in more stable values. At the nozzle exit, the 3D model predicted a lower ejector exit enthalpy, corresponding to reduced vapour quality, likely because it more accurately captures energy exchanges during phase transitions.

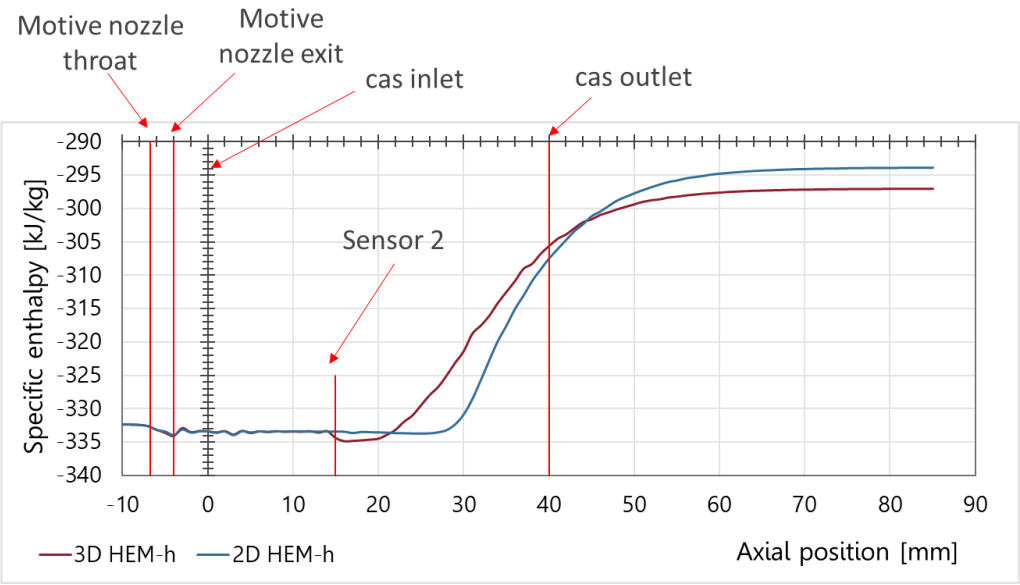


Figure 6.8 – CFD-predicted specific enthalpy along the ejector axis for 2D and 3D HEM-h.

Figure 6.9 presents the fluid density (solid lines) and vapor quality (dashed lines) along the ejector axis, as well as the experimentally measured density at the ejector outlet (single point). As expected for subcooled liquid, density is high in the motive nozzle. At the nozzle throat, flashing occurs, marking the onset of phase change as vapour quality exceed 0%. Until de nozzle-exit (x=-4 mm), both models present very similar results. Beyond this point, in the mixing chamber and constant-area section, density and vapour quality exhibit oscillatory behaviour, reflecting the periodic expansions and compressions of the flow. These oscillations diminish in intensity near x=10 mm, where the density decay slows. By x=15 mm, the oscillations have diminished, and up to this position, both models behave similarly, although the 3D model predicts higher density.

For the 2D model, between x=15 mm and x=29 mm, density decreases steadily, accompanied by a slight reduction in vapour quality. However, at x≈29 mm, their behaviour diverges: while the density maintains its gradual decline, vapour quality exhibits exponential growth, reaching approximately 18% at x=60 mm and remaining constant thereafter until the ejector outlet. In contrast, density decreases from approximately 550 kg/m^3 at x=29 mm to 258 kg/m^3 at the ejector outlet. Although, for x>15 mm, the 3D model predicts more pronounced oscillations in both density and vapour quality, which abruptly cease at x=20 mm, corresponding to the suppression of temperature fluctuations (as shown in Figure 6.7). Beyond this point, similar to the 2D model, density continues to decline while vapour quality increases steadily. In the diffuser region, the 3D model predicts slightly higher density than the axisymmetric approach. At the ejector outlet, it also shows better agreement with experimental density, with relative errors of 7% for vapor quality and 5% for density, compared to 12% and 7%, respectively for the 2D model.

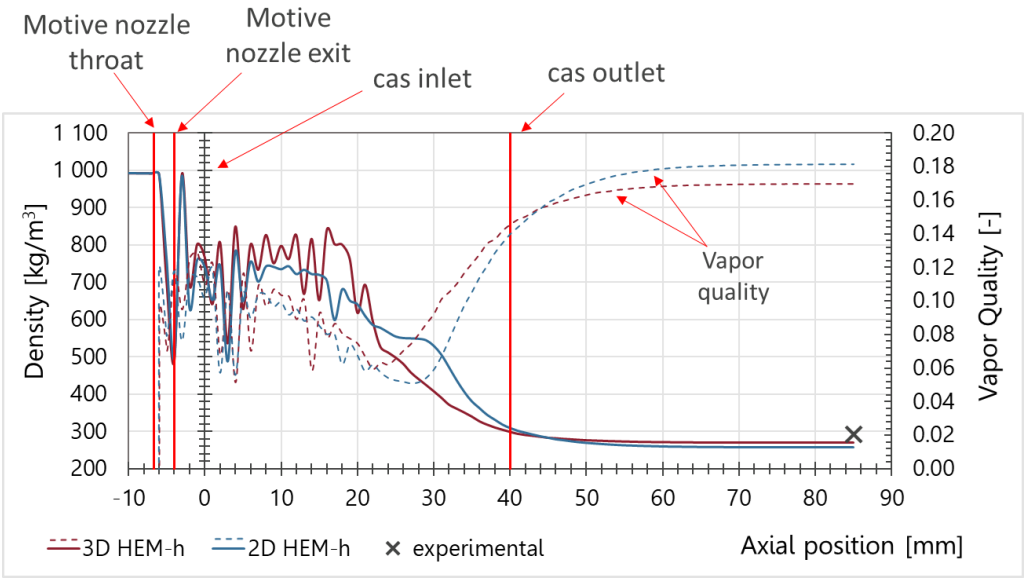


Figure 6.9 – Density (solid lines) and vapor quality (dashed lines) along the ejector axis for the 3D and 2D models (single point experimental density at the ejector outlet also indicated).

The speed of sound in the two-phase CO_2 flow was calculated implementing the model by Lund and Flatten (2010). Figure 6.10 presents the Mach number distribution in the convergent-divergent motive nozzle cross-section, with the top showing results for the 3D model and the bottom for the 2D model. The low Mach number values suggest that the flow remained subsonic within the primary nozzle. However, under the operating conditions of Run 1, the ejector is expected to operate at least in a single-choking regime, meaning the motive flow should choke near the nozzle throat (Angielczyk, 2022).

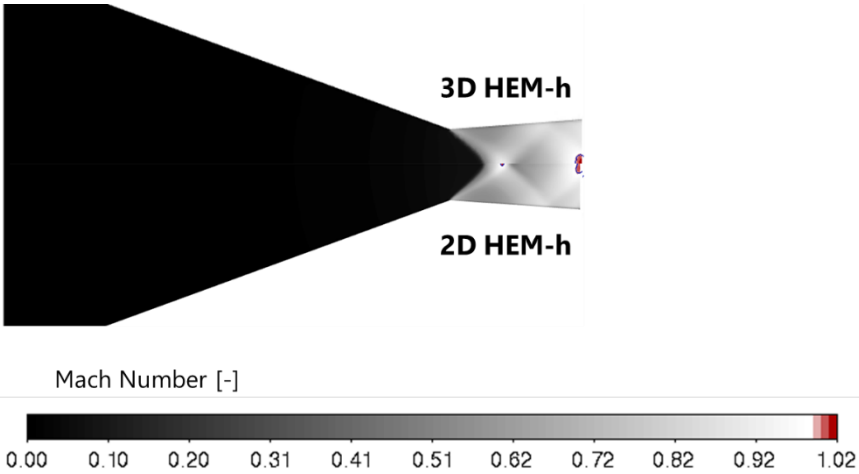


Figure 6.10 – Mach number field over the symmetry plane for the motive nozzle for 2D and 3D HEM-h.

Figure 6.11a) depicts the Mach number field for the mixing chamber and constant area section in both simulations, with the 3D model results displayed on top and the 2D model results on the bottom. It can be seen from the figure that the primary jet was generally subsonic, with small supersonic regions (Ma>1) indicated by blue lines. According to both compound and Fabri-choking theories, the flow remains subsonic throughout the mixing chamber and constant-area section. For a more detailed analysis, Figure 6.11b) depicts the sound speed and Mach number profiles along the ejector axis for the 2D and 3D models. The 3D simulation revealed more pronounced oscillations in sound speed at the constant-area section entrance, particularly up to x=20 mm. Beyond this point, both

models reveal similar sound speed profiles. In terms Mach number, both simulations consistently predict subsonic flow (Ma<1), except near the constant-area section inlet (x=0 mm), where localized supersonic regions appear along the ejector axis. Despite some differences in the mixing chamber and constant-area sections, both models converge to similar results in the diffuser.

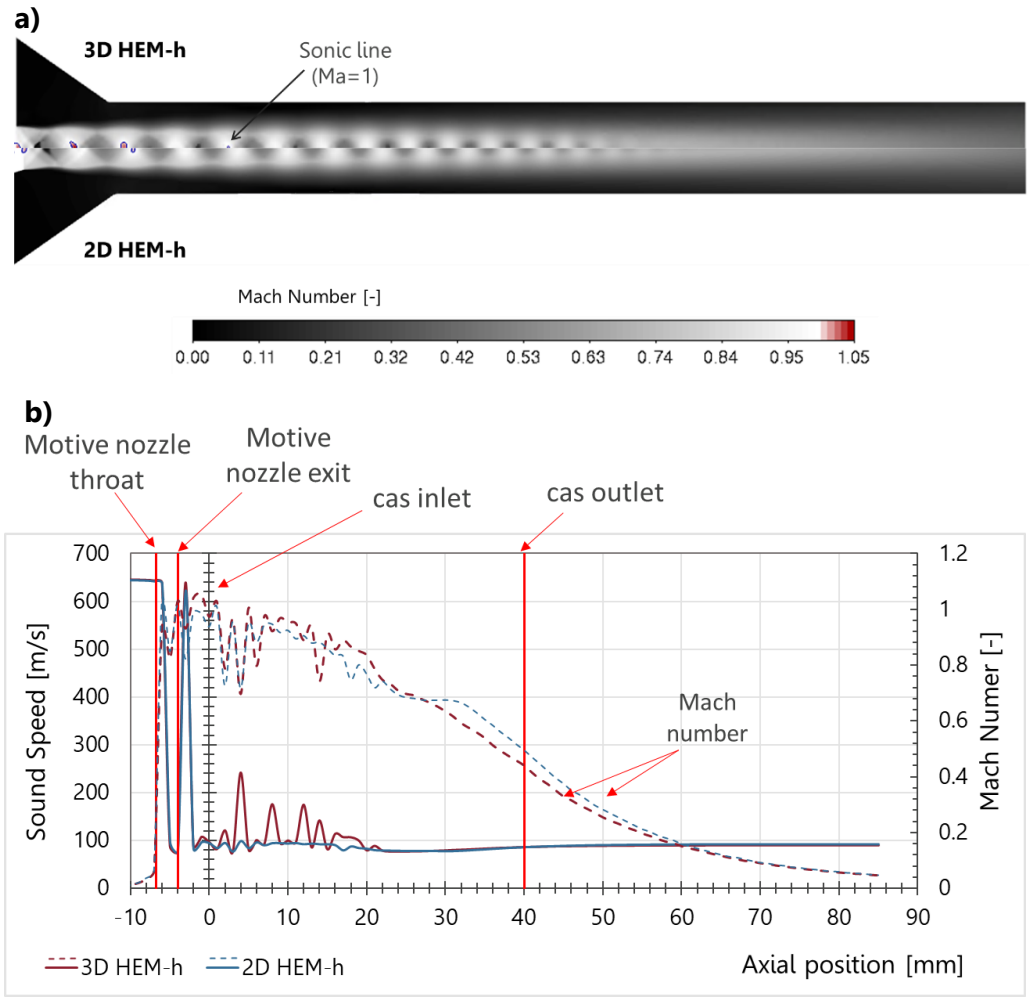


Figure 6.11 –a) Mach number contours over the symmetry plane for the mixing chamber and constant area section; b) Speed of sound (solid lines) and axial Mach number profiles (dashed lines).

Given that the ejector was expected to operate in a single-choke regime and the previous results appeared to underestimate the Mach number values, several simulations were conducted using the 2D HEM-h model to determine the critical back pressure. During these simulations, the ejector inlet conditions remained unchanged, corresponding to Run 1 in Table 6.2, while the ejector outlet pressure was gradually reduced from the experimentally determined value. The results are summarised in Table 6.5. It was observed that the motive mass flow rate ($\dot{m}_{\mathrm{pr}}$) remained constant for all cases, and its value was consistent with the critical flow conditions, confirming that the flow was choked at the primary nozzle throat. This discrepancy suggest that the applied speed of sound model fails to accurately compute the speed of sound under the simulated conditions.

Table 6.5 – Mass flow rate results for the operating curve prediction for the 2D HEM-h.

p_{out} [MPa]	$\dot{m}_{pr}$ [g/s]	$\delta_{\dot{m}_{pr}}$	$\dot{m}_{sec}$ [g/s]	$\delta_{\dot{m}_{sec}}$
2.23	70.018	-	11.207	-
2.00	70.018	0.00%	26.413	57.57%
1.80	70.018	0.00%	45.056	41.38%
1.50	70.018	0.00%	45.130	0.16%

Table 6.6 compares the mass flow rates predicted by the 2D and 3D models for the boundary conditions defined in Run 1. The difference in motive mass flow rate between the two models was as low as 2.20%, indicating that the axisymmetric 2D model provides sufficient accuracy for predicting global variables such as $\dot{m}_{pr}$. However, a more significant discrepancy of 10.5% was observed in the entrained mass flow rate. This difference can be attributed to the limitations of the 2D model in representing the secondary inlet region, where the flow enters axially (see Figure 4.6). In contrast, the 3D model accounts for a radial secondary flow inlet (see Figure 4.7), which more accurately represents the actual configuration of the experimental ejector.

Table 6.6 – Predicted mass flow rates and corresponding mass imbalance.

	2D HEM-h	**3D HEM-h**	**Difference**
$\dot{m}_{pr}$ [g/s]	70.02	68.48	2.20%
$\dot{m}_{sec}$ [g/s]	11.21	10.03	10.5%
Mass imbalance [%]	-0.04%	0.63%	

At the motive nozzle outlet, the significant difference in kinetic energy between the primary and secondary flows dominates the overall flow behaviour, minimizing the influence of the entrained flow on the pressure distribution and in other thermodynamic properties within the mixing chamber. Significant interaction between the two streams occurs primarily in the constant-area section, where mixing leads to a gradual homogenization of flow properties along a given cross-section. In the diffuser, flow deceleration amplifies local variations in thermodynamic properties, an effect that is likely driven by flow separation and shock wave dynamics rather than exclusively by the geometry of the entrained flow inlet. Nevertheless, under the applied boundary conditions, the assumption of axisymmetric flow proved to be valid, enabling a significant reduction in computational cost and complexity while yielding results comparable to those obtained with the 3D simulation.

6.4 Comparison of 3D Symmetric Results for the HEM-h and HEM-e Models

The results of the 3D HEM-h and 3D HEM-e models are discussed in this section. A mathematical description of both models is provided in Section 3.3. To ensure comparability, the simulations were conducted using the same mesh and boundary conditions (Run1 - see Table 6.2). The analysis focuses on both local variables, such as pressure, temperature, and internal energy, as well as global variables, including mass flow rates. For the HEM-h simulations, the speed of sound was calculated using the property function developed by Lund and Flåtten (2010), whereas for the HEM-e

simulations, the formula published by Brennen (2005) was implemented due to the limitations of the former. Using the same initial estimates and convergence criteria (see Section 4.4.4), the HEM-e model converged significantly faster. While the HEM-h model required approximately 18 000 iterations, the HEM-e model converged in only 3 000 iterations.

Table 6.7 summarizes the predicted motive and entrained mass flow rates for both models. The results indicate a negligible difference of 0.08% in the motive mass flow rate between the two models. The entrained mass flow rate shows a slightly higher discrepancy (~1%), which is still within the accuracy range of most flow meters.

Table 6.7 – Predicted mass flow rates and corresponding mass imbalance.

	3D HEM-h	**3D HEM-e**	**Difference**
$\dot{m}_{\mathrm{pr}}$ **[g/s]**	68.48	68.42	0.08%
$\dot{m}_{\mathrm{sec}}$ **[g/s]**	10.03	9.94	0.95%

Figure 6.12a) focuses on the shock train in the mixing and constant area sections, with the top half showing the results for the HEM-e model and the bottom half for the HEM-h model. It can be seen from the figure that both models resulted in a very similar flow structure downstream the nozzle exit plane. It was also found that the calculated minimum and maximum pressures agreed well. For x<5 mm (sensor 1), the shock train is symmetrical for both models, showing similar periods. Beyond this point, the HEM-e model resulted in shorter shock periods, leading to an earlier dissipation of the shock train. This is better visualised in Figure 6.12b) where the static pressure profile at the ejector axis is depicted for HEM-e and HEM-h. The observed differences may be attributed to the explicit accounting for pressure work and dilatation effects. The HEM-e model is expected to provide a more detailed representation of the strength and progression of shock waves, thereby influencing their dissipation dynamics.

Figure 6.13 shows the centreline temperature profiles for both models, along with the experimental data for Run 1. The temperature profiles from the two models closely agree up to x=25 mm. Further downstream, minor differences between the profiles can be observed resulting from the differences in estimating the energy exchange during the mixing process. This behaviour can be a consequence of the explicit inclusion of the pressure work and dilatation effects in the HEM-e formulation, which are important for high-speed compressible flows (Sarkar, S. et al., 1993). In contrast, the HEM-h approach lacks a direct representation of these terms, resulting in less accurate internal energy gradient calculation and higher localized temperature variations near shocks.

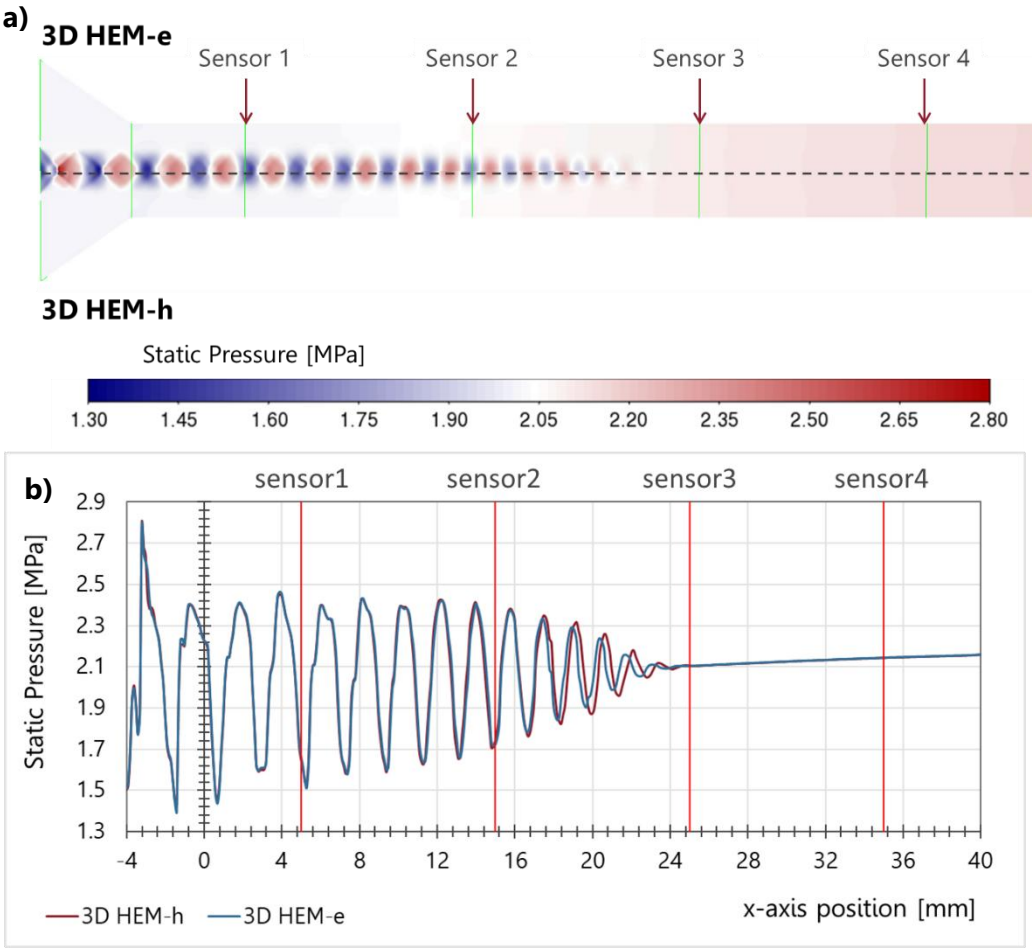


Figure 6.12 – a) Static pressure field and b) axial static pressure profile for the mixing chamber and constant area section.

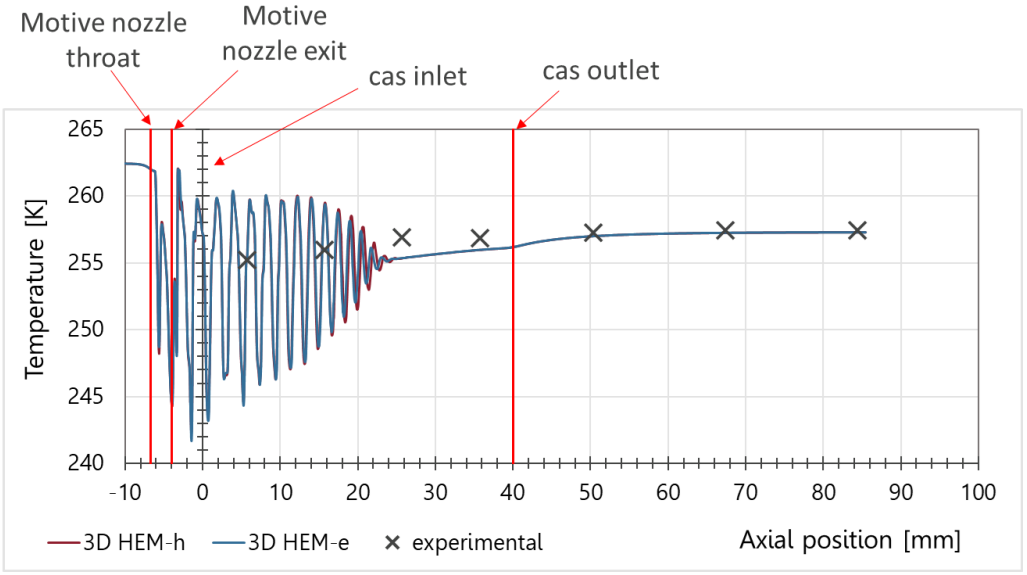


Figure 6.13 – CFD-predicted static temperature along the ejector axis compared to experimental measurements.

Figure 6.14a) illustrates the internal energy field for the mixing chamber and constant-area section, with the HEM-e results shown on the top and the HEM-h results on the bottom. It can be observed in the figure that both models led to very similar results that is consistent with the temperature field shown in Figure 6.13. Minor differences in the axial internal energy profiles are visible in Figure 6.14b) for x>15 mm (sensor 2), which reflect the variations observed in the temperature profile.

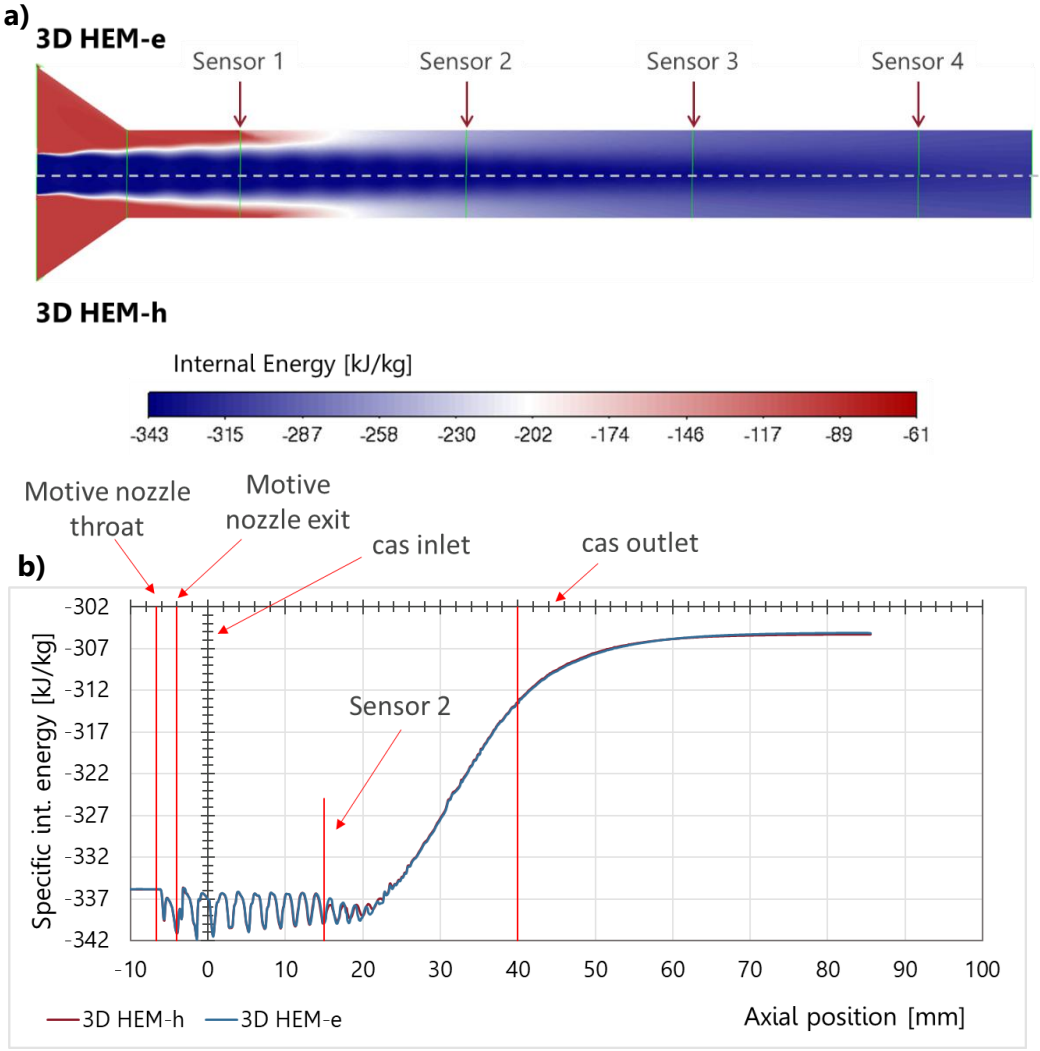


Figure 6.14 – a) Specific internal energy field for the 3D HEM-h model (top) and the 3D HEM-e model (bottom) displayed over a streamwise midspan plane encompassing the mixing chamber and constant-area section; b) CFD-predicted specific internal energy profiles along the ejector axis for HEM-h and HEM-e.

As described in Section 4.3.1, the speed of sound model can be selected via the UDF header prior to starting the simulation. For the HEM-h model, the speed of sound was calculated using the method proposed by Lund and Flåtten (2010), while the HEM-e model utilised Brennen's (2005) approach. To assess the impact of the speed of sound model on the results, the HEM-e model was also implemented using Lund and Flåtten's (2010) approach, ensuring all other simulation parameters (mesh, boundary conditions, and convergence criteria) remained identical (details can be found in Appendix G).

Analysing the results, it was found that significant differences were obtained for the Mach number. Figure 6.15 shows the centreline Mach number distribution for the 3D HEM-h

and 3D HEM-e models, including HEM-e with Brennen's (2005) model (HEM-e-B) and Lund and Flåtten's (2010) model (HEM-e-LF). Brennen's (2005) model predicted considerably higher Mach number, especially when both liquid and vapour phases coexist, essentially all ejector downstream the motive nozzle throat (x>-6.5 mm). Conversely, the HEM-h and HEM-e-LF models produced very similar results.

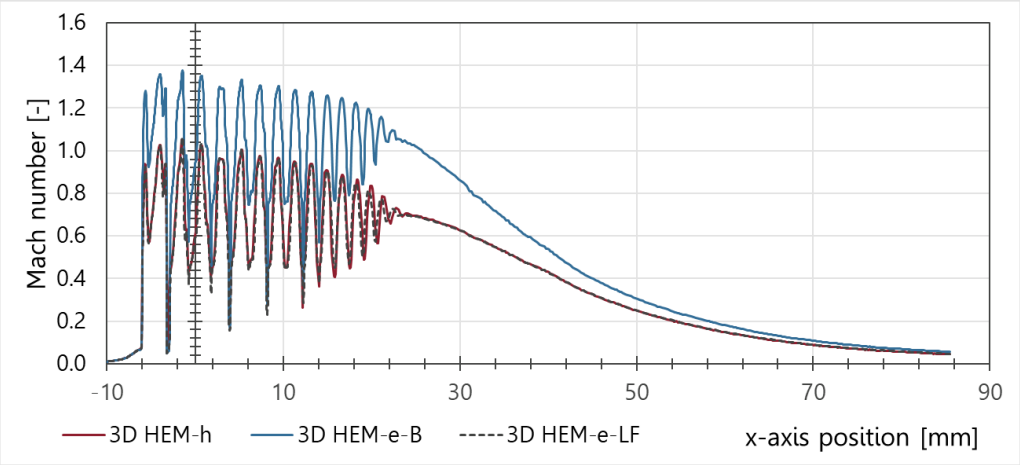


Figure 6.15 – Mach number at the ejector axis for the 3D HEM-h and 3D HEM-e B and LF models.

Figure 6.16 allows a quick comparison of the Mach number distribution inside the motive nozzle for the two models. The top figure corresponds to the 3D HEM-e model using Brennen's (2005) speed of sound function, while the bottom represents the HEM-h model. The flow enters the primary nozzle with a very low Mach number in the liquid phase. In the convergent section, the static pressure decreases, initiating fluid evaporation. This process leads to a velocity increase and a simultaneous reduction in the speed of sound. As a consequence, the Mach number rises after the nozzle throat in both models. However, substantial differences are observed in the computed Mach number within the divergent section. The HEM-h model, which employs Lund and Flåtten's (2010) speed of sound function, predicts Ma< 1 throughout most of the divergent section, which is inconsistent with the expected expansion and evaporation processes. In contrast, the HEM-e model, using Brennen's (2005) function, predicts choked flow at the nozzle throat, followed by expansion in the divergent section, reaching a maximum Mach number of 1.36 at the outlet plane. These results are consistent with the simulated ejector critical backpressure and mass flow rate data presented in Table 6.5. Thus, the findings suggest that Brennen's (2005) speed of sound function is more suitable for simulations two-phase CO_2 ejector flow. According to Fabri-choking theory (Fabri and Siestrunck, 1958), a flow is considered supersonic only if the Mach number exceeds one across the entire cross-section. Based on this criterion, choking is observed at x=-5.9 mm, approximately 0.8 mm downstream of the nozzle throat. This finding challenges the conventional assumption that choking occurs precisely at the nozzle throat.

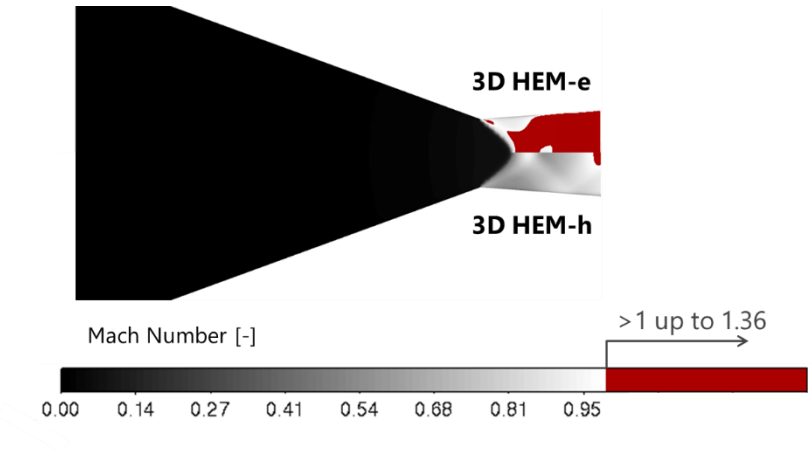


Figure 6.16 – Mach number at the motive nozzle in the symmetric plane for HEM-e and HEM-h model.

In two-phase flows, choking is more complex due to the interaction between phase density variations, phase transitions, and energy exchange mechanisms, which can alter the axial position where the Mach number first reaches unity (Angielczyk, 2022). The downstream shift in the choking location is primarily driven by compressibility effects and the metastable behaviour of the two-phase mixture. However, it is important to note that the HEM does not account for the metastable effects. In this context, density, sound speed, and Mach number deviate from the simplified relationships that govern ideal gas flows. Unlike in ideal gases, where choking depends only on temperature, pressure, and the specific heat ratio, in two-phase flows, the vapour fraction of the working fluid and the energy transfer dynamics between phases also play a critical role (Angielczyk, 2022).

The results show the impact of the chosen speed of sound function in capturing critical flow conditions. Choking at the motive nozzle, followed by subsequent expansion, is essential for adequate ejector operation, since a highly expanded primary jet is needed to entrain the secondary flow effectively. The Mach number distribution in the mixing chamber and constant-area section of the ejector is depicted in Figure 6.17. According to the compound-compressible flow theory, neither model predicts supersonic flow beyond the motive nozzle, which aligns with experimental measurements and confirms a single-choking ejector operation.

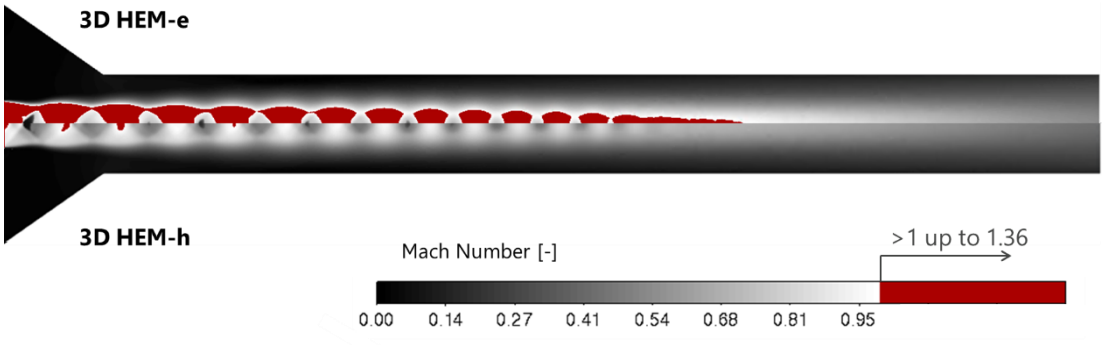


Figure 6.17 – Mach number distribution in the mixture chamber and in constant area section for HEM-e (top half) and HEM-h (bottom half) models.

Based on the results presented in this section, it can be concluded that the developed HEM-e model provides an improved alternative to the commonly used HEM-h approach. From a numerical perspective, it offers better stability, faster convergence, and improved overall balances of the ejector flow. The results also indicate that the inclusion of pressure

dilatation and pressure work effects in the internal energy transport equation impacts the shock train distribution. These terms explicitly account for compressibility effects and high-speed flow dynamics, enabling HEM-e to better capture the physics of turbulent energy dissipation in ejector flows. In contrast, the HEM-h model incorporates these effects indirectly through the turbulent dissipation term, which may lead to reduced accuracy in cases where pressure gradients and compressibility effects are dominant.

6.5 Discussion of the HEM-e model results with and without considering the turbulent kinetic energy source terms

ANSYS FLUENT (ANSYS Inc., 2022a) does not account for pressure dilatation and pressure work in the SST k-ω turbulence transport equations. To assess the impact of these physical phenomena, two additional sources terms ($\dot{S}_{1\mathrm{TKE}}$ and $\dot{S}_{2\mathrm{TKE}}$) were implemented into the model, as described in detail in Section 3.3.4. This section presents the results of the 3D HEM-e simulation with and without these terms, referred to as 3D HEM-e and 3D HEM-e-TKE, respectively. in this section. Both simulations were conducted using the same boundary conditions (Run 1) and numerical mesh to ensure comparability, and in both cases, the speed of sound was calculated using Brennen's (2005) property function. The HEM-e TKE simulation was initialized using the solution from the HEM-e model and required approximately 4 000 iterations to meet the convergence criteria. Table 6.8 presents the predicted motive and entrained mass flow rates for both models, showing negligible differences between them.

Table 6.8 – Predicted mass flow rates and corresponding mass imbalance.

	3D HEM-e	**3D HEM-e TKE**	**Difference**
$\dot{m}_{\mathrm{pr}}$ **[g/s]**	68.42	68.42	0.0%
$\dot{m}_{\mathrm{sec}}$ **[g/s]**	9.94	9.99	-0.54%

Figure 6.18 presents the axial pressure profile for both models, including a detailed view of the shock train dissipation zone. The HEM-e TKE model predicts shock with similar length but with greater amplitude compared to the HEM-e model. The profiles coincide up to x=15 mm (sensor 2), after which the HEM-e TKE model exhibit slightly longer shock wavelengths while maintaining a comparable amplitude.

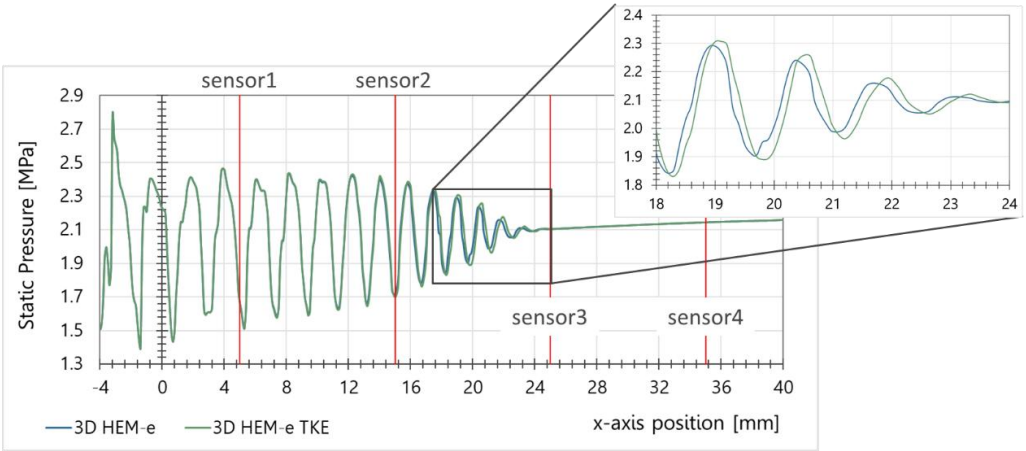


Figure 6.18 – Static pressure along the ejector axis for HEM-e, and HEM-e TKE.

Figure 6.19 illustrates the axial density profile, focusing on the oblique shock train region (15 mm < x < 31 mm). The HEM-e TKE model predicts more intensive density variation across the early shock waves with a rapid decay. Initially the amplitude of the density changes is comparable to that predicted by the HEM-e without TKE. However, the slower attenuation in the HEM-e TKE model results in higher density values further downstream (x≈23.3 mm). This behaviour suggests that the inclusion of TKE sources reduces energy dissipation in the flow, allowing the shock train to extend further downstream.

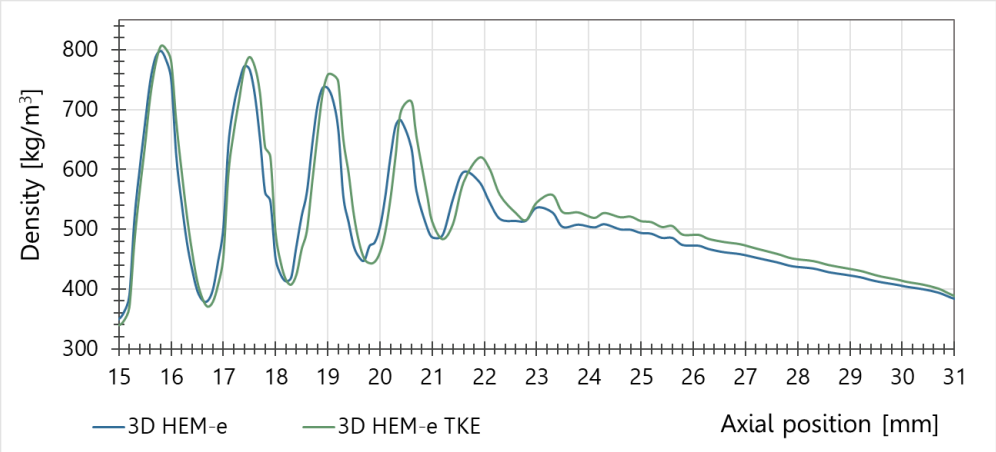


Figure 6.19 – Density along the ejector axis, focusing on the shock train.

Figure 6.20 presents the axial vapour quality profiles between 16 mm < x < 36 mm, comparing the HEM-e and HEM-e TKE models. The results indicate that the HEM-e TKE model predicts lower vapour quality during the shock train. This suggests that the inclusion of turbulence-related effects, such as pressure work and dilatation, modifies the representation of energy exchange and phase transitions during the mixing process. The lower vapour quality predicted by the HEM-e TKE model may indicate a reduced rate of evaporation, possibly due to the redistribution of energy in the compressible, turbulent flow regions. Although both models show similar trends overall, the HEM-e TKE model captures pronounced localised variations in thermodynamic properties, reflecting the impact of turbulence effects. However, it is important to note that there is no significant difference between the models in predicting global flow variables, such as the mass flow rates. Further experimental validation would be required to determine whether the additional complexity introduced by the HEM-e TKE model offers a more accurate representation of the local flow field.

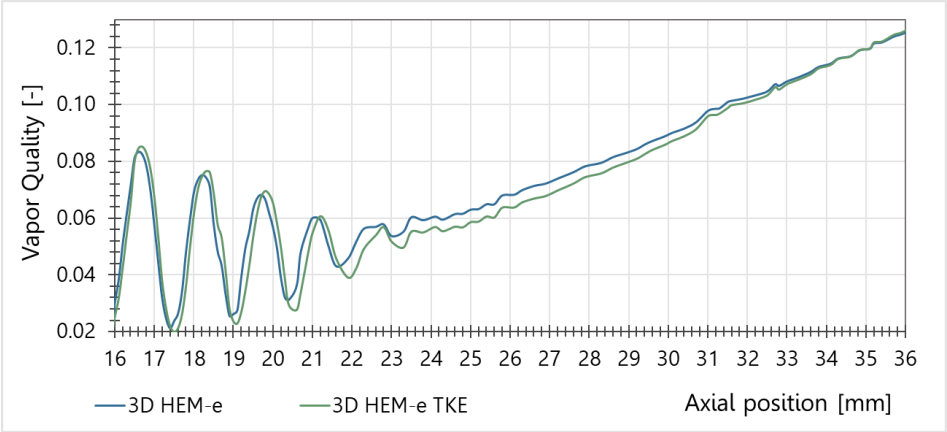


Figure 6.20 – Vapour quality along the ejector axis for HEM-e, and HEM-e TKE.

Based on the results presented in this section, it can be concluded that the HEM-e TKE model showed negligible impact on the global flow variables such as flow rates and the entrainment ratio. Consideration of the pressure dilatation and pressure work in the solution of the turbulent kinetic energy transport equation had a small impact on the local variables such as the density profiles in the shock train and mixing regions. This limited influence of the pressure work and dilatation terms may be attributed to the single-choke regime of the flow, where the effects of compressibility are less pronounced. These findings indicate that, under the tested operating conditions, incorporating these terms into the turbulent kinetic energy equations does not yield notable advantages for ejector flow simulations. Consequently, experimental data are required to investigate the performance of the model under double-choke flow conditions, where compressibility effects may be more pronounced.

Chapter 7

Turbulence is the most important
unsolved problem of classical physics.
Richard Feynman (1964)

Conclusions and recommendations for future research

This chapter summarizes the main findings of this thesis, emphasizing the contributions to the advancement of ejector flow modelling. The conclusions reflect on the accuracy and efficiency of the implemented models, while recommendations for future work propose extending these methodologies to a wider range of operating conditions and refining them to improve predictive capabilities.

The primary objective of this study was to increase the knowledge on ejector flow with the help of numerical modelling techniques regarding both single-phase and two-phase systems. Conventional models often struggle to accurately describe the local flow dynamics, particularly during mixing which is governed by turbulence, shock interactions, and phase transitions. This research addressed a number of issues by integrating advanced computational methodologies into CFD models with a good balance between computational efficiency and accuracy, describing flow physics with a scope to offer valuable tools for ejector optimisation and design.

7.1 Embedded large eddy simulation model for single-phase R1234ze(E) ejector

Based on the results, it can be concluded that the ELES model permits a more fundamental insight of the mixing phenomena in ejectors, when compared to the Reynolds Averaged Navier Stokes (RANS) models. Although the RANS CFD model showed good accuracy for motive mass flow rate, the entrained mass flow rate prediction was weak, particularly under off design (single-choking) ejector operation. Also, the RANS model struggled with simulating local shock dynamics and supersonic-to-subsonic transitions under double-choking conditions. The ELES results demonstrated that resolving approximately 80% of the turbulent kinetic energy (TKE) in the ejector requires a mesh size of 4.07 million cells. Spectral analysis of TKE revealed distinct energy cascade dynamics influenced by shock-vortex interactions, confirming the mesh's ability to capture the critical mixing process. Additionally, the results suggested that further refinement of the numerical mesh in the mixing chamber could enhance resolution and accuracy.

LES results revealed a nearly homogeneous pressure field downstream the constant-area section midpoint (x/L=0.50), indicating the conclusion of the mixing process. The shock train and subsequent normal shock were well predicted and clearly demonstrated by the pseudo-Schlieren images and Q-criterion analysis. The results confirmed the presence of oblique and λ-shock trains. These results demonstrated the ability of LES to resolve vortex structures and turbulence, shedding light on how energy dissipates through the shock, resulting in enhanced mixing in the turbulent mixing region. The axial location of the supersonic-to-subsonic transition was accurately simulated, demonstrating the consistency between flow physics and simulation.

Shock train positions were consistent across time-averaged and instantaneous analyses, although the normal shock exhibited dynamic fluctuations near the end of the turbulent mixing region. Wall shear stress and displacement thickness oscillated near shocks, reflecting the interaction between boundary layers and shock-induced compression and expansion waves. The core pressure profiles showed alternating compression and expansion waves, which gradually smoothed out in the turbulent mixing region, due to the non-equilibrium nature of the flow. Beyond x/L>0.5, the flow stabilised, adapting to the ejector's geometric constraints. ELES successfully captured the evolution of velocity profiles, providing detailed localisation of the fully developed turbulent flow within the constant-area section.

ELES significantly outperformed RANS in several key areas. First, ELES demonstrated superior accuracy in predicting wall pressure and temperature profiles, especially near shock-affected regions. Second, LES captured broader ranges of thermodynamic and flow variables, including temperature (259 K to 315 K), velocity (−55 m/s to 345 m/s), and Mach numbers (up to 2.5), providing a more comprehensive depiction of ejector dynamics. In contrast, RANS averaged out fine-scale fluctuations, leading to smoother but less accurate predictions. Third, while both RANS and ELES underestimated the motive mass flow rate, with average errors of 3% and 5%, respectively, ELES demonstrated greater accuracy in predicting the entrained mass flow rate, achieving an average error of 12.4% compared to 17.2% for RANS.

Despite its advantages, ELES is computationally more demanding than RANS, which limits its practicality for scenarios requiring rapid solutions or iterative design processes. RANS, while less precise, remains adequate for regions where shock interactions are minimal, and turbulence is less dominant. However, in regions dominated by shock dynamics and turbulence, such as the mixing chamber and constant-area section, the limitations of RANS become evident, emphasizing the necessity of LES for accurate predictions of local flow properties.

These findings confirm the indispensable role of LES, particularly within the ELES framework, for advancing ejector research and optimising performance. ELES provides not only a more accurate representation of ejector flow dynamics but also critical insights for designing ejectors capable of achieving higher efficiency in practical applications.

7.2 Two-phase CO_2 ejector simulation

Four different cases were developed to simulate the two-phase flow ejector. The 2D axisymmetric HEM-h model was initially employed as a benchmark. Subsequently, 3D simulations using the same framework were conducted to assess the impact of dimensionality on flow behaviour. The novel internal energy-based model (HEM-e) and its turbulence-enhanced variant (HEM-e TKE) were then applied in 3D, enabling a comprehensive comparison of their capabilities and limitations in predicting ejector performance under a specific operating condition.

The conventional 2D HEM-h model demonstrated good accuracy in predicting motive mass flow rates, with maximum and average relative errors of 5.7% and 3.1%, respectively. This performance is notable, considering the low inlet pressure of 3.48 MPa, whereas previous studies have reported significantly higher errors for motive inlet pressures below 5.9 MPa. However, the model significantly overestimated entrained mass flow rates, likely due to the experimental ejector operating under off-design single-choking conditions. Static wall pressure profiles were underestimated in the initial

section of the constant-area region, primarily due to overpredicted entrained flow rates. While RANS models provided valuable insights into mixing length and general flow characteristics, caution should be exercised when interpreting local flow interactions during mixing due to inherent limitations.

Based on the comparison of 2D and 3D HEM-h models revealed that the 3D approach did not offer substantial additional insight into ejector flow dynamics compared to the 2D approach, even though that the 2D model did not closely resembled the secondary inlet geometry of the modelled ejector. Despite this, both models reasonably agreed in predicting static pressure profiles, with the 3D model indicating a slightly shorter shock train structure. Predictions of motive mass flow rates differed minimally (2.20%), while entrained flow rate predictions showed a more significant discrepancy (10.5%).

The newly developed 3D HEM-e demonstrated notable advantages over the HEM-h, particularly in numerical stability and convergence speed, achieving approximately six times faster convergence. While both models predicted similar global flow variables, such as mass flow rates and entrainment ratio, local flow analysis revealed key differences. The HEM-e predicted shorter shock periods and a faster decay of the shock train in the constant-area section. Moreover, incorporating pressure work and dilatation effects into the turbulent kinetic energy (TKE) transport equation in the HEM-e TKE resulted in higher downstream densities and reduced energy loss. Additionally, vapour quality predictions suggested that the HEM-e TKE captured the impact of compressibility effects on energy exchange and phase transition, leading to slower evaporation during mixing. These findings emphasize the impact of pressure work and dilation effects in energy transfer and phase behaviour in two-phase ejector flows.

Another important conclusion of this thesis concerns the choice of the speed of sound function for two-phase CO_2 flows. It was found that Brennen's (2005) formulation outperformed the model proposed by Lund and Flåtten's (2010). The latter yield Mach number fields that were inconsistent with the expected operating regime of the ejector, whereas Brennen's model provided more accurate and physically consistent results.

7.3 Suggestions for future work

The research work carried out within the framework of this thesis, opened up a number of new questions that need to be answered and issues that should be addressed in future work. One of these concerns the single-phase flow ejector simulations using the ELES model. Unexpectedly high errors in the predicted motive mass flow rate were observed, which could be attributed to the significant portion of the flow domain being simulated with the RANS approach. Additionally, the motive and entrained mass flow rates were found to be highly sensitive to the outlet pressure field in the constant-area section, as determined by the RANS simulations. This dependency imposes a limitation on the overall accuracy of the LES results.

For the two-phase flow ejector simulations, although the developed HEM model demonstrated improvement compared to previously published models, the new sources terms in the turbulent kinetic energy (TKE) transport equation had minimal impact under off design operation. Additionally, the validation of CO_2 ejector models are constrained by the lack of high-quality experimental data. The absence of comprehensive measurements under diverse operating conditions restricts the confidence in CFD generated results explaining the local flow field.

Based on the previously mentioned issues and the findings of this thesis, several topics for future research are proposed to advance ejector flow dynamics and numerical modelling. One is the refinement of the precursor RANS simulation mesh to provide a more detailed boundary condition for the ELES approach. Additionally, expanding the scope of LES beyond ELES could provide improved simulation accuracy. Two specific strategies are suggested. Firstly, employing LES in the nozzle zone could enhance the motive mass flow rates prediction by offering a more accurate resolution of supersonic flow behaviour and shock wave interactions. Secondly, applying LES in the diffuser may lead to more accurate entrained mass flow rate estimations. Further mesh refinement is also recommended in regions with high velocity gradients, particularly where turbulent kinetic energy resolution falls below 80%, to improve the reliability of local flow predictions by capturing complex phenomena with greater accuracy, especially those involving turbulence-shock interactions. Finally, a thorough evaluation of the ELES capabilities in predicting ejector flow behaviour under single-choke operating conditions is recommended, given that RANS methodologies fail to accurately estimate the entrained mass flow rate.

Regarding two-phase ejector flow modelling, it is proposed to study the new model performance under double-choking conditions, placing particular emphasis on capturing details in the mixing process. This study was not undertaken in the present work due to the lack of experimental data under double-choking flow regimes, which are essential for validating the model and accurately assessing the internal pressure and temperature profiles. The availability of such experimental data would provide the necessary basis for further investigation into this phenomenon. A study of the ejector flow under on-design and off-design conditions would be very important for understanding behaviour of ejectors and expanding their application range. The availability of a shared data bank with a large amount of experimental data for CO_2 ejector systems operating under diverse conditions remains a key requirement for model validation. Detailed measurements of pressure, temperature, and mass flow rates throughout the ejector domain would provide a robust empirical basis for enhancing CFD accuracy and model reliability.

It is proposed to apply the developed models for different working fluids, such as hydrocarbons or refrigerant blends, as well as to the evaluation of relatively new design concepts, such as the variable geometry ejector. These developments would broaden the scope of potential applications, fostering innovation in industries that utilise ejector technologies. Furthermore, the HEM-e model has been designed to integrate seamlessly with LES formulations, paving the way for future applications within the ELES framework. Extending ELES to simulate two-phase flow ejectors could provide additional insight into the mixing process and the influence of terms such as pressure work and dilatation on simulation results. While not implemented in the current study, the results indicate that advanced modelling approaches, such as ELES coupled with the HEM-e formulation, hold significant promise for enhancing ejector performance by providing deeper insights into turbulence-shock interactions and mixing dynamics.

Finally, the improvement or development of suitable models to characterize average velocity fluctuations and pressure dilation is necessary. The models applied in this thesis were those available in the literature, whose assumptions do not fully capture the complexity of two-phase ejector flow, particularly the effects of high mean velocity gradients on the averaged velocity fluctuation or the consideration of isotropic turbulence for pressure dilatation.

References

Aidoun, Zine, Khaled Ameur, Mehdi Falsafioon, and Messaoud Badache. 2019. "Current Advances in Ejector Modeling, Experimentation and Applications for Refrigeration and Heat Pumps. Part 2: Two-Phase Ejectors." *Inventions* 4(1): 16. doi:10.3390/inventions4010016.

Aldama, Alvaro A. 1990. 56 *Filtering Techniques for Turbulent Flow Simulation*. Berlin, Heidelberg: Springer Berlin Heidelberg. doi:10.1007/978-3-642-84091-3.

Ameur, Khaled, Zine Aidoun, and Mohamed Ouzzane. 2016. "Modeling and Numerical Approach for the Design and Operation of Two-Phase Ejectors." *Applied Thermal Engineering* 109: 809–18. doi:10.1016/j.applthermaleng.2014.11.022.

Anderson, Dale A., John C. Tannehill, and Richard H. Pletcher. 2020. *Computational Fluid Mechanics and Heat Transfer*. 2nd ed. ed. W. J. Minkowycz and E. M. Sparrow. Fourth edition. | Boca Raton, FL : CRC Press, 2020. | Series: Computational and physical processes in mechanics and thermal sciences: Taylor&Francis. doi:10.1201/9781351124027.

Angielczyk, Wojciech. 2022. "Modelling of CO2 Transonic Flashing Flow through a Convergent-Divergent Nozzle Using the Delayed Equilibrium Model." Bialystok University of Technology. https://bazawiedzy.pb.edu.pl/info/phd/BUTae512bc2473f445685f58daa837e893b?r=achievement&ps=20&title=PhD%2B%25E2%2580%2593%2BModelling%2Bof%2BCO2%2Btransonic%2Bflashing%2Bflow%2Bthrough%2Ba%2Bconvergent-divergent%2Bnozzle%2Busing%2Bthe%2BDelayed%2BEquilibr.

Angielczyk, Wojciech, Jean Marie Seynhaeve, Jerzy Gagan, Yann Bartosiewicz, and Dariusz Butrymowicz. 2019. "Prediction of Critical Mass Rate of Flashing Carbon Dioxide Flow in Convergent-Divergent Nozzle." *Chemical Engineering and Processing: Process Intensification* 143(2). doi:10.1016/j.cep.2019.107599.

ANSYS Inc. 2015. *Best Practice: Scale-Resolving Simulations in ANSYS CFD*. Version 2. https://www.ansys.com/resource-center/technical-paper/best-practice-scale-resolving-simulations-in-ansys-cfd.

ANSYS Inc. 2021a. *ANSYS Fluent Customization Manual*. 2021 R2.

ANSYS Inc. 2021b. *ANSYS Fluent Theory Guide*. 2021 R2.

ANSYS Inc. 2022a. "ANSYS Fluent."

ANSYS Inc. 2022b. "SpaceClaim."

Argyropoulos, C.D., and N.C. Markatos. 2015. "Recent Advances on the Numerical Modelling of Turbulent Flows." *Applied Mathematical Modelling* 39(2): 693–732. doi:10.1016/j.apm.2014.07.001.

Armenio, Vincenzo, Bernard J. Geurts, and Jochen Fröhlich. 2010. 13 *Direct and Large-Eddy Simulation VII*. eds. Vincenzo Armenio, Bernard Geurts, and Jochen Fröhlich. Dordrecht: Springer Netherlands. doi:10.1007/978-90-481-3652-0.

Ashley, C. M. 1934. "Steam Ejector System For Car Conditioning." *Transactions of the American Institute of Electrical Engineers* 53(3): 406–10. doi:10.1109/T-AIEE.1934.5056644.

Bai, Lihang, Siqi Liu, Zheng Ye, and Maogang He. 2019. "Investigation on the Performance of R1234ze(E) in Absorption Refrigeration and Ejection Refrigeration Systems." *Applied Thermal Engineering* 161(July): 114120. doi:10.1016/j.applthermaleng.2019.114120.

Banasiak, Krzysztof, and Armin Hafner. 2011. "1D Computational Model of a Two-Phase R744 Ejector for Expansion Work Recovery." *International Journal of Thermal Sciences* 50(11). doi:10.1016/j.ijthermalsci.2011.06.007.

Bandyopadhyay, Promode R., Daniel J. Stead, and Robert L. Ash. 1990. "The Organized Nature of a Turbulent Trailing Vortex." In *21st Fluid Dynamics, Plasma Dynamics and Lasers Conference*, Reston, Virigina: American Institute of Aeronautics and Astronautics, 1627–33. doi:10.2514/6.1990-1625.

Bardina, J., Joel H. Ferziger, and W. C. Reynolds. 1980. "Improved Subgrid-Scale Models for Large-Eddy Simulation." In *13th Fluid and PlasmaDynamics Conference*, Reston, Virigina: American Institute of Aeronautics and Astronautics. doi:10.2514/6.1980-1357.

Bardina, J., Joel Henry Ferziger, and William Craig Reynolds. 1983. "Improved Turbulence Models Based on Large Eddy Simulation of Homogeneous, Incompressible Turbulent Flows." *Thermosciences Division Department of Mechanical Engineering Stanford University* (Technical Report No. TF-19): 97. https://ntrs.nasa.gov/citations/19840009460.

Bartosiewicz, Yann, Zine Aidoun, Philippe Desevaux, and Yves Mercadier. 2005. "Numerical and Experimental Investigations on Supersonic Ejectors." *International Journal of Heat and Fluid Flow* 26(1): 56–70. doi:10.1016/j.ijheatfluidflow.2004.07.003.

Beithou, Nabil, and Hikmet S. Aybar. 2000. "A Mathematical Model for Steam-Driven Jet Pump." *International Journal of Multiphase Flow* 26(10): 1609–19. doi:10.1016/S0301-9322(99)00116-0.

Besagni, Giorgio. 2019. "Ejectors on the Cutting Edge: The Past, the Present and the Perspective." *Energy* 170: 998–1003. doi:10.1016/j.energy.2018.12.214.

Besagni, Giorgio, and Fabio Inzoli. 2017. "Computational Fluid-Dynamics Modeling of Supersonic Ejectors: Screening of Turbulence Modeling Approaches." *Applied Thermal Engineering* 117: 122–44. doi:10.1016/j.applthermaleng.2017.02.011.

Besagni, Giorgio, Riccardo Mereu, Paolo Chiesa, and Fabio Inzoli. 2015. "An Integrated Lumped Parameter-CFD Approach for off-Design Ejector Performance Evaluation." *Energy Conversion and Management* 105: 697–715. doi:10.1016/j.enconman.2015.08.029.

Besagni, Giorgio, Riccardo Mereu, and Fabio Inzoli. 2016. "Ejector Refrigeration: A Comprehensive Review." *Renewable and Sustainable Energy Reviews* (53): 373–407. doi:10.1016/j.rser.2015.08.059.

Bilicki, Z., and J. Kestin. 1990. "Physical Aspects of the Relaxation Model in Two-Phase Flow." In *Proceedings of the Royal Society of London. A. Mathematical and Physical Sciences*, , 379–97. doi:10.1098/rspa.1990.0040.

Bodys, Jakub, Jacek Smolka, Michal Palacz, Michal Haida, Krzysztof Banasiak, and Andrzej J. Nowak. 2022. "Effect of Turbulence Models and Cavitation Intensity on the Motive and Suction Nozzle Mass Flow Rate Prediction during a Non-Equilibrium Expansion Process in the CO2 Ejector." *Applied Thermal Engineering* 201. doi:10.1016/j.applthermaleng.2021.117743.

Boger, Markus. 2014. "Numerical Modeling of Compressible Two-Phase Flows with a Pressure-Based Method." Universitat Stuttgart. https://www.semanticscholar.org/paper/Numerical-modeling-of-compressible-two-phase-flows-Boger/eb322f2a2a4f4922054772cd579cc52eab13aa3a.

Boris, J. P., F. F. Grinstein, E. S. Oran, and R. L. Kolbe. 1992. "New Insights into Large Eddy Simulation." *Fluid Dynamics Research* 10(4–6): 199–228. doi:10.1016/0169-

5983(92)90023-P.

Bosch, Frank C. van den. 2023. "Physical Processes in Astronomy." http://www.astro.yale.edu/vdbosch/astro320.html.

Bouhanguel, A., P. Desevaux, and E. Gavignet. 2015. "Visualization of Flow Instabilities in Supersonic Ejectors Using Large Eddy Simulation." *Journal of Visualization* 18(1): 17–19. doi:10.1007/s12650-014-0231-4.

Brennen, Christopher Earls. 2005. 9780521848 Fundamentals of Multiphase Flow *Fundamentals of Multiphase Flow*. Pasadena: Cambridge University Press. doi:10.1017/CBO9780511807169.

Carrillo, J.A. Expósito, F.J. Sánchez de La Flor, and J.M. Salmerón Lissén. 2017. "Thermodynamic Comparison of Ejector Cooling Cycles. Ejector Characterisation by Means of Entrainment Ratio and Compression Efficiency." *International Journal of Refrigeration* 74: 371–84. doi:10.1016/j.ijrefrig.2016.11.006.

Ceci, A., S. Pirozzoli, J. Romero, M. Fatica, R. Verzicco, and P. Orlandi. 2022. "Direct Numerical Simulations of Turbulent Pipe Flow at High Reynolds Number." *Physical Review Fluids* 7(11): 110510. doi:10.1103/PhysRevFluids.7.110510.

Chen, Changsi, James J. Riley, and Patrick A. McMurtry. 1991. "A Study of Favre Averaging in Turbulent Flows with Chemical Reaction." *Combustion and Flame* 87(3–4): 257–77. doi:10.1016/0010-2180(91)90112-O.

Chen, Xiangjie, Siddig Omer, Mark Worall, and Saffa Riffat. 2013. "Recent Developments in Ejector Refrigeration Technologies." *Renewable and Sustainable Energy Reviews* 19: 629–51. doi:10.1016/j.rser.2012.11.028.

Chen, Zuozhou, Chaobin Dang, and Eiji Hihara. 2017. "Investigations on Driving Flow Expansion Characteristics inside Ejectors." *International Journal of Heat and Mass Transfer* 108: 490–500. doi:10.1016/j.ijheatmasstransfer.2016.12.040.

Chorin, Alexandre Joel. 1968. "Numerical Solution of the Navier-Stokes Equations." *Mathematics of Computation* 22(104): 745–62. doi:10.1090/S0025-5718-1968-0242392-2.

Ciofalo, Michele. 2022. *Thermofluid Dynamics of Turbulent Flows*. Cham: Springer International Publishing. doi:10.1007/978-3-030-81078-8.

Croquer, Sergio, Yu Fang, Antoine Metsue, Yann Bartosiewicz, and Sébastien Poncet. 2021. "Compound-Choking Theory for Supersonic Ejectors Working with Real Gas." *Energy* 227. doi:10.1016/j.energy.2021.120396.

Croquer, Sergio, Olivier Lamberts, Sébastien Poncet, Stéphane Moreau, and Yann Bartosiewicz. 2022. "Large Eddy Simulation of a Supersonic Air Ejector." *Applied Thermal Engineering* 209(October 2021): 118177. doi:10.1016/j.applthermaleng.2022.118177.

Davidson, P. A. 2015. *Turbulence, an Introduction for Scientists and Engineers*. 2nd ed. Oxford: Oxford University Press.

Demirel, Yaşar, and Vincent Gerbaud. 2019. "1. Fundamentals of Equilibrium Thermodynamics." In *Nonequilibrium Thermodynamics*, Elsevier, 1–85. doi:10.1016/B978-0-444-64112-0.00001-0.

Doehring, A., T. Kaller, S.J. Schmidt, and N.A. Adams. 2021. "Large-Eddy Simulation of Turbulent Channel Flow at Transcritical States." *International Journal of Heat and Fluid Flow* 89: 108781. doi:10.1016/j.ijheatfluidflow.2021.108781.

Dubief, Yves, and Franck Delcayre. 2000. "On Coherent-Vortex Identification in Turbulence." *Journal of Turbulence* 1(2000): N11. doi:10.1088/1468-5248/1/1/011.

Eames, Ian W. 2002. "A New Prescription for the Design of Supersonic Jet-Pumps: The Constant Rate of Momentum Change Method." *Applied Thermal Engineering* 22(2): 121–31. doi:10.1016/S1359-4311(01)00079-5.

Elbarghthi, Anas F A, Saleh Mohamed, Van Vu Nguyen, and Vaclav Dvorak. 2020. "CFD Based Design for Ejector Cooling System Using HFOS (1234ze(E) and 1234yf)." *Energies* 13(6): 1408. doi:10.3390/en13061408.

Elbel, Stefan. 2011. "Historical and Present Developments of Ejector Refrigeration Systems with Emphasis on Transcritical Carbon Dioxide Air-Conditioning." *International Journal of Refrigeration* 34(7): 1545–61. doi:10.1016/j.ijrefrig.2010.11.011.

Elbel, Stefan, and Pega Hrnjak. 2008. "Experimental Validation of a Prototype Ejector Designed to Reduce Throttling Losses Encountered in Transcritical R744 System Operation." *International Journal of Refrigeration* 31(3): 411–22. doi:10.1016/j.ijrefrig.2007.07.013.

Elbel, Stefan, and Neal Lawrence. 2016. "Review of Recent Developments in Advanced Ejector Technology." *International Journal of Refrigeration* 62: 1–18. doi:10.1016/j.ijrefrig.2015.10.031.

F-Chart Software. 2020. "Engineering Equation Solver (EES)."

Fabri, J., and R. Siestrunck. 1958. "Supersonic Air Ejectors." In *Advances in Applied Mechanics*, , 1–34. doi:10.1016/S0065-2156(08)70016-4.

Fang, Xinxin, Chibing Shen, Mingbo Sun, and Zhiwei Hu. 2018. "Effects of Oblique Shock Waves on Turbulent Structures and Statistics of Supersonic Mixing Layers." *Physics of Fluids* 30(11): 1–18. doi:10.1063/1.5051015.

Fang, Yu, Sébastien Poncet, Hakim Nesreddine, and Yann Bartosiewicz. 2019. "An Open-Source Density-Based Solver for Two-Phase CO2 Compressible Flows: Verification and Validation." *International Journal of Refrigeration* 106. doi:10.1016/j.ijrefrig.2019.05.016.

Fanourgakis, George S., J. S. Medina, and R. Prosmiti. 2012. "Determining the Bulk Viscosity of Rigid Water Models." *The Journal of Physical Chemistry A* 116(10): 2564–70. doi:10.1021/jp211952y.

Fenghour, A., William A. Wakeham, and V. Vesovic. 1998. "The Viscosity of Carbon Dioxide." *Journal of Physical and Chemical Reference Data* 27(1). doi:10.1063/1.556013.

Ferziger, Joel H., Milovan Perić, and Robert L. Street. 2020. *Computational Methods for Fluid Dynamics*. 4th editio. Cham: Springer International Publishing. doi:10.1007/978-3-319-99693-6.

Fondrk, V.V. 1952. "Multi-Stage Ejectors for High Vacuum. Presented." *Vacuum* 2(2): 149–50. doi:10.1016/0042-207x(52)90473-9.

Fröhlich, Jochen, and Dominic von Terzi. 2008. "Hybrid LES/RANS Methods for the Simulation of Turbulent Flows." *Progress in Aerospace Sciences* 44(5): 349–77. doi:10.1016/j.paerosci.2008.05.001.

Garnier, E, Nikolaus Adams, and Pierre Sagaut. 2009. Springer *Large Eddy Simulation for Compressible Flows*. Dordrecht: Springer Netherlands. doi:10.1007/978-90-481-2819-8.

Gay, Norman H. 1931. "Refrigerating System." : 7. https://ppubs.uspto.gov/dirsearch-public/print/downloadPdf/1836318.

Gerasimov, Aleksey. 2016. "Quick Guide to Setting up LES-Type Simulations." : 50. http://www.tfd.chalmers.se/~lada/comp_turb_model/postscript_files/Quick_Guide_

to_Setting_Up_LES_version_1.4_for_Lars.pdf.

Germano, Massimo, Ugo Piomelli, Parviz Moin, and William H. Cabot. 1991. "A Dynamic Subgrid-Scale Eddy Viscosity Model." *Physics of Fluids A: Fluid Dynamics* 3(7): 1760–65. doi:10.1063/1.857955.

Ghosal, Sandip, Thomas S. Lund, Parviz Moin, and Knut Akselvoll. 1995. "A Dynamic Localization Model for Large-Eddy Simulation of Turbulent Flows." *Journal of Fluid Mechanics* 286(March): 229–55. doi:10.1017/S0022112095000711.

Giacomelli, Francesco. 2019. "Numerical Modeling of Supersonic Two-Phase Ejectors Working with Natural Refrigerants." Univerity of Florence.

Giacomelli, Francesco, Krzysztof Banasiak, Armin Hafner, Federico Mazzelli, and Adriano Milazzo. 2018. "Experimental and Numerical Investigation on an Ejector for CO2 Vapor Compression Systems." *Refrigeration Science and Technology* 2018-June. doi:10.18462/iir.gl.2018.1392.

Giacomelli, Francesco, Federico Mazzelli, Krzysztof Banasiak, Armin Hafner, and Adriano Milazzo. 2019. "Experimental and Computational Analysis of a R744 Flashing Ejector." *International Journal of Refrigeration* 107: 326–43. doi:10.1016/j.ijrefrig.2019.08.007.

Giacomelli, Francesco, Federico Mazzelli, and Adriano Milazzo. 2016. "Evaporation in Supersonic CO2 Ejectors: Analysis of Theoretical and Numerical Models." *9th International Conference on Multiphase Flow* (May).

Giacomelli, Francesco, Federico Mazzelli, and Adriano Milazzo. 2018. "A Novel CFD Approach for the Computation of R744 Flashing Nozzles in Compressible and Metastable Conditions." *Energy* 162: 1092–1105. doi:10.1016/j.energy.2018.08.050.

Giffard, Henri. 1860. "Improved Feed-Water Apparatus for Steam-Boilers." *United States Patent Office*: 3. https://patents.google.com/patent/US27979.

Gnani, F., H. Zare-Behtash, and K. Kontis. 2016. "Pseudo-Shock Waves and Their Interactions in High-Speed Intakes." *Progress in Aerospace Sciences* 82: 36–56. doi:10.1016/j.paerosci.2016.02.001.

Gullo, Paride, Armin Hafner, Krzysztof Banasiak, Silvia Minetto, and Ekaterini E. Kriezi. 2019. "Multi-Ejector Concept: A Comprehensive Review on Its Latest Technological Developments." *Energies* 12(3): 406. doi:10.3390/en12030406.

Guo, Guang-Jun, and Yi-Gang Zhang. 2001. "Equilibrium Molecular Dynamics Calculation of the Bulk Viscosity of Liquid Water." *Molecular Physics* 99(4): 283–89. doi:10.1080/00268970010011762.

Gupta, Pradeep, Pramod Kumar, and Srisha M.V. Rao. 2022. "Artificial Neural Network Based Shape Optimization of Supersonic Ejectors in the Critical Flow Regime." *Applied Thermal Engineering* 216(February): 119046. doi:10.1016/j.applthermaleng.2022.119046.

Gupta, Pradeep, Srisha M.V. Rao, and Pramod Kumar. 2019. "Experimental Investigations on Mixing Characteristics in the Critical Regime of a Low-Area Ratio Supersonic Ejector." *Physics of Fluids* 31(2). doi:10.1063/1.5078433.

Gupta, Pradeep, Srisha MV Rao, and Pramod Kumar. 2022. "Numerical Studies of a Supersonic Air Ejector Using Large Eddy Simulation." In *Proceedings of the 26thNational and 4th International ISHMT-ASTFE Heat and Mass Transfer Conference December 17-20, 2021, IIT Madras, Chennai-600036, Tamil Nadu, India*, Connecticut: Begellhouse, 631–36. doi:10.1615/IHMTC-2021.940.

Hafner, Armin, Sven Försterling, and Krzysztof Banasiak. 2014. "Multi-Ejector Concept for R-744 Supermarket Refrigeration." *International Journal of Refrigeration* 43: 1–13.

doi:10.1016/j.ijrefrig.2013.10.015.

Haida, Michal, Jacek Smolka, Armin Hafner, Mikolaj Mastrowski, Michal Palacz, Kenneth B. Madsen, Andrzej J. Nowak, and Krzysztof Banasiak. 2018. "Numerical Investigation of Heat Transfer in a CO2 Two-Phase Ejector." *Energy* 163: 682–98. doi:10.1016/j.energy.2018.08.175.

Haida, Michal, Jacek Smolka, Armin Hafner, Michal Palacz, Krzysztof Banasiak, and Andrzej J. Nowak. 2018. "Modified Homogeneous Relaxation Model for the R744 Trans-Critical Flow in a Two-Phase Ejector." *International Journal of Refrigeration* 85: 314–33. doi:10.1016/j.ijrefrig.2017.10.010.

Hassanain, M., E. Elgendy, and M. Fatouh. 2015. "Ejector Expansion Refrigeration System: Ejector Design and Performance Evaluation." *International Journal of Refrigeration* 58: 1–13. doi:10.1016/j.ijrefrig.2015.05.018.

He, S., Y. Li, and R. Z. Wang. 2009. "Progress of Mathematical Modeling on Ejectors." *Renewable and Sustainable Energy Reviews* 13(8): 1760–80. doi:10.1016/j.rser.2008.09.032.

Hemidi, Amel, François Henry, Sébastien Leclaire, Jean Marie Seynhaeve, and Yann Bartosiewicz. 2009. "CFD Analysis of a Supersonic Air Ejector. Part I: Experimental Validation of Single-Phase and Two-Phase Operation." *Applied Thermal Engineering* 29(8–9): 1523–31. doi:10.1016/j.applthermaleng.2008.07.003.

Holgate, Joshua, Alex Skillen, Timothy Craft, and Alistair Revell. 2019. "A Review of Embedded Large Eddy Simulation for Internal Flows." *Archives of Computational Methods in Engineering* 26(4): 865–82. doi:10.1007/s11831-018-9272-5.

Huang, B. J., J. M. Chang, C. P. Wang, and V. A. Petrenko. 1999. "A 1-D Analysis of Ejector Performance." *International Journal of Refrigeration* 22(5): 354–64. doi:10.1016/S0140-7007(99)00004-3.

International Energy Agency. 2018. "The Future of Cooling." https://www.iea.org/reports/the-future-of-cooling (April 18, 2021).

Ishii, Mamoru, and Takashi Hibiki. 2006. *Thermo-Fluid Dynamics of Two-Phase Flow*. 1st ed. Boston, MA: Springer US. doi:10.1007/978-0-387-29187-1.

Ivanov, N. G., and M. A. Zasimova. 2018. "Large Eddy Simulation of Airflow in a Test Ventilated Room." *Journal of Physics: Conference Series* 1038(1): 012136. doi:10.1088/1742-6596/1038/1/012136.

Jarrin, N., S. Benhamadouche, D. Laurence, and R. Prosser. 2006. "A Synthetic-Eddy-Method for Generating Inflow Conditions for Large-Eddy Simulations." *International Journal of Heat and Fluid Flow* 27(4): 585–93. doi:10.1016/j.ijheatfluidflow.2006.02.006.

Jeong, Jinhee, and Fazle Hussain. 1995. "On the Identification of a Vortex." *Journal of Fluid Mechanics* 285(January 1995): 69–94. doi:10.1017/S0022112095000462.

Jiang, Xi, George A. Siamas, Krzysztof Jagus, and Tassos G. Karayiannis. 2010. "Physical Modelling and Advanced Simulations of Gas–Liquid Two-Phase Jet Flows in Atomization and Sprays." *Progress in Energy and Combustion Science* 36(2): 131–67. doi:10.1016/j.pecs.2009.09.002.

Jiang, Zhou, Yongchao Ji, and Jianchun Wang. 2022. "Compressibility Effect on Interaction of Shock Wave and Turbulent Boundary Layer." *Physics of Fluids* 34(7). doi:10.1063/5.0096928.

Kader, B. A. 1981. "Temperature and Concentration Profiles in Fully Turbulent Boundary Layers." *International Journal of Heat and Mass Transfer* 24(9): 1541–44. doi:10.1016/0017-9310(81)90220-9.

Kamin, Manu, James Eblin, and Prashant Khare. 2023. "The NexGen Burner: Non-Reacting Gaseous and Spray Dynamics." *Physics of Fluids* 35(11). doi:10.1063/5.0169823.

Karthick, S. K., Srisha M. V. Rao, G. Jagadeesh, and K. P. J. Reddy. 2017. "Passive Scalar Mixing Studies to Identify the Mixing Length in a Supersonic Confined Jet." *Experiments in Fluids* 58(5): 59. doi:10.1007/s00348-017-2342-x.

Karthick, S. K., Srisha M.V. Rao, G. Jagadeesh, and K. P.J. Reddy. 2018. "Experimental Parametric Studies on the Performance and Mixing Characteristics of a Low Area Ratio Rectangular Supersonic Gaseous Ejector by Varying the Secondary Flow Rate." *Energy* 161: 832–45. doi:10.1016/j.energy.2018.07.135.

Keenan, J. H., and E. P. Neumann. 1942. "A Simple Air Ejector." *Journal of Applied Mechanics* 9: A75–81.

Kim, Sung-Eun, D. Choudhury, and B. Patel. 1999. "Computations of Complex Turbulent Flows Using the Commercial Code Fluent." In , 259–76. doi:10.1007/978-94-011-4724-8_15.

Kim, Won-Wook, Suresh Menon, Won-Wook Kim, and Suresh Menon. 1997. "Application of the Localized Dynamic Subgrid-Scale Model to Turbulent Wall-Bounded Flows." In *35th Aerospace Sciences Meeting and Exhibit*, Reston, Virigina: American Institute of Aeronautics and Astronautics, 1–12. doi:10.2514/6.1997-210.

Kitrattana, Borirak, Satha Aphornratana, Tongchana Thongtip, and Natthawut Ruangtrakoon. 2017. "Comparison of Traditional and CRMC Ejector Performance Used in a Steam Ejector Refrigeration." *Energy Procedia* 138: 476–81. doi:10.1016/j.egypro.2017.10.229.

Klein, M., A. Sadiki, and J. Janicka. 2003. "A Digital Filter Based Generation of Inflow Data for Spatially Developing Direct Numerical or Large Eddy Simulations." *Journal of Computational Physics* 186(2): 652–65. doi:10.1016/S0021-9991(03)00090-1.

Kornhauser, Alan A. 1990. "The Use of an Ejector as a Refrigerant Expander." In *Proceedings of the Intersociety Energy Conversion Engineering Conference*, , 79–84. https://docs.lib.purdue.edu/iracc/82/.

Kracik, Jan, Vaclav Dvorak, Van Vu Nguyen, and Kamil Smierciew. 2018. "Experimental and Numerical Study on Supersonic Ejectors Working with R-1234ze(E)." *EPJ Web of Conferences* 180: 1–10. doi:10.1051/epjconf/201818002047.

Kraichnan, Robert H. 1970. "Diffusion by a Random Velocity Field." *Physics of Fluids A: Fluid Dynamics* 13(1): 22–31. doi:10.1063/1.1692799.

Kudela, Henryk. 2011. "Turbulent Flow." *Lecture n.°3 Turbulent Flow Modelling*: 1–48. http://www.itcmp.pwr.wroc.pl/~znmp/dydaktyka/fundam_FM/Lecture_no3_Turbulent_flow_Modelling.pdf.

Kumar, Anil, Virendra Kumar, PMV Subbarao, Surendra K. Yadav, and Gaurav Singhal. 2022. "Numerical Assessment on the Performance of Variable Area Single- and Two-Stage Ejectors: A Comparative Study." *Proceedings of the Institution of Mechanical Engineers, Part E: Journal of Process Mechanical Engineering* 236(1): 114–25. doi:10.1177/09544089211033129.

Kumar, Virendra, Anil Kumar, Surendra Kumar Yadav, Anshul Yadav, Lalta Prasad, and Jerzy Adam Winczek. 2022. "Numerical Analysis on a Constant Rate of Kinetic Energy Change Based a Two-Stage Ejector-Diffuser System." *Strojniški vestnik - Journal of Mechanical Engineering* 68(5): 368–73. doi:10.5545/sv-jme.2021.7538.

Kumar, Virendra, Gaurav Singhal, and P.M.V. Subbarao. 2018. "Realization of Novel Constant Rate of Kinetic Energy Change (CRKEC) Supersonic Ejector." *Energy* 164: 694–706. doi:10.1016/j.energy.2018.08.184.

Kundu, Pijush K., Ira M. Cohen, and David R. Dowling. 2012a. "Boundary Layers and Related Topics." In *Fluid Mechanics*, Elsevier, 361–419. doi:10.1016/B978-0-12-382100-3.10009-5.

Kundu, Pijush K., Ira M. Cohen, and David R. Dowling. 2012b. "Compressible Flow." In *Fluid Mechanics*, Elsevier, 729–78. doi:10.1016/B978-0-12-382100-3.10015-0.

Labourasse, E., D. Lacanette, A. Toutant, P. Lubin, S. Vincent, O. Lebaigue, J. P. Caltagirone, and P. Sagaut. 2007. "Towards Large Eddy Simulation of Isothermal Two-Phase Flows: Governing Equations and a Priori Tests." *International Journal of Multiphase Flow* 33(1): 1–39. doi:10.1016/j.ijmultiphaseflow.2006.05.010.

Langmuir, I. 1916. "The Condensation Pump: An Improved Form of High Vacuum Pump." *Journal of the Franklin Institute* 182(6): 719–43. doi:10.1016/S0016-0032(16)90056-5.

Lanzafame, R., S. Mauro, and M. Messina. 2013. "Wind Turbine CFD Modeling Using a Correlation-Based Transitional Model." *Renewable Energy* 52: 31–39. doi:10.1016/j.renene.2012.10.007.

Launder, B. E., and N. D. Sandham, eds. 2002. *Closure Strategies for Turbulent and Transitional Flows*. Cambridge University Press. doi:10.1017/CBO9780511755385.

Lemmon, Eric W., Marcia L. Huber, and Mark O. McLinden. 2013. "NIST Reference Fluid Thermodynamic and Transport Properties Database (REFPROP)." doi:https://doi.org/10.18434/T4JS3C.

Leonard, A., and K. Chua. 1989. "Three-Dimensional Interactions of Vortex Tubes." *Physica D: Nonlinear Phenomena* 37(1–3): 490–96. doi:10.1016/0167-2789(89)90153-X.

Li, Tailu, Haiyang Gao, Xiang Gao, and Nan Meng. 2022. "Thermodynamic Performance Comparison of Organic Rankine Flash Cycle with and without Ejector for Geothermal Power Output." *Applied Thermal Engineering* 214(May): 118846. doi:10.1016/j.applthermaleng.2022.118846.

Lilly, Douglas K. 1966. "The Representation of Small-Scale Turbulence in Numerical Simulation Experiments." In *Proceedings of the IBM Scientific Computing Symposium on Environmental Sciences*, , 195–210. doi:10.5065/D62R3PMM.

Lilly, Douglas K. 1992. "A Proposed Modification of the Germano Subgrid-Scale Closure Method." *Physics of Fluids A: Fluid Dynamics* 4(3): 633–35. doi:10.1063/1.858280.

Lin, Chen, Wenjian Cai, Yanzhong Li, Jia Yan, Yu Hu, and Karunagaran Giridharan. 2013. "Numerical Investigation of Geometry Parameters for Pressure Recovery of an Adjustable Ejector in Multi-Evaporator Refrigeration System." *Applied Thermal Engineering* 61(2): 649–56. doi:10.1016/j.applthermaleng.2013.08.033.

Linga, Gaute, and Tore Flåtten. 2019. "A Hierarchy of Non-Equilibrium Two-Phase Flow Models" eds. Philippe Helluy, Jean-Marc Hérard, and Nicolas Seguin. *ESAIM: Proceedings and Surveys* 66(c): 109–43. doi:10.1051/proc/201966006.

Little, Adrienne B., and Srinivas Garimella. 2016. "A Critical Review Linking Ejector Flow Phenomena with Component- and System-Level Performance." *International Journal of Refrigeration* 70: 243–68. doi:10.1016/j.ijrefrig.2016.05.015.

Liu, Fang, Eckhard A. Groll, and Jianxing Ren. 2016. "Comprehensive Experimental Performance Analyses of an Ejector Expansion Transcritical CO2 System." *Applied Thermal Engineering* 98: 1061–69. doi:10.1016/j.applthermaleng.2015.12.017.

Liu, Fangzhou, Deying Li, and Xiping Zeng. 2017. "Research on Energy Saving Technology of Distributing Combined Adjustable Jet Pump." *Procedia Engineering* 205: 738–43. doi:10.1016/j.proeng.2017.10.004.

Lucas, Christian, Henrik Rusche, Andreas Schroeder, and Juergen Koehler. 2014.

"Numerical Investigation of a Two-Phase CO2 Ejector." *International Journal of Refrigeration* 43: 154–66. doi:10.1016/j.ijrefrig.2014.03.003.

Lund, Halvor, and Tore Flåtten. 2010. "Equilibrium Conditions and Sound Velocities in Two-Phase Flows." In *Proceedings of the SIAM Annual Meeting*, , 1–15.

Majchrzyk, Michal, Damian Dziurowicz, Michal Haida, Michal Palacz, Jakub Bodys, Rafal Fingas, Jacek Smolka, and Andrzej J. Nowak. 2022. "Detailed Numerical Investigation of the CO2 Two-Phase Ejector 3-D CFD Model Based on the Flow Visualisation Experiments." *Chemical Engineering and Processing - Process Intensification* 182(February): 109195. doi:10.1016/j.cep.2022.109195.

Mangialardo, Andrea, Walter Borreani, Guglielmo Lomonaco, and Fabrizio Magugliani. 2014. "Numerical Investigation on a Jet Pump Evolving Liquid Lead for GEN-IV Reactors." *Nuclear Engineering and Design* 280: 608–18. doi:10.1016/j.nucengdes.2014.09.028.

Mathey, Fabrice, Davor Cokljat, Jean Pierre Bertoglio, and Emmanuel Sergent. 2006. "Assessment of the Vortex Method for Large Eddy Simulation Inlet Conditions." *Progress in Computational Fluid Dynamics, An International Journal* 6(1/2/3): 58. doi:10.1504/PCFD.2006.009483.

Matsuo, Kazuyasu, Yoshiaki Miyazato, and Heuy-Dong Kim. 1999. "Shock Train and Pseudo-Shock Phenomena in Internal Gas Flows." *Progress in Aerospace Sciences* 35(1): 33–100. doi:10.1016/S0376-0421(98)00011-6.

Mazzelli, Federico, Adrienne B. Little, Srinivas Garimella, and Yann Bartosiewicz. 2015. "Computational and Experimental Analysis of Supersonic Air Ejector: Turbulence Modeling and Assessment of 3D Effects." *International Journal of Heat and Fluid Flow* 56: 305–16. doi:10.1016/j.ijheatfluidflow.2015.08.003.

Medeiros, R. B., J. M. Fusco, K. Ropelato, and G. Aliatti. 2014. "Simulation of Supersonic Flow: Comparison of LES against URANS and RANS Turbulence Models." *Blucher Mechanical Engineering Procedings* 1(1): 2322–32. doi:10.5151/meceng-wccm2012-18813.

Meier, Karsten, Arno Laesecke, and Stephan Kabelac. 2005. "Transport Coefficients of the Lennard-Jones Model Fluid. III. Bulk Viscosity." *The Journal of Chemical Physics* 122(1). doi:10.1063/1.1828040.

Menter, F. R. 1994. "Two-Equation Eddy-Viscosity Turbulence Models for Engineering Applications." *AIAA Journal* 32(8): 1598–1605. doi:10.2514/3.12149.

Mockett, Charles. 2018. 134 *Go4Hybrid: Grey Area Mitigation for Hybrid RANS-LES Methods*. eds. Charles Mockett, Werner Haase, and Dieter Schwamborn. Cham: Springer International Publishing. doi:10.1007/978-3-319-52995-0.

Mousavi, Seyed Mahmood, Reza Kamali, Freshteh Sotoudeh, Nader Karimi, and Danial Khojasteh. 2021. "Large Eddy Simulation of Pseudo Shock Structure in a Convergent–Long Divergent Duct." *Computers and Mathematics with Applications* 81: 823–37. doi:10.1016/j.camwa.2019.10.017.

Nakagawa, M., A. R. Marasigan, T. Matsukawa, and A. Kurashina. 2011. "Experimental Investigation on the Effect of Mixing Length on the Performance of Two-Phase Ejector for CO2 Refrigeration Cycle with and without Heat Exchanger." *International Journal of Refrigeration* 34(7): 1604–13. doi:10.1016/j.ijrefrig.2010.07.021.

Nguyen, D.L., E.R.F. Winter, and M. Greiner. 1981. "Sonic Velocity in Two-Phase Systems." *International Journal of Multiphase Flow* 7(3): 311–20. doi:10.1016/0301-9322(81)90024-0.

Van Nguyen, Vu, Szabolcs Varga, João Soares, Vaclav Dvorak, and Armando Oliveira.

2020. "Applying a Variable Geometry Ejector in a Solar Ejector Refrigeration System." *International Journal of Refrigeration* 113: 187–95. doi:10.1016/j.ijrefrig.2020.01.018.

Nicoud, F., and F. Ducros. 1999. "Subgrid-Scale Stress Modelling Based on the Square of the Velocity." *Flow, Turbulence and Combustion* 62: 183–200. doi:10.1023/A:1009995426001.

Di Nucci, C., D. Pasquali, D. Celli, A. Pasculli, P. Fischione, and M. Di Risio. 2020. "Turbulent Bulk Viscosity." *European Journal of Mechanics, B/Fluids* 84: 446–54. doi:10.1016/j.euromechflu.2020.07.004.

Ogami, Yoshifumi. 2003. "Study of LES Model for the Vortex Method." In *Computational Fluid and Solid Mechanics 2003*, Elsevier, 1072–73. doi:10.1016/B978-008044046-0.50261-X.

Our World in Data. 2024. "Global Primary Energy Consumption by Source." https://ourworldindata.org/grapher/global-energy-consumption-source (January 5, 2025).

Palacz, Michal, Michal Haida, Jacek Smolka, Andrzej J. Nowak, Krzysztof Banasiak, and Armin Hafner. 2017. "HEM and HRM Accuracy Comparison for the Simulation of CO2 Expansion in Two-Phase Ejectors for Supermarket Refrigeration Systems." *Applied Thermal Engineering* 115: 160–69. doi:10.1016/j.applthermaleng.2016.12.122.

Palacz, Michal, Jacek Smolka, Adam Fic, Zbigniew Buliński, Andrzej J. Nowak, Krzysztof Banasiak, and Armin Hafner. 2015. "Application Range of the HEM Approach for CO2 Expansion inside Two-Phase Ejectors for Supermarket Refrigeration Systems." *International Journal of Refrigeration* 59: 251–58. doi:10.1016/j.ijrefrig.2015.07.006.

Pathikonda, Gokul, Mustafa Usta, Michael C. Ahmad, Irfan Khan, Paul Gillis, Shrikant Dhodapkar, Pradeep Jain, Devesh Ranjan, and Cyrus K. Aidun. 2021. "Mixing Behavior in a Confined Jet with Disparate Viscosity and Implications for Complex Reactions." *Chemical Engineering Journal* 403(May 2020): 126300. doi:10.1016/j.cej.2020.126300.

Peng, Shia Hui. 2022. "Hybrid Rans-Les Modelling: Some Recent Development and Aerodynamic Applications." *33rd Congress of the International Council of the Aeronautical Sciences, ICAS 2022* 3: 2168–79.

Pereira, Paulo R., Szabolcs Varga, João Soares, Armando Oliveira, Antonio M Lopes, Fernando G De Almeida, and Joao F Carneiro. 2014. "Experimental Results with a Variable Geometry Ejector Using R600a as Working Fluid." *International Journal of Refrigeration* 46: 77–85. doi:10.1016/j.ijrefrig.2014.06.016.

Pianthong, Kulachate, Wirapan Seehanam, Masud Behnia, Thanarath Sriveerakul, and Satha Aphornratana. 2007. "Investigation and Improvement of Ejector Refrigeration System Using Computational Fluid Dynamics Technique." *Energy Conversion and Management* 48(9): 2556–64. doi:https://doi.org/10.1016/j.enconman.2007.03.021.

Pope, Stephen B. 2000. *Turbulent Flows*. 10th ed. Cambridge University Press. doi:10.4271/210044.

Power, Robert B. 1994. *Steam Jet Ejectors for the Process Industries*. 1st ed. New York: McGraw-Hill, Inc.

Quéméré, P., and P. Sagaut. 2002. "Zonal Multi-domain RANS/LES Simulations of Turbulent Flows." *International Journal for Numerical Methods in Fluids* 40(7): 903–25. doi:10.1002/fld.381.

Rankine, W.J.M. 1869. "Morton's Ejector Condenser." *Journal of the Franklin Institute* 88(6): 377–82. doi:10.1016/0016-0032(69)90750-9.

Rao, Srisha M.V., and Gopalan Jagadeesh. 2014. "Observations on the Non-Mixed Length and Unsteady Shock Motion in a Two Dimensional Supersonic Ejector." *Physics of Fluids* 26(3). doi:10.1063/1.4868879.

Rapp, Bastian E. 2017. "3. Engineering Mathematics." In *Microfluidics: Modelling, Mechanics and Mathematics*, Elsevier, 21–50. doi:10.1016/B978-1-4557-3141-1.50003-4.

Reddick, Christopher, Mikhail Sorin, Hristo Sapoundjiev, and Zine Aidoun. 2016. "Carbon Capture Simulation Using Ejectors for Waste Heat Upgrading." *Energy* 100: 251–61. doi:10.1016/j.energy.2016.01.099.

Reis, Lívia Bueno, and Rafael dos Santos Gioria. 2021. "Optimization of Liquid Jet Ejector Geometry and Its Impact on Flow Fields." *Applied Thermal Engineering* 194: 117–32. doi:10.1016/j.applthermaleng.2021.117132.

Ren, Jianbo, Chao Miao, Yingzhen Wu, Qiang Li, Jianmei Xu, and Lingpin Zhang. 2022. "Geometry Dimension Optimization of a Liquid–Gas Vacuum Ejector for MED-TVC System." *Applied Thermal Engineering* 214(June): 118907. doi:10.1016/j.applthermaleng.2022.118907.

Ren, Xiaotong, Yali Guo, Shengqiang Shen, and Kun Zhang. 2022. "Large Eddy Simulation of Flow Field in Thermal Vapor Compressor." *Frontiers in Energy Research* 10(September): 1–14. doi:10.3389/fenrg.2022.1008927.

Ringstad, Knut Emil. 2023. "CFD Modelling for Improved Components in CO2 and Ammonia Vapour Compression Systems." Norwegian University of Science and Technology. https://ntnuopen.ntnu.no/ntnu-xmlui/handle/11250/3068650.

Ringstad, Knut Emil, Yosr Allouche, Paride Gullo, Åsmund Ervik, Krzysztof Banasiak, and Armin Hafner. 2020. "A Detailed Review on CO2 Two-Phase Ejector Flow Modeling." *Thermal Science and Engineering Progress* 20: 100647. doi:10.1016/j.tsep.2020.100647.

Ristorcelli, J. R. 1993. "A Representation for the Turbulent Mass Flux Contribution to Reynolds- Stress and Two-Equation Closures for Compressible Turbulence." (93). https://apps.dtic.mil/sti/citations/ADA274816.

Salim, M., and S. Cheong. 2009. "Wall Y+ Strategy for Dealing with Wall-Bounded Turbulent Flows." In *International MultiConference of Engineers and Computer Scientists*, Hong Kong, 6.

Samaké, Oumar, Nicolas Galanis, and Mikhail Sorin. 2016. "On the Design and Corresponding Performance of Steam Jet Ejectors." *Desalination* 381: 15–25. doi:10.1016/J.DESAL.2015.11.027.

Sankarlal, T., and A. Mani. 2007. "Experimental Investigations on Ejector Refrigeration System with Ammonia." *Renewable Energy* 32(8): 1403–13. doi:10.1016/j.renene.2006.05.008.

Sarkar, Jahar. 2012. "Ejector Enhanced Vapor Compression Refrigeration and Heat Pump Systems - A Review." *Renewable and Sustainable Energy Reviews* 16(9): 6647–59. doi:10.1016/j.rser.2012.08.007.

Sarkar, S. 1992. "The Pressure-Dilatation Correlation in Compressible Flows." *Physics of Fluids A: Fluid Dynamics* 4(12): 2674–82. doi:10.1063/1.858454.

Sarkar, S., G Erlebacher, and M Y Hussaini. 1993. "Compressible Homogeneous Shear: Simulation and Modeling." In *Turbulent Shear Flows 8*, eds. F. Durst, R. Friedrich, B.E. Launder, F.W. Schmidt, U. Schumann, and J.H. Whitelaw. Berlin, Heidelberg: Springer, Berlin, Heidelberg, 249–67. doi:10.1007/978-3-642-77674-8_18.

Sawalha, Samer. 2008. "Theoretical Evaluation of Trans-Critical CO2 Systems in

Supermarket Refrigeration. Part I: Modeling, Simulation and Optimization of Two System Solutions." *International Journal of Refrigeration* 31(3): 516–24. doi:10.1016/j.ijrefrig.2007.05.017.

Schlüter, J. U., X. Wu, S. Kim, S. Shankaran, J. J. Alonso, and H. Pitsch. 2005. "A Framework for Coupling Reynolds-Averaged With Large-Eddy Simulations for Gas Turbine Applications." *Journal of Fluids Engineering* 127(4): 806–15. doi:10.1115/1.1994877.

Schmitt, Thomas, and Sébastien Ducruix. 2023. "Evaluation of Large-Eddy Simulation Coupled with an Homogeneous Equilibrium Model for the Prediction of Coaxial Cryogenic Flames under Subcritical Conditions." *Aerospace* 10(2): 98. doi:10.3390/aerospace10020098.

Schumann, U. 1975. "Subgrid Scale Model for Finite Difference Simulations of Turbulent Flows in Plane Channels and Annuli." *Journal of Computational Physics* 18(4): 376–404. doi:10.1016/0021-9991(75)90093-5.

Sengupta, Debanjan, Jeffrey N. Cuzzi, Orkan M. Umurhan, and Wladimir Lyra. 2024. "Length and Velocity Scales in Protoplanetary Disk Turbulence." *The Astrophysical Journal* 966(1): 90. doi:10.3847/1538-4357/ad2c89.

Sergent, M. Emmanuel. 2002. "Vers Une Méthodologie de Couplage Entre La Simulation Des Grandes Echelles et Les Modèles Statistiques." École Centrale de Lyon. doi:10.1093/benz/9780199773787.article.b00167791.

Shahzamanian, Behzad, Szabolcs Varga, João Soares, Ana Palmero-Marrero, and Armando Oliveira. 2021. "Performance Evaluation of a Variable Geometry Ejector Applied in a Multi-Effect Thermal Vapor Compression Desalination System." *Applied Thermal Engineering* 195: 117177. doi:10.1016/j.applthermaleng.2021.117177.

Sharma, Bhanuday, and Rakesh Kumar. 2023. "A Brief Introduction to Bulk Viscosity of Fluids." : 1–28. http://arxiv.org/abs/2303.08400.

Shih, Tsan-Hsing, William W. Liou, Aamir Shabbir, Zhigang Yang, and Jiang Zhu. 1995. "A New K-ϵ Eddy Viscosity Model for High Reynolds Number Turbulent Flows." *Computers & Fluids* 24(3): 227–38. doi:10.1016/0045-7930(94)00032-T.

Shur, Mikhail L., Philippe R. Spalart, Mikhail Kh Strelets, and Andrey K. Travin. 2008. "A Hybrid RANS-LES Approach with Delayed-DES and Wall-Modelled LES Capabilities." *International Journal of Heat and Fluid Flow* 29(6): 1638–49. doi:10.1016/j.ijheatfluidflow.2008.07.001.

Smagorinsky, Joseph. 1963. "General Circulation Experiments with the Primitive Equations." *Monthly Weather Review* 91(3): 99–164. doi:10.1175/1520-0493(1963)091<0099:GCEWTP>2.3.CO;2.

Śmierciew, Kamil, Jerzy Gagan, Dariusz Butrymowicz, Michał Łukaszuk, and Henryk Kubiczek. 2017. "Experimental Investigation of the First Prototype Ejector Refrigeration System with HFO-1234ze(E)." *Applied Thermal Engineering* 110: 115–25. doi:10.1016/j.applthermaleng.2016.08.140.

Smolka, Jacek, Zbigniew Buliński, Adam Fic, Andrzej J. Nowak, Krzysztof Banasiak, and Armin Hafner. 2013. "A Computational Model of a Transcritical R744 Ejector Based on a Homogeneous Real Fluid Approach." *Applied Mathematical Modelling* 37(3): 1208–24. doi:10.1016/j.apm.2012.03.044.

Smolka, Jacek, Michal Palacz, Jakub Bodys, Krzysztof Banasiak, Adam Fic, Zbigniew Buliński, Andrzej J. Nowak, and Armin Hafner. 2016. "Performance Comparison of Fixed- and Controllable-Geometry Ejectors in a CO2 Refrigeration System." *International Journal of Refrigeration* 65: 172–82. doi:10.1016/j.ijrefrig.2016.01.025.

Sone, K., and S. Menon. 2003. "Effect of Subgrid Modeling on the In-Cylinder Unsteady

Mixing Process in a Direct Injection Engine." *Journal of Engineering for Gas Turbines and Power* 125(2): 435–43. doi:10.1115/1.1501918.

Sone, Kazuo, Nayan Patel, and Suresh Menon. 2001. "Large-Eddy Simulation of Fuel-Air Mixing in an Internal Combustion Engine." In *39th Aerospace Sciences Meeting and Exhibit*, Reston, Virigina: American Institute of Aeronautics and Astronautics. doi:10.2514/6.2001-635.

Song, Chul Hwa, Seok Cho, and Hyung Seok Kang. 2012. "Steam Jet Condensation in a Pool: From Fundamental Understanding to Engineering Scale Analysis." *Journal of Heat Transfer* 134(3): 1–15. doi:10.1115/1.4005144.

Song, Yulong, Yuan Ma, Haidan Wang, Xiang Yin, and Feng Cao. 2020. "Review on the Simulation Models of the Two-Phase-Ejector Used in the Transcritical Carbon Dioxide Systems." *International Journal of Refrigeration* 119: 434–47. doi:10.1016/j.ijrefrig.2020.04.029.

Sosnowski, Marcin, Jaroslaw Krzywanski, and Renata Gnatowska. 2017. "Polyhedral Meshing as an Innovative Approach to Computational Domain Discretization of a Cyclone in a Fluidized Bed CLC Unit" eds. W. Suwała, M. Dudek, J. Leszczyński, and S. Łopata. *E3S Web of Conferences* 14: 01027. doi:10.1051/e3sconf/20171401027.

Souza, José Francisco Almeida de, Leopoldo Rota de Oliveira, José Luiz Lima de Azevedo, Ivan Dias Soares, and Mauricio Magalhães Mata. 2011. "Uma Revisão Sobre a Turbulência e Sua Modelagem." *Revista Brasileira de Geofisica* 29(1): 21–41. doi:10.1590/S0102-261X2011000100002.

Spalart, Philippe R., W. H. Jou, Mikhail Kh Strelets, and S. R. Allmaras. 1997. "Comments on the Feasibility of LES for Wings and on a Hybrid RANS/LES Approach." In *1st, Advances in DNS/LES: Direct Numerical Simulation and Large Eddy Simulation*, Ruston: Greyden Press, 4–8. https://www.tib.eu/en/search/id/BLCP%3ACN032430355/Comments-on-the-Feasibility-of-LES-for-Wings-and/.

Span, Roland, and Wolfgang Wagner. 1996. "A New Equation of State for Carbon Dioxide Covering the Fluid Region from the Triple-Point Temperature to 1100 K at Pressures up to 800 MPa." *Journal of Physical and Chemical Reference Data* 25(6): 1509–96. doi:10.1063/1.555991.

Sullins, G., and G. McLafferty. 1992. "Experimental Results of Shock Trains in Rectangular Ducts." In *AIAA 4th International Aerospace Planes Conference*, Reston, Virigina: American Institute of Aeronautics and Astronautics. doi:10.2514/6.1992-5103.

Sun, Da-Wen. 1996. "Variable Geometry Ejectors and Their Applications in Ejector Refrigeration Systems." *Energy* 21(10): 919–29. doi:10.1016/0360-5442(96)00038-2.

Taleghani, Sahar Taslimi, Mikhail Sorin, and S. Poncet. 2018. "Modeling of Two-Phase Transcritical CO2 Ejectors for on-Design and off-Design Conditions." *International Journal of Refrigeration* 87: 91–105. doi:10.1016/j.ijrefrig.2017.10.025.

Tashtoush, Bourhan M., Moh'd A. Al-Nimr, and Mohammad A. Khasawneh. 2019. "A Comprehensive Review of Ejector Design, Performance, and Applications." *Applied Energy* 240(May 2018): 138–72. doi:10.1016/j.apenergy.2019.01.185.

Thol, Monika, and Eric W. Lemmon. 2016. "Equation of State for the Thermodynamic Properties of Trans-1,3,3,3-Tetrafluoropropene [R-1234ze(E)]." *International Journal of Thermophysics* 37(3): 28. doi:10.1007/s10765-016-2040-6.

U.S. Department of Energy. 1992. 3 DOE-HDBK-1012/3-92 *Thermodynamics, Heat Transfer and Fluid Flow.* Washington: U.S. Department of Energy. https://www.standards.doe.gov/standards-documents/1000/1012-BHdbk-1992-V1.

De Vanna, F., G. Baldan, F. Picano, and E. Benini. 2024. "High-Reynolds Compressible Flows Simulation with Wall-Modeled LES and Immersed Boundary Method." In *Direct and Large Eddy Simulation XIII*, eds. C. Marchioli, M.V. Salvetti, M. Garcia-Villalba, and P. Schlatter. Springer, Cham, 203–8. doi:10.1007/978-3-031-47028-8_31.

Varga, Szabolcs, Pedro Lebre, and Armando Oliveira. 2012. "CFD Study of a Variable Area Ratio Ejector Using R600a and R152a Refrigerants." *International Journal of Refrigeration* 36: 157–65. doi:10.1016/j.ijrefrig.2012.10.016.

Varga, Szabolcs, Armando Oliveira, and Bogdan Diaconu. 2009a. "Analysis of a Solar-Assisted Ejector Cooling System for Air Conditioning." *International Journal of Low-Carbon Technologies* 4(1): 2–8. doi:10.1093/IJLCT/CTN001.

Varga, Szabolcs, Armando Oliveira, and Bogdan Diaconu. 2009b. "Influence of Geometrical Factors on Steam Ejector Performance - A Numerical Assessment." *International Journal of Refrigeration* 32: 1694–1701. doi:10.1016/j.ijrefrig.2009.05.009.

Varga, Szabolcs, Armando Oliveira, and Bogdan Diaconu. 2009c. "Numerical Assessment of Steam Ejector Efficiencies Using CFD." *International Journal of Refrigeration* 32: 1203–11. doi:10.1016/j.ijrefrig.2009.01.007.

Varga, Szabolcs, Armando Oliveira, Xiaoli Ma, Siddig Omer, Wei Zhang, and Saffa Riffat. 2011. "Experimental and Numerical Analysis of a Variable Area Ratio Steam Ejector." *International Journal of Refrigeration* 34(7): 1668–75. doi:10.1016/j.ijrefrig.2010.12.020.

Varga, Szabolcs, Armando Oliveira, Ana Palmero-Marrero, and Jakub Vrba. 2017. "Preliminary Experimental Results with a Solar Driven Ejector Air Conditioner in Portugal." *Renewable Energy* 109: 83–92. doi:10.1016/j.renene.2017.03.016.

Varga, Szabolcs, João Soares, Rafael Lima, and Armando C. Oliveira. 2017. "On the Selection of a Turbulence Model for the Simulation of Steam Ejectors Using CFD." *International Journal of Low-Carbon Technologies* 12(3): 233–43. doi:10.1093/ijlct/ctx007.

Versteeg, Henk Kaarle, and Weeratunge Malalasekera. 2007. *An Introduction to Computational Fluid Dynamics: The Finite Volume Method*. second. ed. Pearson Education (US). Harlow. http://www.ncbi.nlm.nih.gov/pubmed/6686412.

Vesovic, V., W. A. Wakeham, G. A. Olchowy, J. V. Sengers, J. T. R. Watson, and J. Millat. 1990. "The Transport Properties of Carbon Dioxide." *Journal of Physical and Chemical Reference Data* 19(3): 763–808. doi:10.1063/1.555875.

Wang, Haiying, and Hai Wang. 2019. "Enhance Hydraulic Balance of a District Cooling System with Multiple Jet Pump." *Energy Procedia* 158: 2536–42. doi:10.1016/j.egypro.2019.01.412.

Wilcox, David C. 2006. *Turbulence Modelling for CFD*. 3rd ed. California: DCW Industries, Inc.

Work, L.T., and A. Miller. 1940. "Factor C in the Performance of Ejectors • As a Function of Molecular Weights of Vapors." *Industrial and Engineering Chemistry* 32(9): 1241–43. doi:10.1021/ie50369a040.

Xu, Maosen, Bin Ji, Jialin Zou, and Xinping Long. 2017. "Experimental Investigation on the Transport of Different Fish Species in a Jet Fish Pump." *Aquacultural Engineering* 79: 42–48. doi:10.1016/j.aquaeng.2017.10.001.

Yakhot, Victor, and Steven A. Orszag. 1986. "Renormalization Group Analysis of Turbulence. I. Basic Theory." *Journal of Scientific Computing* 1(1): 3–51.

doi:10.1007/BF01061452.

Yan, Jia, Wenjian Cai, and Yanzhong Li. 2012. "Geometry Parameters Effect for Air-Cooled Ejector Cooling Systems with R134a Refrigerant." *Renewable Energy* 46: 155–63. doi:10.1016/j.renene.2012.03.031.

Yan, Tingjun, Xuhe Zhao, Xiaohe Wang, Jifei Yu, and Yifan Shi. 2018. "Study on Energy Conservation Water Injection System of Offshore Platform Based on Jet Pump." *Journal of Petroleum Science and Engineering* 170(June): 368–73. doi:10.1016/j.petrol.2018.06.039.

Yang, X., X. Long, and X. Yao. 2012. "Numerical Investigation on the Mixing Process in a Steam Ejector with Different Nozzle Structures." *International Journal of Thermal Sciences* 56: 95–106. doi:10.1016/j.ijthermalsci.2012.01.021.

Yang, Xiang I. A., George Ilhwan Park, and Parviz Moin. 2017. "Log-Layer Mismatch and Modeling of the Fluctuating Wall Stress in Wall-Modeled Large-Eddy Simulations." *Physical Review Fluids* 2(10): 104601. doi:10.1103/PhysRevFluids.2.104601.

Yazdani, Miad, Abbas A. Alahyari, and Thomas D. Radcliff. 2012. "Numerical Modeling of Two-Phase Supersonic Ejectors for Work-Recovery Applications." *International Journal of Heat and Mass Transfer* 55(21–22): 5744–53. doi:10.1016/j.ijheatmasstransfer.2012.05.071.

Zaheer, Q., and J. Masud. 2017. "Visualization of Flow Field of a Liquid Ejector Pump Using Embedded LES Methodology." *Journal of Visualization* 20(4): 777–88. doi:10.1007/s12650-017-0429-3.

Zaheer, Syed Qasim, Jehanzeb Masud, and Asim Shabbir. 2018. "Effect of Turbulence Modeling on Realistic Estimation of Flow Characteristics of Liquid Ejector Pump." In *2018 15th International Bhurban Conference on Applied Sciences and Technology (IBCAST)*, IEEE, 658–63. doi:10.1109/IBCAST.2018.8312294.

Zeman, Otto. 1993. "A New Model for Super/Hypersonic Turbulent Boundary Layers." In *31st Aerospace Sciences Meeting*, Reston, Virigina: American Institute of Aeronautics and Astronautics. doi:10.2514/6.1993-897.

Zhdanov, Valery, and Andrei Chorny. 2011. "Development of Macro- and Micromixing in Confined Flows of Reactive Fluids." *International Journal of Heat and Mass Transfer* 54(15–16): 3245–55. doi:10.1016/j.ijheatmasstransfer.2011.04.006.

Zhu, Yinhai, Wenjian Cai, Changyun Wen, and Yanzhong Li. 2009. "Numerical Investigation of Geometry Parameters for Design of High Performance Ejectors." *Applied Thermal Engineering* 29(5–6): 898–905. doi:10.1016/j.applthermaleng.2008.04.025.

Zhu, Yinhai, and Peixue Jiang. 2014. "Experimental and Numerical Investigation of the Effect of Shock Wave Characteristics on the Ejector Performance." *International Journal of Refrigeration* 40: 31–42. doi:10.1016/j.ijrefrig.2013.11.008.

Zuckerwar, Allan J., and Robert L. Ash. 2006. "Variational Approach to the Volume Viscosity of Fluids." *Physics of Fluids* 18(4). doi:10.1063/1.2180780.

Mathematical convection

To help the reader in understanding the mathematical notation used in this thesis, this appendix lists and explains the mathematical conventions used throughout the text.

A.1 Vectors and notation

To begin, it is important to present the general convention adopted for vectors. Vector quantities are displayed with a raised arrow. For example, the velocity vector is represented as shown in Equation (3.36).

$$\vec{u} = \begin{bmatrix} u \\ v \\ w \end{bmatrix} \tag{A.1}$$

The components of a 3-dimensional vector $\vec{x}$ are denoted as x_1, x_2 and x_3. Thus, the coordinate vector can be rewritten as:

$$\vec{x} = \begin{bmatrix} x \\ y \\ z \end{bmatrix} \rightarrow \vec{x} = \begin{bmatrix} x_1 \\ x_2 \\ x_3 \end{bmatrix} \tag{A.2}$$

A.2 Planes and Summation Notation

For an equation describing a plane:

$$a_1 \cdot x_1 + a_2 \cdot x_2 + a_3 \cdot x_3 = c \tag{A.3}$$

where a_i and c are constants, Equation (A.3) can also be written using summation notation as:

$$\sum_{i=1}^{3} a_i \cdot x_i = c \tag{A.4}$$

Applying the Einstein summation convention, where repeated indices imply summation, the equation (A.4) simplifies to:

$$a_i \cdot x_i = c \tag{A.5}$$

A.3 Matrices and Tensors

Matrices are represented using two subscripts, where the first denotes the row number and the second the column number. Common indices used are i, j and k. For example, the viscous stress tensor in 3-dimensional space is given by:

$$\tau_{ij} = \begin{bmatrix} \tau_{11} & \tau_{12} & \tau_{13} \\ \tau_{21} & \tau_{22} & \tau_{23} \\ \tau_{31} & \tau_{32} & \tau_{33} \end{bmatrix} \tag{A.6}$$

For symmetric tensors, such as the viscous stress tensor, the following relationship holds:

$$\tau_{ij} = \tau_{ji} \tag{A.7}$$

A.4 Summative Derivative

The total or substantive derivative of a scalar quantity ∅ describes the rate of change of ∅ along the path of a moving fluid element. It is expressed as:

$$\frac{D\emptyset}{Dt} = \frac{\partial \emptyset}{\partial t} + \frac{\partial x}{\partial t}\frac{\partial \emptyset}{\partial x} + \frac{\partial y}{\partial t}\frac{\partial \emptyset}{\partial y} + \frac{\partial z}{\partial t}\frac{\partial \emptyset}{\partial z}. \tag{A.8}$$

By replacing the velocity vector into Equation (A.8) and applying the Einstein summation convention (Equation (A.5)), the expression simplifies to:

$$\frac{D\emptyset}{Dt} = \frac{\partial \emptyset}{\partial t} + u_i \frac{\partial \emptyset}{\partial x_i} \tag{A.9}$$

Some simplifications along the document can be presented for the derivation process. To better understanding, an example for a derivation process is presented in here:

$$\frac{\partial(\rho\emptyset)}{\partial t} + \frac{\partial(\rho\emptyset u_i)}{\partial x_i} = \left[\rho\frac{\partial \emptyset}{\partial t} + \emptyset\frac{\partial \rho}{\partial t}\right] + \left[\rho u_i \frac{\partial \emptyset}{\partial x_i} + \emptyset\frac{\partial(\rho u_i)}{\partial x_i}\right] \tag{A.10}$$

From equation (A.10), is possible to obtain:

$$\frac{\partial(\rho\emptyset)}{\partial t} + \frac{\partial(\rho\emptyset u_i)}{\partial x_i} = \rho\left[\frac{\partial \emptyset}{\partial t} + u_i\frac{\partial \emptyset}{\partial x_i}\right] + \emptyset\left[\frac{\partial \rho}{\partial t} + \frac{\partial(\rho u_i)}{\partial x_i}\right] \tag{A.11}$$

Recalling the continuity equation:

$$\frac{\partial \rho}{\partial t} + \frac{\partial(\rho u_i)}{\partial x_i} = 0 \tag{A.12}$$

Replacing in equation (A.11) the conclusion presented in equation (A.12), the derivative presented in equation (A.9) is:

$$\frac{\partial(\rho\emptyset)}{\partial t} + \frac{\partial(\rho\emptyset u_i)}{\partial x_i} = \rho\left[\frac{\partial \emptyset}{\partial t} + u_i\frac{\partial \emptyset}{\partial x_i}\right] \tag{A.13}$$

The second term in equation (A.13) is the substantive derivative multiplied by the fluid density (ρ). Concluding that equation (A.9) can be expressed as:

$$\rho\frac{D\emptyset}{Dt} = \frac{\partial(\rho\emptyset)}{\partial t} + \frac{\partial(\rho\emptyset u_i)}{\partial x_i} \tag{A.14}$$

A.5 Gradient and Divergence Operators

Gradient operator (∇) is used to compute the partial derivative of a scalar quantity with respect to all directions in a given coordinate system. It is expressed as:

$$\nabla \emptyset = \frac{\partial \emptyset}{\partial x_i} \vec{\imath} \tag{A.15}$$

In equation (A.15), $\vec{\imath}$ represents the unit vector in the direction of x_i.

The gradient of a vector $\vec{\emptyset}$ can be represented as a second-order tensor:

$$\frac{\partial \emptyset_i}{\partial x_j} = \begin{bmatrix} \frac{\partial \emptyset_1}{\partial x_1} & \frac{\partial \emptyset_1}{\partial x_2} & \frac{\partial \emptyset_1}{\partial x_3} \\ \frac{\partial \emptyset_2}{\partial x_1} & \frac{\partial \emptyset_2}{\partial x_2} & \frac{\partial \emptyset_2}{\partial x_3} \\ \frac{\partial \emptyset_3}{\partial x_1} & \frac{\partial \emptyset_3}{\partial x_2} & \frac{\partial \emptyset_3}{\partial x_3} \end{bmatrix} \tag{A.16}$$

The divergence operator, another form of ∇, computes the scalar partial derivative of a vector field:

$$\nabla \cdot \emptyset = \frac{\partial \emptyset_i}{\partial x_i} \tag{A.17}$$

A.6 Tensor Operations

To illustrate operations involving tensors, consider the multiplication of the stress tensor (τ_{ji}) and the gradient tensor ($\partial \emptyset_i / \partial x_j$) defined in Equation (A.16):

$$\tau_{ji} \frac{\partial \emptyset_i}{\partial x_j} \equiv \sum_{i=1}^{3} \sum_{j=1}^{3} \tau_{ji} \frac{\partial \emptyset_i}{\partial x_j} \tag{A.18}$$

Expanding the summation over j:

$$\tau_{ji} \frac{\partial \emptyset_i}{\partial x_j} \equiv \sum_{i=1}^{3} \tau_{1i} \frac{\partial \emptyset_i}{\partial x_1} + \tau_{2i} \frac{\partial \emptyset_i}{\partial x_2} + \tau_{3i} \frac{\partial \emptyset_i}{\partial x_3} \tag{A.19}$$

Expanding further over i:

$$\begin{aligned} \tau_{ji} \frac{\partial \emptyset_i}{\partial x_j} \equiv \tau_{11} \frac{\partial \emptyset_1}{\partial x_1} + \tau_{21} \frac{\partial \emptyset_1}{\partial x_2} + \tau_{31} \frac{\partial \emptyset_1}{\partial x_3} + \tau_{12} \frac{\partial \emptyset_2}{\partial x_1} + \tau_{22} \frac{\partial \emptyset_2}{\partial x_2} + \tau_{32} \frac{\partial \emptyset_2}{\partial x_3} + \\ + \tau_{13} \frac{\partial \emptyset_3}{\partial x_1} + \tau_{23} \frac{\partial \emptyset_3}{\partial x_2} + \tau_{33} \frac{\partial \emptyset_3}{\partial x_3} \end{aligned} \tag{A.20}$$

A.7 Expansion of the Viscous Stress Tensor

The viscous stress tensor τ_{ji} is expressed as:

$$\tau_{ji} = \mu\left[\left(\frac{\partial u_i}{\partial x_j} + \frac{\partial u_j}{\partial x_i}\right) - \frac{2}{3}\,\delta_{ij}\frac{\partial u_k}{\partial x_k}\right] \tag{A.21}$$

In equation (A.21), δ_{ij} denotes the Kronecker delta ($\delta_{ij} = 1$ if i = j and $\delta_{ij} = 0$ if i ≠ j).

For the term $\partial\tau_{ji}/\partial x_j$, summation must include i, j and k. And expanding the summation over k, results in:

$$\frac{\partial \tau_{ji}}{\partial x_j} \equiv \sum_{j=1}^{3}\frac{\partial}{\partial x_j}\left\{\mu\left[\left(\frac{\partial u_i}{\partial x_j} + \frac{\partial u_j}{\partial x_i}\right) - \frac{2}{3}\,\delta_{ij}\left(\frac{\partial u_1}{\partial x_1} + \frac{\partial u_2}{\partial x_2} + \frac{\partial u_3}{\partial x_3}\right)\right]\right\} \tag{A.22}$$

And then, expanding over j:

$$\begin{aligned}\frac{\partial \tau_{ji}}{\partial x_j} \equiv{}& \frac{\partial}{\partial x_1}\left\{\mu\left[\left(\frac{\partial u_i}{\partial x_1} + \frac{\partial u_1}{\partial x_i}\right) - \frac{2}{3}\,\delta_{i1}\left(\frac{\partial u_1}{\partial x_1} + \frac{\partial u_2}{\partial x_2} + \frac{\partial u_3}{\partial x_3}\right)\right]\right\} + \\ &+ \frac{\partial}{\partial x_2}\left\{\mu\left[\left(\frac{\partial u_i}{\partial x_2} + \frac{\partial u_2}{\partial x_i}\right) - \frac{2}{3}\,\delta_{i2}\left(\frac{\partial u_1}{\partial x_1} + \frac{\partial u_2}{\partial x_2} + \frac{\partial u_3}{\partial x_3}\right)\right]\right\} + \\ &+ \frac{\partial}{\partial x_3}\left\{\mu\left[\left(\frac{\partial u_i}{\partial x_3} + \frac{\partial u_3}{\partial x_i}\right) - \frac{2}{3}\,\delta_{i3}\left(\frac{\partial u_1}{\partial x_1} + \frac{\partial u_2}{\partial x_2} + \frac{\partial u_3}{\partial x_3}\right)\right]\right\}\end{aligned} \tag{A.23}$$

Equation (A.23) then is divided into three equations, for i = 1, 2 and 3:

$$\begin{aligned}\frac{\partial \tau_{j1}}{\partial x_j} \equiv{}& \frac{\partial}{\partial x_1}\left\{\mu\left[2\frac{\partial u_1}{\partial x_1} - \frac{2}{3}\left(\frac{\partial u_1}{\partial x_1} + \frac{\partial u_2}{\partial x_2} + \frac{\partial u_3}{\partial x_3}\right)\right]\right\} + \frac{\partial}{\partial x_2}\left[\mu\left(\frac{\partial u_1}{\partial x_2} + \frac{\partial u_2}{\partial x_1}\right)\right] + \\ &+ \frac{\partial}{\partial x_3}\left[\mu\left(\frac{\partial u_1}{\partial x_3} + \frac{\partial u_3}{\partial x_1}\right)\right]\end{aligned} \tag{A.24}$$

$$\begin{aligned}\frac{\partial \tau_{j2}}{\partial x_j} \equiv{}& \frac{\partial}{\partial x_1}\left[\mu\left(\frac{\partial u_2}{\partial x_1} + \frac{\partial u_1}{\partial x_2}\right)\right] + \frac{\partial}{\partial x_2}\left\{\mu\left[2\frac{\partial u_2}{\partial x_2} - \frac{2}{3}\left(\frac{\partial u_1}{\partial x_1} + \frac{\partial u_2}{\partial x_2} + \frac{\partial u_3}{\partial x_3}\right)\right]\right\} + \\ &+ \frac{\partial}{\partial x_3}\left[\mu\left(\frac{\partial u_2}{\partial x_3} + \frac{\partial u_3}{\partial x_2}\right)\right]\end{aligned} \tag{A.25}$$

$$\begin{aligned}\frac{\partial \tau_{j3}}{\partial x_j} \equiv{}& \frac{\partial}{\partial x_1}\left[\mu\left(\frac{\partial u_3}{\partial x_1} + \frac{\partial u_1}{\partial x_3}\right)\right] + \frac{\partial}{\partial x_2}\left[\mu\left(\frac{\partial u_3}{\partial x_2} + \frac{\partial u_2}{\partial x_3}\right)\right] + \\ &+ \frac{\partial}{\partial x_3}\left\{\mu\left[2\frac{\partial u_3}{\partial x_3} - \frac{2}{3}\left(\frac{\partial u_1}{\partial x_1} + \frac{\partial u_2}{\partial x_2} + \frac{\partial u_3}{\partial x_3}\right)\right]\right\}\end{aligned} \tag{A.26}$$

The result is the sum of equations (A.24) to (A.26):

$$\begin{aligned}\frac{\partial \tau_{ji}}{\partial x_j} \equiv{}& \frac{\partial}{\partial x_1}\left\{\mu\left[\frac{4}{3}\frac{\partial u_1}{\partial x_1} - \frac{2}{3}\left(\frac{\partial u_2}{\partial x_2} + \frac{\partial u_3}{\partial x_3}\right) + \left(\frac{\partial u_2}{\partial x_1} + \frac{\partial u_1}{\partial x_2}\right) + \left(\frac{\partial u_3}{\partial x_1} + \frac{\partial u_1}{\partial x_3}\right)\right]\right\} + \\ &+ \frac{\partial}{\partial x_2}\left\{\mu\left[\frac{4}{3}\frac{\partial u_2}{\partial x_2} - \frac{2}{3}\left(\frac{\partial u_1}{\partial x_1} + \frac{\partial u_3}{\partial x_3}\right) + \left(\frac{\partial u_1}{\partial x_2} + \frac{\partial u_2}{\partial x_1}\right) + \left(\frac{\partial u_3}{\partial x_2} + \frac{\partial u_2}{\partial x_3}\right)\right]\right\} + \\ &+ \frac{\partial}{\partial x_3}\left\{\mu\left[\frac{4}{3}\frac{\partial u_3}{\partial x_3} - \frac{2}{3}\left(\frac{\partial u_1}{\partial x_1} + \frac{\partial u_2}{\partial x_2}\right) + \left(\frac{\partial u_1}{\partial x_3} + \frac{\partial u_3}{\partial x_1}\right) + \left(\frac{\partial u_2}{\partial x_3} + \frac{\partial u_3}{\partial x_2}\right)\right]\right\}\end{aligned} \tag{A.27}$$

Appendix B

Favre averaging rules

Favre averaging is a density-weighted averaging method that needs to be combined with Reynolds averaging, a time-averaging procedure. This appendix explains the mathematical rules and conventions used in the Favre averaging process, highlighting key equations and their implications for turbulence modelling.

B.1 Foundational Principles of Reynolds and Favre Averaging

B.1.1 Scalar Decomposition and Reynolds Averaging

To begin, consider a scalar quantity φ. Using Reynolds decomposition, φ can be expressed as:

$$\varphi = \overline{\varphi} + \varphi' \tag{B.1}$$

In equation (B.1), $\overline{\varphi}$ represents the averaged component of the scalar φ, while φ' denotes the fluctuation around the mean. When averaging φ, the following relationship holds:

$$\overline{\overline{\varphi} + \varphi'} = \overline{\overline{\varphi}} + \overline{\varphi'} \tag{B.2}$$

Applying the Reynolds averaging rules:

$$\overline{\overline{\varphi}} = \overline{\varphi} \tag{B.3}$$

$$\overline{\varphi'} = 0 \tag{B.4}$$

Equation (B.2) simplifies to:

$$\overline{\overline{\varphi}} + \overline{\varphi'} = \overline{\varphi} \tag{B.5}$$

B.1.2 Favre Averaging Definitions

Favre averaging introduces a density-weighted average, represented as:

$$\tilde{\varphi} = \frac{\overline{\rho\varphi}}{\overline{\rho}} \tag{B.6}$$

In this context, φ can also be decomposed into two components:

$$\varphi = \tilde{\varphi} + \varphi'' \tag{B.7}$$

Here, $\tilde{\varphi}$ is the mass-weighted mean, and φ'' is the Favre fluctuation. By applying Reynolds averaging to Equation (B.6), the Favre average can be expanded as:

$$\tilde{\varphi} = \overline{\varphi} + \frac{\overline{\rho'\varphi'}}{\overline{\rho}} \tag{B.8}$$

This introduces the Favre fluctuation as:

$$\varphi'' = \varphi' - \frac{\overline{\rho'\varphi'}}{\overline{\rho}} \tag{B.9}$$

Then, averaging the Favre fluctuation in equation (B.9) results in:

$$\overline{\varphi''} = -\frac{\overline{\rho'\varphi'}}{\overline{\rho}} \tag{B.10}$$

B.1.3 Pressure and Density Averaging

Unlike scalars, pressure (p) and density (ρ) cannot be mass-weight averaged. Their decomposition remains consistent with Reynolds averaging:

$$p = \overline{p} + p' \tag{B.11}$$

$$\rho = \overline{\rho} + \rho' \tag{B.12}$$

B.1.4 Key Relations in Favre Averaging

Multiplying a scalar by the mass density (ρ) and applying Favre averaging yields an important conclusion. For instance:

$$\overline{\rho\varphi} = \overline{(\overline{\rho} + \rho')(\tilde{\varphi} + \varphi'')} \tag{B.13}$$

By developing the equation (B.13) applying the previous presented equalities and rules, in the end, the expression can be written as:

$$\overline{\rho\varphi} = \overline{\rho\varphi} + \overline{\rho}\,\overline{\varphi''} + \overline{\rho}\tilde{\varphi} + \overline{\rho\varphi''} - \overline{\rho}\tilde{\varphi} - \overline{\rho}\,\overline{\varphi''} \tag{B.14}$$

Resulting in:

$$\overline{\rho\varphi''} = 0. \tag{B.15}$$

Another essential relation involves two Favre fluctuations:

$$\overline{\rho\varphi''\phi''} = \overline{\rho}\widetilde{\varphi''\phi''}. \tag{B.16}$$

B.2 Application of Favre Averaging to Governing Equations

In this section, Favre averaging is applied to the governing equations for continuity, momentum, energy, and kinetic energy. The derivation process is detailed to demonstrate how this averaging procedure transforms the equations and introduces additional terms crucial for turbulence modelling.

These equations are developed based on commonly accepted assumptions in the scientific literature (Anderson et al., 2020), which include:

1. fluctuations in the molecular viscosity have been neglected;
2. $\left|-\overline{\rho u_i'' u_i''}\right| \gg \left|\overline{\tau_{ij}''}\right| then\ \overline{\tau_{ij}''} \approx 0$;
3. $\left|\frac{\partial^2 \tilde{T}}{\partial x_j^2}\right| \gg \left|\frac{\partial^2 \overline{T''}}{\partial x_j^2}\right| then\ \overline{T''} \approx 0.$

B.2.1 Favre Averaging the Continuity Equation

The continuity equation in its general form is expressed as:

$$\overline{\frac{\partial \rho}{\partial t} + \frac{\partial (\rho u_j)}{\partial x_j}} = 0 \tag{B.17}$$

Applying Favre averaging, the density term becomes:

$$\overline{\frac{\partial \rho}{\partial t}} = \overline{\frac{\partial (\overline{\rho} + \rho')}{\partial t}} \Leftrightarrow \overline{\frac{\partial \rho}{\partial t}} = \frac{\partial \overline{\rho}}{\partial t} + \overline{\frac{\partial \rho'}{\partial t}} \Leftrightarrow \overline{\frac{\partial \rho}{\partial t}} = \frac{\partial \overline{\rho}}{\partial t} \tag{B.18}$$

For the velocity term, Favre averaging simplifies to:

$$\overline{\frac{\partial \rho u_j}{\partial x_j}} = \overline{\frac{\partial \left(\rho (\tilde{u}_j + u_j'')\right)}{\partial x_j}} \Leftrightarrow \overline{\frac{\partial \rho u_j}{\partial x_j}} = \frac{\partial \left(\overline{\rho \tilde{u}_j} + \overline{\rho u_j''}\right)}{\partial x_j} \Leftrightarrow \overline{\frac{\partial \rho u_j}{\partial x_j}} = \frac{\partial (\overline{\rho} \tilde{u}_j)}{\partial x_j} \tag{B.19}$$

Combining these results, the Favre-averaged continuity equation is written as:

$$\frac{\partial \overline{\rho}}{\partial t} + \frac{\partial (\overline{\rho} \tilde{u}_j)}{\partial x_j} = 0 \tag{B.20}$$

B.2.2 Favre averaging the momentum equation

The average form of the momentum equation is expressed as:

$$\overline{\frac{\partial (\rho u_i)}{\partial t} + \frac{\partial (\rho u_i u_j)}{\partial x_j}} = \overline{-\frac{\partial p}{\partial x_i} + \frac{\partial \tau_{ji}}{\partial x_j}} \tag{B.21}$$

Using Favre averaging, the time-dependent term becomes:

$$\overline{\frac{\partial (\rho u_i)}{\partial t}} = \frac{\partial (\overline{\rho} \tilde{u}_i)}{\partial t} \tag{B.22}$$

The convective term is averaged as:

$$\overline{\frac{\partial(\rho u_i u_j)}{\partial x_j}} = \frac{\overline{\partial\left(\rho(\tilde{u}_i + u_i'')(\tilde{u}_j + u_j'')\right)}}{\partial x_j} \Leftrightarrow$$

$$\Leftrightarrow \frac{\overline{\partial(\rho u_i u_j)}}{\partial x_j} = \frac{\partial\left(\overline{\rho}\tilde{u}_i\tilde{u}_j + \overline{\rho u_j''}\tilde{u}_i + \overline{\rho u_i''}\tilde{u}_j + \overline{\rho u_i'' u_j''}\right)}{\partial x_j} \Leftrightarrow \tag{B.23}$$

$$\Leftrightarrow \frac{\overline{\partial(\rho u_i u_j)}}{\partial x_j} = \frac{\partial\left(\overline{\rho}\tilde{u}_i\tilde{u}_j + \overline{\rho u_i'' u_j''}\right)}{\partial x_j}$$

Combining these terms, the Favre-averaged momentum equation is:

$$\frac{\partial(\overline{\rho}\tilde{u}_i)}{\partial t} + \frac{\partial(\overline{\rho}\tilde{u}_i\tilde{u}_j)}{\partial x_j} + \frac{\partial\left(\overline{\rho u_i'' u_j''}\right)}{\partial x_j} = -\frac{\partial\overline{p}}{\partial x_i} + \frac{\overline{\partial\tau_{ji}}}{\partial x_j} \tag{B.24}$$

B.2.3 Favre averaging the single-phase energy equation

The average of the energy equation is expressed as:

$$\overline{\frac{\partial}{\partial t}\left[\rho\left(e + \frac{u_i u_i}{2}\right)\right] + \frac{\partial}{\partial x_j}\left[\rho u_j\left(e + \frac{u_i u_i}{2}\right) + u_j p\right]} = \overline{\frac{\partial}{\partial x_j}\left(\kappa\frac{\partial T}{\partial x_j}\right) + \frac{\partial(u_i\tau_{ji})}{\partial x_j}}. \tag{B.25}$$

The averaging process for the left side of the equation (B.25) is divided in two steps, each corresponds to a group identified with square parentheses:

1. Averaging the time dependent term:

$$\overline{\frac{\partial}{\partial t}\left[\rho e + \frac{\rho u_i u_i}{2}\right]} = \frac{\partial}{\partial t}\left[\overline{\rho}\tilde{e} + \frac{\overline{\rho}\tilde{u}_i\tilde{u}_i}{2} + \frac{\overline{\rho u_i'' u_i''}}{2}\right] \tag{B.26}$$

2. Averaging the 2nd term is simpler by steps:

$$\overline{\frac{\partial}{\partial x_j}(\rho u_j e)} = \frac{\partial}{\partial x_j}\left(\overline{\rho}\tilde{e}\,\tilde{u}_j + \overline{\rho e'' u_j''}\right) \tag{B.27}$$

$$\overline{\frac{\partial}{\partial x_j}\left(\rho u_j\frac{u_i u_i}{2}\right)} = \frac{\partial}{\partial x_j}\left(\tilde{u}_j\frac{\overline{\rho}\tilde{u}_i\tilde{u}_i}{2} + \tilde{u}_j\frac{\overline{\rho u_i'' u_i''}}{2} + \overline{\rho u_j''\,u_i''}\tilde{u}_i + \overline{u_j''\,\frac{\rho u_i'' u_i''}{2}}\right) \tag{B.28}$$

$$\overline{\frac{\partial}{\partial x_j}(u_j p)} = \frac{\partial}{\partial x_j}\left(\tilde{u}_j\overline{p} + \overline{u_j'' p}\right) \tag{B.29}$$

The right side of equation (B.25) has three terms, being each averaged as:

$$\overline{\frac{\partial(k\,\nabla T)}{\partial x_j}} = \frac{\overline{\partial\left(k\,\nabla(\tilde{T} + T'')\right)}}{\partial x_j} \Leftrightarrow \overline{\frac{\partial(\kappa\,\nabla T)}{\partial x_j}} = \frac{\partial(\kappa_L\tilde{T})}{\partial x_j} + \frac{\partial(\kappa_L\overline{T''})}{\partial x_j} \tag{B.30}$$

$$\overline{\frac{\partial(pu_j)}{\partial x_j}} = \frac{\overline{\partial\left(p(\tilde{u}_j + u_j'')\right)}}{\partial x_j} \Leftrightarrow \overline{\frac{\partial(pu_j)}{\partial x_j}} = \frac{\partial\left(\overline{p\tilde{u}_j} + \overline{pu_j''}\right)}{\partial x_j} \Leftrightarrow \tag{B.31}$$

$$\Leftrightarrow \overline{\frac{\partial p u_j}{\partial x_j}} = \frac{\partial(\overline{p}\tilde{u}_j)}{\partial x_j} + \frac{\partial\left(\overline{p}\overline{u_j''}\right)}{\partial x_j} + \frac{\partial\left(\overline{p' u_j''}\right)}{\partial x_j}$$

$$\overline{\frac{\partial(u_i\tau_{ji})}{\partial x_j}} = \overline{\frac{\partial\left(\tau_{ji}(\tilde{u}_i + u_i'')\right)}{\partial x_j}} \Leftrightarrow \overline{\frac{\partial(u_i\tau_{ji})}{\partial x_j}} = \frac{\partial\left(\overline{\tilde{u}_i(\tilde{\tau}_{ji} + \tau''_{ji})} + \overline{u_i''\tau_{ji}}\right)}{\partial x_j} \Leftrightarrow$$
$$\Leftrightarrow \overline{\frac{\partial u_i\tau_{ji}}{\partial x_j}} = \frac{\partial(\tilde{u}_i\tilde{\tau}_{ji})}{\partial x_j} + \frac{\partial(\tilde{u}_i\overline{\tau''}_{ji})}{\partial x_j} + \frac{\partial\left(\overline{u_i''\tau_{ji}}\right)}{\partial x_j} \quad \text{(B.32)}$$

Combining the conclusions from equations (B.26) to (B.32) with the momentum equation (B.25), the Favre averaged expression can be written as:

$$\frac{\partial}{\partial t}\left[\overline{\rho}\tilde{e} + \frac{\overline{\rho}\tilde{u}_i\tilde{u}_i}{2} + \frac{\overline{\rho u_i'' u_i''}}{2}\right] + \frac{\partial}{\partial x_j}\left[\overline{\rho}\tilde{e}\,\tilde{u}_j + \tilde{u}_j\frac{\overline{\rho}\tilde{u}_i\tilde{u}_i}{2} + \tilde{u}_j\frac{\overline{\rho u_i'' u_i''}}{2} + \tilde{u}_j\overline{p}\right] +$$
$$+\frac{\partial}{\partial x_j}\left[\overline{\rho e'' u_j''} + \overline{\rho u_j''}\,\tilde{u}_i\tilde{u}_i + \overline{u_j''\frac{\rho u_i'' u_i''}{2}} + \overline{\overline{p}u_j''} + \overline{p' u_j''}\right] = \quad \text{(B.33)}$$
$$= \frac{\partial(\kappa_L\tilde{T})}{\partial x_j} + \frac{\partial(\kappa_L\overline{T''})}{\partial x_j} + \frac{\partial\left(\tilde{u}_i\tilde{\tau}_{ji} + \overline{u_i''\tau_{ji}}\right)}{\partial x_j}$$

In equation (B.33) the terms in yellow can be aggregated and obtain:

$$\frac{\partial}{\partial x_j}\left[\overline{\rho e'' u_j''} + \overline{\overline{p}u_j''}\right] = \frac{\partial\left(c_p\overline{\rho u_j'' T}\right)}{\partial x_j}. \quad \text{(B.34)}$$

Considering the turbulent transport of heat, is possible to:

$$\frac{\partial}{\partial x_j}\left(c_p\overline{\rho u_j'' T}\right) = -\frac{\partial}{\partial x_j}\left(\kappa_T\frac{\partial\tilde{T}}{\partial x_j}\right). \quad \text{(B.35)}$$

The pressure dilatation, turbulent transport, and molecular diffusion of turbulent energy – highlighted in blue in equation (B.33) - can be modelled as follows:

$$\frac{\partial\left(\overline{p' u_j''}\right)}{\partial x_j} + \frac{\partial}{\partial x_j}\left[\overline{u_j''\frac{\rho u_i'' u_i''}{2}}\right] - \frac{\partial\left(\overline{u_i''\tau_{ji}}\right)}{\partial x_j} \approx -\frac{\partial}{\partial x_j}\left[\left(\mu + \frac{\mu_T}{\sigma_T}\right)\frac{\partial k}{\partial x_j}\right] \quad \text{(B.36)}$$

However, once the turbulent kinetic energy is small compared to enthalpy, these terms are often neglected.

The thermal conductivity can be replaced by an effective variable that includes the laminar and turbulent component, as:

$$\kappa_{eff} = \kappa_L + \kappa_T \quad \text{(B.37)}$$

And similar to the stress tensor:

$$\tau_{ji_{eff}} = \tilde{\tau}_{ji} - \overline{\rho u_j''\, u_i''} \quad \text{(B.38)}$$

The pink terms in equation (B.33) can be written as:

$$\frac{\partial\left(\tilde{u}_i\tilde{\tau}_{ji}\right)}{\partial x_j}-\frac{\partial}{\partial x_j}\left[\overline{\rho u_j''\,u_i''}\tilde{u}_i\right]=\frac{\partial\left(\tilde{u}_i{\tau_{ji}}_{eff}\right)}{\partial x_j} \tag{B.39}$$

Knowing that the density-averaged total energy is defined as:

$$\overline{\rho}\widetilde{E}\;=\overline{\rho}\widetilde{e}\;+\frac{\overline{\rho}\tilde{u}_i\tilde{u}_i}{2}+\frac{\overline{\rho u_i''u_i''}}{2} \tag{B.40}$$

The final averaged energy equation for single-phase flow can be expressed as:

$$\frac{\partial\left(\overline{\rho}\widetilde{E}\right)}{\partial t}+\frac{\partial\left(\overline{\rho}\widetilde{E}\right)}{\partial x_j}=\frac{\partial\left(\overline{k}_{eff}\widetilde{T}\right)}{\partial x_j}-\frac{\partial\left(\tilde{u}_j\overline{p}\right)}{\partial x_j}+\frac{\partial\left(\tilde{u}_i{\tau_{ji}}_{eff}\right)}{\partial x_j} \tag{B.41}$$

B.2.4 Favre averaging the two-phase energy equation

The average of the general momentum equation is expressed as:

$$\overline{\frac{\partial(\rho e)}{\partial t}+\frac{\partial\left(\rho u_j e\right)}{\partial x_j}}=\overline{-p\frac{\partial u_j}{\partial x_j}+\tau_{ji}\frac{\partial u_i}{\partial x_j}+\frac{\partial}{\partial x_j}\left(k\frac{\partial T}{\partial x_j}\right)}. \tag{B.42}$$

The averaging process for the left side of the equation (B.42) is divided in two steps:

1. Averaging the time dependent term:

$$\overline{\frac{\partial(\rho e)}{\partial t}}=\frac{\partial(\overline{\rho}\widetilde{e})}{\partial t} \tag{B.43}$$

2. Averaging the 2nd term:

$$\begin{aligned}\overline{\frac{\partial\left(\rho u_j e\right)}{\partial x_j}}=\frac{\overline{\partial\left(\rho(\tilde{u}_j+u_j'')(\tilde{e}+e'')\right)}}{\partial x_j}\Leftrightarrow\\ \Leftrightarrow\overline{\frac{\partial\left(\rho u_j e\right)}{\partial x_j}}=\frac{\partial\left(\overline{\rho}\tilde{u}_j\tilde{e}+\overline{\rho u_j''}\tilde{e}+\overline{\rho e''}\tilde{u}_j+\overline{\rho u_j''e''}\right)}{\partial x_j}\Leftrightarrow\\ \Leftrightarrow\overline{\frac{\partial\left(\rho u_j e\right)}{\partial x_j}}=\frac{\partial\left(\overline{\rho}\tilde{u}_j\tilde{e}+\overline{\rho u_j''e''}\right)}{\partial x_j}\end{aligned} \tag{B.44}$$

The right side of equation (B.42) has three terms, being each averaged as:

$$\begin{aligned}\overline{p\frac{\partial u_j}{\partial x_j}}=\overline{p\frac{\partial\left(\tilde{u}_j+u_j''\right)}{\partial x_j}}\Leftrightarrow\overline{p\frac{\partial u_j}{\partial x_j}}=\overline{p\frac{\partial\tilde{u}_j}{\partial x_j}}+\overline{p\frac{\partial u_j''}{\partial x_j}}\Leftrightarrow\\ \Leftrightarrow\overline{p\frac{\partial u_j}{\partial x_j}}=\overline{p}\frac{\partial\tilde{u}_j}{\partial x_j}+\overline{p}\frac{\partial\overline{u_j''}}{\partial x_j}+\overline{p'\frac{\partial u_j''}{\partial x_j}}\end{aligned} \tag{B.45}$$

$$\overline{\tau_{ji}\frac{\partial u_i}{\partial x_j}} = \overline{\tau_{ji}\frac{\partial\left(\tilde{u}_i + u_i''\right)}{\partial x_j}} \Leftrightarrow \overline{\tau_{ji}\frac{\partial u_i}{\partial x_j}} = \overline{\left(\tilde{\tau}_{ji} + {\tau_{ij}}''\right)\frac{\partial \tilde{u}_i}{\partial x_j}} + \overline{\tau_{ji}\frac{\partial u_i''}{\partial x_j}} \Leftrightarrow$$
$$\Leftrightarrow \overline{\tau_{ji}\frac{\partial u_i}{\partial x_j}} = \tilde{\tau}_{ji}\frac{\partial \tilde{u}_i}{\partial x_j} + \overline{{\tau_{ij}}''\frac{\partial \tilde{u}_i}{\partial x_j}} + \overline{\tau_{ji}\frac{\partial u_i''}{\partial x_j}} \tag{B.46}$$

$$\overline{\frac{\partial(\kappa\,\nabla T)}{\partial x_j}} = \overline{\frac{\partial\left(\kappa\,\nabla\left(\tilde{T} + T''\right)\right)}{\partial x_j}} \Leftrightarrow \overline{\frac{\partial(\kappa\,\nabla T)}{\partial x_j}} = \frac{\partial\left(\overline{\kappa\,\nabla\tilde{T}}\right)}{\partial x_j} + \frac{\partial\left(\overline{\kappa\,\nabla T''}\right)}{\partial x_j} \tag{B.47}$$

Combining the details from equations (B.43) to (B.47) and the considerations previous presented, the Favre averaged expression can be written as:

$$\frac{\partial(\overline{\rho}\tilde{e})}{\partial t} + \frac{\partial\left(\overline{\rho}\tilde{u}_j\tilde{e} + \overline{\rho u_j'' e''}\right)}{\partial x_j} = \left[-\overline{p}\frac{\partial \tilde{u}_j}{\partial x_j} - \overline{p}\frac{\partial \overline{u_j''}}{\partial x_j} - \overline{p'\frac{\partial u_j''}{\partial x_j}}\right] +$$
$$+\left[\tilde{\tau}_{ji}\frac{\partial \tilde{u}_i}{\partial x_j} + \overline{\tau_{ji}\frac{\partial u_i''}{\partial x_j}}\right] + \left[\frac{\partial}{\partial x_j}\left(\kappa\frac{\partial \tilde{T}}{\partial x_j}\right)\right] \tag{B.48}$$

B.2.5 Favre averaging the kinetic energy equation

The average of the general kinetic energy equation is expressed as:

$$\overline{\frac{\partial(KE)}{\partial t} + \frac{\partial\left(u_j\,KE\right)}{\partial x_j}} = \overline{-u_i\frac{\partial p}{\partial x_i} + u_i\frac{\partial \tau_{ji}}{\partial x_j}}. \tag{B.49}$$

In equation (B.49) KE is the kinetic energy, and it is defined as:

$$KE = \frac{\rho u_i u_i}{2}. \tag{B.50}$$

Averaging the kinetic energy results in:

$$\overline{\frac{\rho u_i u_i}{2}} = \overline{\frac{\rho\left(\tilde{u}_i + u_i''\right)\left(\tilde{u}_i + u_i''\right)}{2}} \Leftrightarrow \overline{\frac{\rho u_i u_i}{2}} = \overline{\frac{\rho\left(\tilde{u}_i\tilde{u}_i + 2\tilde{u}_i u_i'' + u_i'' u_i''\right)}{2}} \Leftrightarrow$$
$$\Leftrightarrow \overline{\frac{\rho u_i u_i}{2}} = \frac{\overline{\rho}\tilde{u}_i\tilde{u}_i}{2} + \overline{\rho u_i''}\tilde{u}_i + \overline{\frac{\rho u_i'' u_i''}{2}} \Leftrightarrow \overline{\frac{\rho u_i u_i}{2}} = \frac{\overline{\rho}\tilde{u}_i\tilde{u}_i}{2} + \overline{\frac{\rho u_i'' u_i''}{2}} \tag{B.51}$$

The averaging process of each term of the left side of equation (B.49) are:

$$\overline{\frac{\partial(KE)}{\partial t}} = \frac{\partial}{\partial t}\left(\frac{\overline{\rho}\tilde{u}_i\tilde{u}_i}{2} + \overline{\frac{\rho u_i'' u_i''}{2}}\right) \tag{B.52}$$

$$\overline{\frac{\partial\left(u_j\,KE\right)}{\partial x_j}} = \frac{\partial}{\partial x_j}\overline{\left(\left(\tilde{u}_j + u_j''\right)KE\right)} \Leftrightarrow \overline{\frac{\partial\left(u_j\,KE\right)}{\partial x_j}} = \frac{\partial\left(\tilde{u}_j\,\overline{KE}\right)}{\partial x_j} + \frac{\partial\left(\overline{u_j''\,KE}\right)}{\partial x_j} \Leftrightarrow$$
$$\Leftrightarrow \overline{\frac{\partial\left(u_j\,KE\right)}{\partial x_j}} = \frac{\partial}{\partial x_j}\left[\tilde{u}_j\left(\frac{\overline{\rho}\tilde{u}_i\tilde{u}_i}{2} + \overline{\frac{\rho u_i'' u_i''}{2}}\right)\right] + \frac{\partial\left(\overline{u_j''\,KE}\right)}{\partial x_j} \tag{B.53}$$

The last term in equation (B.53) can be extended as:

$$\begin{aligned}
&\frac{\partial\left(\overline{u_j''\,KE}\right)}{\partial x_j}=\frac{\partial}{\partial x_j}\left(\overline{u_j''\,\frac{\rho u_i u_i}{2}}\right)\Leftrightarrow\\
&\Leftrightarrow\frac{\partial\left(\overline{u_j''\,KE}\right)}{\partial x_j}=\frac{\partial}{\partial x_j}\left(\overline{u_j''\,\frac{\rho\left(\tilde{u}_i\tilde{u}_i+2\tilde{u}_i u_i''+u_i''u_i''\right)}{2}}\right)\Leftrightarrow\\
&\Leftrightarrow\frac{\partial\left(\overline{u_j''\,KE}\right)}{\partial x_j}=\frac{\partial}{\partial x_j}\left(\frac{\overline{\rho u_j''}\tilde{u}_i\tilde{u}_i}{2}\right)+\frac{\partial}{\partial x_j}\left(\overline{\rho u_j''u_i''}\tilde{u}_i\right)+\frac{\partial}{\partial x_j}\left(\overline{u_j''\,\frac{\rho u_i''u_i''}{2}}\right)\Leftrightarrow\\
&\Leftrightarrow\frac{\partial\left(\overline{u_j''\,KE}\right)}{\partial x_j}=\frac{\partial}{\partial x_j}\left(\overline{\rho u_j''u_i''}\tilde{u}_i\right)+\frac{\partial}{\partial x_j}\left(\overline{u_j''\,\frac{\rho u_i''u_i''}{2}}\right)
\end{aligned}\tag{B.54}$$

The averaging process for the right side equation terms is given by:

$$\begin{aligned}
&\overline{u_i\frac{\partial p}{\partial x_i}}=\overline{\left(\tilde{u}_i+u_i''\right)\frac{\partial(\overline{p}+p')}{\partial x_i}}\Leftrightarrow\overline{u_i\frac{\partial p}{\partial x_i}}=\overline{\left(\tilde{u}_i+u_i''\right)\left(\frac{\partial\overline{p}}{\partial x_i}+\frac{\partial p'}{\partial x_i}\right)}\Leftrightarrow\\
&\Leftrightarrow\overline{u_i\frac{\partial p}{\partial x_i}}=\tilde{u}_i\frac{\partial\overline{p}}{\partial x_i}+\overline{u_i''}\frac{\partial\overline{p}}{\partial x_i}+\overline{u_i''\frac{\partial p'}{\partial x_i}}
\end{aligned}\tag{B.55}$$

$$\begin{aligned}
&\overline{u_i\frac{\partial\tau_{ji}}{\partial x_i}}=\overline{\left(\tilde{u}_i+u_i''\right)\frac{\partial\tau_{ji}}{\partial x_i}}\Leftrightarrow\overline{u_i\frac{\partial\tau_{ji}}{\partial x_i}}=\overline{\tilde{u}_i\frac{\partial\left(\tilde{\tau}_{ji}+\tau_{ji}''\right)}{\partial x_i}}+\overline{u_i''\frac{\partial\tau_{ji}}{\partial x_i}}\Leftrightarrow\\
&\Leftrightarrow\overline{u_i\frac{\partial\tau_{ji}}{\partial x_i}}=\tilde{u}_i\frac{\partial\tilde{\tau}_{ji}}{\partial x_i}+\overline{u_i''\frac{\partial\tau_{ji}}{\partial x_i}}
\end{aligned}\tag{B.56}$$

The general equation averaged for kinetic energy has the form of:

$$\begin{aligned}
&\frac{\partial}{\partial t}\left(\frac{\overline{\rho}\tilde{u}_i\tilde{u}_i}{2}+\frac{\overline{\rho u_i''u_i''}}{2}\right)+\frac{\partial}{\partial x_j}\left[\tilde{u}_j\left(\frac{\overline{\rho}\tilde{u}_i\tilde{u}_i}{2}+\frac{\overline{\rho u_i''u_i''}}{2}\right)\right]+\frac{\partial}{\partial x_j}\left(\overline{\rho u_j''u_i''}\tilde{u}_i\right)+\\
&+\frac{\partial}{\partial x_j}\left(\overline{u_j''\,\frac{\rho u_i''u_i''}{2}}\right)=-\tilde{u}_i\frac{\partial\overline{p}}{\partial x_i}-\overline{u_i''}\frac{\partial\overline{p}}{\partial x_i}-\overline{u_i''\frac{\partial p'}{\partial x_i}}+\tilde{u}_i\frac{\partial\tilde{\tau}_{ji}}{\partial x_i}+\overline{u_i''\frac{\partial\tau_{ji}}{\partial x_i}}
\end{aligned}\tag{B.57}$$

To better explain, some terms of equation (B.57) are coloured. The terms that belong to the mean kinetic energy equation are coloured in orange, for the turbulent kinetic energy in blue and purple the ones that need to be manipulated in order to separate the turbulent term from the average.

The purple term from equation (B.57) can be written as:

$$\frac{\partial}{\partial x_j}\left(\overline{\rho u_j''u_i''}\tilde{u}_i\right)=\tilde{u}_i\frac{\partial\left(\overline{\rho u_j''\,u_i''}\right)}{\partial x_j}+\overline{\rho u_j''\,u_i''}\frac{\partial\tilde{u}_i}{\partial x_j}\tag{B.58}$$

Recalling that:

$$\frac{\overline{\rho u_i''u_i''}}{2}=\overline{\rho}k\tag{B.59}$$

Finally, the mean and turbulent kinetic energy can be expressed as:

$$\frac{\partial}{\partial t}\left(\frac{\overline{\rho}\tilde{u}_i\tilde{u}_i}{2}\right)+\frac{\partial}{\partial x_j}\left(\tilde{u}_j\frac{\overline{\rho}\tilde{u}_i\tilde{u}_i}{2}\right)+\tilde{u}_i\frac{\partial\left(\overline{\rho u_j''\,u_i''}\right)}{\partial x_j}=-\tilde{u}_i\frac{\partial\overline{p}}{\partial x_i}+\tilde{u}_i\frac{\partial\tilde{\tau}_{ji}}{\partial x_i} \tag{B.60}$$

$$\frac{\partial(\overline{\rho}k)}{\partial t}+\frac{\partial\left(\overline{\rho}k\tilde{u}_j\right)}{\partial x_j}+\overline{\rho u_j''\,u_i''}\frac{\partial\tilde{u}_i}{\partial x_j}+\frac{\partial}{\partial x_j}\left(\overline{u_j''\frac{\rho u_i''u_i''}{2}}\right)= \\ =-\overline{u_i''}\frac{\partial\overline{p}}{\partial x_i}-\overline{u_i''\frac{\partial p'}{\partial x_i}}+\overline{u_i''\frac{\partial\tau_{ji}}{\partial x_i}} \tag{B.61}$$

Equation (B.61) can be written in a more common way, by extending the two last terms as:

$$-\overline{u_i''\frac{\partial p'}{\partial x_i}}=-\frac{\partial\left(\overline{u_i''p'}\right)}{\partial x_i}+\overline{p'\frac{\partial u_i''}{\partial x_i}} \tag{B.62}$$

$$\overline{u_i''\frac{\partial\tau_{ji}}{\partial x_j}}=\frac{\partial\left(\overline{u_i''\tau_{ji}}\right)}{\partial x_j}-\overline{\tau_{ji}\frac{\partial u_i''}{\partial x_j}} \tag{B.63}$$

Replacing the terms in equations (B.62) and (B.63) in (B.61), the turbulent kinetic energy transport equation can be expressed as:

$$\frac{\partial(\overline{\rho}k)}{\partial t}+\frac{\partial\left(\overline{\rho}k\tilde{u}_j\right)}{\partial x_j}=\left[-\overline{\rho u_j''\,u_i''}\frac{\partial\tilde{u}_i}{\partial x_j}\right]+\left[-\overline{\tau_{ji}\frac{\partial u_i''}{\partial x_j}}\right]+\left[-\overline{u_i''}\frac{\partial\overline{p}}{\partial x_i}+\overline{p'\frac{\partial u_i''}{\partial x_i}}\right]+ \\ +\left[-\frac{\partial\left(\overline{u_i''p'}\right)}{\partial x_i}+\frac{\partial\left(\overline{u_i''\tau_{ji}}\right)}{\partial x_j}-\frac{\partial}{\partial x_j}\left(\overline{u_j''\frac{\rho u_i''u_i''}{2}}\right)\right] \tag{B.64}$$

Major differences between the HEM-e and HEM-h models

This appendix presents the equations used in the enthalpy-based energy equation model (HEM-h) and highlights the key differences compared to the internal energy-based equation model (HEM-e).

The HEM-h model was first applied to steady-state ejector flow simulations by Smolka et al. (2013). Its transport equation is expressed as:

$$\frac{\partial\left(\overline{\rho}\widetilde{h}\,\tilde{u}_j\right)}{\partial x_j}-\frac{\partial}{\partial x_j}\left(\left(\frac{\mu_T}{\sigma_T}+\kappa/\left(\frac{\partial\tilde{h}}{\partial T}\right)_p\right)\frac{\partial\widetilde{h}}{\partial x_i}\right)=\dot{S}_{1\mathrm{h}}+\dot{S}_{2\mathrm{h}}+\dot{S}_{3\mathrm{h}} \tag{C.1}$$

In equation (C.1) $\dot{S}_{1\mathrm{h}}$, $\dot{S}_{2\mathrm{h}}$ and $\dot{S}_{3\mathrm{h}}$ represent source terms corresponding to mechanical energy, the irreversible dissipation of kinetic energy fluctuation, and the dissipation of turbulent kinetic energy, respectively. These source terms are defined as follows:

$$\dot{S}_{1\mathrm{h}}=\tilde{u}_i\frac{\partial\overline{p}}{\partial x_i} \tag{C.2}$$

$$\dot{S}_{2\mathrm{h}}=(\mu+\mu_T)\cdot\left\{2\cdot\left[\left(\frac{\partial\tilde{u}}{\partial x}\right)^2+\left(\frac{\partial\tilde{v}}{\partial y}\right)^2+\left(\frac{\partial\tilde{w}}{\partial z}\right)^2\right]+\left(\frac{\partial\tilde{u}}{\partial y}+\frac{\partial\tilde{v}}{\partial x}\right)^2+\left(\frac{\partial\tilde{u}}{\partial z}+\frac{\partial\tilde{w}}{\partial y}\right)^2+\left(\frac{\partial\tilde{v}}{\partial z}+\frac{\partial\tilde{w}}{\partial y}\right)^2\right\}-\frac{2}{3}\cdot\bar{\rho}\cdot k\cdot\frac{\partial\tilde{u}_k}{\partial x_k} \tag{C.3}$$

$$\dot{S}_{3\mathrm{h}}=-\overline{\rho}\cdot\tilde{u}_i\cdot\frac{\partial k}{\partial x_k} \tag{C.4}$$

Both models share similar terms and approaches for modelling the transport equation. However, the internal energy-based equation (HEM-e) explicitly incorporates pressure dependency in its formulation, resulting in additional terms that are absent in the HEM-h model. These terms are the pressure dilatation (C.5) and pressure work (C.6), defined as:

$$p_{\mathrm{d}}=\overline{\frac{p'\partial u_i''}{\partial x_i}} \tag{C.5}$$

$$p_{\mathrm{w}}=\overline{u_i''}\frac{\partial\overline{p}}{\partial x_i} \tag{C.6}$$

When the enthalpy is Favre-averaged, the term associated with turbulent transport is modelled using the Boussinesq hypothesis. In this process, the effects of pressure dilatation and pressure work are embedded within the turbulent dissipation term. Consequently, while the HEM-h model indirectly accounts for these effects, they are not explicitly represented in its formulation, unlike the HEM-e model. This distinction underscores the enhanced accuracy of HEM-e in capturing compressibility effects and high-speed flow dynamics.

C.1 Integration of the Homogeneous Equilibrium Model enthalpy-based (HEM-h) with UDFs

Figure C.1 shows the enthalpy transport equation (Equation (C.1)) along with the macros required to resolve its terms.

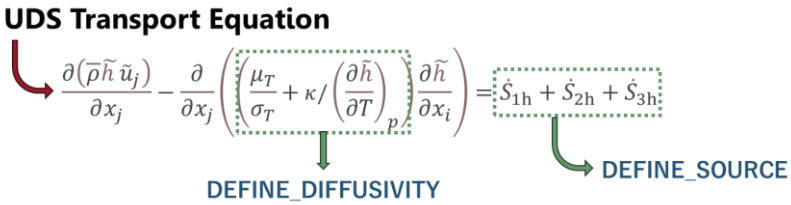


Figure C.1 –Transport equation of the UDS enthalpy, and identification of the model specific macros to compute the diffusivity term and sources.

In total, three source terms were defined for the RANS model. Figure C.2 presents the sources for a 3D simulation, while Figure C.3 demonstrates those for a 2D axisymmetric case. For this UDF two DEFINE_ON_DEMAND were implemented to allow optional execution, reducing computational overhead to compute the temperature and vapor quality.

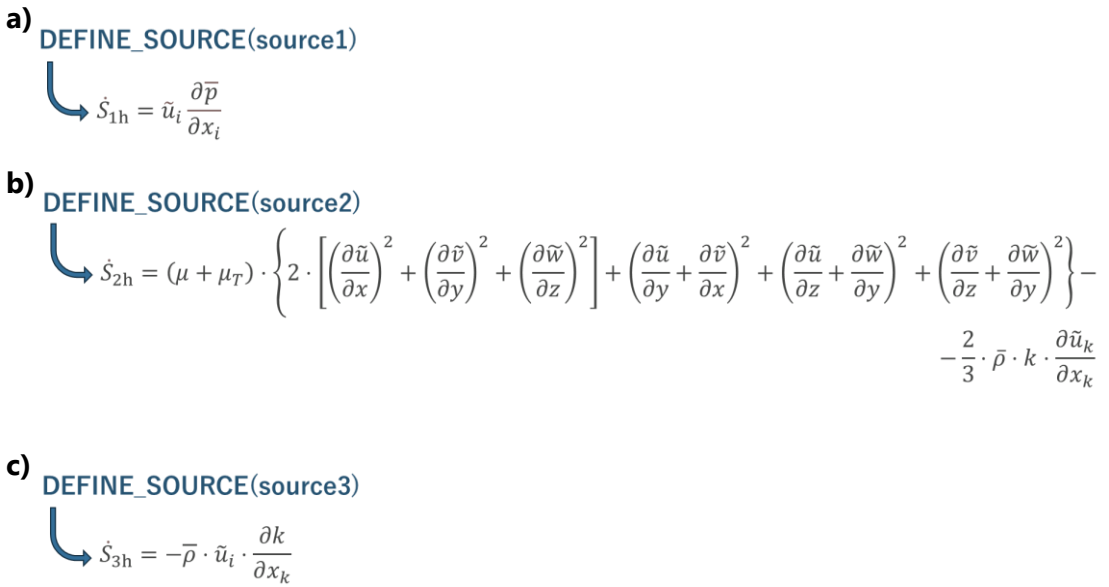


Figure C.2 – Sources for the enthalpy transport equation for a 3D simulation: a) mechanical energy; b) irreversible dissipation of kinetic energy fluctuation; c) dissipation of turbulent kinetic energy.

a) DEFINE_SOURCE(source1)

$$\dot{S}_{1h} = \tilde{u}\frac{\partial \overline{p}}{\partial x} + \tilde{v}\frac{\partial \overline{p}}{\partial y}$$

b) DEFINE_SOURCE(source2)

$$\dot{S}_{2h} = (\mu + \mu_T)\cdot\left\{2\cdot\left[\left(\frac{\partial \tilde{u}}{\partial x}\right)^2 + \left(\frac{\tilde{v}}{y}\right)^2 + \left(\frac{\partial \tilde{v}}{\partial y}\right)^2\right] + \left(\frac{\partial \tilde{u}}{\partial y} + \frac{\partial \tilde{v}}{\partial x}\right)^2 - \frac{2}{3}\left(\frac{\partial \tilde{u}}{\partial x} + \frac{\tilde{v}}{y} + \frac{\partial \tilde{v}}{\partial y}\right)^2\right\} -$$

$$-\frac{2}{3}\cdot\bar{\rho}\cdot k\cdot\left(\frac{\partial \tilde{u}}{\partial x} + \frac{\tilde{v}}{y} + \frac{\partial \tilde{v}}{\partial y}\right)$$

c) DEFINE_SOURCE(source3)

$$\dot{S}_{3h} = -\overline{\rho}\cdot\left(\tilde{u}\cdot\frac{\partial k}{\partial x} + \tilde{v}\cdot\frac{\partial k}{\partial y}\right)$$

Figure C.3 – Sources for the enthalpy transport equation for a 2D axisymmetric simulation: a) mechanical energy; b) irreversible dissipation of kinetic energy fluctuation; c) dissipation of turbulent kinetic energy.

Experimental setup details

D.1 R1234ze-E - Experimental setup and instrumentation details

Details about the experimental work can be found in Śmierciew et al. (2017).

Figure 5.1 illustrates a diagram of the experimental setup and the corresponding p-h diagram.

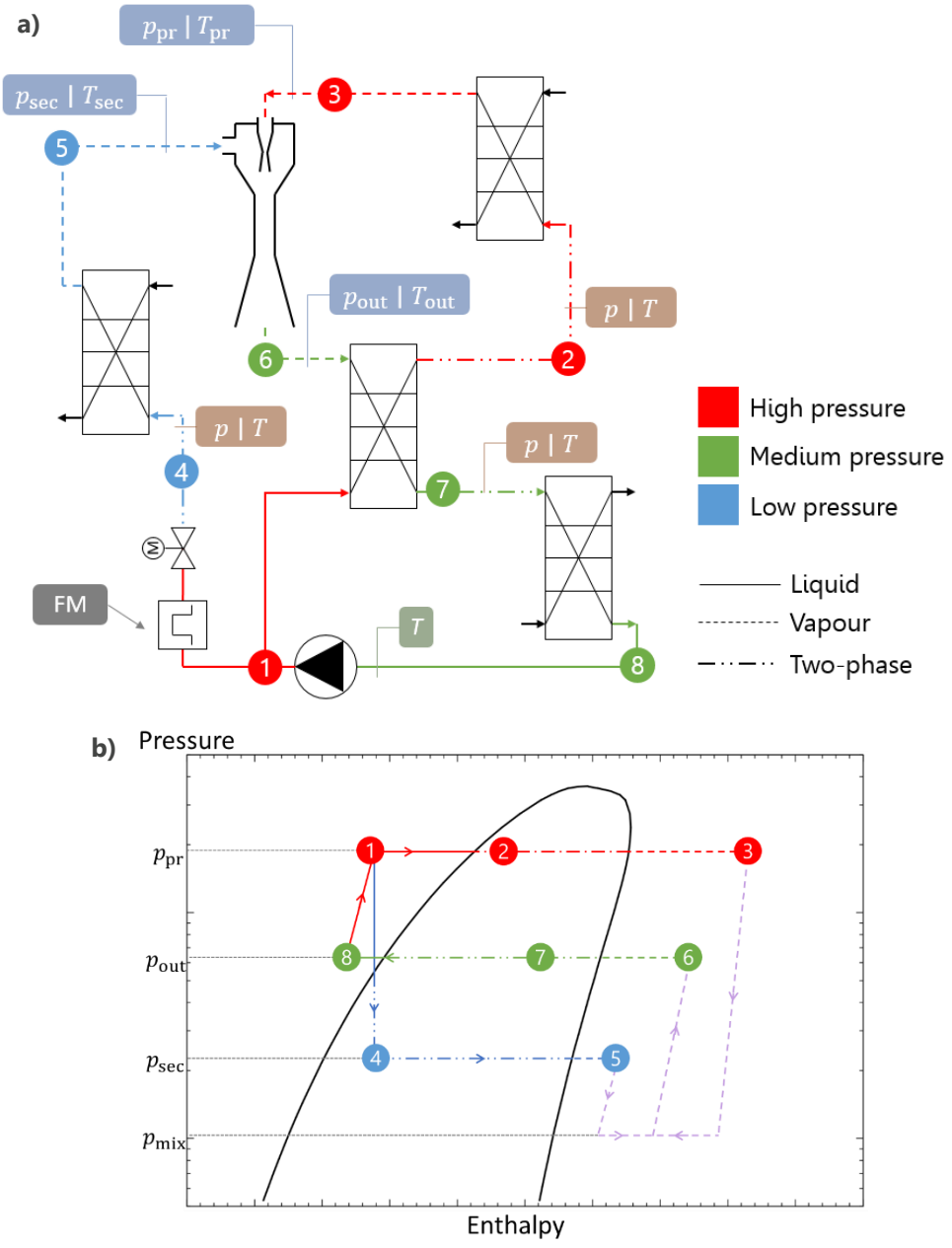


Figure D.1 - Simplified diagram of the ejector test rig (a) and the corresponding theoretical p-h diagram (b).

D.1.1 Experimental Setup

- Division and Expansion (1 → 2): The high-pressure liquid is divided; one part goes to a heat exchanger, and the rest is expanded in the throttling valve (1 → 4).
- Vapour Generation (2 → 3): The flow enters a vapour generator, where the liquid is completely evaporated to reach superheated vapour, which then enters the ejector as the motive flow.
- Evaporation (4 → 5): The expanded liquid (4) evaporates until it reaches superheated vapour and is entrained through the ejector suction chamber.
- Ejector (3 + 5 → 6): The high-pressure vapour expands inside the ejector and entrains the low-pressure vapour. The flow leaves the ejector as a single-phase mixture.
- Heat Exchange (6 → 7): The ejector outflow pre-heats the high-pressure liquid (1) in an internal heat exchanger.
- Condensation (7 → 8): The vapour is condensed until it reaches a liquid state.
- Pressurisation (8 → 1): The liquid pressure is increased in the pump.

D.1.2 Measurement Points and Parameters

- Motive flow properties: pressure and temperature measured immediately before the motive chamber inlet (p_{pr}, T_{pr}).
- Entrained flow properties: pressure and temperature assessed inside the suction chamber (p_{sec}, T_{sec}) and the flow meter (FM) measures the entrained flow rate ($\dot{m}_{sec}$).
- Outflow properties: pressure and temperature assessed in the diffuser outlet (p_{out}, T_{out}).
- Profile of the flow inside the ejector:
    - Seven temperature sensors are mounted inside the entrained flow convergent, five in the constant area section and one in the diffuser, all positioned perpendicular to the stream in glands.
    - Seven pressure transducers are mounted in the wall of the entrained flow convergent, in the ejector's constant area section and one in the diffuser.
- Other points of interest: temperature sensors, pressure transducers and flow meters are positioned at various points on the testing stand that are not illustrated in Figure 5.1a).

D.1.3 Measurement Instruments

- Temperature measurement: Resistance Temperature Detector (RTD – Pt100) with accuracy of 0.20%;
- Pressure measurement: pressure transducers with accuracy of 0.25%;
    - Scale: 0-2.5 MPa to the motive stream;
    - Scale: 0-1 MPa to the other locations
- Density and flow rate measurement: Coriolis mass flow meters with accuracy of 0.15%.

D.2 CO_2 - Experimental setup and instrumentation details

Figure D.2 illustrates a diagram of the experimental setup and the corresponding p-h diagram.

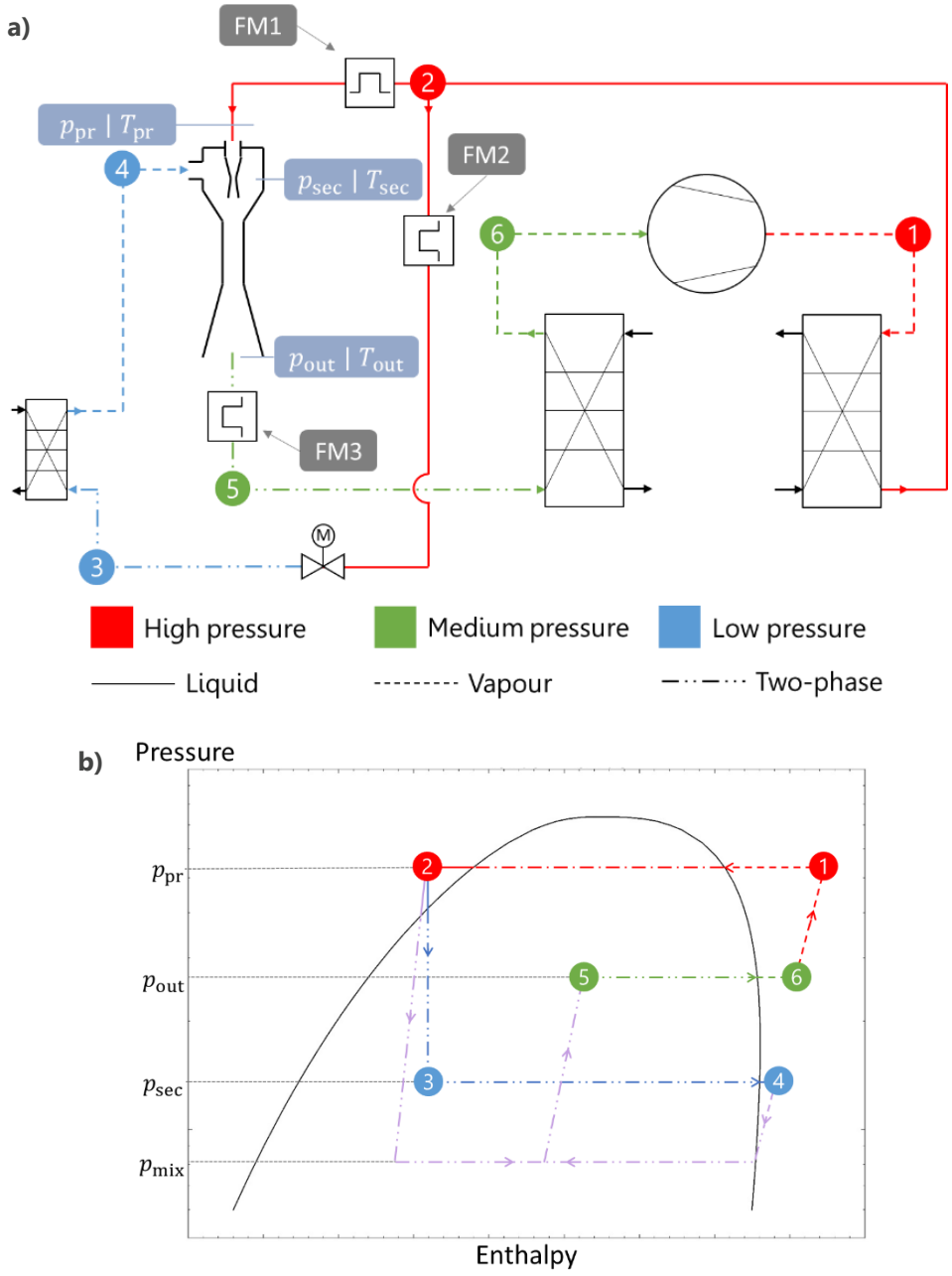


Figure D.2 - Simplified diagram of the ejector test rig (a) and the corresponding theoretical p-h diagram (b).

D.2.1 Experimental Setup

- Condensation (1 → 2): The high-pressure vapour is condensed until it reaches a liquid state.

- Division and Expansion (2): The high-pressure liquid is divided; one part supplies the ejector nozzle with the primary mass flow, and the rest is expanded in the throttling valve (2 → 3).
- Evaporation (3 → 4): The expanded liquid (3) evaporates until it reaches a superheated vapour state and is entrained through the ejector suction chamber.
- Ejector (2 + 4 → 5): The high-pressure liquid expands inside the ejector and entrains the low-pressure vapour. The flow leaves the ejector as a two-phase mixture.
- Evaporation (5 → 6): The two-phase flow evaporates completely until it becomes superheated vapour.
- Compression (6 → 1): The vapour pressure is increased in the compressor.

D.2.2 Measurement Points and Parameters

- Motive flow properties: pressure and temperature measured immediately before the motive chamber inlet (p_{pr}, T_{pr}) and the flow meter (FM1) determines flow density (ρ_{pr}) and mass flow rate ($\dot{m}_{pr}$).
- Entrained flow properties: pressure and temperature assessed inside the suction chamber (p_{sec}, T_{sec}) and the flow meter (FM2) measures the entrained flow rate ($\dot{m}_{sec}$).
- Outflow properties: pressure and temperature assessed in the diffuser outlet (p_{out}, T_{out}) and the flow meter (FM3) measures the fluid density (ρ_{out}).
- Profile of the flow inside the ejector:
  - Seven temperature sensors mounted inside the constant area section and diffuser in glands, positioned perpendicular to the stream.
  - Four pressure sensors mounted in the wall of the ejector's constant area section.

D.2.3 Measurement Instruments

- Temperature measurement: calibrated type T-thermocouples (Czaki TP-201 and TP-361);
  - Accuracy ±0.4 K within specified test range;
  - Mutual deviations ≤ ±0.1 K.
- Pressure measurement: WIKA S-10 pressure transmitters;
  - Pressure span 1,000 psi (6.89 MPa);
  - Accuracy < 0.25% of span.
- Density and flow rate measurement: Endress+Hauser Coriolis mass flow meters;
  - Maximum measurement uncertainty:
    → 0.1% for liquids and 0.5% for gases in terms of mass flow rate;
    → ±0.5 kg/m³ for liquid density.

Turbulence Modelling Parameters and Terms in FLUENT

This appendix details the key terms and equations used in the FLUENT turbulence modelling framework. The equations for turbulent viscosity, turbulent Prandtl numbers, turbulent kinetic energy dissipation, specific dissipation rate production, and cross-diffusion terms are provided, alongside the relevant definitions and blending functions.

E.1 Turbulent viscosity

The turbulent viscosity (μ_T) is defined as:

$$\mu_T = \frac{\overline{\rho}k}{\omega}\frac{1}{\max\left[\frac{1}{\alpha^*}, \frac{S\,F_2}{0.31\omega}\right]} \tag{E.1}$$

In Equation (E.1) S represents the strain rate magnitude:

$$S = \sqrt{2\,\widetilde{S}_{ij}\,\widetilde{S}_{ij}} \tag{E.2}$$

In Equation (E.1) the coefficient α^* damps the turbulent viscosity causing a low-Reynolds number correction, and is defined by:

$$\alpha^* = \left(\frac{\alpha_0^* + \frac{Re_T}{R_k}}{1 + \frac{Re_T}{R_k}}\right) \tag{E.3}$$

The damping functions, as well as the constants used in this model are expressed as follows:

$$Re_T = \frac{\overline{\rho}k}{\mu\omega} \tag{E.4}$$

$$R_k = 6 \tag{E.5}$$

$$\alpha_0^* = \frac{\beta_i}{3} \tag{E.6}$$

$$\beta_i = F_1 0.075 + (a - F_1)0.0828 \tag{E.7}$$

$$F_2 = \tanh\left(\left[max\left\{\frac{2\sqrt{k}}{0.09\omega y}, \frac{500\mu}{\overline{\rho}y^2\omega}\right\}\right]^2\right) \tag{E.8}$$

Where y is the distance to the next surface.

E.2 Turbulent Prandtl number for k and ω

The turbulent Prandtl numbers for k (σ_k) and ω (σ_ω) are defined as:

$$\sigma_k = \frac{1}{\frac{F_1}{1.176} + 1 - F_1} \tag{E.9}$$

$$\sigma_\omega = \frac{1}{\frac{F_1}{2} + \frac{1 - F_1}{1.168}} \tag{E.10}$$

Where F_1 is a blending function defined as:

$$F_1 = \tanh(\phi_1^4) \tag{E.11}$$

The argument ϕ_1 is computed as:

$$\phi_1 = \min\left[\max\left(\frac{\sqrt{k}}{0.09\omega y}, \frac{500\mu}{\overline{\rho} y^2 \omega}\right), \frac{4\overline{\rho} k}{1.168 D_\omega^+ y^2}\right] \tag{E.12}$$

In equation (E.12) D_ω^+ is the positive portion of the cross-diffusion term, defined as:

$$D_\omega^+ = \max\left[\frac{2\overline{\rho}}{1.168\omega}\frac{\partial k}{\partial x_j}\frac{\partial \omega}{\partial x_j}, 10^{-10}\right] \tag{E.13}$$

E.3 Turbulent kinetic energy dissipation

The dissipation term for turbulent kinetic energy includes the coefficient β_i^*, which is defined as:

$$\beta_i^* = 0.09\left(\frac{\frac{4}{15} + \left(\frac{Re_T}{R_\beta}\right)^4}{1 + \left(\frac{Re_T}{R_\beta}\right)}\right) \tag{E.14}$$

where $R_\beta = 8$.

E.4 Specific dissipation rate production

The production term for the specific dissipation rate is expressed as:

$$-\overline{\rho u_i'' u_j''}\frac{\alpha\omega}{k}\frac{\partial \tilde{u}_i}{\partial x_j} \tag{E.15}$$

Here, the ratio $\alpha\omega/k$ is defined as:

$$\frac{\alpha\omega}{k} = \frac{\alpha^{\#}\overline{\rho}}{\mu_T} \tag{E.16}$$

With:

$$\alpha^{\#} = \alpha_{\infty}\left(\frac{\alpha_0^* + \frac{Re_T}{R_\omega}}{1 + \frac{Re_T}{R_\omega}}\right) \tag{E.17}$$

In equation (E.17) R_ω is a constant with value 2.95. The coefficient α_∞ is computed using:

$$\alpha_\infty = F_1\alpha_{\infty,1} + (1 - F_1)\alpha_{\infty,2} \tag{E.18}$$

With:

$$\alpha_{\infty,1} = \frac{0.075}{0.09} - \frac{0.41^2}{2\sqrt{0.09}} \tag{E.19}$$

$$\alpha_{\infty,2} = \frac{0.0828}{0.09} - \frac{0.41^2}{1.168\sqrt{0.09}} \tag{E.20}$$

E.5 Specific dissipation rate dissipation

The dissipation term for the specific dissipation rate is given by:

$$\beta = \beta_i\left[1 - \frac{\beta_i^*}{\beta_i}1.5f(Ma_T)\right] \tag{E.21}$$

where β_i and β_i^* are defined in earlier equations.

E.6 Cross-diffusion

The cross-diffusion term is characterised by the coefficient σ_d:

$$\sigma_d = \frac{2(1 - F_1)}{1.168} \tag{E.22}$$

Properties interpolation algorithm

Figure F.1 shows the flow chart of the interpolation algorithm. Here, x is a thermodynamic property, the caps variables (as X, P and E) identify the corresponding property matrix. In this code, in case of the cell pressure (p) or internal energy (e) falls out of the range, the specific property will be set for the maximum or minimum pressure/internal energy.

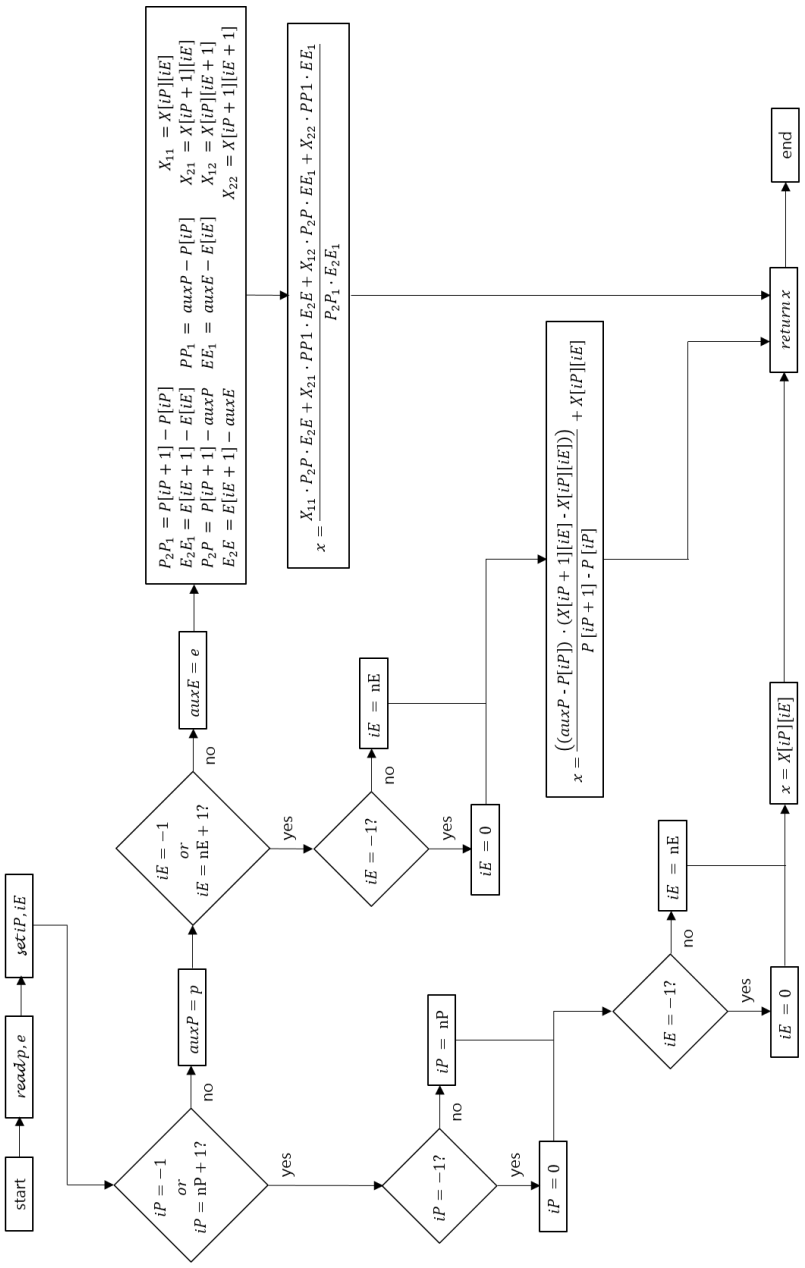


Figure F.1 – Flow chart of the interpolation algorithm.

Figure F.2 illustrates the flow chart of the algorithm used to calculate iP (for iU the algorithm is same). In this context, p represents the pressure read at the cell center, [0]

and $p[\mathrm{nP}]$ are the minimum and maximum pressures in the property table. If the pressure at the cell center is below the minimum tabled pressure, iP is assigned a value of -1; if it is higher than the maximum, iP is set to $\mathrm{nP}+1$. This allows for easy verification of whether the cell center pressure falls within the table pressure range.

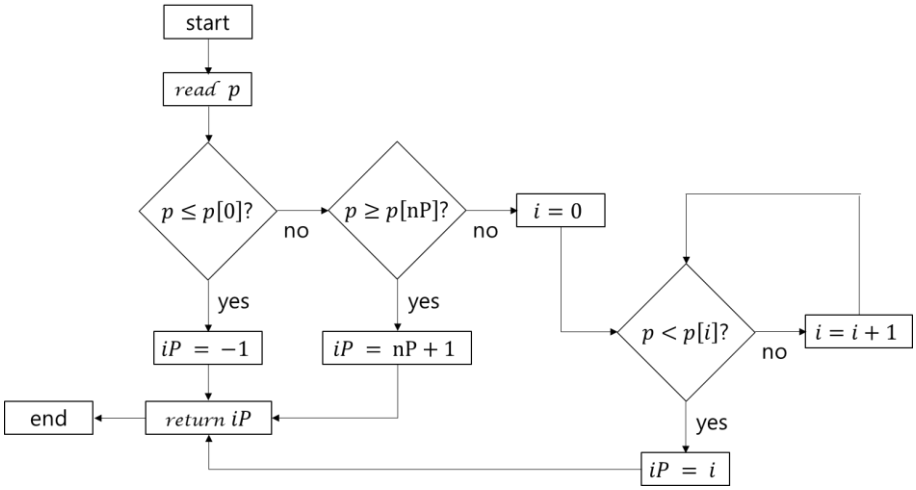


Figure F.2 – Flow chart of the algorithm of the function used to compute iP.

Sound speed models assessment – the impact on the numerical simulations

This appendix compares the HEM-e model using Brennen's (2005) sound speed model (HEM-e-B) and Lund and Flåtten's (2010) model (HEM-e-LF).

Figures G.1 and G.2 show that the pressure and density profiles remain nearly identical for both sound speed models, with no visible differences along the ejector axis. However, Figures G.3 and G.4 reveal minor discrepancies in specific internal energy and vapour quality, particularly at the end of the constant area section and near the diffuser inlet (x ≈ 40 mm). The HEM-e-LF model predicts slightly higher internal energy and vapour quality compared to HEM-e-B.

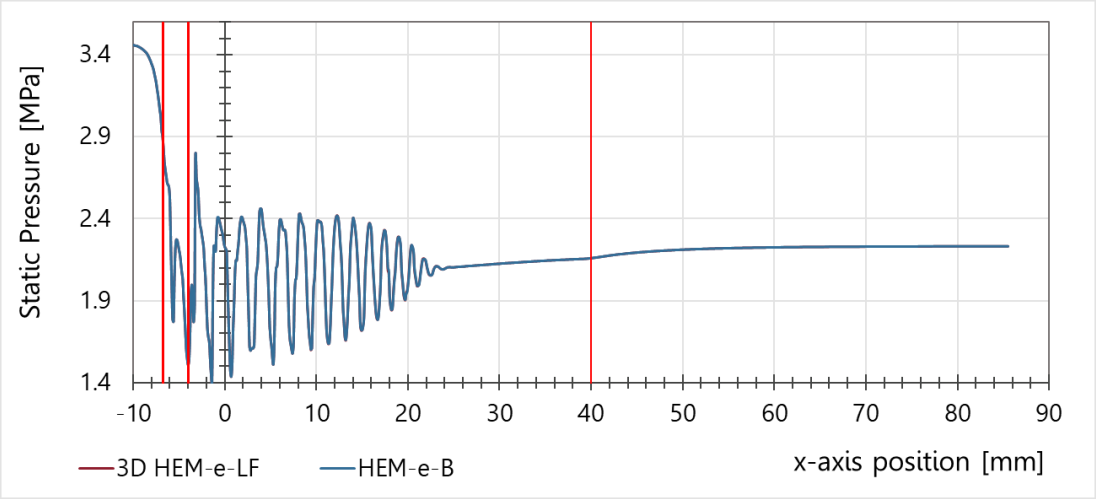


Figure G.1 – Predicted pressure profiles along the ejector axis.

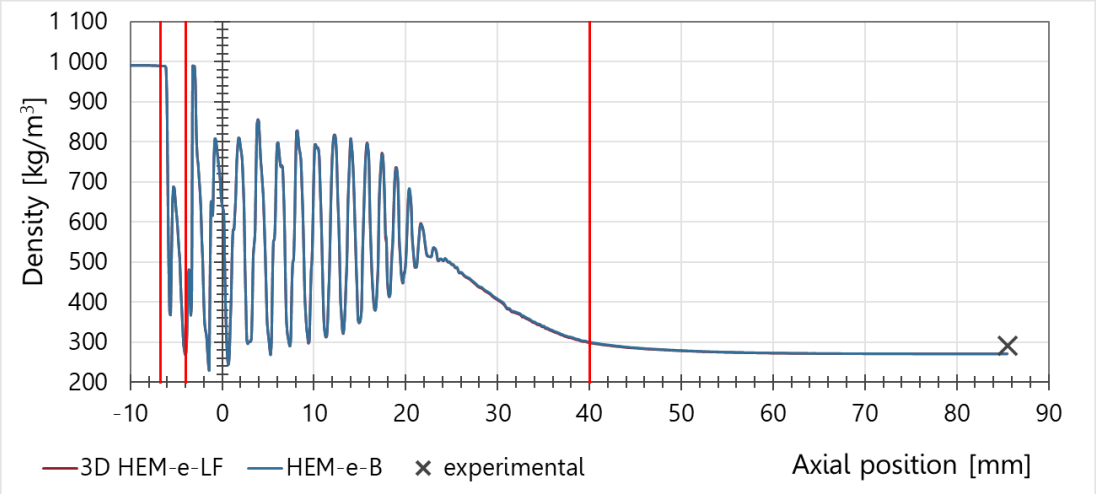


Figure G.2 – Predicted density profiles along the ejector axis.

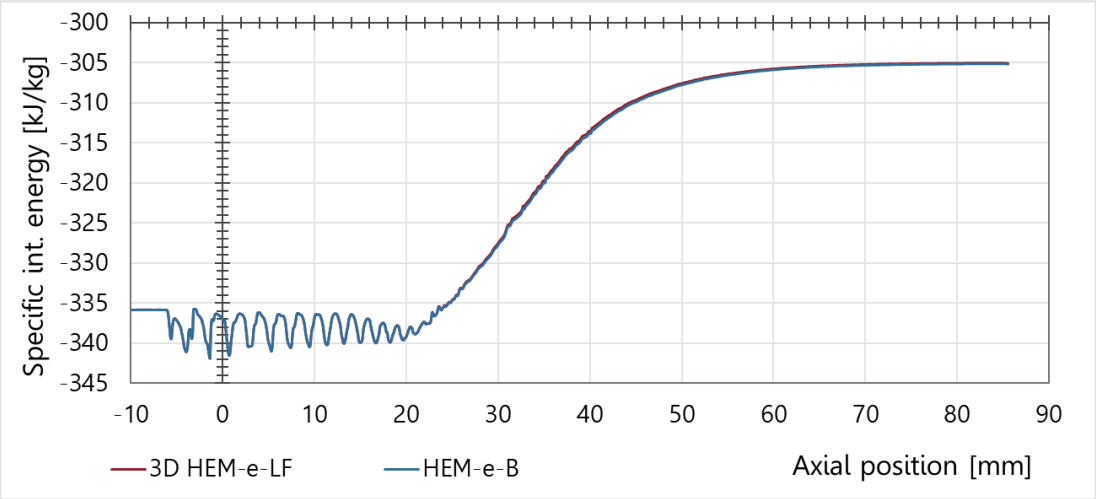


Figure G.3 – Predicted specific internal energy profiles along the ejector axis.

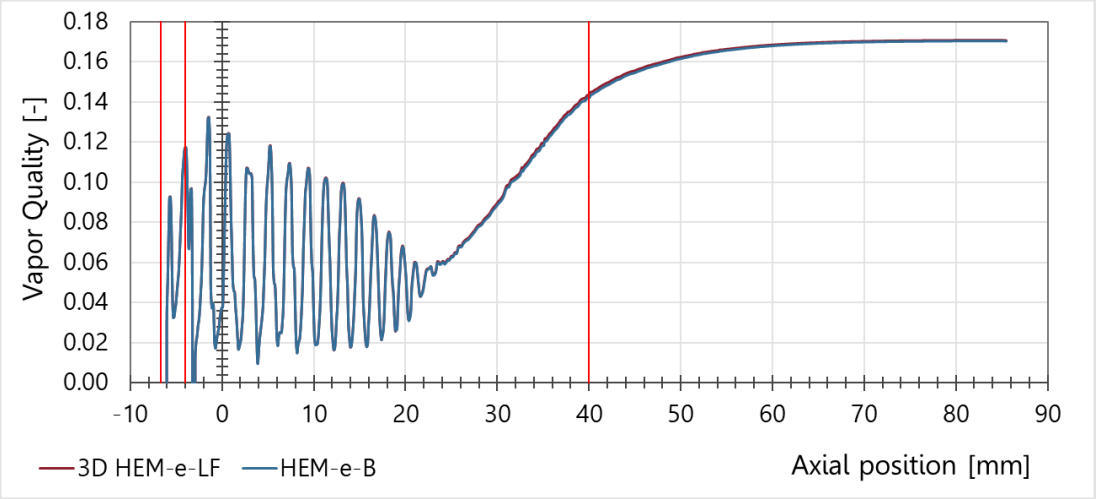


Figure G.4 – Predicted vapour quality profiles along the ejector axis.

Figure G.5 illustrates the sound speed along the ejector axis for both models. Although the profiles appear similar, they are offset, with HEM-e-B consistently predicting higher sound speed values. This offset impacts the Mach number, and consequently, the vapour quality and internal energy predictions.

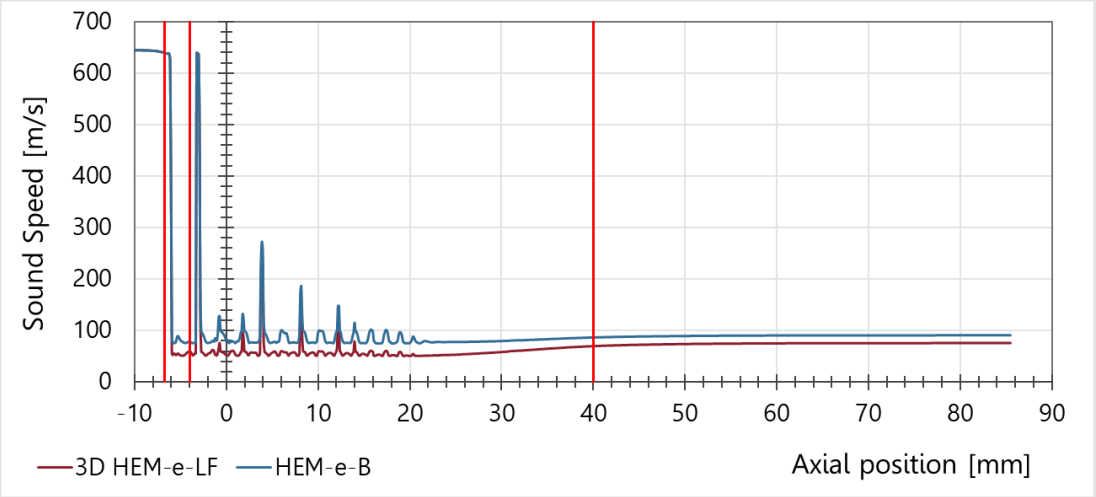


Figure G.5 – Predicted sound speed along the ejector axis.

As explained in Section 4.3.1, the developed HEM-e model incorporates five different sound speed models, offering flexibility for users to select the most appropriate option. The models and references are as follows:

- B: Brennen (2005);
- LF: Lund and Flatten (2010);
- NWG: Nguyen, Winter, and Greiner (1981);
- AAO: Ameur, Aidoun, and Ouzzane (2016);
- GMM: Giacomelli, Mazzelli, and Milazzo (2018).

The Mach numbers computed using each model are compared in Figure G.6. Brennen's model predicts the highest Mach numbers and is the only one achieving supersonic flow at the motive nozzle, aligned with the ejector's operating curve. The AAO model produces results similar to LF, while NWG predicts the lowest Mach numbers.

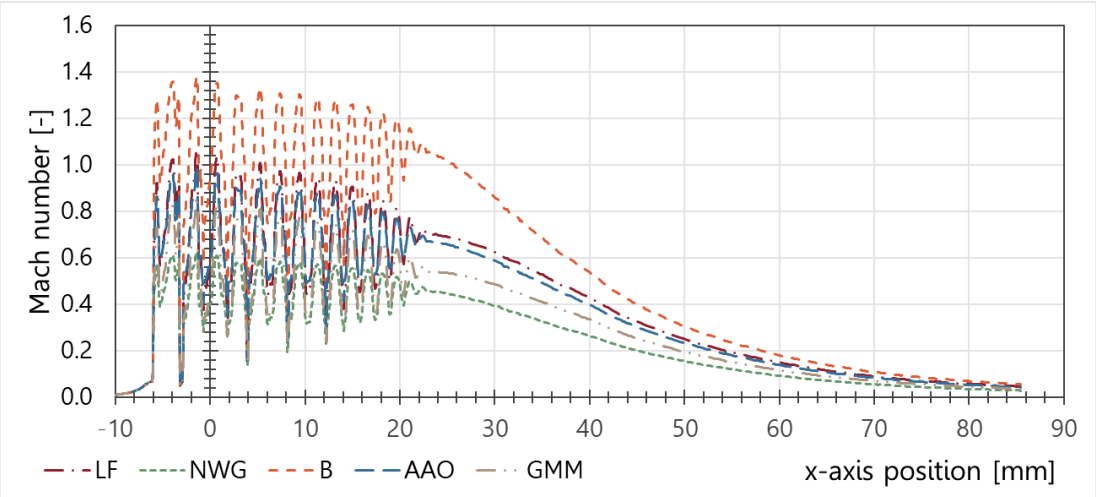


Figure G.6 – Predicted Mach number profiles along the ejector axis for different sound speed models.

The results indicate that Brennen's (2005) sound speed model is the most accurate for simulating the operating regime observed in this study. Its predictions of choked flow and supersonic behaviour at the motive nozzle align closely with the ejector operating curve.